Graphene based mechanical and electronic devices in optimized environments : from suspended graphene to in-situ grown graphene/boron nitride heterostructures

Hadi Arjmandi-Tash

UNIVERSITÉ DE GRENOBLE

THÈSE

Pour obtenir le grade de

DOCTEUR DE L'UNIVERSITÉ DE GRENOBLE

Spécialité: **Nano-électronique et Nanotechnologies**

Arrêté ministériel: 7 août 2006

Présentée par

Hadi ARJMANDI-TASH

Thèse dirigée par **Vincent BOUCHIAT**

Préparée au sein du **Département Nanosciences de l'Institut Néel** dans **l'École Doctorale de Physique**

Graphene based mechanical and electronic devices in optimized environments: from suspended graphene to in-situ grown graphene/boron nitride heterostructures

Dispositifs électroniques et mécaniques en graphène sous environnement optimal: du graphène suspendu aux hétérostructures graphène/nitrure de bore

Thèse soutenue publiquement le **27 Mai 2014**

Devant le jury composé de:

Dr. Martine MAYNE-L'HERMITE Chercheur, Expert Senior à l'Iramis, CEA-Saclay	Rapporteur
Dr. Anthony AYARI Chargé de Recherche, Institut Lumière-Matière, Lyon	Rapporteur
Dr. Vincent DERYCKE Chercheur à l'Iramis, CEA-Saclay	Examinateur
Dr. Cécile NAUD Chargée de Recherche à l'Institut Néel, CNRS-Grenoble,	Examinateur
Dr. Manuel NUNEZ-REGUEIRO Directeur de Recherche à l'Institut Néel, Grenoble,	Examinateur
Dr. Vincent BOUCHIAT Directeur de Recherche à l'Institut Néel, Grenoble,	Directeur de Thèse

Abbreviations

AFM ..... Atomic Force Microscopy

CVD ..... Chemical Vapor Deposition

FIB ..... Focused Ion Beam

h-BN ..... hexagonal Boron Nitride

IPA ..... Isoropyl Alcohol

MC ..... Magnetoconductance

MIBK ..... Methyl Isobutyl Ketone

MR ..... Magnetoresistance

NMP N-Methyl-2-Pyrrolidone

PMMA ..... Poly(Methyl Methacrylate)

SEM ..... Scanning electron microscope

WL ..... Weak Localization

WAL ..... Weak Antilocalization

XPS ..... X-ray Photoelectron Spectroscopy

List of Figures

List of Tables

Contents

Synopsis of This Work

Charge carriers in graphene form two-dimensional gases which are exposed to the surroundings, unprotected. Therefore the electrical performance of graphene is extremely sensitive to the environmental conditions; specifically charged impurities at its interface with the substrate as well as topological perturbations inherited from the underlying substrate can account for the degradation of its carrier transport properties. Optimizing the environment by supporting graphene with a neutral and crystalline hexagonal boron nitride buffer layer is a technique to get rid of the parasitic effects of the substrate which is one of the objectives of this work. In this case, the effects of the improved substrate on the phase coherence transport of the carriers are assessed and compared with a reference graphene/silica device through low-temperature weak localization interference measurements. Also a novel technique for *in-situ* fabrication of such heterostructures is introduced and examined. Removing the substrate and suspending graphene is another approach for optimization of the graphene environment which is the other important topic covered in this thesis. In this sense and after introducing an improved recipe for preserving the quality of graphene throughout the complicated fabrication process, we probe the room- and low-temperature performance of graphene based nano-electro-mechanical devices. The obtained data are used for characterizing the thermal expansion of CVD graphene.

Questions Addressed in This Work

Today hexagonal boron nitride (h-BN) is considered as the best substrate for graphene [1]. Its neutral, very flat surface and crystalline structure that matches well with graphene are considered as its most important qualities. Some aspects of this stacking like the mean free path of the charge carriers in both exfoliated [1] and CVD [2] graphene, or the distortion of the band structure of graphene [3] have been studied before. However there are still many open questions: for example so far no study about the effect of this substrate on the phase-coherent interference effects like weak localization, Fabry-Pérot oscillations and Josephson effects has been reported. So there is a big question regarding the influence of the substrate (h-BN) on the phase coherent phenomena and corresponding length of the carriers in graphene. *Chapter 2* shows our experimental results on the effect of the h-BN buffer layer on the transport properties of graphene at low temperatures. We will focus mainly on the weak localization effect in graphene and compare the corresponding scattering and coherence lengths on h-BN and silicon wafer, showing that h-BN can help improve the phase coherence length of the carriers as their mean free paths.

Typical techniques used for transferring graphene on h-BN flakes are normally very time-consuming and requires a lot of care to preserve its quality. Although there are some attempts for chemically growing graphene directly on top of the h-BN flakes [4][5], none of them are optimized in terms of the growth process as well as the size and quality of the resultant graphene. In a separate chapter of this thesis (*Chapter 3*), the question of the possibility of directly growing large and high quality graphene on h-BN flakes will be addressed. There we introduce a new technique for *in-situ* growing graphene/h-BN stacks in which precursors have indirect access to catalyst. The introduced method has some advantages over the normal transferring techniques. Also the transport and Raman signatures of such graphene are compared with the typical transferred ones.

Chapter 4 mainly deals with suspending graphene that provide another technique to eliminate the substrate-related perturbations. To what extent one can preserve the quality of graphene by doing this? What are the techniques which are utilized to fabricate this kind of samples and how can we improve them? These are the questions answered in this chapter. There we will see that by removing the substrate and associated charged impurities, indeed one can improve the transport properties of graphene in some senses. Different techniques which are commonly used for fabrication of these devices are reviewed and an improved recipe to obtain very clean and high quality graphene is introduced. Once the suspended graphene devices are realized, the next question is: can one use such devices as mechanical resonators? If yes, what are the possible techniques to excite such devices and detect their oscillations? This chapter covers the answers for such questions. There we show that indeed it is possible to drive suspended graphene to vibrate; the methods for actuation and detection of them are also described. In addition, we will see the effect of the process residual and gate-related electrostatic stresses on the mechanical resonance frequency. We will go further by introducing another source of stress which is thermal stress; its effect on the resonance frequency and quality factor of the resonators will be discussed. The low-temperature results can be employed to extract the coefficient of the thermal expansion of CVD graphene.

Main Results and Organization of the Manuscript

This manuscript, begins by reviewing the important properties of graphene in the *Introduction*. From different points of view, graphene has many interesting properties; however its most important electrical, mechanical and thermal characteristics which are addressed in the later chapters are presented here. The main idea of this chapter is to provide and gather all the necessary theories and experimental results which are essential to understand and drive our later analysis.

In *Chapter 2* we will introduce graphene/h-BN heterostructures. The main advantages of using a h-BN buffer layer to support graphene are reviewed and after describing the fabrication technique, we will focus on the low temperature transport properties of such systems. The samples consist of long CVD graphene ribbons lying on both h-BN and on silicon; this gives the opportunity to readily examine the effects of the substrate. We see improvements in the low-temperature zero-field transport characteristics of the quasiparticles of graphene

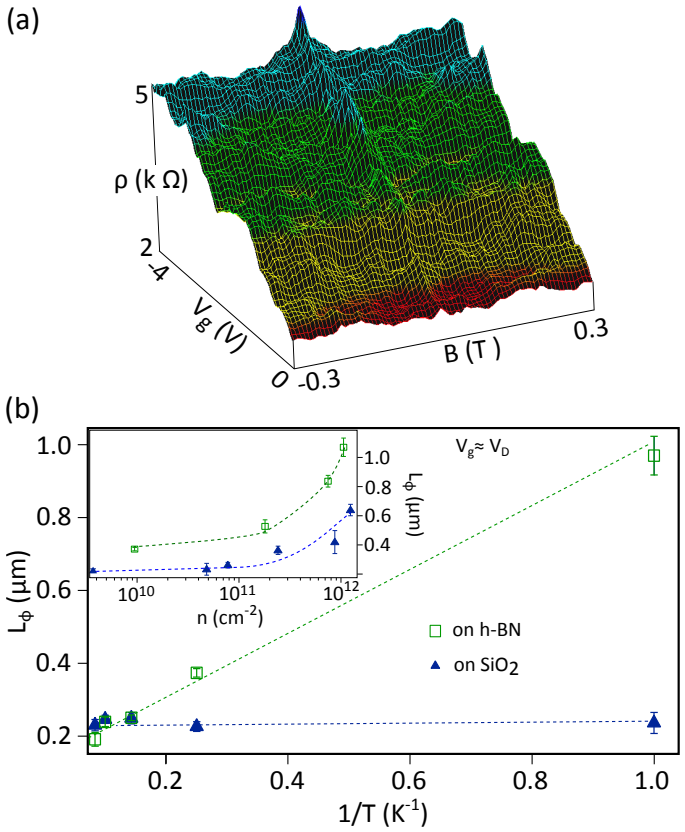

Figure 0.1: Weak localization analysis of our devices a) In a sweeping magnetic field, weak localization shows up as a peak in the resistivity of the devices, at vanishing field. b) Measurements of the phase coherence length (L_ϕ) as a function of the inverse temperature (1/T, main panel) and carrier density (n, inset figure) on graphene lying on h-BN and on silicon: Our analyses confirm h-BN improves L_ϕ in most of the density and temperature ranges we have measured.

once it lies on h-BN. Next we focus on the low-field weak localization interference effect of the samples. We fit our results with existing models and try to extract the characteristic lengths involved. Interestingly we see that h-BN can enhance the phase coherence length of the charge carriers. We have examined the effect of the temperature and carrier density on this effect (Figure 0.1).

A new method for fabricating graphene/h-BN heterostructures which we call *proximity-driven CVD growth* is the main point addressed in *Chapter 3*. Considering the difficulties and disadvantages of fabricating such devices by transferring graphene on h-BN flakes, few methods have been developed for *in-situ* fabricating the structures *e.g.* in a CVD process and by skipping the catalyst. However such techniques suffers from very long fabrication durations and small size of the graphene crystals (both as results of the absence of the catalyst) as well as low transport quality of the final devices. In this chapter, we introduce a novel method which differs from all the previously reported similar works in the sense that the catalyst is still present: precursors decompose on the typical Cu foils in the usual CVD process and then the resultant carbon atoms migrate on top of the already exfoliated h-BN flakes on this Cu foil and form a graphene layer. We have characterize such systems extensively with Raman and AFM techniques, directly after the growth and after transferring the stack on silicon wafer. Also the transport measurements have been performed and the results are compared with similar devices fabricated by typical transferring techniques. Our devices show the charge carrier mobilities of $\approx 20,000 cm^2/V.s$ which is far above that of devices made in the other direct growth techniques. Figure 0.2 shows selection of results reported in this chapter.

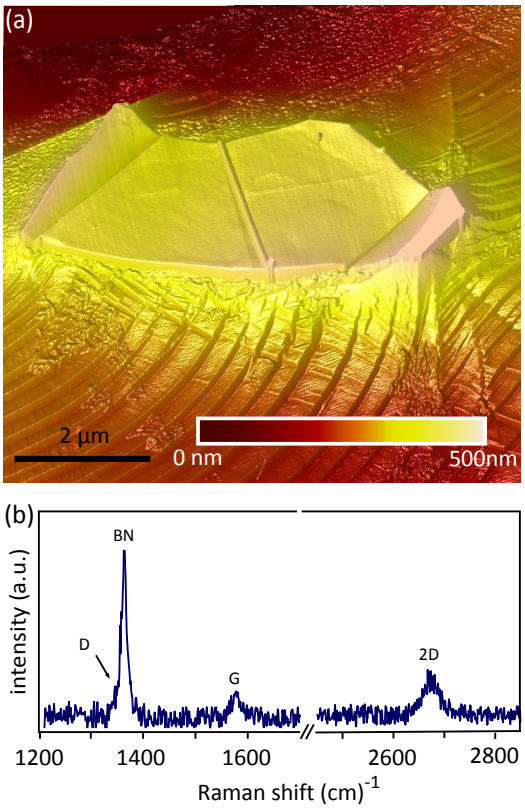

Figure 0.2: Selection of the results of our introduced proximity-driven in-situ CVD growth technique of graphene/h-BN stacks
a) Topography AFM mapping of a h-BN flake exfoliated on the Cu foil after the growth process
b) Raman analyses on this flake reveals the characteristic D, G and 2D modes of graphene together with BN signature which proves the growth of graphene in this technique.

Chapter 4 deals with CVD graphene based nano-electro-mechanical systems. Graphene possesses outstanding mechanical properties which makes it a good candidate as the active element of nano-resonators. In this chapter and after reviewing the most important reports in this area so far, we first introduce an enhanced fabrication recipe to preserve the quality of graphene in the complected fabrication procedure. The main idea of this recipe is to protect the surface of graphene with a polymeric layer through the process which minimizes deposition of the contaminations as well as the risk for the formation of the wrinkles and defects by the chemicals. At the end of the fabrication step, we manage to fabricate arrays of high quality suspended graphene devices ready for excitation. later we focus on the mechanical resonance measurements and assess the effects of the electrostatic- and temperature-induced stresses on the resonance parameters. By employing the existing models, we manage to extract the coefficient of the thermal expansion of CVD graphene and compare it with the exfoliated one. Few of the results of this chapter are illustrated in Figure 0.3

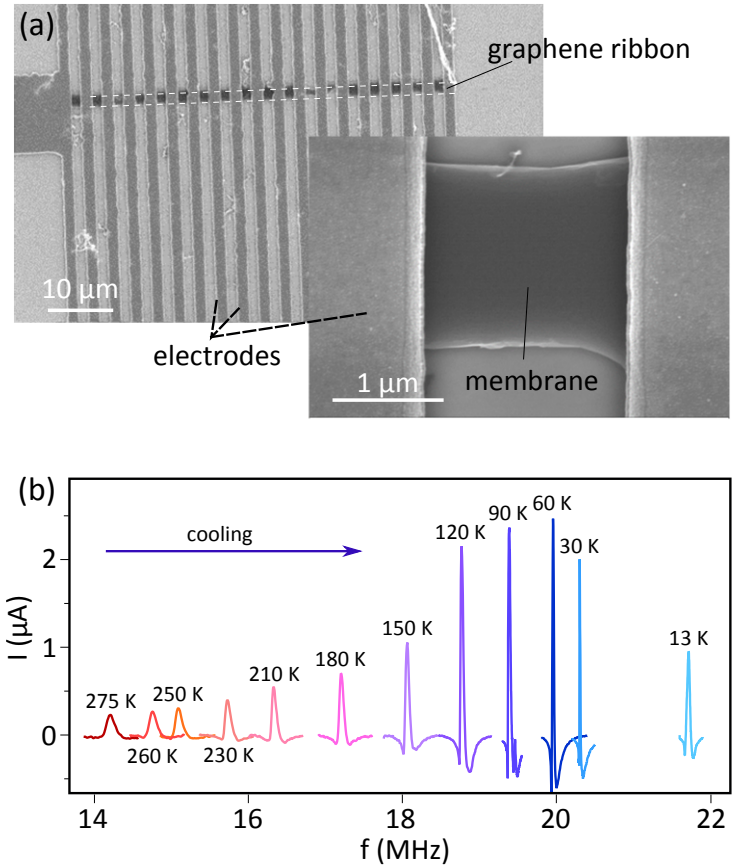

Figure 0.3: Selection of the results reported in Chapter 4
a) Our improved recipe for fabrication of the devices leads to the realization of the arrays of high quality suspended graphene devices.
b) Thermal stress improves the mechanical resonance parameters in such devices while cooling.

Introduction

The single layer two-dimensional material formed of carbon atoms bounded to each other in a honeycomb lattice which is referred to as *graphene* is now one of the extensively studied materials in the world. This material is the building block for some other graphitic materials with other dimensionalities including zero-dimensional buckyballs, rolled and one-dimensional carbon nano-tubes and stacked 3-dimensional graphite [6][7].

The fast uptake of interests in graphene is primarily due to a number of exceptional properties which have been predicted or observed in it, including highly mobile and gate tunable carrier density [8], superior thermal conductivity [9][10], extremely high optical opacity [11], anomalous quantum Hall effect [12][13] and outstanding mechanical performance [14][15]. Besides all such appealing properties, we have to consider the fact that there is no protective layer for the carriers in graphene; thus electrons and holes are easily accessible and manipulatable. This distinguishing trait works as a *double-edged sword*: From one side, it makes graphene a promising material for making hybrid systems as just by putting different materials with diverse properties close to, one can functionalize it [16][17]. On the other side, this accounts for the ultra-high sensitivity of graphene to the environmental conditions. Here the quality of the underlying substrate plays an important role for defining its characteristics in applications. Optimizing the environment by removing the substrate or by supporting graphene with a neutral and crystalline hexagonal boron nitride buffer layer are the techniques to get rid of the parasitic effects of the substrate and is the objective of this work.

The goal of this chapter is to collect, introduce and summarize the important characteristics of graphene and theories developed for describing them; here we focus only on those of graphene properties which are recalled and used in the next chapters. We start by reviewing the history of graphene, from the early observation of the multilayer and rather thick graphite to the isolated monolayer graphene. Then the electronic properties of graphene which arise from its honeycomb lattice is extensively studied. Topics like ballistic and diffusive transport, mobility and scattering mechanisms in graphene are covered there. At the next section, by describing the electrical performance of the graphene carriers under the magnetic field, we prepare the basics for the discussions covered in chapter 2. Mechanical and thermal properties of graphene are the last topics covered in this introductory chapter.

1.2 History of Graphene

Decomposing bulk graphite to its components has had a long history dating back to the 10^{th} century. In this section, we review the important milestones in the history of graphene.

1.2.1 Early Observations of Graphene

The term *graphene* is a name constructed by combining the prefix of *graphite* to the suffix *-ene* used to name a molecular entity. It was firstly assigned officially to single layers of graphite by German chemist, Hanns-Peter Boehm [18] and he is among the first who has observed and identified single layers of graphene [19]. The technique they used is based on the chemically exfoliated graphite oxide: Bulk graphite can be oxidized by reacting with strong oxidants like sulfuric acid, potassium permanganate or sodium hydroxide. This process results in expanding the graphite interlayers to the point of decomposition into constituent graphene oxide flakes. They have measured the thickness of graphene layers with transmission electron microscopy (TEM) and x-ray diffraction techniques; However they are not the first who has analyzed few layer graphene with TEM since the first observations of ultra thin graphite flakes using TEM is reported by Von G. Ruess and F. Vogt [20], 20 years before Boehm's work. Figure 1.1-a and b show examples of the TEM observations reported in the Ruess's and Bohem's papers.

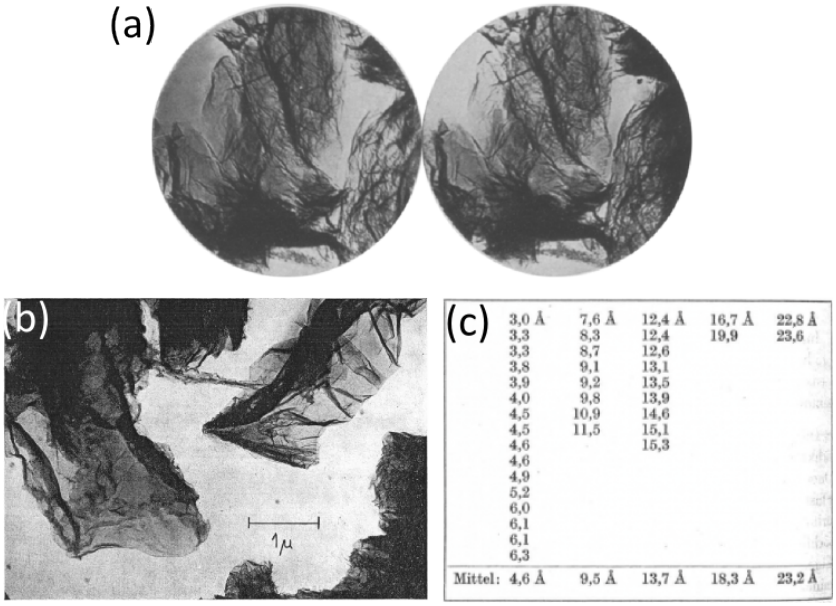

Figure 1.1: The first microscopic observations of few and monolayer graphite samples using the transmission electronic microscopy (TEM) technique
a) The earliest report on the TEM observation of graphite by Ruess and Vogt [20]. They have done this work in 1948.
b) Images of the thin (few- and monolayer) graphene flakes observed by Boehm et al in 1962 [19].
c) Table showing the measured thicknesses of the flakes reported in Boehm's paper. Note that sub-nanometer thick (thus single layer) graphene layer is indeed observed.

The thinnest graphene layer Boehm measured in his experiments (Figure 1.1-c) is 3 Åthick, a thickness which we now know corresponds to monolayer graphene. This is a direct proof that they are the first who managed to observe graphene. Interestingly, Boehm never called his experiments a discovery; they believed that what they made is in the line of the exfoliating graphite which has a long history back to 1840 [21].

1.2.2 From Early Observations Towards Isolation of Graphene

Shall we call it discovery or not, apparently the existence of stable monolayer graphene layers was forgotten or overlooked by the community of physicists for a long time. Maybe the fact that their paper was published in a language different than English (it was written in German) has probably to do with it. For decades before mid 2000's, monolayer graphene has been presumed not to be stable in a free state [22] as fluctuations were expected to induce collapse or crumbling.

This common mistake continued until 2002, when the US patent number 7071258 was filed by Bor Jang and Wen Huang [23]. Titled *nano-scaled graphene plates* and assigned to *Nanotek Instruments*, it describes a technique to realize final graphene sheets after few chemical, thermal and mechanical treatments. This technique starts by partially or fully carbonizing the polymer precursors to obtain graphite crystals in micro and nano-scales. Alternatively they propose

thermal treatment of petroleum and coal to obtain the same. At the next step, they exfoliate these small crystals, *e.g.* by a rapid thermal shock. The process finishes by mechanical attrition treatment (ball milling for example) to produce the plates. In their patent, they have introduced a conceptual sketch of producing graphene sheets by unrolling carbon nanotubes (Figure 1.2) which indeed turned out to be an interesting technique to generate carbon nanoribbons [24][25].

Not only this is the first patent for producing graphene, but also the term nano-scale graphene plates (NGP) *which is advertised by some companies today is invented by them.*

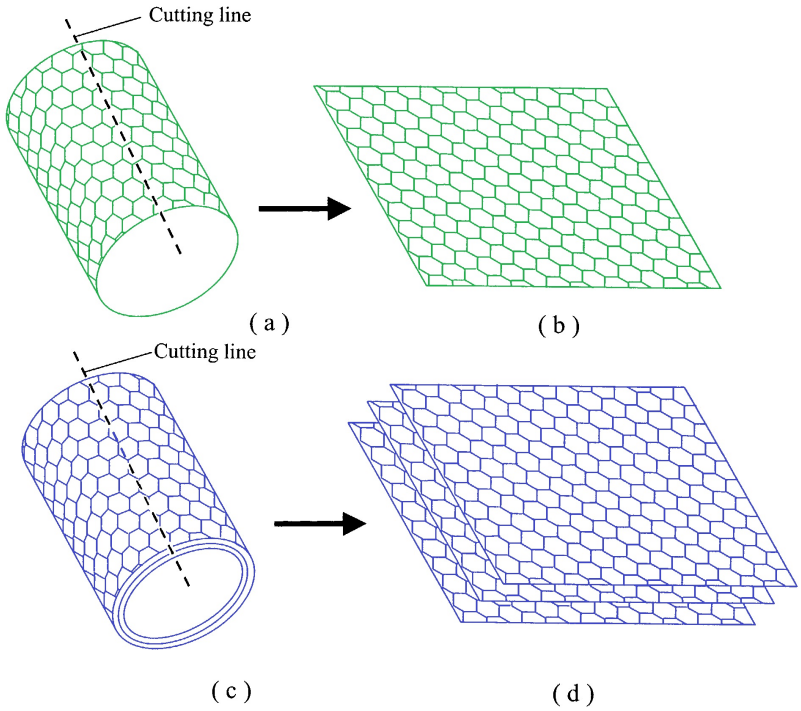

Figure 1.2: Unzipping carbon nanotubes for fabricating carbon nanoribbons
The first patent for producing graphene layers signed by B. Jang and W. Huang reveals a conceptual sketch for producing graphene sheets by unrolling single- or multi-walled carbon nanotubes. Figure adopted from [23].

Shigeo Horiuchi is another scientist who had an important contribution in the history of graphene. In 2003, he and his coworkers managed to develop a technique based on the oxidation of graphite, to realize very thin graphitic flakes which they referred to as *carbon nanofilms (CNF)* [26]. Using high-resolution transmission electron microscopy and electron diffraction they studied the stacking sequence of the graphene sheets which they call *carbon six-membered-ring planes*. In their next paper [27], they tried to count the number of the stacked layers in CNF using electron diffraction intensity technique. Their published TEM images seems to detect single graphene sheets(Figure 1.3).

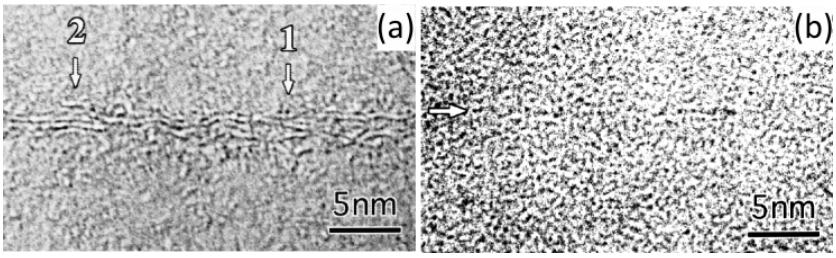

Figure 1.3: Selected of the results reported in Horiuchi's paper [27]
a) and b) High-resolution TEM images they obtained from graphite samples after chemical exfoliation: They believe that at the site marked by arrows in (a) graphene layers separate into branches. Also the hardly visible dark line along the arrow in (b) corresponds to a single graphene layer.

The most important step in the history of graphene was paved when K. S. Novoselov and A. K. Geim refined a known cleaving technique and succeeded to repeatedly isolate pristine monolayered graphene on silicon substrates. In this technique, exfoliation of graphite is done by peeling flakes with a scotch-tape [28]. This handy and cheap technique can effectively lead to high quality graphene flakes. This discovery rapidly lead to another publication [8] describing the electron transport properties of graphene for the first time. Even though what they did was not the discovery of graphene, they triggered all the graphene activities leading to discovering all its outstanding properties one by one. This was one of the important reasons persuading the *Royal Swedish Academy of Sciences* to select them for the *Nobel Prize* in physics in 2010.

Volume 438 of the Nature journal in which Novoselov and Geim published their second work also contained another outstanding article about exploring electronic properties of graphene [12]; This work was done by a group in Columbia University lead by Philip Kim.

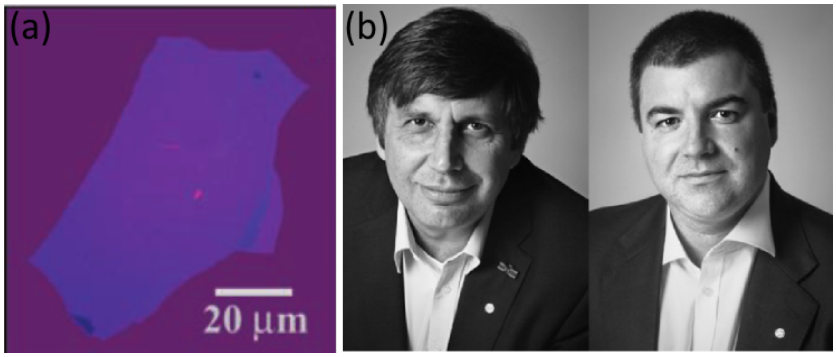

Figure 1.4: The first isolation of graphene
a) The first optical image of the the fewlayer graphene reported by Novoselov et al [28]
b) Andre Geim (left) and Konstantin Novoselov (right) were awarded the Nobel Prize in physics in 2010 for their achievements in isolation and characterization of graphene.

1.3 Electronic Transport Properties in Graphene

Graphene has unique electronic properties which arises from its 2D characters and specific hexagonal crystalline structure. In this section, after having described the crystal of graphene, important electron transport properties of graphene will be introduced.

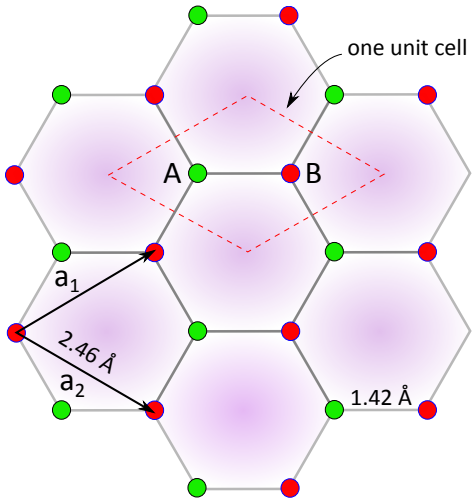

Figure 1.5: Honeycomb lattice of graphene
The lattice of graphene composes of two merged triangular sublattices with $\vec{a_1}$ and $\vec{a_2}$ as the lattice unit vectors. A unit cell of graphene is defined by the dashed lines there which contains two atoms from A and B sublattices.

1.3.1 Crystalline Structure and Energy Dispersion of Electronic states

In graphene, each carbon atom is bonded to two neighboring ones through strong covalent bounds to make a dense hexagonal (honeycomb-like) 2D lattice; The atomic density of graphene is 36 carbon atoms per nanometer square. One can then see graphene as an infinitely large molecule which is the structural building block of other carbon allotropes including graphite, carbon nanotubes and fullerenes; The interlayer distance between graphene layers when they are piled up in the form of graphite is measured 3.35 Å.

Figure 1.5 shows a schematic representation of the crystalline structure of graphene. Here $\vec{a_1}$ and $\vec{a_2}$ are lattice vectors defined as: $\vec{a_1} = a(\sqrt{3}/2, 1/2)$ and $\vec{a_2} = a(\sqrt{3}/2, -1/2)$ where $|\vec{a_1}| = |\vec{a_2}| = a = 2.46$ Å. In the reciprocal space, the lattice vectors of graphene are given by $b_1 = \frac{2\pi}{3a_0}(1, \sqrt{3})$ and $b_2 = \frac{2\pi}{3a_0}(1, -\sqrt{3})$. For a pristine graphene, the Hamiltonian can be written as:

$$H = -t \sum_{i,j,\sigma} (a^{\dagger}_{\sigma,i} b_{\sigma,j} + h.c.) - t' \sum_{i,j,\sigma} (a^{\dagger}_{\sigma,i} a_{\sigma,j} + b\dagger\sigma, i b_{\sigma,j} + h.c.). \quad (1)$$

In this equation, $a_{i,\sigma}$ and $(a)^{\dagger}_{\sigma,i}$ are respectively the annihilator and creator operators for electrons with spin σ while a and b refers to the sites A and B in the lattice. This equation for Hamiltonian is obtained using tight-binding method considering that electron can hop to the nearest and second nearest-neighbors. The energy bands obtained from this Hamiltonian was calculated as early as 1947 by Wallace [29] long before graphene became popular:

$$E_{\pm}(\vec{k}) = \pm t\sqrt{3 + f(\vec{k})} - t' f(\vec{k}), \quad (2)$$

where $f(\vec{k}) = 2\cos(\sqrt{3} k_y a) + 4\cos(\frac{\sqrt{3}}{2} k_y a)\cos(\frac{3}{2} k_x a)$. In these equations, while $\vec{k}$ refers to the wave vector of the electrons, t and t' are of the energy unit and correspond to the nearest-neighbor and second nearest-neighbor hopping energies. Also the plus and minus signs apply for the upper and lower electron bands respectively. Theoreticians normally skip the second-order hopping mechanism

(terms containing the t' parameter in above equations) to simplify the relations. In this case by solving the Equation 2 for continues values of k_x and k_y, one can plot the famous band structure of graphene (Figure 1.6-a). Here the upper sheet corresponds to the conduction band while the valence band is represented by the bottom surface. At two points within the *Brillouin zone* of graphene, the valence and conduction bands touch each other which are normally referred to as *Dirac points* and labeled by K and K' wave vectors. Close to these points, the energy bands can be approximated by a conical shape, as the energy dispersion has a linear dependence with the wave vector:

$$E_{\pm}(q) \approx \pm\hbar v_f \mid k - K \mid, \tag{3}$$

while v_f is the *Fermi velocity* which is calculated to be $v_f \approx 1 \times 10^6 m/s$ [29]. This is the velocity which carriers travel in graphene and is $1/300$th the speed of light. Then, one can see this equation as a limit of the Einstein's *energy-momentum relation* $E = \sqrt{m^2c^4 + p^2c^2}$ with $m = 0$ and $c = v_f$. This is why the carriers in graphene are called *massless particles*. The facts that the energy disperse linearly with momentum and the conduction and valence band touches each other in single points without energy gap are the most important aspects of the energy dispersion relation in graphene [30].

1.3.2 Gate Tunable Charge Carriers

One of the most interesting properties of graphene is the fact that the sign and density of charge carriers (electrons and holes) can be adjusted with an electrostatic gate voltage. Indeed, one can apply a gate voltage to graphene and correspondingly change the level of the *Fermi energy* and thus the population of the carriers there. Figure 1.6-b shows typical field dependent behavior of the resistivity $\rho = 1/\sigma$, (σ: conductivity) of graphene. Pristine and high quality graphene devices show maximum resistivity of $\approx 6.5\,k\Omega$ at zero gate voltage which corresponds to the Dirac point position. Any charged impurities and contaminations close to the graphene may shift the position of the Dirac point. Simple equation can be employed to calculate the density of the carriers (n) in an arbitrary applied gate voltage (V_g):

$$n = C(V_g - V_D)/e. \tag{4}$$

Here C is the *gate capacitance* of the substrate while V_D and e respectively refers to the position of the charge neutrality point and to the elementary charge. For typical graphene devices backgated with 285 nm oxide covered silicon wafers, the population of the carriers is of the order of 10^{12} electrons per centimeter square for a gate voltage of $V_g - V_D \approx 10\,V$. In theory, while the gate voltage approaches the charge neutrality point, the density also goes to zero and thus the device becomes less conductive. The term electronic *mobility* shown by μ link the conductivity to the charge carrier carrier densities:

$$\mu_{FE} = \frac{\sigma}{en}. \tag{5}$$

This equation is based on the *Drude model for conductivity* [31]. The mobility calculated here is density dependent and thus is called *field-effect mobility*. Besides, there is another commonly utilized definition for the mobility which is referred to as *density-independent mobility* (μ_c) and is based on the self-consistent diffusive transport model [32]:

$$\mu_c = \frac{1}{en}[(1/\sigma - \rho_s)^{-1} - \sigma_0]. \tag{6}$$

In this equation, ρ_s is a constant contribution to the resistivity from short-range scatterers (*e.g.* crystalline defects) and σ_0 is the residual conductivity at the Dirac point. The mobility obtained here is charge-independent and is attributed to the long-range charged impurity Coulomb scatterers.

Mobility of graphene is normally reported in the unit of $cm^2/V.s$ and is one of the important quantitative parameters revealing the quality of graphene for nanoelectronics. Both intrinsic (defect density) and extrinsic (charge environment, etc) contributions may affect it and thus its values depends a lot on the fabrication techniques and environment. A couple of years ago, graphene with a room-temperature mobility of $\mu_c \approx 20,000\,cm^2/V.s$ was considered a high quality sample; but recent progresses in the fabrication techniques makes graphene devices with mobilities higher than $100,000\,cm^2/V.s$ normally achievable [33][34][35].

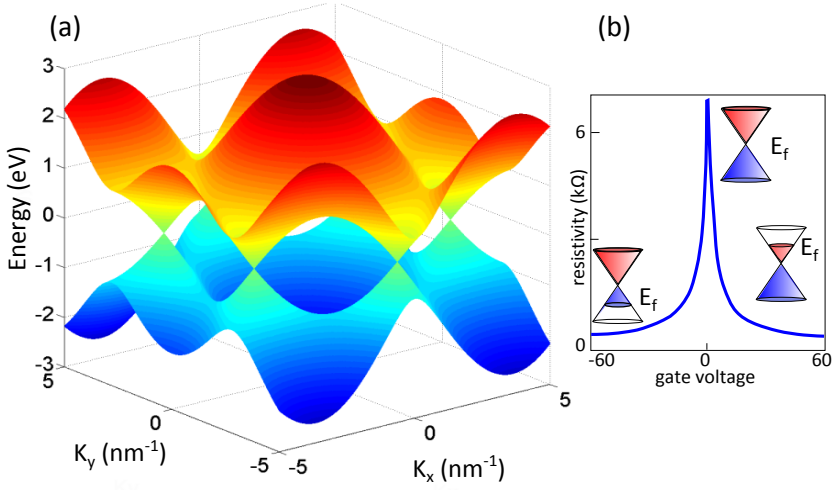

Figure 1.6: Gate dependent carrier density in graphene
a) Energy spectrum of graphene calculated by (Equation 2) and skipping the second neighbors interactions
b) Gate dependent resistivity of graphene: By changing the applied gate voltage one can tune the Fermi energy level and population as well as the type of the carriers in the graphene lattice.

1.3.3 Ballistic Transport in Graphene

Carriers in graphene experience different kinds of scattering events which tend to limit its electronic mobility; The length through which an electron or hole can travel in between two subsequent scattering events is called *mean free path (l)*.

Theoreticians normally consider two distinct transport regimes depending on the ratio of l/L where L is the length of the devices. In the limit when the mean free path is comparable or larger than the length of the sample, transport is said to be *ballistic*. Here the *Landauer formalism* [36] can be employed to describe the conductivity:

$$\sigma_{ballistic} = \frac{L}{W}\frac{4e^2}{h}\sum_{n=1}^{\infty} T_n. \tag{7}$$

In this equation the sum is over all the available transport channels with the transmission probability of T_n.

1.3.4 Scattering Mechanisms in Graphene

On the other limit, when the mean free path is much less than the device length, the transport is said to be *diffusive*; here the carriers experience many elastic and inelastic scattering events traveling from one electrode to the other one. There are few models to describe the conductivity under this regime, but to understand them, we need to review different scattering mechanisms in graphene. Parasitic potential due to the charged impurities on the substrate, crystalline defects and phonons of the lattice are considered as the most important sources of scattering in graphene [32][37][38][30]. However, the degree of their importance is not the same and at different thermal or density regimes they become more or less dominant.

1.3.4.1 Charged Impurities

Coulomb scatterers is another name for *charged impurities* and is considered as the most effective scattering mechanism in graphene [32][39][37]. Electrostatic potentials like buried charges at the surface of the substrate can effectively influence the transport of the carriers even though there are very far from each other. This is the reason that this type of scatterers is called a *long-range* scattering mechanism. Adam and coworkers employed a semi-classical approach to modelize their effect on the conductivity (σ) [39]:

$$\sigma = \frac{20e^2}{h}\frac{n}{n_i}. \tag{8}$$

This equation is obtained by considering a homogeneous distribution of the impurities with the density of n_i; it is valid for the graphene on SiO_2/Si substrate and high carrier density regime ($n \gg n_i$).

In the other regime when carrier density is in the order of the impurities, the conductivity of the graphene saturates with a value of σ_{sat} which will be discussed later(section 1.3.6)

1.3.4.2 Crystalline Defects

Natural defects existing in the crystal of the graphene or occurring in the fabrication process of the devices is another remarkable source of the scattering in graphene. The earliest theory paper to model the transport in graphene [32] modelized this kind of defects as *zero-range* scatterers, which only turns to be important when the density of the carrier is very high. Later Stauber *et al* [37]

developed another theory which considers these defects as *mid-gap states*. In this model, strong disorders associated with the voids are modeled as deep potential wells which can influence the transport of the carriers not only at high gate voltages but also close to the Dirac point, in the low carrier density regime. We will review this model in more details in Section 1.3.6.

1.3.4.3 Lattice Phonons

At finite temperature, the transport of the quasiparticles in graphene is affected by crystalline vibrations of graphene. They form a fundamental scattering source, *i.e.*, they can affect the mobility at finite temperatures even in the absence of all extrinsic scattering sources. Theoreticians suggest to skip the effect of all the phonon modes of graphene except the *longitudinal acoustic (LA)* one since the energy scales of the other modes are normally too high to provide a valuable scattering channel in typical temperature ranges [30]. Here two different transport regimes are considered which is determined by the characteristic *Bloch-Gruneissen temperature* (T_{BG}) [38]: $T_{BG} = 2k_F v_{ph}/k_B$, where k_B, k_F and v_{ph} refer to the Boltzmann constant, Fermi wave vector of graphene ($k_F = \sqrt{n\pi}$) and sound velocity. This paper show that for high carrier density ($n > 10^{12}\,cm^{-2}$) and in the regime when $T \gg T_{BG}$, the resistivity of the device is linearly dependent to the temperature $\rho \propto T$ while in the other limit $T \ll T_{BG}$, $\rho \propto T^4$.

1.3.5 Electronic Conductivity at Low Density Regime

Being a semimetal, the density of states in graphene and thus its conductivity is expected to vanish around the Dirac point (Figure 1.6). However, the experimental observations show that by reducing the density, conductivity of graphene saturates at a finite value (σ_{sat}). The earliest report on the field dependent transport measurement of graphene [8] showed that the majority of their samples have minimum conductivity of $\sigma_{sat} = 4e^2/h$ (corresponding to $\rho_{max} = h/4e^2$) and thus they believe that the quantum unit of conductance $4e^2/h$ is the universal value for all graphene samples (Figure 1.7-a). In contrary, Tan and his coworkers [40] measured the total number of 19 samples which show minimum conductivity values between $2 - 10\,e^2/h$ at low density limit (Figure 1.7-b). So they conclude that there is no universal value for the conductivity. The saturation value of the conductivity is still under debate, however as the recent measurement results with high quality samples seems to support the idea of having universal conductivity [34].

There are few papers talking about the effect of topographical corrugations of graphene in the formation of such electron-hole puddles [41], however it seems that the influence of the charged impurities has attracted more attention in the graphene community.

Regardless of its value, the origin of this saturation of conductivity is another question. Most literature believe that the trapped charged impurities close to the graphene sheet (on the substrate for example) collapses the area of the graphene into puddles of electrons and holes which causes spatial fluctuations in doping levels [32]. The average variation of the local Dirac point from the Fermi energy characterizes an energy bandwidth $E_{F\,sat}$, within which the effect of gating is limited to a rearrangement of carriers between electrons and holes without considerably changing the entire carrier density. This picture is more supported now after experimentally observation of electron and hole puddles [42](Figure 1.7-c).

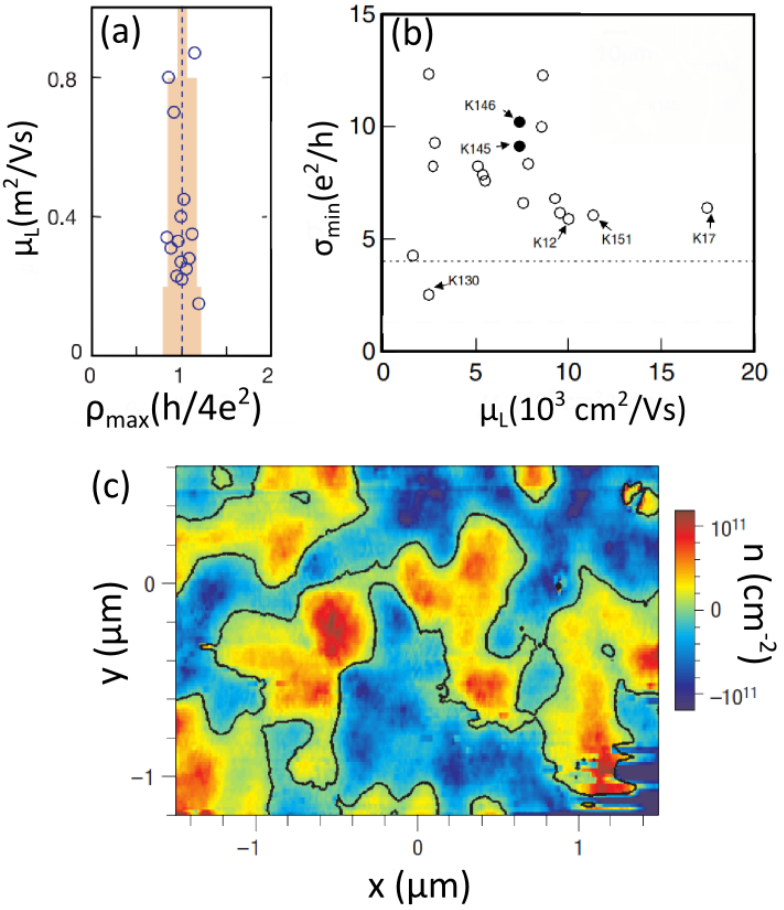

Figure 1.7: Remarkable studies about the value and origin of the minimum conductivity in graphene
a) The value (open circles) and histogram (orange background)) of the maximum resistivity ($\rho = 1/\sigma$) of the measured samples with different mobilities (μ) by [8]: Most of the samples show minimum conductivity of around $\sigma_{sat} = 4e^2/h$. Figure is reprinted with adoptions.
b) Results of a similar works done by [40]: The minimum conductivity of the samples they made do not show any remarkable trend. The open and filled circles here corresponds to different samples and the dotted horizontal line show the value of $4e^2/h$. Figure is reprinted with adoptions.
c) Experimentally observed local charge inhomogeneities near the charge neutrality point in graphene: This mapping is done with low-temperature STM measurements. Figure is adapted from [42].

1.3.6 Transport Models in the Diffusive Regime

There are few models developed for describing the transport of graphene in the diffusive regime which are normally derived from the *Boltzmann theory* for conductivity [43]. Such models are in general based on the estimation of the scattering time (the timespan between two subsequent scattering events) corresponding to different scattering mechanism at different regimes. Proposing relations to calculate the conductivity in applications and dealing with the universal conductivity are the major points addressed in such papers.

The first model of this kind is proposed by Hwang and his coworkers [32]. They claimed that almost all experimental findings can be explain by utilizing the Boltzmann theory and by renormalizing the carrier density close to the Dirac point with the potential fluctuations due to the residual charge densities. There is no universal conductivity extracted from their theory and thus it does not match with some of the works predicting a minimum conductivity of $4e^2/h$ for graphene. However the most important criticism for their work is that only at high density of charge impurities ($> 10^{12}\,cm^{-2}$) does their theory match with the mobilities observed experimentally.

The next important model is proposed by [39]:

$$\sigma(n) = \begin{cases} \frac{Ce^2}{h}\frac{n^*}{n_{imp}} \text{ for } n < n^*, \\ \frac{Ce^2}{h}\frac{n}{n_{imp}} \text{ for } n > n^*. \end{cases} \tag{9}$$

In this model, n and n_{imp} respectively refer to the density of the carriers (calculated by Equation 4) and density of the charged impurities. n^* corresponds to the density below which the electron and hole puddles start to form and thus the conductivity saturates. Dimensionless parameter C depends on the dielectric parameters of the substrate and is set to 20 for SiO_2 wafers. In this model, conductivity depends linearly to the charge density (for $n > n^*$), so it fails to describe the conductivity in high quality samples which are normally characterized by strong sublinear conductance [44][1][33]. Furthermore, in this model at the low density regime $n < n^*$, the conductivity saturates at a value defined by $\sigma_{sat} = \frac{20e^2}{h}\frac{n^*}{n_{imp}}$ which is very close to the reported $\sigma_{sat} = 4e^2/h$ for *dirty* samples ($n_{imp} \sim 3.5 \times 10^{12}\,cm^{-2}$). For *clean* samples ($n_{imp} \sim 2 \times 10^{11}\,cm^{-2}$), conductivity saturates at $\sigma_{sat} = 8e^2/h$ which does not match with experimental results.

Another important model is proposed by Stauber and coworkers [37]. Using the semi-classical Boltzmann theory they developed a theory based on scattering by *mid-gap states*. In this model, strong disorders associated with the voids are modeled as deep potential wells. Such states can happen because of the crystalline defects like vacancies, cracks or because of the impurities on the substrate and graphene boundaries. The resulting scattering time, scales logarithmically with wave vector k, as follows:

$$\sigma_{vacancies} = \frac{2e^2}{h}\frac{k_F^2}{\pi n_d}\ln(k_F R_0)^2, \tag{10}$$

here n_d and R_0 refer to the density and characteristic size of the defects respectively. The most important predictions of this theory are:

- Dirty samples have quasi-universal minimum conductivities.
- Clean samples have higher minimal conductivities.
- Increasing the gate voltage leads to a sublinear behavior of the conductivity. The results of this theory match well with the experimental reports assuming an equal concentration for long-range Coulomb scatterers and vacancies of the order of $n_i \approx 10^{10}$ to $10^{11} cm^{-2}$.

1.4 Graphene under Magnetic Field

Measuring the transport properties of graphene in the presence of the magnetic field was one of the first experiments done after successful realization of the monolayer graphene sheets [8][12]. In this section, we are going to review the fundamental physics relevant to the *quantum Hall effects (QHE)* and *localization* phenomena in graphene. In each subsection the most important experimental reports will be discussed.

1.4.1 Pseudospin and Chirality

We can see the two-dimensional nature of graphene as a gas of electrons in *x-y* plane which is confined by very high potentials in the *z* direction. The graphene sheet can work as a potential well with infinite walls. An electron traveling in such 2D lattice of graphene is rather different from the typical materials because of the existence of the two lattice sites; this will invoke the concept of *chirality*.

As we discussed before (Section 1.3.1), at low carrier densities around the Dirac point, the energy dispersion of the electrons is linear and they mimic massless charged carriers. Around the *K* point, the Hamiltonian of graphene (Equation 1) can be simplified in the form of:

$$H = \hbar v_F \begin{pmatrix} 0 & k_x - ik_y \\ k_x + ik_y & 0 \end{pmatrix} = \hbar v_F \vec{\sigma} \cdot \vec{k}, \tag{11}$$

and the motion of electrons in the continuum limit is described by [45]:

$$-i\hbar v_F \vec{\sigma} \cdot \vec{\nabla} \psi_K(\vec{r}) = E \Psi_K(\vec{r}), \tag{12}$$

where $\vec{\sigma} = (\sigma_x, \sigma_y)$ refers to vector *Pauli matrices* and $\Psi_K(\vec{r})$ is a *2D spinor* wavefunction [30]. Similar relation of the Equation 12 can be written for the *K′* point. The presence of the two independently equivalent *A* and *B* sublattices leads to the *chirality* in graphene energy spectrum, in which the two linear branches intersecting at the charge neutrality point become independent from each other; this suggest the presence of a *pseudospin* quantum index which is very similar to the electron spins. All the electrons which originate from the same sublattice (*A* or *B* in Figure 1.5) possess the same pseudospin (lets say *up* spin) which is different from the others coming from the other sublattice (*down* spin); however since

both the sublattices have the same contribution on the density, the pseudospin is a linear combination of the *up* and *down* pseudospins.

The existence of two Dirac points at K and K′ provides the energies of the quasiparticles in graphene an extra degree of degeneracy called *valley degeneracy*. So considering two times degeneracy for the real and two times for the pseudospins, the energy in monolayer graphene is 4 times degenerate. Valley degeneracy can be lifted in the presence of intervalley scattering mechanisms between K and K' points; however only strong lattice-scale scattering can account for that.

Figure 1.8 describes the concept of *chirality* in graphene. The energy spectrum of graphene is the result of superposition of the energy bands originating from the K and K' points (corresponding to the A and B sublattices in Figure 1.5). An electron with energy E which has momentum $+k$ (propagating in the positive direction in the k space) belongs to the same branch of the spectrum (shown in red in this figure) of another electron with the same energy in the other valley traveling in the opposite direction (with momentum $-k$), *i.e.* they have the same pseudospin pointing in the same direction. The projection of the pseudospin in the direction of the motion is additional built-in symmetry between electron and hole parts.

It is shown that the state Ψ_K (equation 12) acquires an extra phase of π on a closed trajectory [12]. Referred to as *Berry phase*, this π-shift is very important to understand the weak localization in graphene.

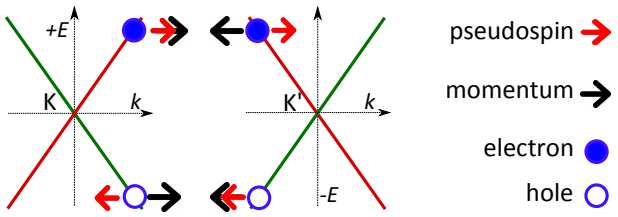

Figure 1.8: Schematic representation of the pseudospin and chirality in graphene Two dimensional diagram of the energy spectrum of graphene corresponding to the K and K′ points in a unit cell: the origin of the spectrum is highlighted by the red and green lines. The pseudospin is parallel to the momentum in one valley and antiparallel to the momentum in the other; thus, the two valleys host quasiparticles with opposite chiralities.

1.4.2 Weak Localization and Antilocalization in Graphene

At low temperature, the particle-wave duality of charge carriers becomes detectable through quantum interference effects. A major interference phenomenon taking place in mesoscopic systems is the so-called *weak localization* which is first addressed theoretically by Altshuler [46]. The presence of interference between coherent electrons manifests itself in a disordered conductor as an increase of the overall resistivity. By applying a magnetic field, quantum interferences are reduced which leads to an increase in the conductivity of the device. Such positive corrections in the conductivity in a magnetic field are the signature of weak localization.

This interference effect relies on diffusion by defects and thus the experimental realization of the weak localization can be used to probe the nature of the defects as well as the carriers in the system [47]. Later in 2002 Suzuura *et al* [48] reported their calculations about weak localization in a disordered two-dimensional honeycomb lattice. They showed that for a certain regime of the interaction with the impurity potentials, such corrections can have a negative sign; which is refereed to as *weak antilocalization*. Even though Suzuura's calculations were done before the realization of monolayer graphene, for years after, experimentalists failed to measure this effect clearly; there were rather some reports about either suppression or presence of the weak localization in graphene [49][50] or even transition from weak localization to antilocalization [51] in graphene. The first indisputable report was done by Tikhonenko [52] who demonstrated how to switch from weak localization to weak antilocalization in a graphene device by tuning the temperature and the carrier density.

A simplified explanation of the weak (anti)localization can be done considering classical paths (with associated amplitude and phase) connecting two points A and B in a two-dimensional disordered conductor (Figure 1.9-a). An electron paving each path experiences a number of scattering events which are depicted as segments on this figure. The scattering is assumed to be elastic, so ending to a well defined phase acquired along each path. Since there are infinite number of paths between these two points, with different lengths and acquired phases, the interference over them averages to zero and consequently, no conductivity divergence from classical Drude model is expected. However, the interferences associated to the closed paths as in Figure 1.9-b play a major role. One may find two electrons starting from a given point C and diffusing along the same closed path in opposite clockwise and counterclockwise directions. The phases acquired by these electrons, $\varphi_{\circlearrowleft}$ and $\varphi_{\circlearrowright}$ are exactly the same. Consequently, when the electrons return back to the starting point, they make constructive interferences, increasing the probability for backscattering which accounts for a decrease in conductivity [46]. This process of circulating in opposite directions can be also viewed as the motion of a particle and its corresponding time-reversed counterpart in opposite directions; this signifies that such interference is based on the time reversal symmetry. By applying a weak magnetic field perpendicular to the plane of motion, the time-reversal symmetry is violated (because $\varphi_{\circlearrowleft}$ and $\varphi_{\circlearrowright}$ are no longer the same), restoring the conductivity and giving rise to a negative magnetoresistance.

This assumption is not valid for the case of fully coherent samples in which the interference between different arbitrary paths gives rise to quantum corrections like Universal Quantum Fluctuations.

Being based on the phase coherence of electrons, any inelastic scattering which destroys the phase information spoils weak localization. Collisions with phonons or other electrons is an example of such inelastic scattering which sets the *phase coherence length* for suppression of the interference effect. Typically shown by L_ϕ, *dephasing length* is another name for this length scale. In the presence of such scattering mechanisms, only the closed paths that are short enough compared to the dephasing length contribute in the constructive interference. Increasing the temperature normally reduces the L_ϕ and thus in order to see such effects, one needs to cool the sample down to very low temperatures.

The fact that electrons in graphene own an additional quantum number of pseudospin (described in Section 1.4.1) modifies the picture for weak localization

in graphene to a large extent. Here the long-range scattering charged impurities in the substrate are not able to back-scatter the chiral quasiparticles (Figure 1.9-c) for the conservation of the pseudospin. At low magnetic field, their effect is then suppressed, as manifested by an enhancement of the conductivity which is referred to as weak antilocalization. Through closed trajectory loops, the pseudospin stays parallel to the momentum; here for the clockwise and anticlockwise paths, the pseudospins rotate by $+\pi$ and $-\pi$ and thus the difference between the rotation angle of pseudospins of electrons at the end is 2π. However we have to keep in mind that the rotation of the 2π of the pseudospins of the electrons is accompanied by a *Berry phase* shift of π which destroys the constructive interference by putting the electrons out of phase. This is another similarity between actual spin and pseudospin of the electrons: a 2π rotation, does not return the wave function back to its initial state.

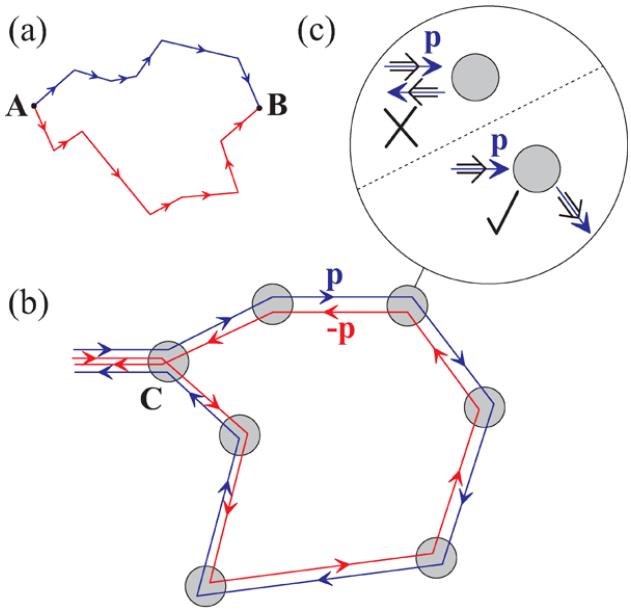

Figure 1.9: Basics of weak localization in graphene
a) Two arbitrary classical paths in a disordered two-dimensional conducting system which link points A and B
b) Such paths, when make closed loops, can contribute in the weak localization correction.
c) Because of the conservation of pseudospin in graphene, backwards scattering is not possible by long-range scatterers, while side and forward directions are allowed.
figure is reprinted from [53].

1.4.3 Landau Levels and Quantum Hall Effects

In the presence of a magnetic field B, the continuous energy spectrum of graphene for the electron and hole branches splits into quantized levels, referred to as *Landau levels LL* of specific energies defined as:

$$E_n = sgn(n)\sqrt{2e\hbar v_F^2|n|B}. \tag{13}$$

Here $n = 0, \pm1, \pm2, \pm3...$ is the *Landau level index*(Figure 1.10). The energy E is measured with respect to the Dirac point. Each level is four-fold degenerate due to the pseudospin and real spin degeneracies. If the Fermi level of graphene is tuned by applying a gate voltage so as to fall in between the Landau levels (the so-called *integer quantum Hall regime*) the longitudinal current is carried by the edge states with no resistance (Figure 1.10-b, red curve). At the same time, the transverse resistance (Hall resistance) saturates at the values of $R = h/e^2\nu$ (Figure 1.10-b, black curve). The allowed values of ν which is normally called *filling factor* is one of the important characteristics of graphene. The early measurements show that ν can only take the following integer values: $\pm2, \pm6, \pm10, ... \pm 4(n + 1/2)$ [54] which differs very much from the other two-dimensional systems and even from bi- and fewlayer graphene samples. So the observation of the plateaus corresponding to these filling factors in magnetoresistance measurements is a fingerprint of monolayer graphene.

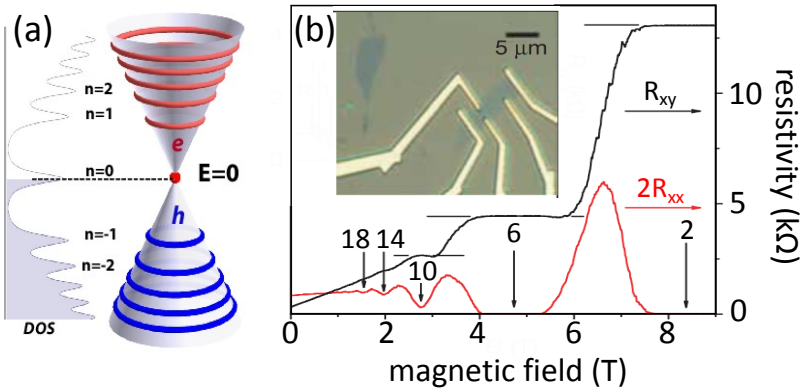

Figure 1.10: Quantum Hall effect in graphene under high magnetic field
a) Under magnetic field, the density of states of graphene splits into the Landau levels with index n. The levels are not equally spaced but the zero level is always pinned to the E=0. Image is adapted from [55].
b) Hall resistance (black) and magnetoresistance (red) curves measured from a monolayer graphene sample at low temperature and under the fixed magnetic field of 9 T. The filling factors are indicated by vertical arrows and numbers. The values of the quantized resistance of $h/e^2\nu$ are shown by horizontal lines. The inset is an optical micrograph of the measured sample. Figure is adapted from [12].

1.5 Mechanical and Thermal Properties

Carbon atoms in a perfect graphene crystal are covalently bonded to each other and form a hexagonal crystalline lattice. Monolayer graphene pieces are typically realized lying on a substrate or as clamped and suspended sheets. In the latter case, graphene is sufficiently isolated from the surroundings to exhibit intrinsic properties. Generally, mechanical properties of solids depend on the quality of the crystal: presence of structural defects like dislocations and grain boundaries. A clear example is that elastic properties like *stiffness* and *Young's modulus* of a crystalline material depend a lot on the strength of the atom-atom inter-

actions whereas its *yield stress* depends on the concentration of the crystalline defects [56]. The fact that graphene can be fabricated in a pristine and defect free state is a promising property indicating that we can expect high mechanical performance [14].

The most important experimental analysis of the mechanical and elastic properties of monolayer graphene was done in 2008 in Columbia university by Lee *et al* [15]. They used the tip of an atomic force microscope (AFM) to press on monolayer graphene sheets which are suspended over circular wells.

The measurement technique which is used by Lee is very similar to the method, published one year before by Frank et al [14]. They had extracted a Young's modulus of 0.5 TPa for doubly clamped samples which is half the value reported in Lee's work.

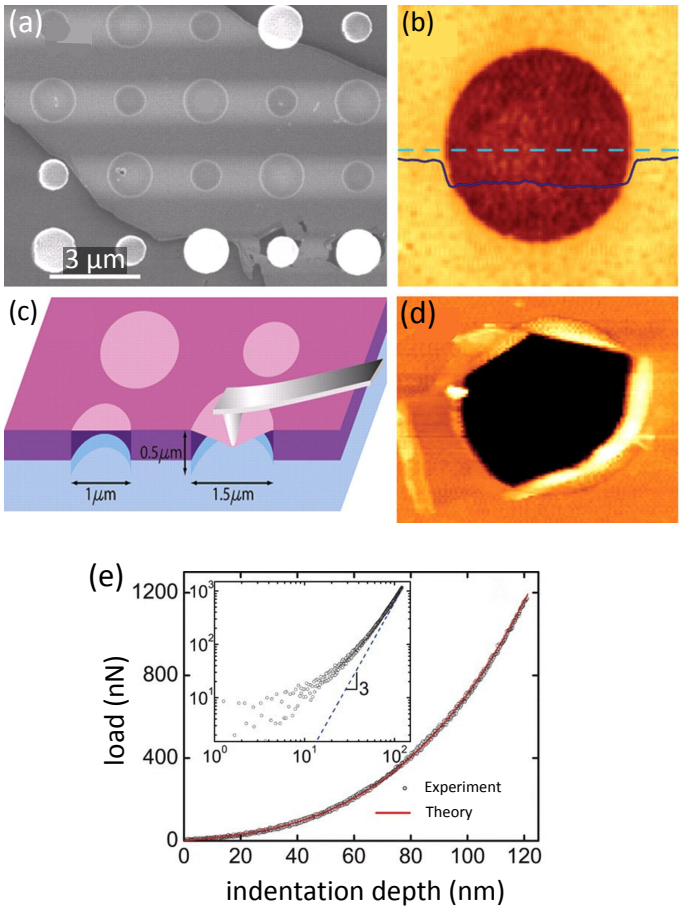

Figure 1.11: Images of the sample and process of experiments done by Lee and coworkers [15]
a) SEM image of a large flake of monolayer graphene spans on an array of circular holes
b) AFM image of the sample on one of the holes with a height profile along the dashed line with a step height of about 2.5 nm
c) Schematic representation of their experiment technique
d) AFM image of one of the samples after breakage
E) Loading/unloading curve and fitting with the theory: The inset figure shows that the curve approaches cubic behavior at high loads.

The measurement technique and some of their results are summarized in Figure 1.11. They have found that graphene shows both nonlinear elastic behavior and brittle fracture *i.e.* breaks suddenly without showing a plastic deformation.

They show that graphene has a tremendous Young's modulus of 1.0 TPa which is 5 times the typical values of stainless steels. Based on their findings, the fracture of graphene happens while the stress exceeds 130 GPa, this is the highest ever measured for materials.

Very high Young's modulus in graphene comes together with ultra low mass, thanks to its 2D structure. The combination of these two properties in this material, makes graphene an appealing material for *nano-elecro-mechanical systems (NEMS) i.e.* the suspended graphene membranes are expected to show very high resonance frequencies. In *Chapter 4* we will discuss about such applications in more details.

Thermal properties of graphene also have been under the focus of much research. The first experimental investigation of the thermal conductivity of graphene has been done by Balandin *et al* [9]. In this work, they employed a confocal micro-Raman spectrometer to probe the dependence of the Raman *G* peak position on the excitation laser source. Variation of the laser excitation power focused on a graphene layer changes the local temperature of graphene which is monitored, thanks to the *G* peak's temperature sensitivity. The local temperature rise as a function of the laser power gives information about the value of the thermal conductivity. Figure 1.12 describes the technique and a sample used in this measurement. By doing such measurements, they obtained an extremely high value of the thermal conductivity up to 5300 W/mK at room temperature, showing that graphene can outperform carbon nanotubes in heat conduction and thermal managements.

In addition to its conductivity, the coefficient of the thermal expansion (CTE) of graphene is very interesting. The early theory works have predicted a negative CTE for graphene in large range of the temperature [57] meaning that it is expected to expand while cooling. This prediction which is due to the out of plane vibrations of the lattice, was later confirmed experimentally [58]. We will discuss more about this in Section 4.8.4.

1.6 Conclusion

Graphene is a material with superior and sometimes unique electrical, mechanical, thermal and chemical properties; however the combination of all of these appealing characteristics in a single object is also unique, making it one of the most interesting materials have ever found. It has been the topic of thousands of investigations in the past decade and thus, the number of the reports published about, can be considered as another unique feature.

Being formed of a monolayer of atoms and its huge surface to bulk ratio makes graphene very sensitive to the environmental properties; this highlights the importance of controlling and engineering the surrounding of graphene to catch its superior properties. This thesis work has been started to probe graphene in optimized environments. The technique and devices we have employed and the results will be covered throughout the rest of this manuscript.

In this chapter, the history of graphene, from the early observation of the multilayer and rather thick graphite to the isolated monolayer graphene, is presented. Most of the appealing electrical properties of graphene originate from its band

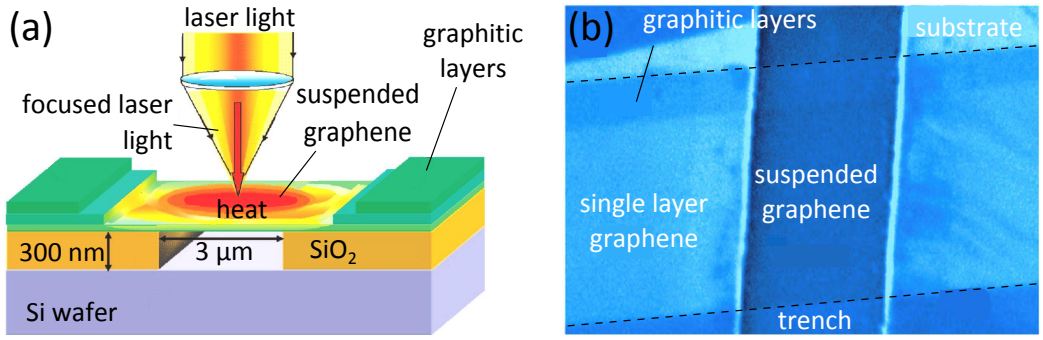

Figure 1.12: First measurement of the thermal conductivity of graphene [9]
a) Schematic representation of the measurement technique: Variation in the laser excitation power leads to the modulation of the temperature of the graphene which is monitored by the position of the G peak. In a precisely controlled position and the energy of the beam as well as the geometry of the sample, one can calculate the thermal conductivity of graphene based on the measured temperature.
b) SEM image of one of the samples used in this experiment: the scale of the sample is not mentioned in the original paper.
Figures are reprinted with adoptions.

structure which depends on the crystalline structure of graphene. Here the basic equations governing the energy and motion of the quasiparticles have been presented. To complete the picture of the transport of the charge carriers in the absence of the external magnetic field, different scattering mechanisms in the diffusive limit as well as the models developed for describing the motion of the carriers have been discussed. Magnetic field is an important parameter which affects the electrical performance of graphene like most other materials. In a separate section of this chapter, we analyzed the behavior of the quasiparticles at both high and low magnetic field regimes. Low-field characteristics of graphene is rather different from most other conducting materials in the sense that the chirality of the quasiparticles accounts for the suppression of the backscattering leading to the weak antilocalization; this concept has been also introduced in this section which gives an insight into our later analyses. At the end of this introductory chapter, we have reviewed the most important mechanical and thermal properties of graphene; some of which will be used in our analyses of the graphene based nano-electro-mechanical systems in chapter 4 of this manuscript.

Phase-Coherent Weak Localization in Graphene on h-BN Buffer Layer

Considering the monoatomic nature of graphene, the substrate used for supporting it plays a major role and may dramatically modify its properties. Moreover even more complex heterostructures can be made using different buffer layers in precisely chosen sequences to promote specific properties. In this way, hexagonal boron nitride (h-BN) is an outstanding material and can be considered as a complementor of graphene. This is mainly because of its neutral and flat surface as well as crystalline structure which matches well with graphene.

Heterostructures made from graphene on h-BN have been under the focus during the recent years, especially zero-field transport of such systems has been studied extensively. However the behavior of these heterostructures in the presence of the magnetic field is not fully understood yet. Weak localization is an important quantum interference effect which can be explored at vanishing perpendicular magnetic field. Being relied on the phase coherent transport of charge carriers, such measurements can reveal information about the nature of inelastic scattering mechanisms which can limit the phase coherence of the carriers. There are some well-known scattering mechanisms which are proven to break the phase coherence in conductors including graphene, however the effect of the h-BN buffer layer on such mechanisms has not been studied. The most important question in this field is: Can using h-BN buffer layers lead to any improvement in the coherence length -as it does for the mean free path of the carriers- or not? There is no straightforward answer for this question because what we gain by having a h-BN buffer layer (reduced Coulomb perturbations from the substrate and improved flatness) do not have any proven influence on the inelastic scattering events. In this chapter we will discuss such issues.

This chapter starts by reviewing all the substrate induced effects that can affect the charge transport in graphene. We will review and compare properties of the most popular materials used for supporting graphene in the following section. Hexagonal boron nitride will be extensively studied there and its advantages for supporting graphene will be addressed. Later, the fabrication process of our samples will be described. Atomic force microscopy is employed to qualify the surface of the h-BN flakes; the results of which will come next in this section. Transport measurements both at zero and low magnetic fields are extensively addressed in the following section. There, we will see that using h-BN layers can indeed help to regain partially the properties of the pristine graphene. Also weak localization interference in graphene on h-BN and on silicon wafers will be minutely investigated. This chapter ends by summarizing all the achievements in the *results and discussion* section.

2.2 Introduction

Besides progress in the field of graphene, other similar two dimensional materials like isolated few layer hexagonal boron nitride (h-BN) and molybdenum disulphide (MoS_2) have become attractive; not only because of their intrinsic properties [59][60] but also because they can be used together with graphene in making heterostructures exhibiting new features [1][61]. In this approach, the basic idea is very simple (though experimentally challenging): to superimpose an isolated monolayer or few layer graphene crystal over another two-dimensional mono- or few layer crystal. This system itself makes a new hybrid device to probe the properties of graphene or, by repeating the process over and over, one can make more complex bottom up heterostructures. We can think about making such artificial materials in terms of playing with *lego blocks* [62]. Weak van der Waals' force keep the whole structure together and in-plane strong covalent bonds tie the atoms in each plane.

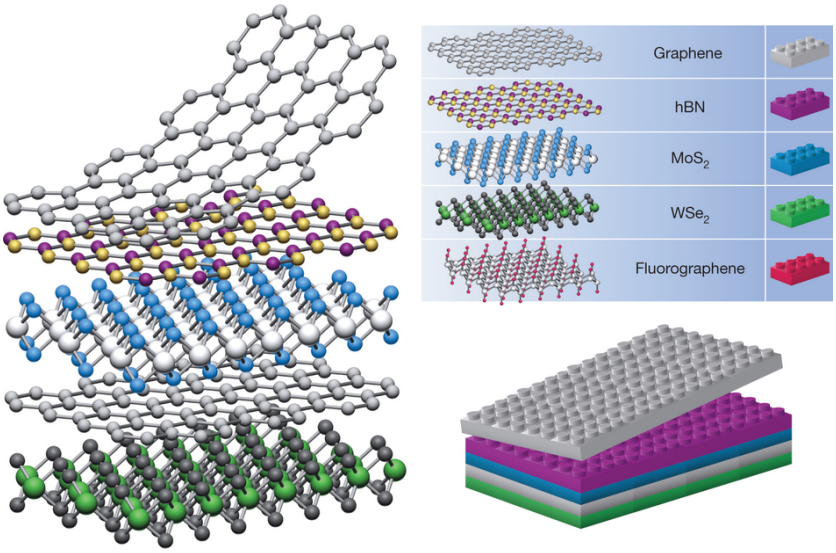

Figure 2.1: Building complex heterostructures based on mono- and few layer 2D materials (reprinted from [62]) Planner isolated thin crystals can be viewed as Lego blocks (right panel) which make the construction of layered structures out of mixed materials possible.

Improving or modifying the intrinsic properties of graphene is an important goal followed in such approaches [1][33][63][3]. Carriers in graphene are accessible without any protection and this makes its properties very sensitive to the environment. This opens up the opportunity of engineering its properties by carefully building up the surrounding.

2.2.1 Influences of Substrate on the Transport in Graphene

In the previous chapter, we reviewed different scattering mechanisms that quasiparticles in graphene may experience traveling from one electrode to another. For a high quality graphene obtained by exfoliation of graphite, the contribution of crystalline defects in the total resistivity can be negligible; then scattering by

charged impurities in the vicinity of graphene as well as by the crystalline vibrations are the most important scattering mechanisms. We also have to consider the effect of corrugations in the graphene sheet which can limit the carrier mobility. Considering the origin of these mechanisms, we realize that scattering by phonons is an intrinsic mechanism which sets a fundamental upper limit for the conductivity; however the other two effects are mainly sample dependent and by optimizing the device fabrication technique and environment we can minimize their contribution in the total conductance of the devices.

2.2.1.1 Charged Impurities on the Substrate

Charged impurity is the term normally referred to localized charged particles which happen to sit on the graphene sheet during the fabrication process or initially present on the substrate before transferring graphene on it. For the latter case, dangling chemical bonds on the substrate or ions trapped in the process of oxidizing the silicon substrate can be considered as such impurities. The water molecules trapped in between the graphene and substrate in the *wet* transferring process of CVD graphene is another source of such impurities. Hwang [32] first pointed out their effects in his theoretical article (Figure 2.2). In his model, long-range impurities with a density of n_i are located in a plane parallel to the graphene sheet with a relative distance of (d) in between. He shows that by increasing the density of these impurities or when they become closer to graphene, the conductivity and thus the mobility of the sample are reduced.

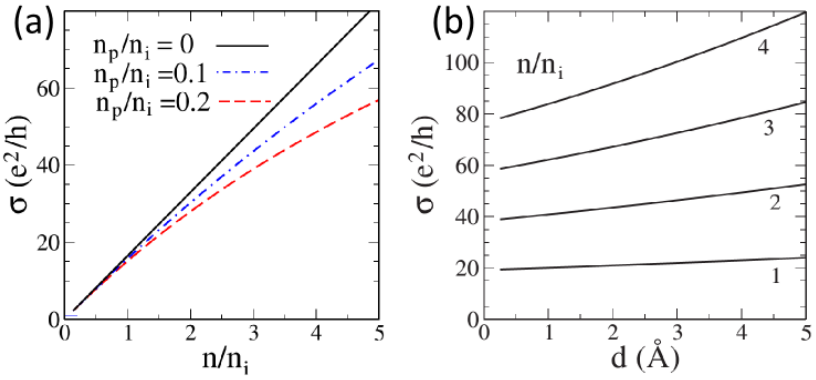

Figure 2.2: Effect of the charged impurities on the conductivity of graphene devices a) Sublinear conductivity at high density which is a signature of high quality graphene devices is more likely to happen in the samples with a low population of Coulomb impurities (n_i) compared to the density of short-range point defects (n_p). b) For a constant density of charged impurities, reducing the distance between the impurity plane and graphene (d) strengthens the effect of this scattering which shows up by reduction in the conductivity. Figure is reprinted from [32].

Sublinear conductance which is normally seen in high quality samples with low concentration of charged impurities (n_i) [44][1][34], is well described by Hwang's model. Figure 2.2-a compares the results for different values of n_i. Here we see that at low carrier density (n) (or at low n/n_i ratio as plotted there) the conductivity (σ) shows a linear dependency on the density. In this regime,

the short-range point defects (with the density n_p) do not have any influence on the carriers and long-range scatterers are dominant. In the other regime and by increasing the carrier density, the difference between the curves becomes evident: while the conductivity of the curves with higher n_i (lower n_p/n_i ratio) keeps increasing in a constant rate, σ has a weaker dependency to n and tends to approach a constant value for low impurity densities. Linear and weak dependencies of σ to n are the signatures of the long- and short-range scattering mechanisms respectively, which arise from the corresponding relaxation times [30]. While the relaxation time between two subsequent long-range scattering events depends to the square root of n ($\tau_{l.r} \propto \sqrt{n}$), it is different for the short-range ones: $\tau_{s.r} \propto 1/\sqrt{n}$. Thus the conductivity $\sigma \propto \sqrt{n}\tau(n)$ will have a linear dependency to n when charged impurities are dominant and tends to saturate when the short-range point defects are dominant.

2.2.1.2 Dielectric Properties of the Substrate

Typical substrates used for graphene devices *e.g.* silicon wafers, usually suffer from a high population of charged impurities. However the dielectric environment of the substrate has an important role in the reduction of the Coulomb potential associated with such impurities. This was addressed first in a theoretical work by Jena *et al* in 2007 [64]. Figure 2.3-a shows a result of their modeling. They found that in a semiconductor surrounded by dielectric environment, the electric potential (depicted by associated field lines here) corresponding to a localized charged ion (impurity) felt by a traveling carrier depends on the relative dielectric constants of the semiconductor (ϵ_s) and of the environment (ϵ_e). For the case when ($\epsilon_e < \epsilon_s$) the field lines bunch closer inside the semiconducting material, leading to the enhancement of the Coulomb interaction. One year after and based on this finding, Jan and his coworkers [65] successfully managed to reduced the influence of charged impurities by engineering the surrounding dielectric environment; they did it by depositing layers of ice on graphene while being measured (Figure 2.3-b). These two works highlight the importance of dielectric engineering on the transport properties of graphene. The newly achieved ballistic transport in graphene encapsulated in between hexagonal boron nitride flakes [33][35] can be interpreted in terms of these findings.

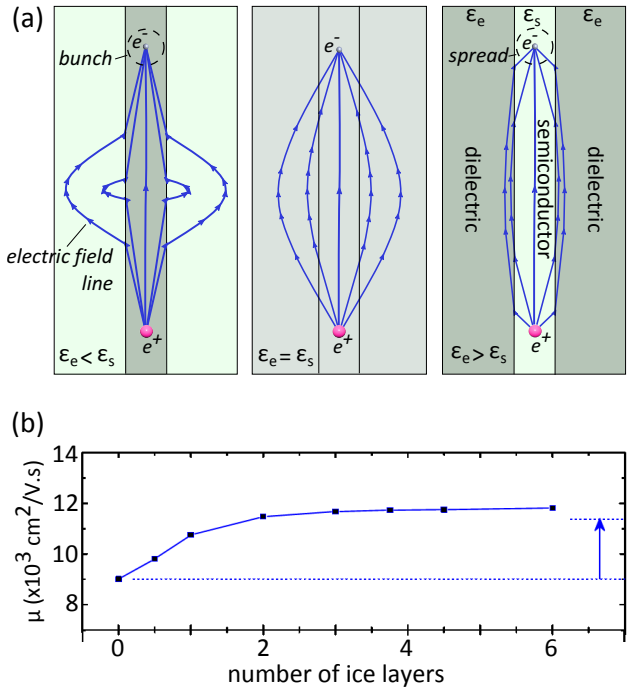

Figure 2.3: Effect of the dielectric environment on the Coulomb interaction between the carrier and charged impurities
a) Jena et al showed that by sandwiching a semiconducting layer (graphene for example) in between two dielectric material with high dielectric constants, the interaction of the electrons and impurities reduces [64]. In this figure which is adopted from the original report, ϵ_s and ϵ_e refer to the dielectric constant of the semiconductor and environment respectively. [65].
b) Results of the experiments done by Jang et al [65]: They show that improving the dielectric environment enclosing the graphene (by adding the layers of ice on the device) leads to enhancement of the mobility of the sample. The initial mobility for the sample and theoretical expectation after covering the device with ice layers are shown by dashed lines there. Image is adapted from the original report.

2.2.1.3 Surface Roughness of the Substrate

Graphene placed on a substrate follows its corrugation which induces remarkably high stress in a graphene lattice [67]. The p_z orbitals of the carbon atoms which are responsible for the charge transport are unprotected and thus the ripples and corrugations which are extrinsically inherited from the substrate can limit the mobility of the quasiparticles [67]. This was the topic of some theoretical and experimental research [68][69][70][71]. Regardless of their effect in reducing the mobility of the quasiparticles, some theories consider such corrugations as the origin of the formation of the electron-hole puddles near the Dirac point [42][72] as well as the strong suppression of weak localization at low magnetic field [49]. Some reports also mention the effect of the substrate induced ripples in increasing the chemical reactivity of graphene [73].

Some studies report the presence of corrugations even at the surface of the free standing graphene [66]. They believe that formation of these ripples is a kind of intrinsic property of graphene, necessary for stabilizing it against thermal instabilities. Such evidences raised debates on whether graphene is truly a 2D structure or not.

2.3 Graphene on Hexagonal Boron Nitride

Finding a more suitable substrate for supporting graphene is the next goal pursued by many research groups once monolayer graphene was isolated. In this section, we will shortly review the most important materials used for this purpose so far; then we will focus on h-BN and try to discuss about its advantages compared to the other substrates. Remarkable transport achievements on graphene/h-BN samples also will be discussed in this section.

2.3.0.4 Important Materials for Supporting Graphene

Silicon wafers are the most common substrate for making graphene devices. This is not only because it is very cheap and easily accessible but also since its processing is well documented; furthermore with simple oxidization techniques, one can turn a thin layer on its surface to a high quality insulator, this is an important property which makes gating of graphene easily possible. However there is a high population of charged impurities on the surface of typically used silicon wafers which happens during the oxidation process or because of the dangling bonds of the SiO_2 phase. The other important disadvantage of such wafers to make graphene devices is its roughness: silicon dioxide formed in this manner has an amorphous structure and thus its surface is very rough compared to crystalline dielectric materials. Consequently silicon wafers are not the ideal substrate to support graphene.

Mica is one of the first materials tested for substitution of silicon wafers [70]: it has a very flat and crystalline structure, thus graphene on mica approaches atomic flatness. Figure 2.4-a to c shows the comparative surface characterization of graphene on mica and on SiO_2 using non-contact atomic force microscopy (AFM). The roughness of the graphene on silicon measured there is on the order of 168 pm (half width at half maximum of the corresponding histogram in part c) which is very similar to the bare SiO_2. This is seven times higher than the obtained value on mica (24 pm). Ultra flatness of the graphene deposited on mica is very important but mica's insulating nature prevents backgating which discards its use.

Giovannetti's prediction has been never realized yet and is under strong doubt.

Hexagonal boron nitride (h-BN) is another candidate for supporting graphene. Giovannetti et al [74] are the first who theoretically investigated electronic structure of graphene/h-BN systems using *ab initio* density functional calculations functional calculations. This work published in 2007, shows that placing graphene on hexagonal boron nitride can open up a bandgap at the Dirac point of graphene. Three years after, the first and most important experimental study of such systems has been published by C. Dean and his coworkers [1]. In this work, they report the fabrication and characterization of graphene/h-BN systems with exfoliated mono- and bilayer graphene. Such devices possess high carrier mobilities as well as carrier homogeneities that are almost an order of magnitude better than similar devices on silicon wafers. Figure 2.4-d compares the surface roughness of h-BN with silicon as is measured and reported in this paper. This worked has been followed by another paper from the same group [2] confirming the advantages of h-BN for supporting CVD graphene.

In the following sections we will review the important properties of h-BN to be used as a substrate for graphene.

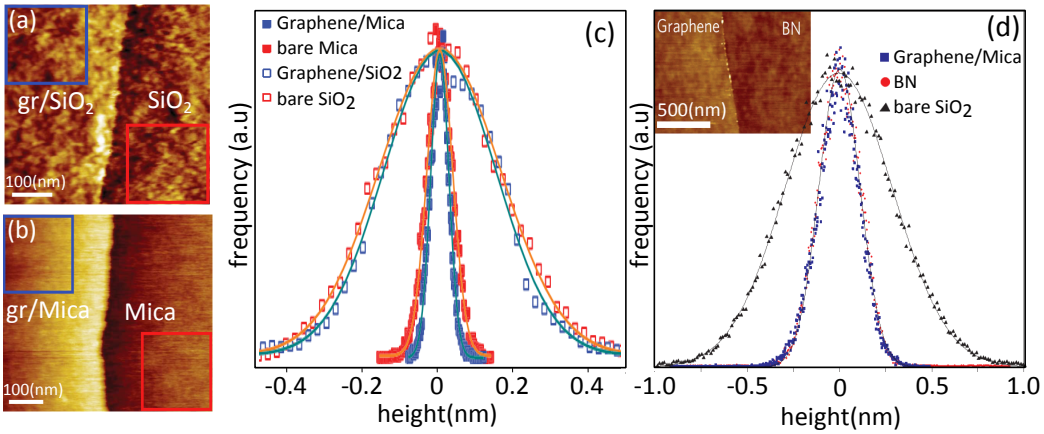

Figure 2.4: Roughness analysis of graphene on different substrates
(a-c) Results of the experiments done by Lui et al [70]: Non contact atomic force microscopy analysis show that -due to the crystalline structure of mica- the surface roughness of graphene/mica is much improved in comparison to the typical graphene/SiO_2 devices. Interestingly and by comparing the roughness of graphene/mica with bare mica as well as graphene/SiO_2 with bare SiO_2, we see that graphene itself can enhance the corrugation of the underlaying substrate. Blue and red squares in figure (a) and (b) mark the area used for calculating the corresponding histograms in (c). These figures are reprinted with adaptation from [70].
(d) Roughness analysis of graphene on h-BN flakes: the roughness of the graphene on h-BN sample is remarkably lower than graphene on SiO_2 and very similar to the bare h-BN. Inset figure here shows the area in which this analysis is performed. Comparing the histograms in (c) and (d), we see that the flatness of mica is remarkably better than the reported h-BN. This figure is adapted from [1].

2.3.0.5 Hexagonal Boron Nitride

h-BN is a dielectric isomorph of graphite in which boron and nitrogen atoms are placed at inequivalent *A* and *B* sublattices in a *Bernal stacking* order. Figure 2.5-a illustrates the crystalline structure of h-BN. Based on its source and application, h-BN comes in the form of crystals of different sizes, before exfoliation. In this work, we have used industrial h-BN powders (Figure 2.5-b and c) produced by *MOMENTIVE performance materials* with >90% purity.

Similar to graphite, bulk h-BN is composed of two-dimensional layers in which strong ionic bonds link the boron and nitrogen atoms in each sheet. Van der Waals' attraction exist between the layers in the bulk material. Thin h-BN flakes can be deposited using the scotch-tape technique, similar to graphene [75]. The obtained flakes are inert and supposedly without dangling bonds.

We have reviewed the roughness analysis of h-BN in Figure 2.4-d. The measured roughness of graphene on h-BN devices are remarkably higher than for graphene deposited on mica; still it remains much lower than the samples fabricated on SiO_2 substrates. However the greatest advantage of h-BN over mica or similar crystalline substrates (like sapphire), comes from its layered structure.

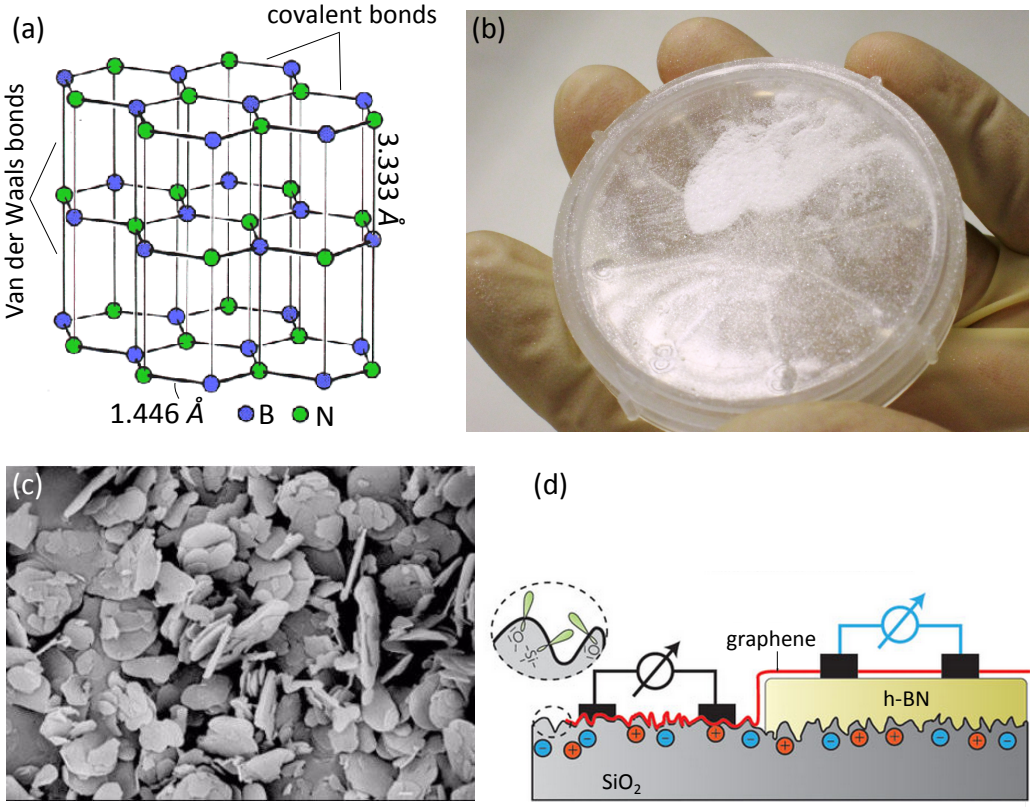

Figure 2.5: Hexagonal boron nitride crystals
a) Crystalline structure of hexagonal boron nitride: Boron and nitrogen atoms are bounded in Bernal stacked 2-dimensional sheets of hexagonal lattices. Figure is adapted from [76].
b) Hexagonal boron nitride before exfoliation in the powder form
c) SEM image of the h-BN powder: the typical size of each flake is of the order of 500µm. Image is reprinted from .
d) Schematic representation showing the advantages of the h-BN as a support for graphene: surface roughness of hexagonal boron nitride is much reduced compared to SiO_2. Also the random Coulomb potential due to the dangling bonds or trapped charged impurities is negligible on h-BN. Figure is adapted from [78].

Indeed, mechanical exfoliation makes it possible to make a relatively thin (10 nm to 100 nm) h-BN buffer layers on SiO_2 before graphene transfer. Such exfoliated flake thickness is enough to smoothen the SiO_2 roughness and to suppress the random potentials associated with charged impurities, while being thin enough for electrostatic gating. Moreover, the lattice symmetry and size of h-BN are very close to graphene.

To summarize, the most important characteristics of h-BN as a supporting material for graphene in transport applications are:

- atomically flat surface, due to the crystalline structure
- neutrality because of the absence of dangling bonds
- insulator with a large band gap, which makes it useful for gating

- compatible with the exfoliation technique and thus easy to fabricate
- hexagonal lattice parameter very close to that of graphene

Figure 2.5-d schematically illustrates the advantages of using h-BN buffer layer in between graphene and silicon wafer. Some of the important characteristics of bulk h-BN are collected and compared with graphite in Table 1.

Table 1: comparision of the important properties of bulk hexagonal boron nitride and graphite

	bulk h-BN	graphite
Bond Length	1.446 [79]	1.42
Interlayer Distance	3.333 [79]	3.42
Density*	$\approx 2.1\,gr/cm^3$ [80]	$2.26\,gr/cm^3$ [81]
Bandgap	5.97 eV [82]	-
Dielectric Constant	3-4 [1]	-
Breakdown Voltage	0.7 V/nm [1]	-
Refractive Index	1.8 [83]	≈ 2.6 [84]
Bulk Modulus	36.5 GPa [83]	34 GPa* [85]
Thermal Conductivity*	4 W/cm.K [79]	2.5 W/cm.K† [86]
Melting Point	1650°C [80]	3500°C [81]

* measured closed to the room temperature
* for single crystal 2H graphite
† measured perpendicular to the c-axis

2.3.0.6 Transport Properties of Graphene on h-BN

In the past section, we studied the superior properties of h-BN which help to boost the electrical performance of graphene in applications. Figure 2.6-a shows the resistance of a graphene on h-BN device as function of gate voltage. This device is made using CVD graphene grown in our lab and subsequently transferred onto the h-BN flake. In a very short range of the gate voltage, the device switches between very high and base resistance which is a signature of the high mobility of the carriers. Such a high mobility (140,000 $cm^2/V.s$) has never been reported for supported graphene on any other substrate other than h-BN.

Part b of this figure shows measurements on a graphene on h-BN sample near the neutrality point [87]. Such measurements demonstrate that atomically flat h-BN surface results in the very flat graphene layers; we also can clearly see

a *moiré* pattern due to the coupling of the lattices of the graphene and h-BN (top left figure). Based on such measurements, they have mapped the charge inhomogeneity at the neutrality point (bottom figures). Unlike for graphene on silicon sample, electron-hole puddles are nearly absent on h-BN because of the reduced density of charged impurities.

In section 2.2.1.2, we reviewed the importance of an improved dielectric environment in reducing long-range scattering events. The dielectric constant of h-BN ($\epsilon_r \approx 3-4$) is not very much different from SiO_2 ($\epsilon_r = 3.9$). However by putting another layer of h-BN on top of graphene (replacing vacuum of $\epsilon_r = 1$ with h-BN) to make graphene sandwiched in between two h-BN dielectric planes improves the mobility. Indeed Mayorov et al [33] have used such geometry and reached ballistic transport with micrometer scale mean free path for the first time in a supported graphene. Similar encapsulated device was reported recently by Wang *et al* [35]: they manage a *1D* contact between the metal electrodes and the side of graphene in between the two h-BN layers.

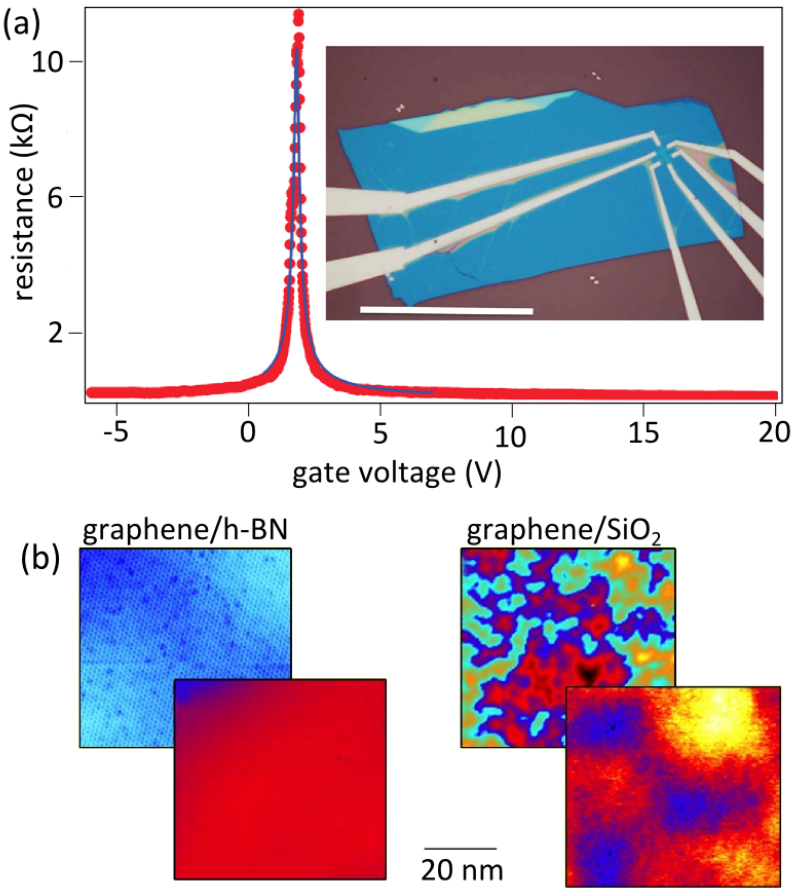

Figure 2.6: Graphene on hexagonal boron nitride
a) Example of a graphene/h-BN field effect results obtained on home made CVD graphene on h-BN device (Main panel): very sharp peak at the neutrality point is the signature of high mobility. The continuous line is the fit with the diffusive transport model (Equation 6) from which a mobility of 140,000 $cm^2/V.s$ is extracted. Inset is the optical image of the corresponding device. This sample is fabricated by Z. Han (Institut Néel) who transferred graphene on h-BN flake at Columbia University (Dean group, New York). Measurements were performed by B. Piot (LNCMI).
b) Scanning tunneling microscopy (STM) measurement of graphene on hexagonal boron nitride (left) and silicon (right) substrates. For both samples, topography and local charge density maps are positioned at the back and front respectively. Figure is adapted from [87].

2.4 Fabrication and Characterization

After reviewing all the advantages of h-BN for making graphene devices in the previous parts, this section will describe the fabrication process of our samples. We have used AFM technique to analyze the roughness of the h-BN flakes right after exfoliation which will also be discussed in this section.

2.4.1 Fabrication Process

Fabrication process of our devices is illustrated in Figure 2.7. We start by mechanically exfoliating h-BN flakes on silicon wafers using scotch tape technique, in the same manner as graphene exfoliation [28] (Figure 2.7-a). The thickness of the oxide layer of the wafer is $\approx 285\,nm$; the hexagonal boron nitride we use is initially in the form of powder from a commercial source (*MOMENTIVE Performance Materials*).

The exfoliation process should be done very carefully to prevent any deposition of glue from the tape on the flakes. At this point, an AFM characterization of the h-BN surfaces is mandatory to select the most appropriated flakes for subsequent graphene transfer in terms of roughness. At the next step, we need to transfer graphene on them (Figure 2.7-b). In this work we use graphene grown on copper in our CVD system. There are two main reasons for this choice: First, our team has developed a transfer process [88] that allows controlling the defect formation in graphene during copper etching which is an issue for the observation of low-temperature quantum interference effects associated by structural defects. Second, fabrication of such devices in which graphene should be aligned precisely on top of the h-BN flakes is much easier with millimeter size CVD graphene compared to the micrometer scale and randomly distributed exfoliated graphene.

CVD graphene grown on copper foil is most often transferred onto wafers using a *wet* technique, described as follows [88]. The process starts by spin coating the surface of graphene -which is not in contact with copper- with PMMA as a support and protection. The catalytic copper layer is etched away by exposing it to the suitable etchant. Indeed, we first used sodium persulfate $Na_2S_2O_8$ diluted solution to remove Cu which appears to damage graphene whereas the use of ammonium persulfate $(NH_4)_2S_2O_8$ induced no defects on graphene. One can refer to [88] for detailed analysis of the effect of the etchant on the properties of graphene.

Using ammonium persulfate for etching copper is firstly reported by John William Turrentine in 1907 [89]. In his experiments, he noticed that it can etch the other metals like nickel, cadium, and iron in acceptable rates. This is also the solution which is used to etch away the excessive copper on printed circuit boards (PCBs).

We note that at the time of this experiment, dry transferring method had not developed yet, so wet technique was employed for fabrication of our devices.

Graphene which is supported by a PMMA layer is now washed in DI water to get rid of all the chemicals and ions that may create defects or doping. Then it is *fished* and transferred from water onto the final substrate. Polar water molecules which normally happen to be trapped in between graphene and the substrate may wash out the advantage of having h-BN flakes as the reduction of the charged impurities. So *dry* transferring techniques have been developed [2].

At the next step, we pattern graphene. This process is done using a *deep UV lithography* technique with a tailor-made mask for the geometry design of the graphene ribbon. The pattern is aligned on top of the graphene/h-BN of interest. By exposing and removing the redundant area of the graphene with oxygen plasma, we end up with a long graphene ribbon with $1-2\,\mu m$ width. It is partially lying on the h-BN flake wile the major part of it is on the SiO_2 wafer.

Now *e-beam lithography* is utilized and followed by *metallization* to deposit electrode material. It should be thick enough to provide a good contact crossing the edge of the flake.

The final device is illustrated in (Figure 2.7-c). The most important points one has to keep in mind in fabricating such devices are as follows:

- Many of the chemicals used to strip and develop resists in nanofabrication processes damage graphene and should be avoided. This includes *NMP*, MF26, microdeveloper etc. We have found that acetone and IPA are safe and we can expose graphene to them for long times to remove PMMA residuals. Also MIBK used for development after e-beam lithography step is quite harmless for a short duration.

- The thickness of the h-BN flake is a very important parameter: roughness and charged impurities from the underlying SiO2 are still sensible through a thin (less that $\approx 5\,\mathrm{nm}$) h-BN flake [90]. Also a thick flake needs a thicker metallic contacts which normally leads to lift-off problems.

- PMMA residuals on graphene can lead to reduction of the mobility of the device and shift the position of the Dirac peak. An annealing process is normally necessary at the final step of the fabrication to remove such residuals.

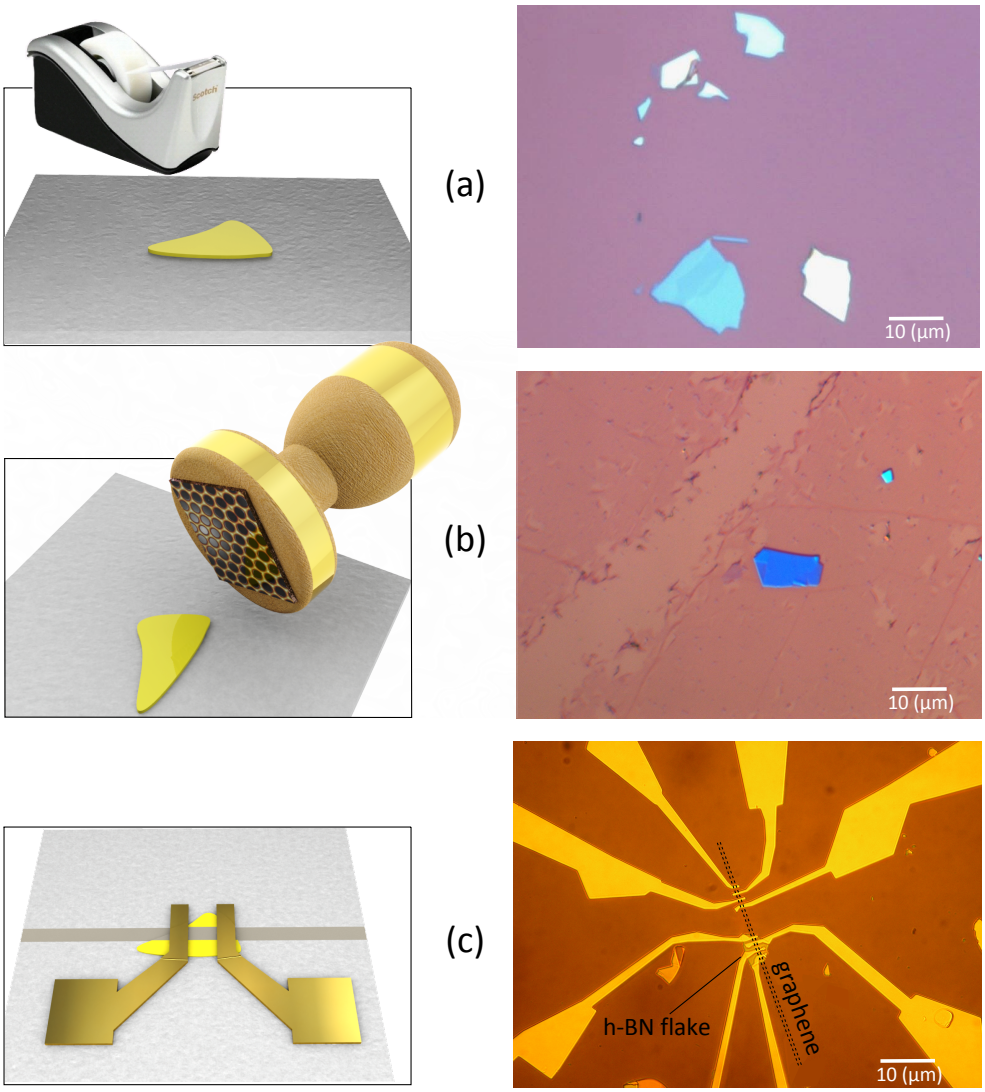

Figure 2.7: Schematic and real representations of the fabrication procedure
a) In a typical scotch tape exfoliation technique [28][1], h-BN flakes are deposited on silicon wafers.
b) Large scale CVD graphene is transferred (wet or dry process) on the sample covering the flakes.
c) After patterning graphene (O_2 plasma etch) and designing electrodes (e-beam lithography), the sample is ready for measurements.

2.4.2 Surface characterization of h-BN Flakes

The cleanliness and flatness of the surface of h-BN flakes are important issues in order to manage high quality samples. They can be quantitatively characterized by atomic force microscopy (AFM). Figure 2.8-a and b shows two examples of flakes characterized by AFM right after exfoliation. Both flakes are from the same source but have different thicknesses as commonly observed from the mechanical exfoliation technique: while the flake in part *a* is rather thin (just 10 nm) the thickness of the other one is 140 nm as measured from vertical cuts on the AFM images. Moreover, they both exhibit typical features induced by the exfoliation

process which will be discussed below; however intrinsic crystalline defects like grain boundaries (partially visible at the left bottom corner of figure *b*) are not directly related to the fabrication and will not be addressed here:

- Mechanical exfoliation can create wrinkles in h-BN (marked by *A*) which can propagate over long distance (more than 10 µm in Figure 2.8-a). Thicker flakes are less subject to wrinkling due to their higher stiffness.

- Thinner flakes can be torn (*B*)

- Both flakes exhibit folded zones, of the whole flake (thin sample) or of some upper layers (thick flake) which is denoted by *C*.

- Flakes are impacted by small dots on the wafer which could be contaminations or process debris. Tagged by *D*, small bumps on the flakes with lateral sizes very similar to the dots on the wafer can be attributed to the inherited roughness from the substrate. The population of such bumps on the flake looks to be higher on the thin flake comparing to the thicker one. This could be partially because the wafer in *figure a* is more contaminated compared to the other one; but it also could be that the thicker flake can smoothen the roughness from the wafer more effectively.

- Some larger bumps on both flakes (tagged by *E*) do not correspond to any similar contamination on the wafer. Thus they could originate from other contamination sources like trapped air molecules below the flake.

- Large features with smooth surfaces and no sharp edges (tagged by *F*) are glue residuals deposited from the scotch tape. If the process of exfoliation is not done precisely (*i.e.* some lateral movements occur during the exfoliation), even the surface of the flakes can be highly contaminated by such glue residuals that require post treatment to be removed.

To understand the effect of the h-BN flakes on diminishing the roughness of the substrate, in part *c* of this figure, we focus on a small area marked by the red square in *a*. Here we see some dots on the substrate and some bumps on the flake which we believe are of the same origin. We have subtracted the thickness of the flake in this AFM topography image for a better comparison. Part *d* shows the height profiles along paths #1 and #2, which go over a contamination on the substrate and on the flake respectively. We can clearly see that while the height of the dot through path #1 exceeds 4 nm, the height on path #2 is less than 1 nm. Moreover the associated width on path #2 is almost two times that on path #1 which shows that the flake is partially suspended close to the underlying dot. Such a trend is observed on all the measured similar features and thus it can

only be attributed to the diminishing of the roughness of the substrate by the flake.

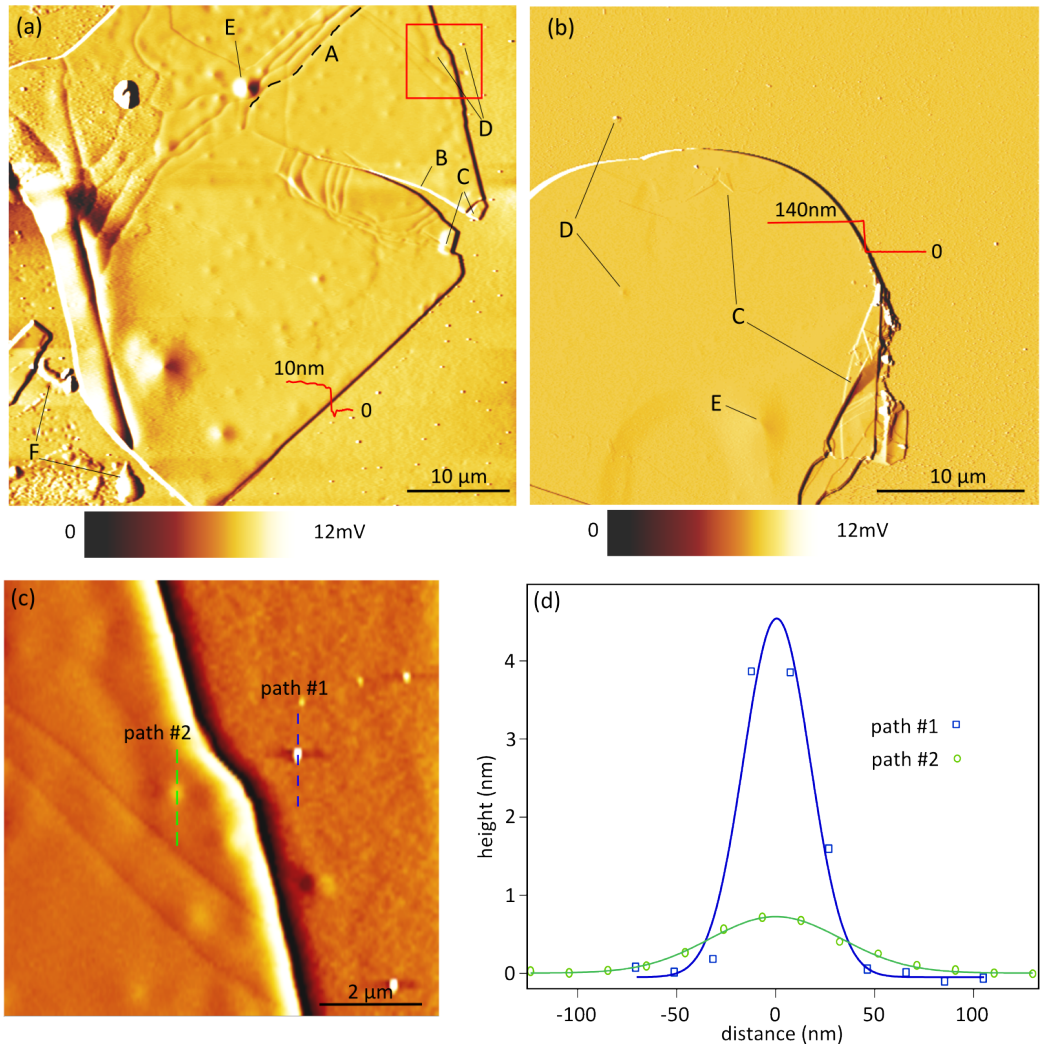

Figure 2.8: AFM analysis showing the possible defects at the surface of the h-BN flakes a) and (b) AFM mapping of the amplitude of the error signal for two h-BN flakes with different thicknesses: The step height profile of each flakes are attached to the figure closed to the measured line. Some interesting areas are tagged by letters which include A: ripples, B: tearing, C: folding, D: external contaminations, E: bumps and F: glue residuals.This mapping is done right after the exfoliating of the h-BN flakes without any post treatment. No glue is visible on the BN flakes.
c) Topography mapping of the area marked by the red square in (a): Some dots due to the contaminations on the surface of the wafer and the related corrugations on the flake are visible here. The thickness of the flake is subtracted for the sake of clarity.
d) Height profiles along the lines #1 and #2 marked in (c)

Such AFM analysis show that h-BN flakes, when precisely exfoliated and in the appropriated thickness range, can help to reduce of the roughness associated to external contaminations on the substrate. Furthermore since h-BN has a 2D crystalline structure, intrinsically it has much flatter surface compared to the underlying amorphous silica. We have investigated this aspect in more details,

which is summarized in Figure 2.9. Part *a* and *b* show the topography of the silicon wafer and h-BN flake respectively (zoomed on Figure 2.8-b regions on the sample). As a reference and to test the sensitivity of our measurements, we have probed the surface of a sapphire crystal (part *c*). Very high roughness of the silica surface compared to the other materials is clear at first glance. We plot the height profiles through arbitrary lines inside the windows *a*, *b* and *c* in part *d*. *Step edges* of the sapphire are clearly visible and correspond to a small tilt in the cut surface of the crystal comparing to the lattice surface, which is normally referred to as the *miscut angle*. Probing such edges is a guarantee of the high accuracy of our measurements. On the surface of h-BN, we do not see nor expect to see such features, just because the exfoliation of the h-BN flakes happens in between the parallel layers. The roughness measured on h-BN flake is comparable to that on sapphire, and far lower than the very sharp features measured on the silicon. Histogram of the height distributions plotted in part *e* can give a quantitative measure of the roughness. In this figure, we see that the distribution of the heights are very close for h-BN and sapphire. A kind of a plateau is visible at the top of the sapphire histogram with a width comparable to the periodic heights observed in *d*: this is only an artifact coming from a misfit of the flattening of the AFM image due to the steps. Interestingly, the height distribution we measure on h-BN is very similar to what is reported in Dean's paper [1] (Figure 2.4); this shows that the industrial h-BN source we are using passes the same standard in terms of the roughness (though not in terms of flake size).

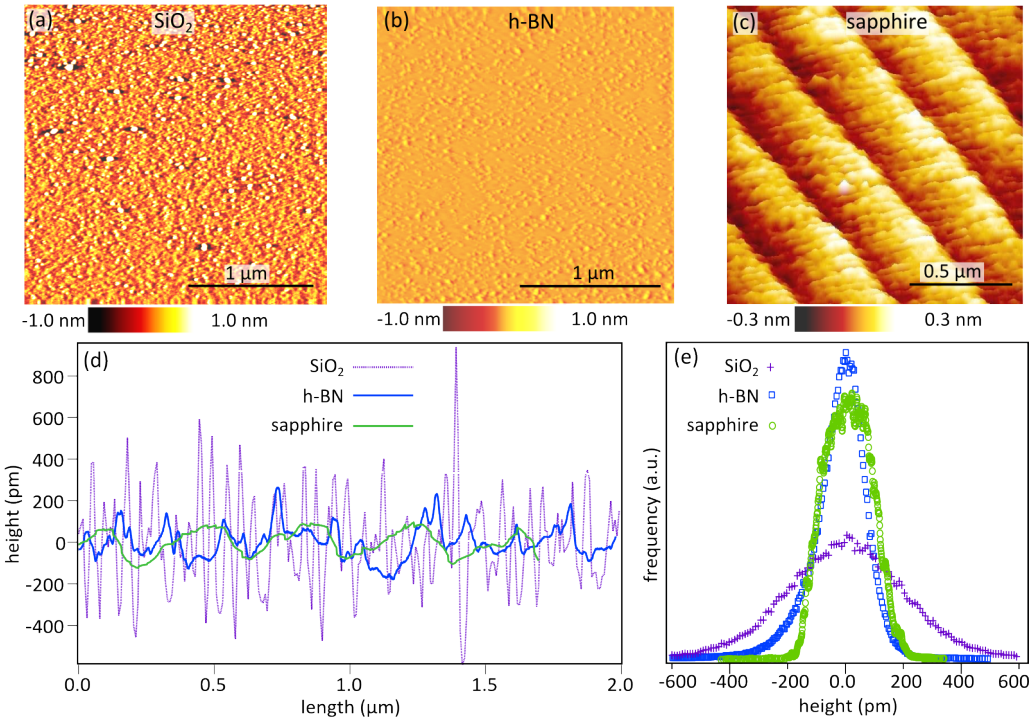

Figure 2.9: Roughness comparison of different substrates
a), (b) and (c): height mapping of the surfaces of the silica, h-BN and sapphire respectively
d) Height profile through arbitrary lines in the corresponding mappings in a, b *and* c
e) Histogram of the height distribution over the whole windows of a, b *and* c*: histogram areas have been normalized.*

In this section, the fabrication process of the samples was reviewed. Our AFM analysis after exfoliating h-BN flakes show that the surface roughness we can obtain from our h-BN sources is comparable with the best results reported in literatures. At the next step one can start electrical measurement of the already fabricated devices.

2.5 Electronic Transport Measurements

One great advantage of using transferred CVD graphene to realize devices is that it allows us to have continuous macroscopic monolayers (Figure 2.7-b) we can pattern into any desired geometry. For example, the sample Figure 2.7-c involves a single graphene ribbon connected in a region sitting on silica and in a next region sitting on h-BN. It realizes a good platform to analyze the effect of the substrate on the transport properties of graphene. Indeed the graphene made device on h-BN and SiO_2 are just few to ten micrometers apart and made out of the same graphene ribbon. Also they have passed exactly the same fabrication processes and the devices are of similar square geometries ($\approx 1.2\,\mu m$). Consequently the substrate is the only parameter which is different. First electronic transport measurements involve resistivity measurements at zero magnetic field. Following measurements use a perpendicular field to assess the influence of the

substrate on the magnetoresistance. All measurements reported here are performed on the sample of Figure 2.7-c.

2.5.1 Zero-Field Transport Measurements

The first electrical characterization of a graphene device consists in measuring the so-called *field effect curve* (Figure 2.10) providing the resistivity of a device as a function of the backgate voltage. The measurement technique is rather simple: a *DC* voltage is applied to the silicon backgate while the resistivity of the devices are measured using a *lock-in technique* in a *four-probe* configuration. The resistivity corresponds to the linear response regime of the transistor as no *DC* voltage is applied to the source and the lock-in oscillator is set to 50 mV only. By gradually sweeping the gate voltage (typically in the −20 V to +20 V range), the *Fermi level* and thus the carrier density shifts which allows one to determine the Dirac peak position.

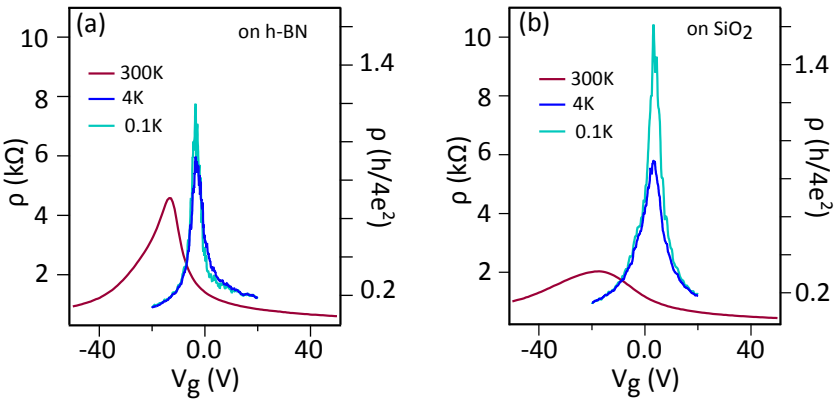

Figure 2.10: Field effect measurement of the samples at different temperatures a) gr/h − BN and (b) gr/SiO_2 samples were cooled down from 300 K to 0.1 K and measured using a lock-in 4-probe configuration. Note that the 300 K measurements were performed in a different apparatus than for the lower temperatures, so the shift in the position of the Dirac peaks can be attributed to the change in the environment.

Analyses begin by probing the effect of the temperature on the devices as summarized in Figure 2.10. One can observe some interesting features by comparing the curves in this figure:

- The maximum resistivity corresponding to the minimum carrier density (Dirac points) of the devices are located at ≈ −3 V and ≈ +3 V for graphene on h-BN (gr/h − BN) and graphene on silica (gr/SiO_2) respectively at low temperatures. A Dirac point located close to zero volt, is something expected for graphene on h-BN devices, due to the low amount of charged doping. The curves at 300 K are measured in a different set-up and we can see the effect of the environment in shifting the position of the Dirac point very clearly. This indicates the high sensitivity of the graphene devices to the surrounding atmosphere.

- Curves corresponding to the gr/h − BN are remarkably *narrower* than the gr/SiO_2 at the same temperatures. In such measurement, the minimum

width of the curves are inversely dependent to the residual charge density (n_{sat}, Equation 9) at the neutrality point [1][2] meaning that the density of the charged impurities is less for the $gr/h-BN$ sample. By increasing the temperature the increased scattering by the lattice phonons gives rise to the broadening of the curves.

- For gr/SiO_2, reducing the temperature between 300 K and 4 K gives a sharper curve which is an indication of the increased mobility; however by further cooling, the curve becomes broader with an increase in the maximum resistivity. Such behavior at low temperatures is the signature of the localization of the carriers which happens due to the increased ratio of the phase coherence length over the mean free path [91].

- The minimum resistivity (ρ_{min}) of graphene is controlled by the short-range scattering mechanisms like crystalline defects which depend on the graphene growth and fabrication process. The fact that we obtained similar ρ_{min} for both samples is an indication that the graphene pieces on the h-BN and on silicon are intrinsically very similar; this is crucial for ruling out the effects associated to the inhomogeneity of the graphene in the later analysis.

Now we focus more on the 4 K data. Figure 2.11-a replots the field effect curves of both devices together at this temperature. Here one can clearly see that both maximum resistivities are very close to the predicted universal value of $\rho_{uni} = h/4e^2$. The measured ρ_{max} for the $gr/h-BN$ at the other temperatures (Figure 2.10) also are not very far from this universal value, which is not the case for gr/SiO_2. Besides we see a clear discrepancy in the slopes on the electron and hole sides of Dirac peaks. Such discrepancy can be attributed to the nature of the dopants close to the graphene which can make either electrons or holes more favorable than the other to travel through the device. Doping by the metal of the contacts [92] can also make unbalanced transport for the electrons and holes.

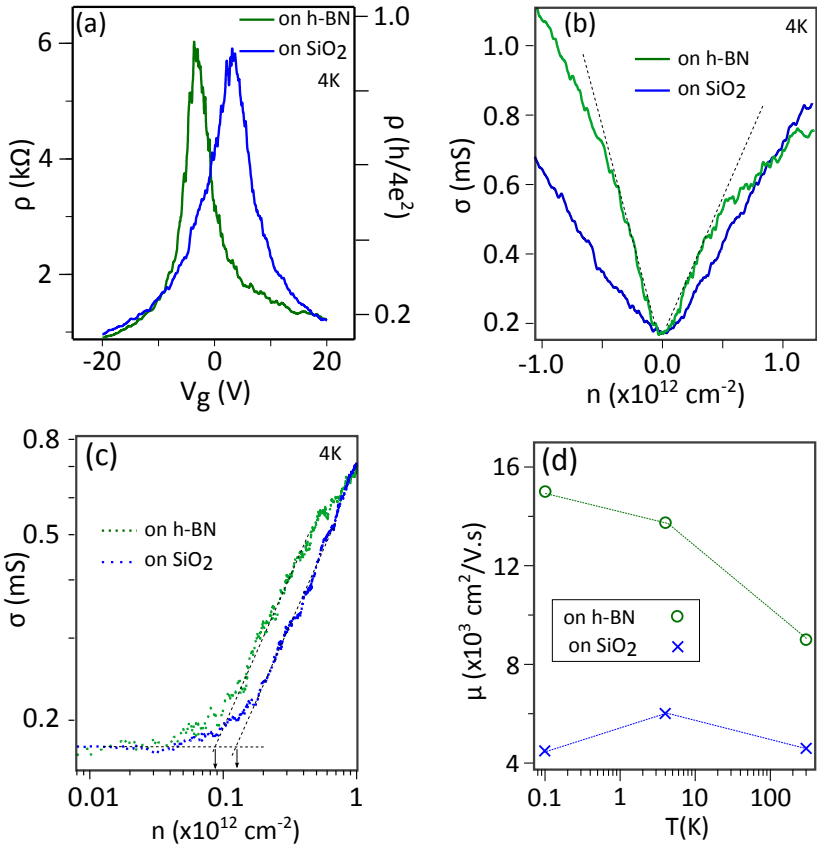

Figure 2.11: Comparison of the zero-field electronic characteristics of the gr/h − BN and gr/SiO$_2$ devices
a) Comparison of the gate dependency of the resistivity of the samples (ρ) at 4 K: Both devices have a maximum resistivity close to the predicted universal value of graphene $\rho = h/4e^2$ at the Dirac point. Also the position of the Dirac point is very close to zero for both of the samples. The hole side of the gr/h − BN (left half) and the electron side of the gr/SiO$_2$ (right half) are steeper than the other halves of the other device which is an indication of the different doping natures for the devices.
b) Conductivity (σ) of the same samples as a function of the carrier density (n) measured at 4 K: Broken lines are the tangents to the curves at low densities.
c) Saturation of the conductivity of the devices close to the Dirac point
d) Mobility of the samples as a function of the temperature: The values are obtained by fitting with the diffusive transport model [32]. For each sample, the side (electron and holes) which shows higher mobility is plotted here.

The conductivity of the devices ($\sigma = 1/\rho$) as a function of the carrier density (n) are plotted on part *b*. While σ evolves linearly in n for gr/SiO$_2$ in both sides, it shows a strong sublinear behavior for gr/h − BN sample. This behavior follows qualitatively the results of the model proposed by [32] (Figure 2.2) and can be attributed to the lower ratio of n_p/n_i (n_p: short-range point defects, n_i: long-range charged impurities) which is expected to be the case for a gr/h − BN device due to less charged impurities. For the same carrier density, we can clearly see that the conductivity of the gr/h − BN is higher than the gr/SiO$_2$ one implying a higher mobility for the graphene on h-BN sample.

As we discussed in the Introduction chapter, the field effect mobility of graphene devices can be calculated as $\mu_{FE} = \sigma/en$, so for a fixed n, sample with higher σ is of higher mobility.

We can see the effect of the remaining charged impurities more clearly close to the Dirac point. Log scale plot of the conductivity (Figure 2.11-c) shows a saturation by lowering the carrier density at $\sigma_{sat} = 1.7 \times 10^{-4}\,S = 1.1 \times 4e^2/h$. This is well described by the formation of electron-hole puddles [32][44]; however this saturation start to happen at different densities (n_{sat}) for the two devices (marked by arrows in the figure) which is controlled by the corresponding densities of impurities. From these data we can extract $n_{sat}^{gr/h-BN} = 0.9 \times 10^{12} cm^{-2}$ and $n_{sat}^{gr/SiO_2} = 1.3 \times 10^{12} cm^{-2}$. Theory developed by Adam *et al* [39] (see the Equation 9 in the introduction) can be employed to calculate the density of charged impurities for the devices:

$$\sigma_{sat} = \frac{20e^2}{h}\frac{n_{sat}}{n_i} \Rightarrow \begin{cases} n_i = 4 \times 10^{12} & \text{for } gr/h-BN; \\ n_i = 5.9 \times 10^{12} & \text{for } gr/SiO_2. \end{cases}$$

These values are obtained by considering the same dielectric properties for h-BN and silicon. We can see that, by using the h-BN buffer layer, the density of the charged impurities felt by carriers in graphene appears to be reduced by more than 30%. This is not a huge reduction but still large enough to improve the transport of the graphene device to a large extent. The $n_i^{gr/h-BN} = 4 \times 10^{12}$ looks rather high since the surface of the h-BN is assumed to be completely neutral; such impurities could be due to the external contaminations deposited on the graphene during the fabrication or cooling the sample. The trapped water molecules between graphene and the h-BN flake can also be responsible. Besides, one has to keep in mind that the h-BN powder used, is for industrial applications and is not fully pure; so some external and charged contaminations are highly possible to exist on the flake.

The mobility of the samples can be extracted based on the diffusive transport model (Equation 6) which is plotted in part *d*. One can see at the first glance that for the whole temperature range, the conductivity of $gr/h-BN$ is higher than the one of gr/SiO_2. This was of course predictable considering all the advantages of h-BN for supporting graphene. On the other hand, starting from room temperature, the mobility raises for both samples down to 4 K. This can mainly be attributed to the suppression of the phonon scattering. However by further cooling, while the mobility of $gr/h-BN$ still increases, it falls for gr/SiO_2. This can also be attributed to the localization, some evidences of which were observed in the field effect curves. Localization of the carriers in a two-dimensional material depends on the ratio l/L_ϕ, (l: mean free path, L_ϕ: coherence length) [91]. In the case where $L_\phi \gg l$, self intersecting trajectories increases the possibility of localizing quasiparticles at intersection points which leads to reduction of the conductivity. As we will see in the next section, for our system (like for most other graphene devices), cooling the sample raises L_ϕ while the mean free path is largely suppressed by the high population of the charged impurities for gr/SiO_2, leading to this localization.

2.5.2 Low-Field Transport Measurements

In the previous section, we have probed the effect of the substrate on the transport properties of graphene at zero magnetic field. A clear charge carrier mobility enhancement together with a strong reduction of the onset of the inhomogeneitity by reducing formation of electron-hole puddles are the main achievements of having h-BN buffer layer for graphene. In this section, we evaluate the effects related to the substrate under the perpendicular magnetic field. Weak localization is an important phenomena measured at vanishing field in graphene and reveals information about the characteristic length scales associated to the scattering in graphene. We will discuss about this effect extensively in this section.

As we have discussed earlier (Section 1.4.3), the density of states of graphene splits into the discrete *Landau levels* under magnetic field. Formation of such levels show oscillations in the longitudinal resistivity as well as plateaus in the transverse *Hall resistivity* while sweeping the gate voltage or the magnetic field. It is convenient to visualize such processes by measuring the conductance as a function of the carrier density and magnetic field. The resulting map known as *fan diagram of Landau levels* [93] is shown in Figure 2.12-a and b. For each *filling factor* ν (corresponding to an specific Landau level) and once the electron density equals to $n(B) = B\nu/\Phi_0$ ($\Phi_0 = h/e$), the Hall conductance remains constant at the value $\sigma = \nu e^2/h$. Then, originated from the center (B=0, n=0) and fanning out with the slop $dn/dB = \nu/\Phi_0$, plateaus appear as stripes in such diagrams. In this system, the applied magnetic field is not strong enough to completely split the levels. Also since a well defined *Hall bar geometry* is not used, the longitudinal and Hall conductivities are mixed to each other; all these makes assignment of Landau levels difficult. The expected constant-conductance stripes for different filling factors are marked in Figure 2.12-a and b. Splitting the Landau levels at a specific magnetic field, depends on the quality of the device [34]. By comparing the mapping in *a* and *b* we see that the levels are more developed in $gr/h-BN$ indicated by sharper line separating Landau levels; this is due to the higher mobility of the carriers.

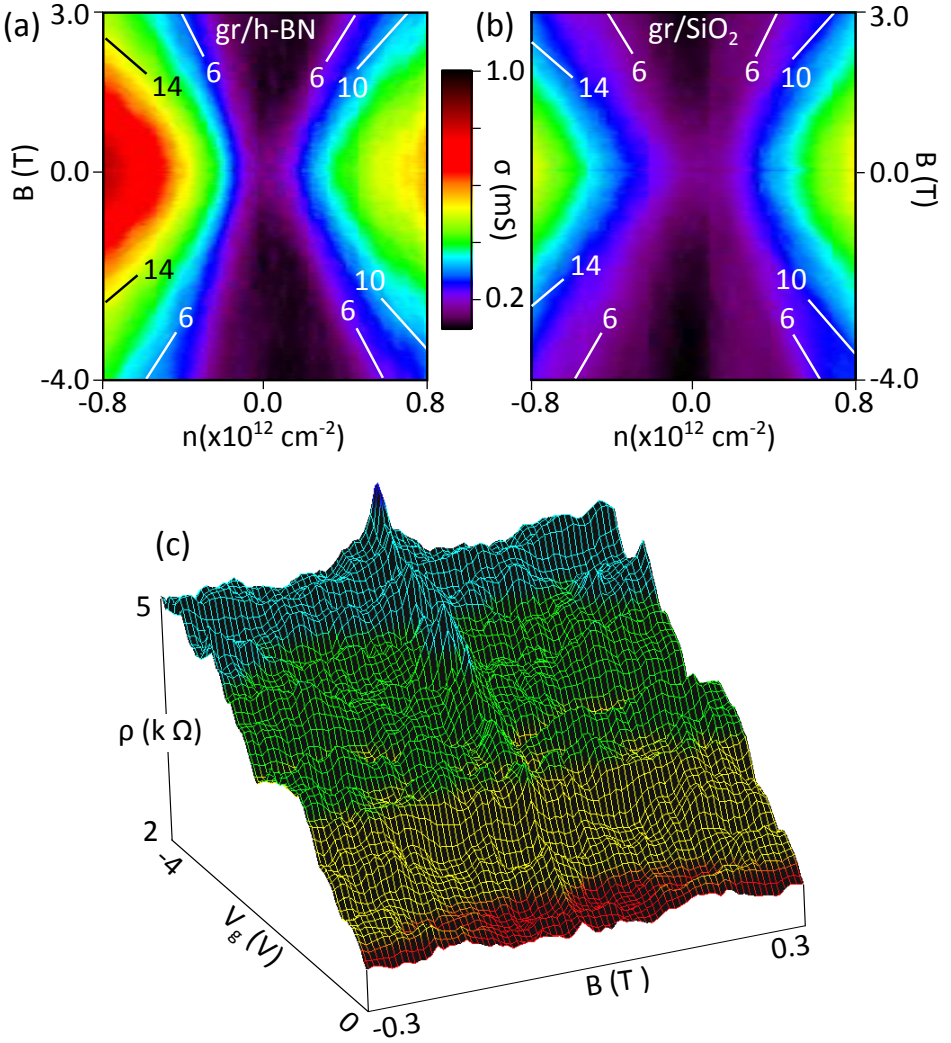

Figure 2.12: Magnetoconductance measurements in graphene on h-BN and on silica
a) and (b) Landau level fan diagram of the conductance of gr/h — BN and gr/SiO_2 samples as a function of the carrier density (n) and magnetic field (B): Some of the expected stripes corresponding to different filling factors are marked there. Both of the graphs are measured at 4 K.
c) Low field magnetoresistance in gr/h — BN: The formation of the weak localization interference is evidenced as a peak in the resistivity close to B=0 in all the gate voltage range. This color map is measured at 4 K.

As seen in Figure 2.12-c, the magnetoresistance of both h-BN and silicon-based devices exhibit a peak around zero magnetic field, a phenomenon which is the signature of weak localization (WL) effects. We will focus on this signal for the rest of the chapter. One can refer to the section Section 1.4.2 where details about the theory underlying these signals are introduced.

We have measured several weak localization signals at different temperatures and charge carrier densities for both graphene devices. Figure 2.13 shows some of the measured signals. Each curve is obtained by measuring the conductance while sweeping the magnetic field at a fixed gate voltage and temperature (which are detailed in the caption and legend). The Y-axis denoted as $\Delta\sigma$ is the conduc-

tivity correction term, defined as $\Delta\sigma = \sigma(B) - \sigma(0)$. Back and forth traces are plotted together after a small parasitic field hysteresis (attributed the flux trap in the cryostat environment) has been canceled (by manually setting the apex of the curves at $B = 0$).

The theory for weak localization in graphene was developed in great details by McCann [94] by adapting the concepts of WL in metals to graphene. He derived the following formula:

$$\Delta\sigma(B) = \frac{e^2}{\pi\hbar}\left[\left(\frac{B}{B_\phi}\right) - F\left(\frac{B}{B_\phi + 2B_i}\right) - 2F\left(\frac{B}{B_\phi + B_*}\right)\right]. \tag{14}$$

In this relation, $F(z) = ln\, z + \psi(\frac{1}{2} + \frac{1}{z})$, $B_{\phi,i,*} = \frac{\hbar c}{4eL^2_{\phi,i,*}}$ in which ψ is the digamma function. Also while B shows the magnetic field, $L_{\phi,i,*}$ respectively stands for the phase coherence, *intervalley* and *intravalley* scattering lengths. The corresponding relaxation times can be directly calculated knowing the diffusion constant D through $L^2_{\phi,i,*} = D\tau_{\phi,i,*}$. There are few variations of this model in the literature and we can similarly rewrite the above formula as :

$$\Delta\sigma(B) = \frac{e^2}{\pi\hbar}\left[F\left(\frac{\tau_B^{-1}}{\tau_\phi^{-1}}\right) - F\left(\frac{\tau_B^{-1}}{\tau_\phi^{-1} + 2\tau_i^{-1}}\right) - 2F\left(\frac{\tau_B^{-1}}{\tau_\phi^{-1} + \tau_*^{-1}}\right)\right]. \tag{15}$$

Here τ_B refers to the effect of the magnetic field expressed in time units through: $\tau_B^{-1} = 4eDB/\hbar$. There are two equivalent approaches dealing with this model in WL studies: either one extracts $L_{\phi,i,*}$ from the fits and then calculates the $\tau_{\phi,i,*}$ using the existing relation or inversely, extracting the relaxation times from the fits and then calculating the corresponding lengths. In both approaches, in order to have any information about the relaxation times, we need to know the diffusion coefficient (D) under the same conduction regime. However as in graphene, D is not well defined close to the Dirac point (which is the region of our focus in most of the present measurements), we will keep all our results in terms of $L_{\phi,i,*}$ rather than $\tau_{\phi,i,*}$. However since discussion about the corresponding relaxation times can help to understand the physics behind, we qualitatively invoke $\tau_{\phi,i,*}$ whenever needed. The continuous lines in Figure 2.13 are the best fit using Equation 14.

A simplification can be made for the function *F(z)*. Since in all experiments performed at low fields, z is always much lower than 1, the function in Equation 15 can be simplified as $F(z) = z^2/24$ and then Equation 15 can be rewritten as [52]:

$$\Delta\sigma(B) = \frac{e^2}{24\pi\hbar}\left(\frac{4eDB\tau_\phi}{\hbar}\right)^2\left(1 - \frac{1}{(1 + 2\tau_\phi/\tau_i)^2} - \frac{2}{(1 + \tau_\phi/\tau_*)^2}\right). \tag{16}$$

One of the main features introduced by defects in WL of graphene is that the interference of carriers belonging to the same valley in a time-reversal manner [53] can be destroyed by the scattering on large defects. Indeed such defects induce intervalley scattering and thus break chirality [94][95]. Graphene ripples may have the same effect as they induce fluctuations of the effective magnetic field thus

destroying the interference[49]. In our system, the roughness of the graphene inherited by conforming the underlying substrate can indeed reduce the τ_*^{-1} intravalley scattering rate for the gr/SiO_2 device. Long-range charged impurities at the surface of the silicon wafer induce fluctuations on a range much larger than the graphene lattice constant therefore they are not able to break the chirality and affect the pseudospin [94]. This is why they do not have any strong influence in reducing τ_*. However such impurities can effectively work as scattering sites for inducing constructive interferences between the time-reversal trajectories. Sharp defects like voids in the lattice of the graphene are believed to be able to backscatter the quasiparticles between two valleys, such intervalley scattering are able to mix the two valleys [52]. Consequently in the case that high population of the intravalley scatterers (low τ_*) can suppress the localization due to the interference within a valley, high intervalley scattering is needed to restore it back by mixing the two valleys.

What is called *weak antilocalization (WAL)* (Section 1.4.2) is characterized by a negative slope in the magnetoconductivity. It comes from the two last terms with the negative signs in the Equation 15; For a perfect graphene lattice without any intravalley as well as intervalley scattering mechanism, τ_i and τ_* both diverge and thus the magnetoconductivity is purely controlled by the last term which leads to a *pure* weak antilocalization signal; this is first experimentally seen in [52]. Just the other way around, for a sample with very high population of the defects (intra- and intervalley scatterers), the first term in the equation plays the most important role while the other terms with negative slopes are suppressed; this leads to the weak localization condition.

Now and based on this developed theories, we interpret the important features of our magnetoconductance data presented in the panels of Figure 2.13 and considering the following observations:

- At first glance, we notice that the WL dips around zero-field are *normally* deeper for $gr/h-BN$ compared to the gr/SiO_2 reference sample measured in similar gate and temperature conditions. This general feature is reproducible in most data shown in this figure. The depth of the WL correction mainly depends on the phase coherence length (L_ϕ); At zero magnetic field, all trajectories with lengths smaller than L_ϕ are able to interfere constructively thus creating localization. So the longer the L_ϕ the more trajectories can contribute in the localization and thus the stronger the WL correction effect. One can see this direct and strong dependency of $\Delta\sigma(B)$ to τ_ϕ in Equation 16. Based on the observed magnetoconductance effect, we can directly infer that the coherence length on the $gr/h-BN$ appears to be significantly longer compared to the gr/SiO_2 sample at different measurement regimes.

- For h-BN supported sample in *a* the magnetoconductance exhibits a downturn at low field, which is not seen in the silica-supported sample (*b*). This downturn which is characterized by the negative slope in the magnetoconductance and is a clear signature of the influence of WAL, arises from the second and third therm in the Equation 15. Being specifically related to the chirality of the graphene, it can be suppressed when the intravalley

This assumption is supported by the fact that both samples are made on chip from the same graphene and very close to each other; Also the similar residual resistivities far from the Dirac points, which are measured in both of the samples (Figure 2.10) confirms this assumption.

scattering rate is higher than intervalley one ($\tau_* \ll \tau_i$) [94][53]. Assuming that the τ_i which is controlled by sharp crystalline defects is similar for both the devices, we can attribute the inversion of slope to the higher intravalley scattering rate for the silica supported sample. Among all the parameters which can affect the intravalley scattering rate, the difference of surface corrugation between the two samples can be the only change invoked. Previously, the roughness of the graphene deposited on silicon wafer is reported to be strong enough to suppress all the weak localization effects [49] by creating some random magnetic fields. It seems that corrugations are not that strong in our gr/SiO_2 sample however it still can account for the suppression of the WAL in some cases.

- The width of magnetoconductance dips are also different for gr/SiO_2 and $gr/h-BN$ devices. This behavior is clear in panels *a* and *b* and even more in panel *f* which corresponds to the measurements performed at 4 K. Scattering events shown in Figure 1.9 can happen due to charged impurities, substrate related corrugations and crystalline defects. Assuming that the graphene crystal is the same for both the samples, the two former scattering events are seldom in $gr/h-BN$ samples; in the other words, the return trajectories making constructive interference in $gr/h-BN$ are expected to be longer in this sample. The phase accumulated by an electron traveling in a closed loop under perpendicular magnetic field is expressed as the circulation of the *vector potential*: $\theta = \frac{e}{\hbar}\oint \vec{A}.\vec{dl} = \pm\frac{\pi BS}{\phi_0}$ ($\vec{A}$: vector potential, $\vec{dl}$: small section of the trajectory, S: area of the loop, ϕ_0: flux quantum) [91]. This implies that by increasing the magnetic field, the constructive interferences are destroyed more rapidly in $gr/h-BN$, which accounts for narrower dips. Spacing between the scatterers sets a lower limit for the length of the trajectories; the upper limit is set by the coherence length. So by increasing the temperature, reduction of the $Ł_\phi$ accounts for reduction of the average areas (S) and thus the dips become wider. This result is consistent with the previously reported data [51]. The broadening of the peaks measured at higher temperatures is more pronounced (panel *c*). However as will be shown later, the coherence length saturates below 7 K for gr/SiO_2 at the Dirac point, thus decreasing temperature does not improve $Ł_\phi$ as no remarkable change in the dip widths between 1 K and 7 K (part *d*) is visible.

- By comparing the temperature dependency of the curves (panels *c* and *d*) some interesting features are also observed: While at the lowest temperature, non of the samples exhibit any downturn, increasing the temperature shows manifestations of WAL. The negative terms in Equation 16 which control the weak antilocalization are inversely dependent to the τ_ϕ/τ_i and τ_ϕ/τ_* ratios. Reducing the τ_ϕ by increasing the temperature, signifies the negative terms and weak antilocalization appears. The reduction in the depth of the dips at higher temperatures can also be explained in terms of the reduced phase coherence length.

- Besides decreasing τ_ϕ, increasing τ_i also reduces the τ_ϕ/τ_i term showing up WAL. Short-range crystalline defects are mainly responsible for the intervalley scattering events which scales with the density of the carriers. Suppressed weak antilocalization at part *a* at high densities can be explained by reduced τ_i at this regime [50].

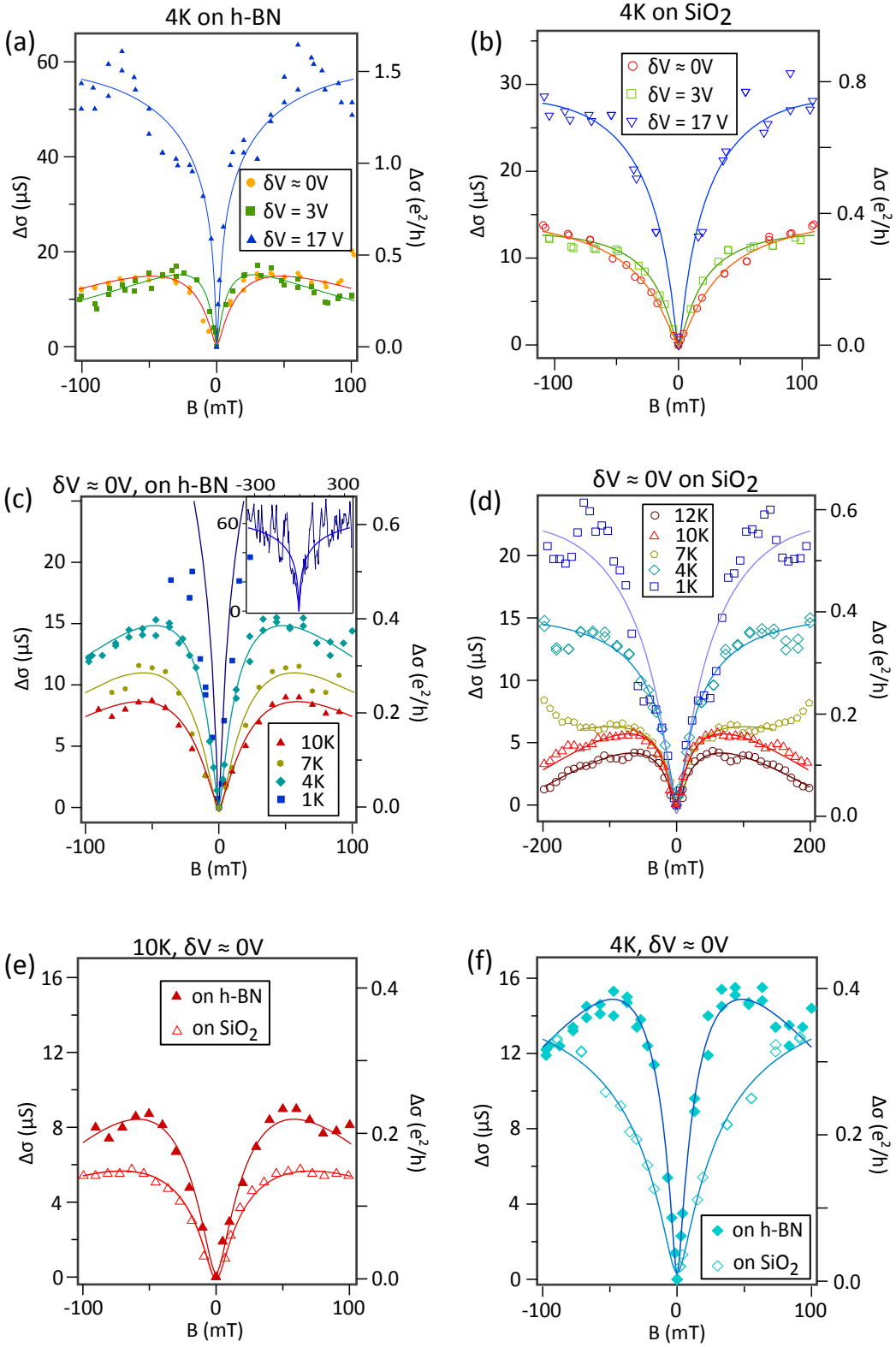

Figure 2.13: Low magnetic field magnetoconductance in gr/h — BN and gr/SiO_2 devices
(a) and (b) Effect of doping measurements at different charge carrier densities at 4 K; δV denotes the gate shift from the Dirac point.
(c) and (d) Effect of temperature on the samples: all the measurements are performed at the Dirac point.
(e) and (f) Direct comparison of the data from gr/h — BN and gr/SiO_2 devices at 10 K (e) and 4 K (f).
Continuous lines in all the panels are the best fits with the existing theory (Equation 14).

By fitting the measured magnetoconductance data with the model (Equation 14), the corresponding lengths for both devices at different temperatures and charge carrier densities can be extracted. Figure 2.14 summarizes all the results. Panel *a* depicts the density dependence of the phase coherence lengths for both of the samples. It can clearly be seen that the coherence length for the $gr/h-BN$ device is almost twice the gr/SiO_2 at all densities, confirming that h-BN buffer layer does improve the coherence of charge carriers. Phase coherence is known to be destroyed by inelastic scattering events such as electron-electron interactions [51][50][52] as well as by electron-phonon interactions [52] and magnetic impurity scattering [96][97]. The way h-BN can affect these mechanisms are not well studied yet and not enough evidence exists to make any conclusions.

Intervalley scattering lengths of the devices as a function of the carrier density is depicted in panel *b*. Short-range scattering mechanisms which affects L_i normally show up at higher densities, this is why a reduction of the L_i can be seen when increasing the density. Crystalline defects like voids are one of the most important intervalley scattering mechanisms, however considering that the lattice of the graphene for both devices have the same density of defects, the fact that L_i^{gr/SiO_2} is always less than $L_i^{gr/h-BN}$ invokes an additional scattering mechanisms which is stronger in gr/SiO_2. Substrate roughness is considered as another source for the intervalley scattering in the samples strongly attached to the substrate [94]. Considering the relative roughnesses of the h-BN and silicon, it seems it plays an important role in reduction of the L_i^{gr/SiO_2} in our experiments.

We see the same trend of the increased intravalley scattering events in gr/SiO_2 compared to $gr/h-BN$ in part *c* of this figure. However, unlike L_i, there is no remarkable density dependence in L_*. Considering all intravalley scattering mechanisms, it seems that only ripples and corrugations of the graphene, inherited from the underlying substrate are different for gr/SiO_2 and $gr/h-BN$ which can increase the intravalley scattering rate in the former.

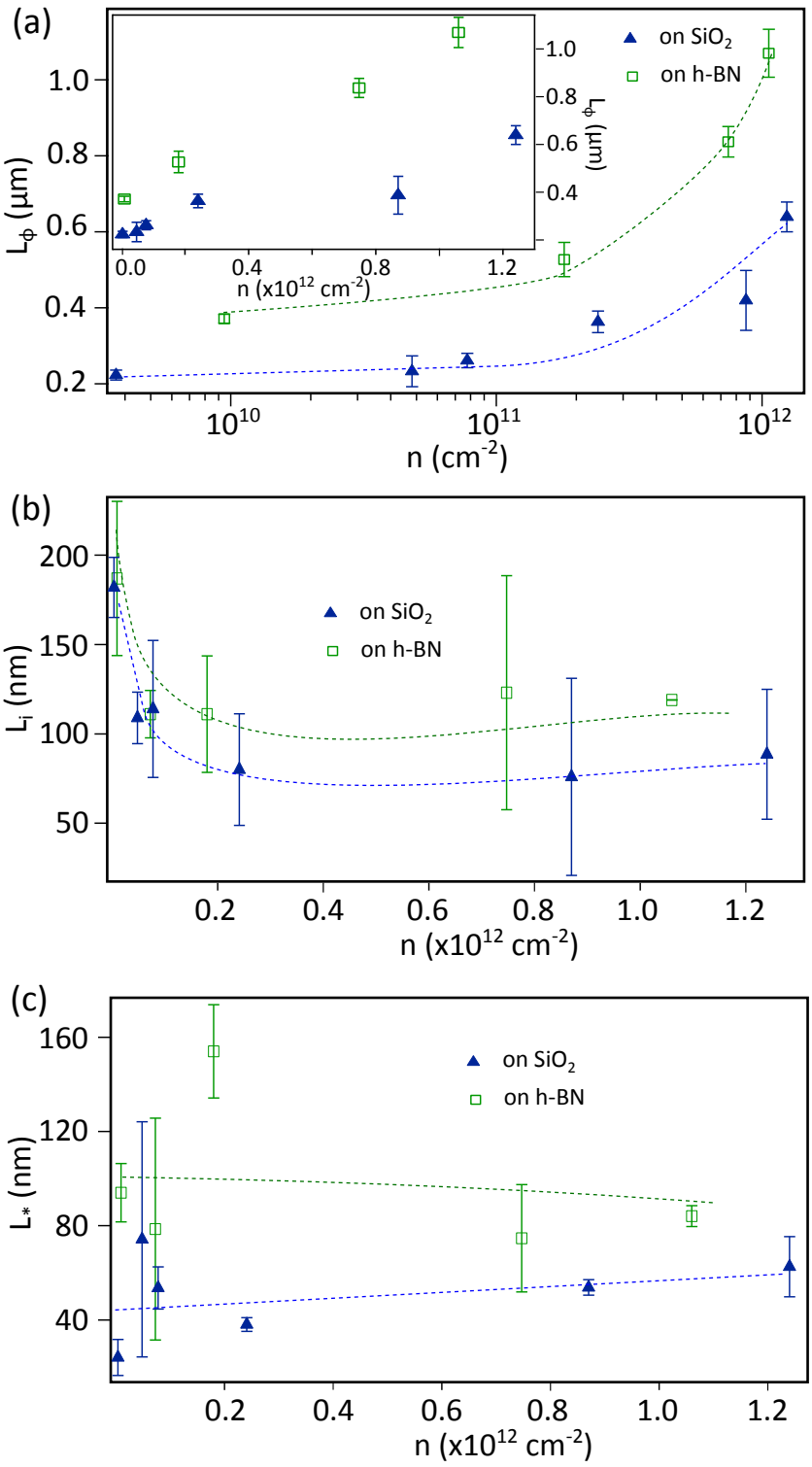

Figure 2.14: Characteristic lengths playing roles in the weak localization as a function of the carrier density in the samples
a) Semi-log plot of the phase coherence length (L_ϕ) for the gr/h − BN and gr/SiO_2 devices: While L_ϕ is remarkably longer in gr/h − BN comparing to the gr/SiO_2 device, increasing the carrier density improves it for both of the samples. Inset figure shows the same data in linear scale.
b) and (c) Intervalley (L_i) and intravalley (L_*) as functions of the carrier density for gr/h − BN and gr/SiO_2 devices
All the data are obtained by fitting the data measured at at 4 K with the theory of the weak localization in graphene (Equation 15). The dashed lines in all the cases are guides for the eyes.

Now we turn to investigate the temperature dependency of the coherence lengths. The results are shown in Figure 2.15. Direct comparison of the L_ϕ for the samples are plotted in *a*. It appears that coherence length linearly depends on the inverse temperature in the $gr/h-BN$ sample. Such $1/T$ dependence has been reported for τ_ϕ close to the Dirac point in previous experiments of grahene [51][52] and is attributed to the dominant electron-electron interactions in this regime. However coherence length shows a complete saturation for the gr/SiO_2 sample. In panel *b*, we see that by increasing the gate voltage, a similar saturation happens at $\delta V = 3\,V$ but at a higher length. Further increasing the gate voltage helps to get rid of such saturation and recover the expected linear trend as seen in the $\delta V = 17\,V$ curve. At low carrier density, the formation of the electron-hole puddles [32][42] limits the coherence of the quasiparticles in gr/SiO_2 which explain the saturation. As we reviewed in the previous sections, at vanishing carrier densities, the charged impurities close to graphene leads to the formation of a landscape with coexisting electron and hole puddles. This inhomogeneity can modify the geometry of conducting paths and decrease the effective dimensions of the sample, ending the saturation of the L_ϕ (see the Figure 2.6-b).

The temperature dependency of L_ϕ for $gr/h-BN$ is plotted in panel *c* for very low and high carrier density regimes. As we saw in Figure 2.14, increasing the density leads to improvements in the coherence length in our samples. For $\delta V = 17\,V$ such improvement is so fast that L_ϕ reaches the size of the sample at $4\,K$. By further cooling, surprisingly we do not see any peaks associated to the weak localization in the sample (inset figure). We can explain this behavior in terms of the rapid increase in the intervalley scattering by the edges of the device, when the carriers starts to feel it at high L_ϕ. The increased intervalley scattering destroys all the interference effects associated with the carriers belonging to the same valley and leads to a constant resistance.

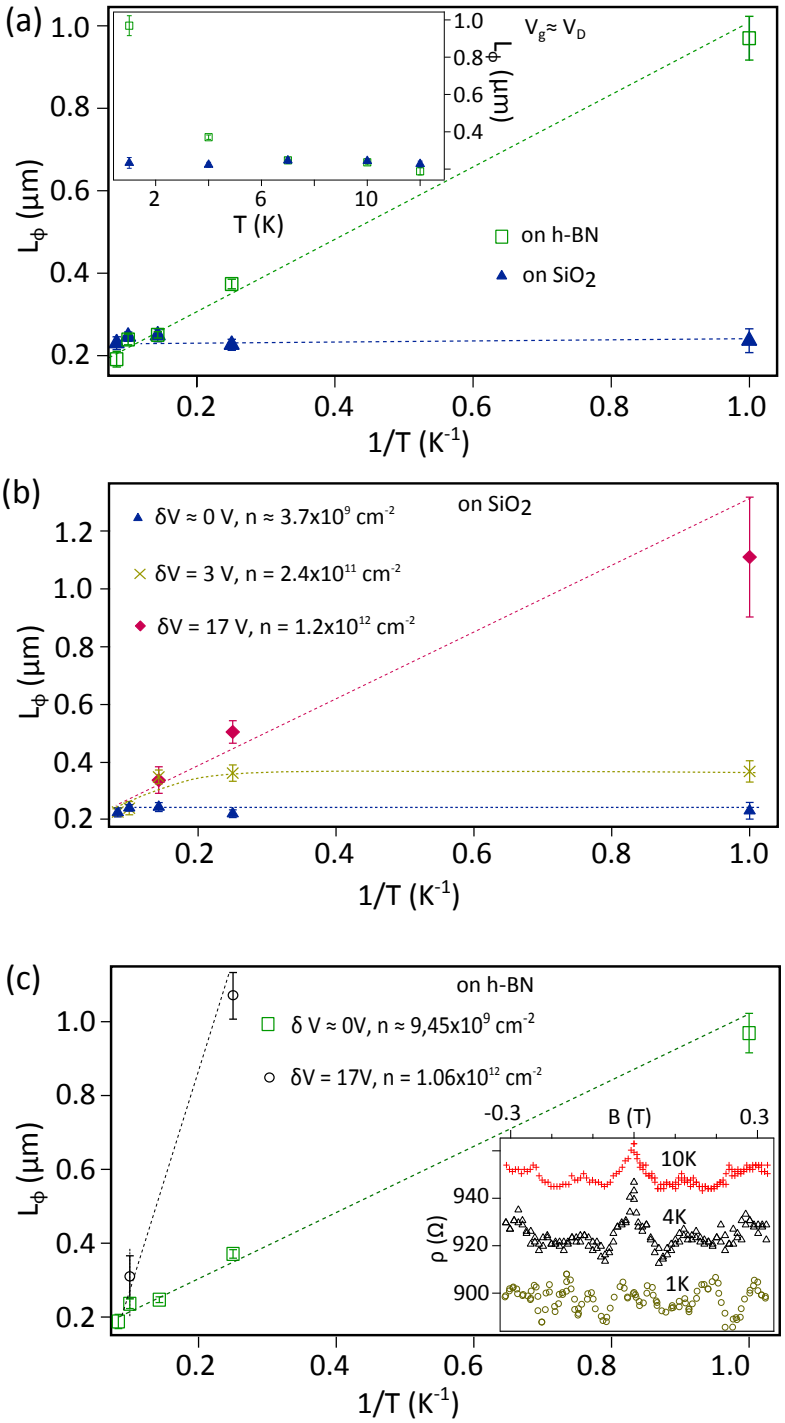

Figure 2.15: Coherence length as a function of the temperature for the devices
a) Comparison of the behaviors of the coherence lengths for gr/h − BN and gr/SiO_2 at the gate voltage close to the Dirac point versus inverse temperature: While cooling the sample, the L_ϕ for gr/h − BN increases monotonically, it saturates rapidly for the gr/SiO_2. Inset is the same data plotted as a function of the temperature.
b) Temperature dependency of the L_ϕ for the gr/SiO_2 at different densities: Electron and hole puddles limit the coherence length of the carriers at low densities.
c) Temperature dependency of the L_ϕ for the gr/h − BN at different carrier densities: no clear saturation as what is seen for the case of gr/SiO_2 is detectable for the gr/h − BN. In high doping regime, L_ϕ reaches the length of the sample very rapidly at 4 K; further cooling of the sample (inset figure) leads to elimination of the weak localization.
Dashed lines in all the cases are guides for the eyes. Also $\delta V = |V_g - V_D|$ where V_D: Dirac point voltage.

2.5.3 Results and Discussion

Electron transport properties of graphene is highly dependent on the environmental conditions; especially the substrate on which graphene sheet lies has tremendous influence on its properties. Two-dimensional hexagonal boron nitride has proven advantageous to support and to make heterostructures based on graphene; it has atomically flat and neutral surface and its crystal structure matches well with graphene's. The advantages of h-BN in increasing the mobility and mean free path of carriers in graphene have been proved earlier [1][2][33] but surprisingly there is no phase coherent transport of quasiparticles [98] *e.g.* proximity induced Josephson effect, weak localization, aperiodic conductance fluctuations or Fabry-Pérot interference is reported in graphene/h-BN systems so far; thus the effect of the substrate on the coherent transport of graphene is still under question. In this work we tried to shed some light on this question by analyzing the low field magnetoconductance properties in graphene devices fabricated on h-BN flakes and comparing with devices on silicon substrates.

This study began by fabricating backgated transistors made of few-microns-wide CVD graphene stripes deposited on silica and on h-BN flakes. Both devices are made ten micrometers away from each other and thus one can be quite confident that the intrinsic properties of graphene (such as density of internal defect) is the same for both devices.

Room and low-temperature field effect measurements at zero magnetic field are the first electrical measurements, done. The improved electronic mobility on graphene deposited on h-BN is clearly visible.

Then, we have compared the low-field magnetoconductance of both devices. Weak localization in graphene strongly differs from other thin films in the sense that unlike other materials in which only inelastic scattering and spin-flip due to the magnetic impurities play roles in weak localization interferences [99][96], elastic scattering events also can contribute in such effects in graphene. Chirality of the charge carriers in graphene is the key point in understanding the theory of WL in graphene. There are some elastic scattering mechanisms including scattering by surface ripples, dislocations and large defects in the lattice of the graphene [49][95] which are able to break the chirality and thus destroy the constructive interference by electrons with opposite momentum and belonging to the same valley. Characterized by the rate τ_s^{-1}, they are referred to as *intravalley* scattering. Besides such events, *trigonal warping* which happens at the rate τ_w^{-1} and due to the anisotropy of the Fermi surface is another mechanism which can effectively destroy such interferences. At some circumstances, electrons from different valleys also can interfere and restore the WL; which can be accounted for by elastic scattering by large defects in the order of lattice parameter. These are referred to as *intervalley* scattering and are characterized by the rate τ_i^{-1}.

We probed magnetoconductance in graphene sample on h-BN buffer layer and compared the results with adjacent graphene on silicon wafer; this gives the opportunity to directly measure the effect of the substrate on the characteristic lengths including phase coherence length in graphene. We did such measurements at different temperature and carrier densities including the Dirac point. In all the measurement regimes, clear improvements in the phase coherence lengths

are observed. Having graphene on h-BN rules out largely the substrate related perturbations and helps graphene to regain its pristine properties. The nature of such perturbations which can affect the coherence length in graphene on silicon is not completely clear and needs more investigations. However the effect of the elastic sharp scattering due to the roughness of the substrate is clear comparing the intervalley and intravalley scattering lengths. The region close to the Dirac point is very important in this experiment since the charged impurities can show up by the formation of the electron-hole puddles. The destructive effects of splitting the area of graphene into such electron-rich and hole-rich regions on the conductivity of graphene is previously reported [42] which is evident in our zero-field transport results. Moreover, we show here that the coherence length of the quasiparticles also can be limited inside the puddles manifested by the saturation of the L_ϕ at low densities.

Proximity-Driven Direct Growth of Graphene on Hexagonal Boron Nitride

In the previous chapter, the main advantages of using a h-BN buffer layer on preserving the transport properties of graphene are reviewed. So far, graphene/h-BN heterostructures have been fabricated mainly through transfer processes, which may lead to structural uncertainties due to the random stacking between graphene and h-BN substrate. Also reducing the quality of the h-BN/graphene interface is highly possible. In this chapter we demonstrate the direct growth of large scale graphene on h-BN fakes pre-exfoliated on copper foil in a usual chemical vapor deposition (CVD) process. The growth follows the van der Waals epitaxy mechanism in which weak interaction presents in between the substrate and the growing film. Raman analysis confirms the growth of graphene and show that graphene tends to follow the orientation of the underlying h-BN crystals. Transport measurements prove that the interface of the graphene/h-BN is very clean. Even though at high carrier concentration the conductivity of the electrons is suppressed by the crystalline defects, we obtain high mobilities at lower densities which to the best of our knowledge, is the highest reported for the CVD graphene grown on a non-catalytic surface so far.

3.2 Introduction

Charge transport in supported graphene is highly limited by the charge impurities at the interface of graphene and substrate [44][34][32] and this is the most important reason for using hexagonal boron nitride (h-BN) buffer layers in between the graphene and its supporting substrate in transport applications. Such a system was first successfully realized by [1] and they obtained carrier mobilities as high as 140,000 $cm^2/V.s$ which were not reachable on supported devices before. Later work [2] also confirms the advantages of h-BN for CVD graphene. Recently it has been proven that, by sandwiching graphene between two h-BN layers, one can obtain very high mean free paths and reach the ballistic transport even at room temperature [33][35]. Having crystalline structure with a lattice parameter close to that of graphene as well as its ultra smooth surface are the other remarkable properties of h-BN, assisting to approach the ultimate electronic properties of graphene [100].

In all these reports, CVD or exfoliated graphene is first isolated on an intermediate substrate and then transferred on h-BN. This process is not an ideal technique and has some disadvantages: contaminating the surface of h-BN and graphene is highly possible during this process and air or water molecules might be trapped at the interface. Also graphene can be damaged or wrinkled. Further-

more, graphene and h-BN can take any arbitrary relative orientation and thus any result that depends on the strong coupling of these layers is not easily reproducible. Macroscopic alignment of graphene on h-BN flakes is another issue which is normally very time consuming. This is why transfer-free direct growth of graphene on h-BN techniques is highly demanded. The main advantage of such a technique is that the interface of graphene and h-BN is realized *in-situ* and thus there is no external contaminant that can be trapped in between.

Necessity for the presence of a catalyst in standard CVD process, copper for example, is an important hindrance for the development of direct growth techniques. Even though there are few attempts for skipping the catalyst in very long CVD processes to grow graphene on exfoliated h-BN flakes, the resultant graphene crystals are normally too small for transport applications [101][102][103] and/or with low carrier mobilities [5][104]. In addition there are some methods developed for growing both graphene and h-BN in the same chamber to make graphene/h-BN stacks [105][106][107][108]; these techniques lead to the formation of too thin layers of h-BN, not enough to smoothen the roughness of the final substrate and diminishing the effect of the random potentials resting on the wafer.

In this chapter, we present a technique for directly growing graphene on thick/large h-BN flakes which are pre-exfoliated on typical copper foils used in CVD growth processes. This chapter starts by describing the concept of a superlattice which happens due to the superposition of graphene and h-BN crystals. There we will try to show how it affects the band structure and transport properties of graphene. A review of the techniques and results reported for making such heterostructures by directly growing graphene on thick h-BN flakes is presented in the next section. Van der Waals epitaxy is a growth mechanisms which can explain epitaxial growth between materials without dangling bounds and it seems it plays an important role in our growth technique. In a separate section, we will try to briefly explain this mechanism. The main body of this chapter is the section which comes after in which our proximity growth technique is explained. Different subsections there cover the comprehensive optical and transport analysis of the grown samples. The data obtained from such samples with similar results one can get from transferred graphene/h-BN devices are compared. Reviewing the results, discussion about them and propositions for improving the technique come in the final section of this chapter.

3.3 Graphene on h-BN Superlattice

The electronic band structure of graphene is reviewed in Section 1.3. Near the Dirac point, the density of states of graphene disperses linearly with energy which is governed by the massless Dirac equation. The conduction and valence bands in graphene intersect at the Dirac points and thus there is a zero bandgap. *Klein tunneling* known as *Klein paradox* also is an important characteristic of the band structure of graphene which prevents the formation of such gaps [109]. On the other hand, periodic potentials can affect the propagation of charge carriers in graphene by means of various superlattice potentials. They can induce new Dirac points but are not able to open bandgaps in graphene, because of the

chiral nature of the Dirac fermions. Scanning tunneling microscopy (STM) is a powerful tool to probe the superlattice generated in graphene lying on crystalline substrates through the produced *moiré patterns*. In this way, hexagonal boron nitride is of particular interests since it is an insulator and can couple to graphene very weakly by van der Waals forces. Strongly neutral and charge-free surface is another important property of h-BN for this purpose.

Moiré is an interference effect in which a secondary pattern is generated when, for example, two very similar patterns with a small displacement or rotation in between are superimposed [110].

Graphene on h-BN heterostructure was first probed by tunnelling microscopy by [111]; the first evidence of a moiré patterns in this work indicates that graphene conforms to h-BN. Similar work has been performed later by [112]. As an important work in this field, Yankowitz *et al* [3] showed theoretically and experimentally that the periodic potential associated to h-BN which is felt by the carriers in graphene, leads to the generation of new Dirac points at energies dependent on the wave vector of the superlattice (λ_{SL}) which is a function of the mismatch angle (Φ) between the lattices (see Figure 3.1-a):

$$\lambda_{SL} = \frac{(1+\delta)a}{\sqrt{2(1+\delta)(1-\cos\Phi)+\delta^2}}. \tag{17}$$

In this relation, $a = 2.46\,\text{Å}$ and $\delta = 1.8\%$ are the lattice parameter of graphene and the mismatch between graphene and h-BN lattices. The extra and superlattice induced Dirac points which are referred to as *satellite Dirac points (SDPs)*, show up as the formation of two symmetrical dips in the local density of states probed by tunnelling microscopy. They are of the energies:

$$E_{SDP} = \pm\frac{\hbar v_f |\vec{G}|}{2} = \pm\frac{2\pi\hbar v_F}{\sqrt{3}\lambda_{SL}}. \tag{18}$$

Here $\vec{G}$ represents the reciprocal superlattice vector and $v_F \approx 10^6\,\text{m/s}$ is the Fermi velocity of quasiparticles in graphene. Examples of the measurements showing such Φ dependent dips are presented in Figure 3.1-b. SDPs were observed later in the gate dependent resistivity measurements in directly grown graphene on h-BN devices [5].

Equation 17 and Equation 18 are important relations to calculate Φ *i.e.* besides moiré mapping, the dips appearing in the transport data can be used to calculate the rotation angles between graphene and h-BN lattices in such heterostructures. However, the necessity to cool down the sample to measure the relevant data is the important hindrance in both of the techniques. Recently Eckmann *et al* [113] introduced a third method based on Raman spectroscopy which can be performed even at room temperature. In this systematic study, they fabricate many graphene/h-BN devices and by doing low temperature transport measurements and based on the positions of the SDPs, they calculate the rotation angles using Equation 17 and Equation 18. By recording Raman spectra on the same samples they noticed that the rotation angle can affect the width of the *2D* band of graphene. They conclude that the following correlation exist between the λ_{SL} and full width at half maximum of the *2D* peak in such systems:

$$FWHM(2D) = 2.6\lambda_{SL} + 5,\ \lambda_{SL} > 6\,nm \tag{19}$$

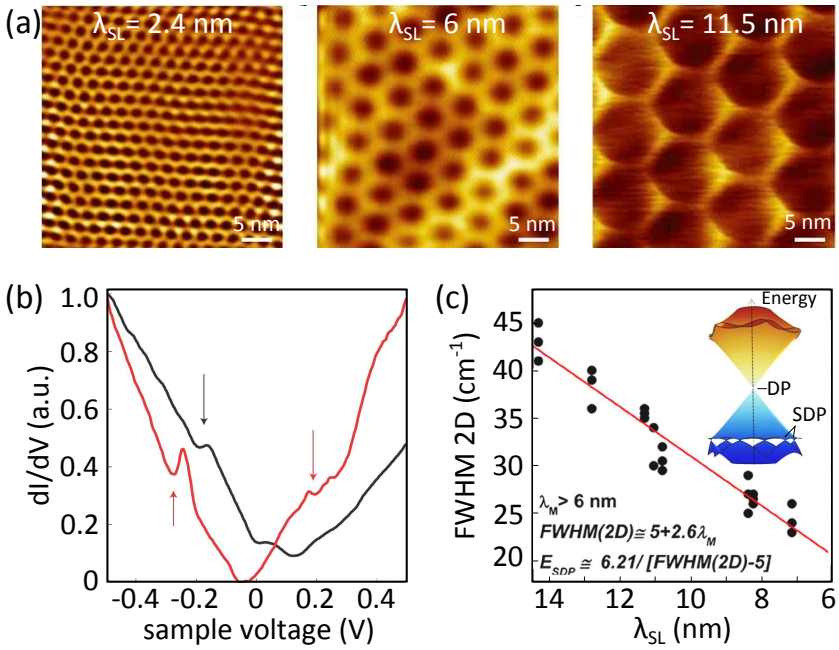

Figure 3.1: Probing the superlattice of graphene/h-BN heterostructures
a) Moiré pattern as the primary indication of the supperlattice in graphene on h-BN heterostructures: Depending on the relative orientation of the graphene and h-BN, different superlattice wavelengths can form (λ_{SL}, $0\,nm < \lambda_{SL} < 14\,nm$, Equation 17). Figure is adopted from [3].
b) Satellite Dirac points show up as dips marked by arrows in the dI/dV curves as measured by Yankowitz et al: The black and red curves correspond to the samples with moiré wavelengths of 9.0 nm and 13.4 nm respectively.
c) Correlation between the width of the 2D band of graphene and superlattice wavelength: Eckmann2013 et al shows that simple relation exists between the full width at half maximum of the Raman 2D band of graphene (lying on h-BN) and the corresponding λ_{SL} (Equation 19). Inset shows the formation of the satellite Dirac points in the density of states of graphene. Figure is adopted from [113].

Example of their results are presented in Figure 3.1-c.

A brief description about the formation of the superlattice in graphene on h-BN systems as well as important works and existing techniques to probe them were presented in this section. All the samples measured in these works are fabricated by transferring exfoliated monolayer graphene on thick h-BN flakes. However there are some techniques reported for directly growing CVD graphene to make such stacking which will be reviewed in the next section.

3.4 Reports on Directly Growing Graphene on h-BN

Considering that the field of graphene on h-BN is still very young, only few reports have been published so far showing the possibility of the *in-situ* fabrication of the graphene/h-BN stacking. In this section, a brief review of the techniques and important achievements reported in this field is presented. We have col-

lected the works here in which graphene is grown on thick h-BN flakes which are suitable for the transport applications.

The first paper about directly growing CVD graphene on hexagonal boron nitride was submitted just four months after the birth of the graphene/h-BN systems [1]. Published by Ding *et al* [101], this paper shows the possibility of growing few layer graphene on h-BN powders through the typical chemical vapor deposition technique. Raman spectroscopy and high resolution TEM techniques are used to confirm the presence of graphene after the growth and to measure its thickness. The size of the graphene domains is not clear and since growth is done on h-BN powders, there is no transport measurement data reported in this work. Some of their results are shown in Figure 3.2-a and b.

The fact that so rapidly after the first realization of graphene/h-BN systems [1], the works for directly growing graphene on h-BN start being reported shows the importance and demands for such techniques in improving the quality of the stacking.

Few months after, the second work was reported by Son *et al* [102]. In this work, h-BN flakes are mechanically exfoliated on a silicon wafer. This sample is inserted into an atmospheric pressure CVD chamber in which graphene is grown. Having done the growth in the temperature range between 900°C to 1000°C, they notice increases in the density of the graphene pads by raising the growth temperature (Figure 3.2-c and d). Graphene flakes obtained have rounded shapes with the thicknesses of the order of 0.5 nm. AFM, Raman and XPS analysis have been performed to confirm the growth and characterize the graphene after the growth.

Later another group reported a similar work [103]. Like the Son's experiment, graphene is grown on hexagonal boron nitride flakes exfoliated on silicon wafer, but through low pressure CVD process. They noticed that screw dislocations on the flakes are favorable nucleation sites. The slow growth rate in such processes is very evident in this work; a growth duration of 6 hours only leads to the formation of graphene grains of maximum 270 nm in diameter (Figure 3.2-e to g). Most of the graphene domains obtained are single layer as is confirmed by Raman analysis.

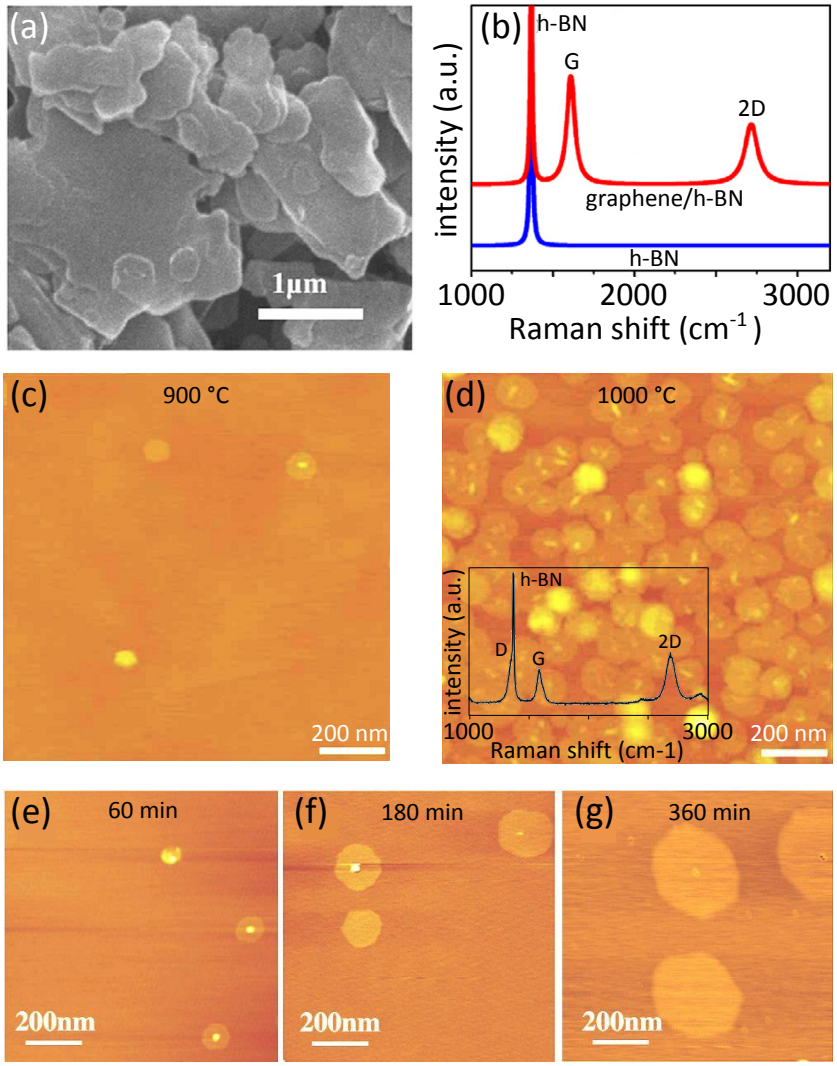

Figure 3.2: Early reports on the direct growth of graphene on thick h-BN flakes
a) and (b) Results of Ding et al [101]: Graphene is grown on h-BN powders through a CVD process. The Raman spectra on (b) are taken from bare h-BN powder and after the growth.
c) and (d) Results of Son et al [102]: The effect of the growth temperature on the density of the obtained flakes is reported as AFM mappings in this work. The density has raised a lot as the temperature increased from 900°C to 1000°C. This growth lasts for 2 hours. The inset in (d) shows an example of the Raman data obtainable from this sample.
e), (f) and (g) Results of Tang et al[103]: In this report we can clearly see the growth rate is very low in such techniques due to the absence of catalyst. AFM measurements shown in these figures are done after 1, 3 and 6 hours.
All the figures are reprinted with adoptions.

In a collaborative work between several groups in Spain, US, UK and Japan, the next paper appeared in 2012 [114]. Unlike the previous experiments, graphene is grown by molecular beam epitaxy (MBE) using solid carbon sources. They realized that graphene has grown non-uniformly suggesting the surface morphology and other individual characteristics of the h-BN flakes, may play a significant role. Also Raman analysis reveals that the growth is independent of the flux of

carbon atoms, indicating that the carbon atoms are of very high mobilities on the neutral h-BN surface; this conclusion matches well with *van der Waals epitaxy* picture (Section 3.5) in which weak interaction improves the mobility of adatoms. Temperature is the main parameter affecting the growth rate and number of the graphene layers in their work. Raman and AFM are characterization techniques they have employed. Examples of the Raman spectra they obtained from the samples grown at 930°C are shown in Figure 3.3-a which are measured on the spots marked by *A* and *B* in the inset figure. While the characteristics graphene signals appear at point *A*, the signal in *B* shows much broader Raman bands without any 2D signature indicating much lower quality graphitic layers. Figure 3.3-b shows examples of the AFM data in which small graphene flakes are visible.

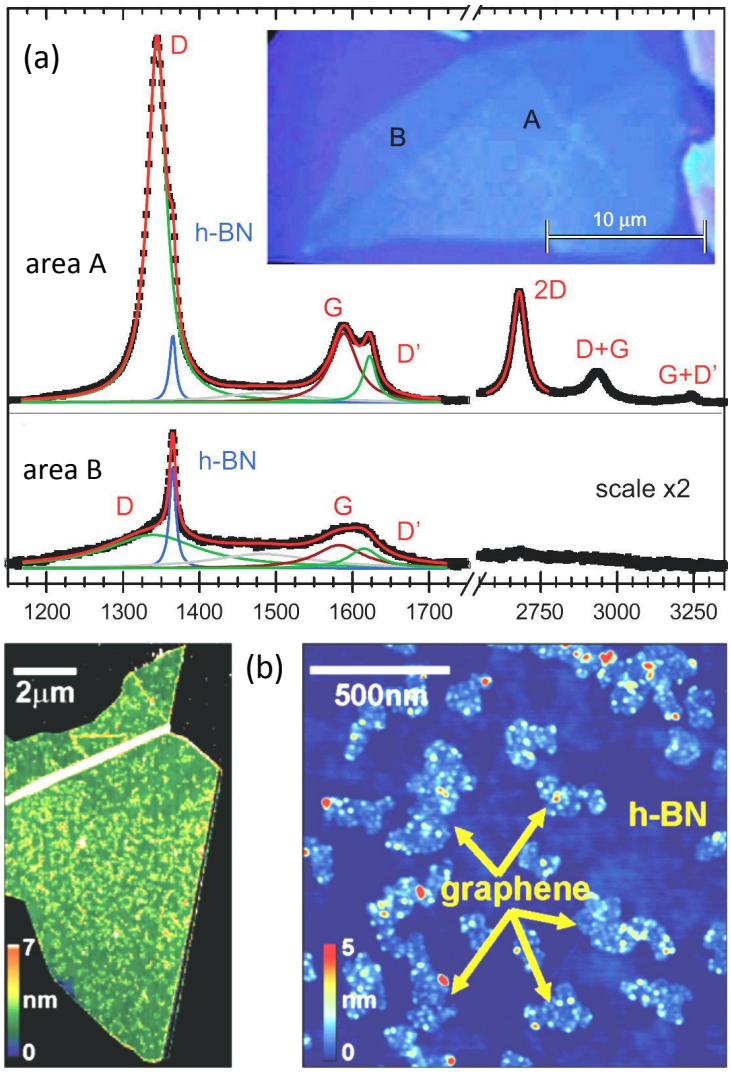

Figure 3.3: Result reported by Garcia et al [114] [115]
a) Raman spectra measured on two spots on the sample shown in the inset: While the formation of monolayer graphene is confirmed in the signal measured at A, the absence of the 2D band as well as broad D and G peaks show that the carbon material grown on B possesses graphitic characteristics.
b) Example of the AFM data reported in this work: grown graphene domains partially but uniformly cover the h-BN flake. Small scale AFM mapping on the right shows graphene flakes suffer from the formation of little bubbles during the growth.

The most successful work so far in this field was published in 2013 [5]. They utilize plasma-assisted CVD technique to grow graphene on mechanically exfoliated h-BN flakes. Large area, epitaxial and single crystal graphene domains directly grown on the h-BN flakes are obtained for the first time. Breaking down the methane molecules with a remote plasma source eliminates the need for a catalyst; this enhances the growth rate and hence the domains size. The cleanness of the flakes is high enough that they manage to observe the moiré pattern associated to superposition of graphene and h-BN crystals by AFM analysis. It shows that graphene crystalline orientation follows the one of the underlying h-BN. The size of the graphene is limited by the size of the h-BN flake which is

still large enough to fabricate devices for transport experiments. The signature of the superposition of the lattices as extra Dirac points in the resistivity and quantum Hall effect measurements reveals at low temperature. Their graphene shows a maximum mobility of $5,000\,cm^2/V.s$ at $1.5\,K$.

Tang *et al* published another paper [4] two years after their first work,[103]. They use the same fabrication procedure as in their earlier report; however they try to investigate the heterostructures by using AFM similar to [5]. Moiré pattern in this work also is used to confirm the alignment of the graphene and the substrate.

All the important works in which graphene is directly grown on h-BN flakes are briefly described in this section; Table 2 also summarizes the techniques and properties of the obtained graphene. We note that there are some other reports for growing graphene on other non-catalytic substrates and thus they have not been covered in this section. One of the latest examples of such reports is the work done by Chen *et al* [104] in which micrometer-sized graphene flakes (as big as $11\mu m$) are chemically grown on dielectric substrates in very long growth processes (up to 72 hours) which they call it *near-equilibrium CVD method*. They have done such growths on dielectric chips of polycrystalline $Si_3N_4/SiO_2/Si$, SiO_2/Si, quartz and sapphire.

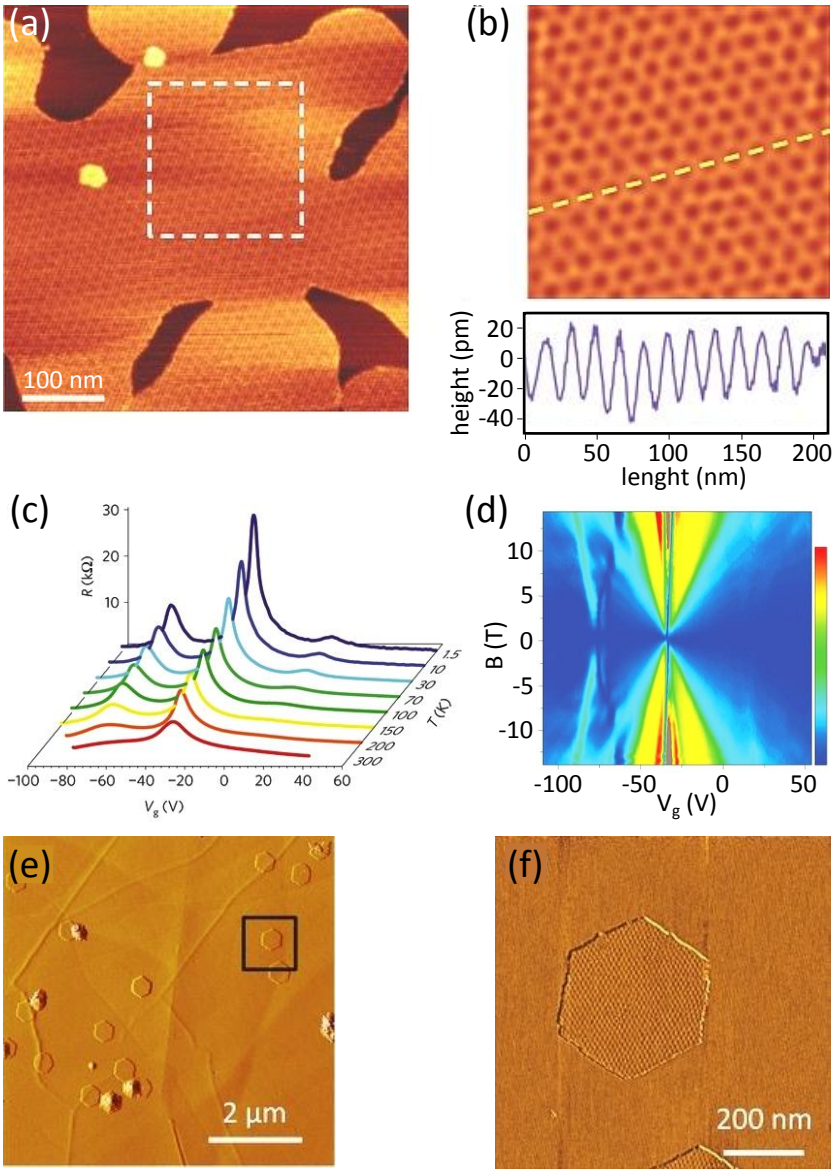

Figure 3.4: Result of the experiments reported by Yang et al [5] (a to d) and Tang et al [4] (e and f)
a) Moiré pattern due to the superposition of the graphene and h-BN lattices, b) Filtered inverse fast Fourier transform of the pattern which is visible in the dashed square in a, height profile along the dashed line is shown in the lower part. The periodicity of the oscillations can be used to calculate the rotation angle between the lattices.
c) Gate dependence of the resistivity measured at different temperatures: satellite peaks shown at the left and right side of the Dirac point are due to the formation of the super-lattice. d) This effect also shows up as the pattern at the left side of the fan diagram of the R_{xy} in the quantum hall measurement.
e) Topography of the small graphene flakes and (f) Moiré pattern reported in Tang's work.
All the figures are reprinted with adoptions. The mappings shown in a, b, e and f are done with AFM.

Table 2: Summary of reports about directly growing graphene on thick h-BN flakes

report	process	precursor	temperature	duration	size	thickness
Ding [101]	CVD	CH_4 (50-90 sccm)	1000°C	3-8 min*	NM	> 6 L
Son [102]	CVD	CH_4 (30-50 sccm)	900-1000°C	2 hrs	100 nm	≈ 0.5 nm
Tang [103]	CVD	CH_4 (5 sccm)	1200°C	1-6 hrs	<270 nm	ML
Garcia [114]	MBE	solid carbon	600-930°C	40.6 min	nm-scale	ML
Yang [5]	PECVD	CH_4**	≈ 500°C	≫ 3 hrs	µm-scale	ML& BL
Tang [4]	CVD	CH_4 (5 sccm)	1200°C	1-5 hrs	µm-scale	ML& BL

NM: not mentioned in the paper, ML: monolayer, BL: bilayer
* The size of the graphene flakes are not investigated in this work and it is very unlikely that they exceed few nanometers in such a short growth.
** The flow rate of methane is not reported in this paper.

3.5 van der Waals Epitaxy

In the case of fabricating heterostructures by depositing a material on a substrate and by considering the terminating layers of the materials, at least 2 mechanisms are considerable: In materials with terminating layers full of dangling bonds *e.g.* unsatisfied covalent bonds, atoms in one material can be connected only to the atoms of very similar lattice; this is because the covalent bonds are very sensitive to the length and the angle between the atoms. This is an important hindrance in epitaxial growth between materials with very different lattice parameter. Figure 3.5-a schematically illustrates this situation. For the case of ionic materials obtained by bonding between alkali metals and halogens, formation of an intermediate layer of few nanometers solves the constriction of the lattice mismatch. In such structures, the lattice parameter switches smoothly from that of the substrate to the lattice constant of the film. The other case can be found in between two materials with perfect terminating surfaces and no dangling bonds (Figure 3.5-b). The absence of the dangling bonds can lead to the formation of very sharp interfaces with small amount of defects. This growth mechanism is referred to as *van der Waals epitaxy* and can be realized even in the presence of large lattice mismatches. For fabricating high quality and very thin (atomic-order thickness) heterostructures, van der Waals epitaxy is qualified to be one of the most powerful techniques. Large organic molecules like Phthalocyanine [116] and C_{60} have been grown on cleaved MoS_2 substrates by this principle. As interesting efforts [117][118] (Figure 3.5-c), the surface of the freshly cleaved MoS_2 is covered with a very thin layer of GaSe; AFM nano-lithography strips partially the surface of MoS_2 into nanoscale holes or grooves. SEM investigations after a short C_{60} growth time show that only bare MoS_2 nano-regions are covered by C_{60} molecules which are more favorable sites considering the van der Waals epitaxy picture.

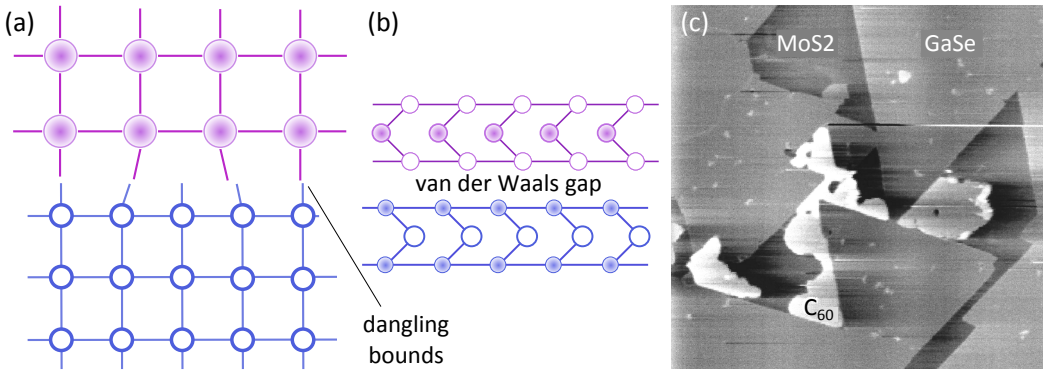

Figure 3.5: van der Waals epitaxy growth
a) For the growth of materials with dangling bonds, the lattice mismatch is considered as an important hindrance for reaching epitaxial condition.
b) The weak van der Waals interaction between the substrate and film in materials with no dangling bonds, epitaxial growth can be realized for any level of lattice mismatch. Figures (a) and (b) are made by inspiration from [119]
c) Example of the successful realization of epitaxy in between materials with weak van der Waals interactions: Figure is reprinted with adoptions from [118].

3.6 Proximity-Driven Direct Growth of Graphene on h-BN

Different techniques for directly growing graphene on thick h-BN flakes have been briefly presented in Section 3.4, a summary of which is collected in Table 2. The fact that in all these techniques, the catalyst material for CVD growth is skipped, very long reaction times are needed to decompose the amount of precursor materials required to form acceptably large enough graphene flakes. Using plasma activation upstream the flow to break the CH_4 molecules, is a technique used by Yang *et al* [5] to cope with this limitation; however the growth still lasts for several hours. The obtained mobility in this technique ($5,000\,cm^2/V.s$) is commonly reachable in graphene lying on SiO_2, so it seems the absence of the catalyst can eliminate the important benefits one can get by making such heterostructures.

Considering all these limitations, we introduce a new technique for directly growing graphene on h-BN in which methane can have indirect access to the catalyst and thus we use the term *proximity-driven direct growth* to address it. High spatial mobility of the carbon atoms which is predicted in van der Waals epitaxy (Section 3.5) and has been realized before in such heterostructures [114] is the key point to understand the growth mechanism. The obtained graphene is probed by different techniques right after the growth (*DG* directly grown graphene) as well as after transferring on a silicon wafer (*TG*). Also low temperature transport properties of such heterostructures is examined. All the details of the technique and measurements results are covered in this section.

3.6.1 Process Flow

The process flow for proximity growth of graphene is illustrated in Figure 3.6. In all the techniques for directly growing graphene on h-BN reported so far (Section 3.4) h-BN is mechanically exfoliated on silicon wafer and thus in the absence of the catalyst, the graphene is grown on the final sample. However in our method, h-BN flakes are exfoliated on Cu foils which are typically used in CVD process [88] (Figure 3.6-I) and then put in the CVD chamber. Using normal growth recipes, the graphene is grown both on the h-BN as well as on the Cu foil. Table 3 summarizes the parameters used for this growth. In the next steps we use a so-called *dry transferring* technique to transfer the graphene/h-BN stacks on a silicon wafer. For that, we spin a layer of PMMA ($\approx 300\,nm$) on the sample and attach a layer of thermal release tape (TRT) on it (III). These two layers are used to support graphene/h-BN in the subsequent steps. Cu foil is then etched away by using suitable chemicals (IV). Then the graphene/h-BN sample is rinsed in DI water to remove any ionic species. This sample supported by TRT is rigid enough to take it out from the water bath and dry it by using a nitrogen gun. Without doing this step there is small chance that the potential associated to the polarized water molecules affect the transport properties of graphene. We note that the support from TRT layer is crucial at this stage; the PMMA layer also is needed between TRT and graphene since the glue residuals from TRT directly attached to graphene is very difficult (almost impossible) to clean. By pressing the sample against the surface of a wafer which is turned to be hydrophilic (by a previous piranha (H_2SO_4 and H_2O_2, 3:1) treatment), the sample attaches to the wafer (V). TRT can now be removed easily after a short annealing at $\approx 120°C$ and for $\approx$5 minutes (VI). The normal acetone/ IPA treatment can strip the PMMA layer at this step (VIII) and graphene/h-BN/SiO_2 sample is now ready for the later measurements (VIII).

The dry transferring techniques are normally more favorable than the wet techniques in making such heterostructures in order to minimize the possibility of trapping water molecules in between graphene and h-BN surfaces.

This process of etching with chemicals is explained in more details in Section 2.4.1.

If h-BN is thick enough, this parasitic potential is less considerable.

Table 3: Parameters used for the proximity CVD growth

1st annealing*	2nd annealing**	growth temperature	growth time	growth atmosphere	pressure
350°C- 60 min	1000°C- 60 min	1000°C	90 sec	CH_4 (3 sccm), H_2 (700 sccm)	1 mbar

* The 1st step of annealing is used to remove the glue residuals on the sample
** This step of annealing is typically used in normal CVD processes to improve the surface quality of Cu foils. Its importance in our technique needs to be investigated.

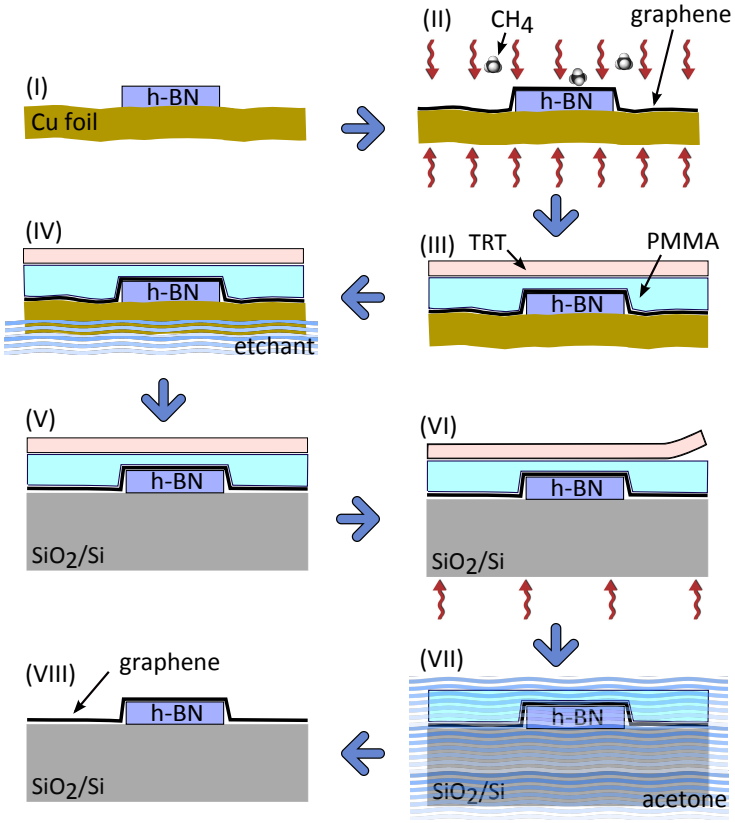

Figure 3.6: Growth and transferring process of the samples
h-BN is first mechanically exfoliated on the copper foil (I). Then through a typical CVD process, graphene is grown on the foil covering h-BN flakes (II). After cooling, Poly(methyl methacrylate) (PMMA) is spun on the sample and thermal release tape (TRT) is used to support them (III). At the next step Cu foil is etched away by using a right solution of ammonium persulfate (IV). After washing the sample with distilled water, it is dried out using a nitrogen gun and is transferred on a surface activated wafer (V). Finally by applying heat (VI) and treatment with acetone (VII), TRT and PMMA are removed one after the other.

3.6.2 Initial Characterization of the Graphene on Cu Foil

Right after the growth, some analyses are done to qualify as-grown graphene. AFM and SEM images of one of the samples are shown in Figure 3.7-a and b respectively. h-BN flake mainly lies on the Cu foil even though some of its bottom layers might have sunk into the foil at the high temperature of the CVD process. The surface of the flake looks very flat as is demonstrated in the zoomed AFM map in Figure 3.7c which is taken from an area defined by dashed line in the SEM image. A histogram of the height distribution measured inside an arbitrary window of 400 by 400 nm^2 inside this area is shown in Figure 3.7-d. The width of this graph (< 4 Å) is consistent with the previous report [1] and our analysis of bare h-BN flakes (*Chapter 2*); this indicates that the surface quality of the h-BN is preserved passing the high temperature process. Raman spectrum measured on the flake is shown in Figure 3.7-e. Appearance of the graphene characteristic *D*, *G* and *2D* bands together with the h-BN signal in this spectrum confirms the

growth and existence of the graphene. Similar spectra are obtained on all the points probed on this flake.

One can compare the zoomed out AFM mapping in Figure 3.7-a and c with similar data reported by Garcia's paper [115] which is illustrated in Figure 3.3-b. We see that while graphene in their work is in the form of small flakes which are bumped up as the result of their growth technique, the proximity induced growth leads to the formation of a continuous sheet, covering all the surface of the sample and thus is not distinguishable from the h-BN in the AFM mapping. Also the absence of any bubble is very clear in the focused image as well as on the height distribution histogram (Figure 3.7-c and d).

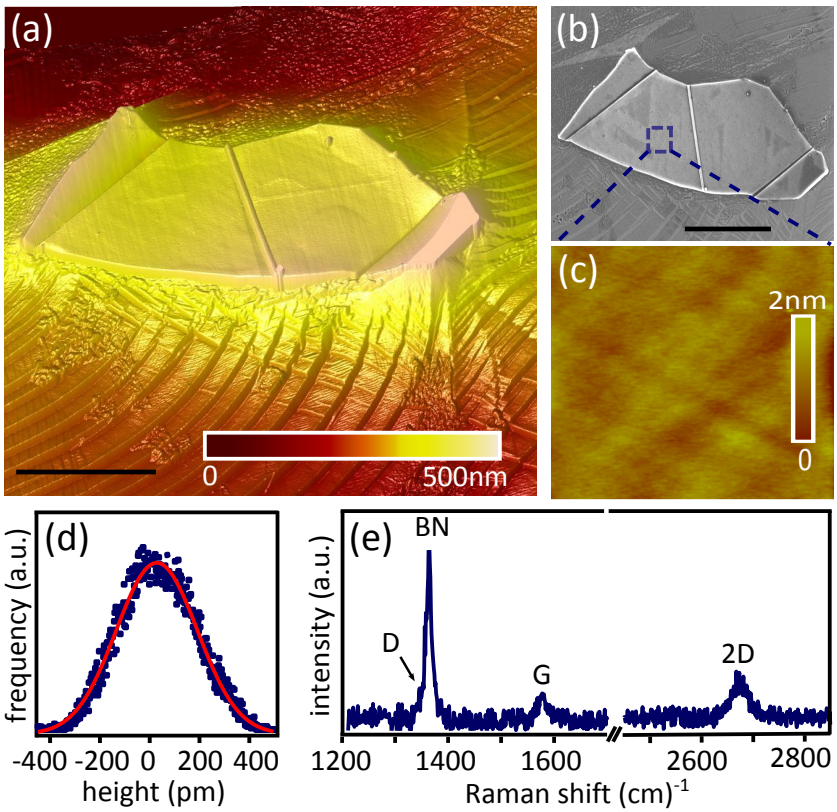

Figure 3.7: Initial analysis of the graphene/h-BN stack on the copper foil and right after the growth
a) AFM and (b) SEM images of an example of the h-BN flakes on the copper foil after the CVD process: Graphene has covered continuously all the area and thus is not identifiable in these images. Scale bars measure 2 µm.
c) AFM image focused on the area defined by the dashed line in (b), and (d) corresponding histogram of the height distribution. Solid line is a Gaussian fit to the distribution.
e) Typical Raman spectrum measured on this sample (laser wavelength: 532 nm). The background photoluminescence is subtracted by means of a polynomial function.

3.6.3 Growth Mechanism

h-BN related materials are known to be chemically stable even at high temperatures [82] *i.e.* it does not meddle in the chemical process for the formation of the

graphene layer. Here we consider and weigh different possibilities which may justify our observation of growing graphene on h-BN through this CVD process:

A first scenario is that methane molecules land on the h-BN surface already in a partly de-hydrogenated state, in which they are more reactive and thus liable to react together and form graphene. Such a process was invoked and ascribed to the presence of Cu atoms in the vapor phase [120][121]. This process however has a very low yield, compared to that resulting in the formation of graphene on Cu. While 20 sccm of methane and a 30 minute growth was needed to achieve full coverage [120][121], in our case, 3 sccm and 90 s are sufficient. This process, if presents, can thus only have a marginal contribution here.

As the next scenario, we can consider that the surface of h-BN is turned catalytically active by the diffusion of copper on top. If the diffused copper is large enough to make 3D clusters there, it would induce a roughness well beyond what we observed in our AFM measurements (Figure 3.7-d). This picture is only considerable if we assume that the diffused copper form a thin film on h-BN with a roughness comparable with crystalline materials.

The last possible scenario is that methane is cracked away from the h-BN surface, on Cu, and the resulting carbon adatoms diffuse towards the surface of h-BN, where it condenses in the form of graphene above a critical carbon adatom concentration. It seem this is the most important picture which can explain and match our observations. Migration of the carbon atoms to the surface of the h-BN is the key point governing the rate of the formation of graphene on h-BN here. Our later analysis in Section 3.6.4 shows that graphene on h-BN has formed at the same rate of on the surrounding copper foil which implies a high mobility of carbon atoms on h-BN which has been confirmed before [114][115]. This matches with the picture of van der Waals epitaxy, reviewed in Section 3.5.

3.6.4 In-depth Optical Analysis After Transfer

We now turn to analyze graphene once it has been transferred onto a silicon wafer. An oxygen plasma etching step after transferring, provides further evidence that graphene has overgrown the h-BN flake: the width of the resulting graphene ribbon, which can be assessed by the careful inspection of optical and SEM images (Figure 3.8-a and b) and more readily by Raman mapping of the graphene's *G* mode (Figure 3.8-c), is identical on top of h-BN and away from it, which would not be possible if graphene would lie between h-BN and Cu (before transferring) or between h-BN and wafer (after transferring). Figure 3.8-c also reveals the presence of another graphene region which shares a common edge with the h-BN flake proving that it has been masked by the flake through the plasma process. This region is not detected in the optical (Figure 3.8-a) nor in SEM images (Figure 3.8-b) and thus is not lying on the surface. For the wavelength we use, the absorption of the hexagonal boron nitride is negligible [122] thus this graphene could be located at any level below the surface of h-BN even at the backside. We note that Raman visibility of the graphene through covering h-BN flakes is a known phenomenon [123].

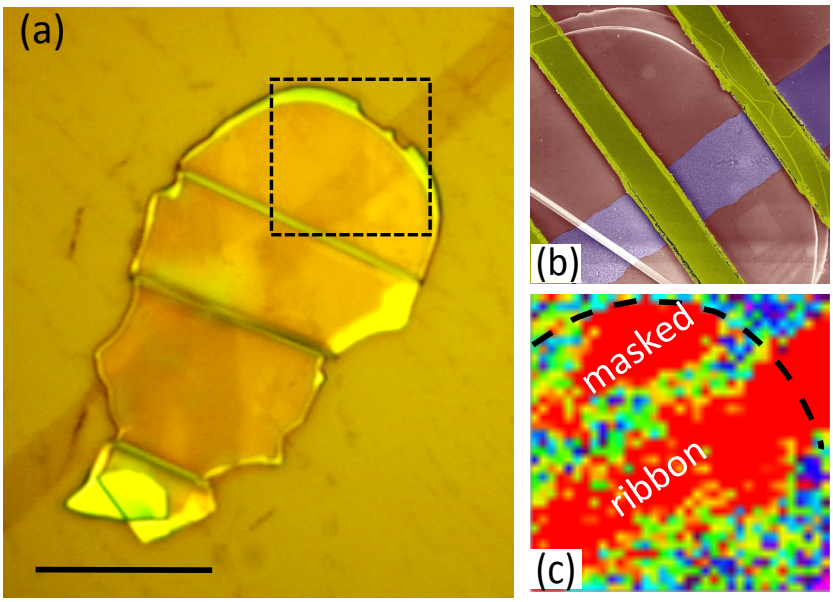

Figure 3.8: Raman analysis after transferring the sample on a silicon wafer
a) Optical micrographe image of a rather large h-BN flake: The scale bar here shows 10μm.
b) False color SEM image of the area defined by the dashed lines in (a)
c) The corresponding intensity map of the Raman G-band of the graphene: The border of the h-BN flake is identified by the dashed line here.

Examples of the Raman spectra of graphene measured on a h-BN flake (S1) and in a very close vicinity of it, on the silicon wafer (S2) are shown in Figure 3.10-c. This flake is the same sample used for the transport measurements (optical micrograph is shown in the inset of Figure 3.10-a) and these Raman data are measured before electrode deposition. Both 2D peaks there can be fitted well with a single Lorentzian shape which is one of the signatures of a single layer graphene [124]. It is shown later that the full width at half maximum (FWHM) of grown samples (including this sample) converge to 46 cm^{-1} which is a proof of monolayer graphene with almost a perfect alignment regarding h-BN orientation.

We start the analysis by focusing on the defect band. Deconvoluting the signal close to the BN and G peaks displays D (1346 cm^{-1}) and D′ (1622 cm^{-1}) modes (inset figure), the ratio of which ($I_D/I_{D'}$) carries the information about the nature of the defects in graphene [125]. Here we obtain $I_D/I_{D'} = 6.5$ for S1 which is very close to the value reported for vacancies. This means that the crystal structure of our grown graphene suffers from the high population of voids which could be the result of disorder happening during the migration of the carbon atoms on the flake. For the graphene lying on the silicon wafer, the intensity of D is very low (there is no visible D′) which is a character of high quality graphene.

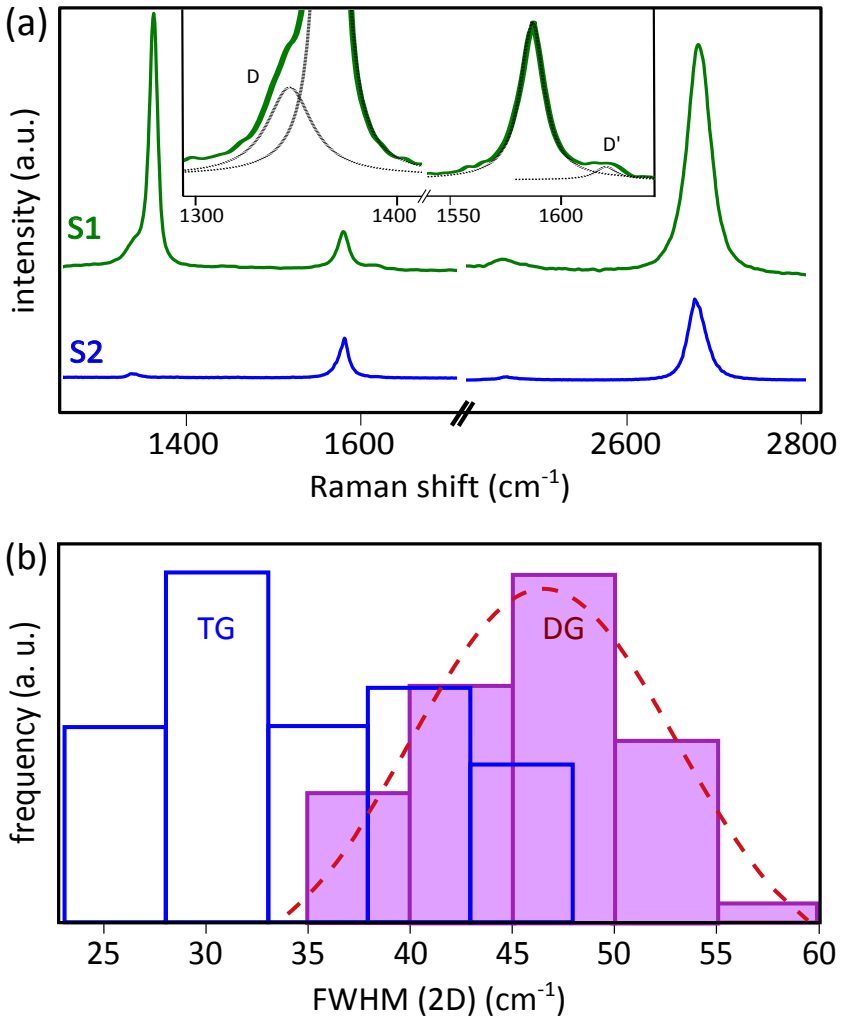

Figure 3.9: Comparison of the Raman signatures of directly grown (DG) and transferred graphene (TG) devices
a) Raman spectra measured on the h-BN flake (S1) and on the nearby silicon wafer (S2) of the samples used for the transport measurements (Figure 3.10-a). The inset figure is the same data of S1 focused in a small range. Deconvoluted curves by a Lorentzian fitting are plotted there by the black dotted lines.
b) Distribution of the width of the 2D peaks for DG and TG devices: Data of DG is obtained by analyzing a set of 20 devices. It follows a Gaussian distribution depicted by the dashed line. 30 transferred graphene devices have been used to obtain distribution of TG.
All the Raman data shown here are measured with an excitation energy of 2.33 eV.

It was recently demonstrated that the width of the *2D* peak in such stacking is very sensitive to the relative rotational angle between graphene and h-BN crystals [113]. This experiment is reviewed earlier (Section 3.4, and Figure 3.1-c) and now their results are used to interpret our data. Figure 3.9-b compares the distribution of the width of the Raman *2D* band of many *TG* and *DG* devices. The samples made by transferring graphene, the FWHM of *2D* peaks ranges between $\approx 20\,\mathrm{cm}^{-1}$ up to $\approx 50\,\mathrm{cm}^{-1}$, without showing any trend. However it seems the directly grown devices are centered around $\approx 46\mathrm{cm}^{-1}$ and the

distribution follows a Gaussian relation. This width is very close to the value predicted by Eckmann *et al* for the precisely aligned graphene and h-BN lattices and thus we can conclude that the lattice of graphene follows h-BN crystal due to the van der Waals coupling.

3.6.5 Transport Measurements

At the next step, by patterning the graphene and depositing electrodes, we fabricate samples for transport measurements. For the sake of comparison and in addition to a device with directly grown graphene (DG), we have fabricated another sample by a two step transferring method (TG). Graphene in this device has been grown with similar parameters of the directly grown sample. Transport measurements have been done at 80 K and in a similar scheme as what is described in the previous chapter. Figure 3.10 summarizes our results.

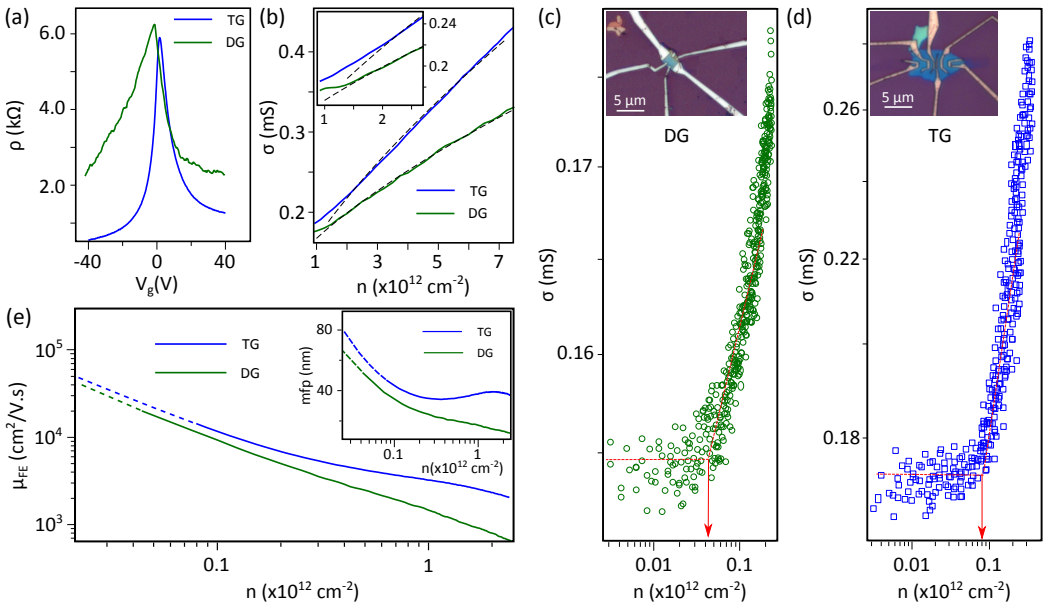

Figure 3.10: Comparison of the transport properties of a directly grown graphene (DG) with a device made by transferring similar CVD graphene (TG)
a) Gate dependence of the resistivity of the samples
b) Corresponding conductivity of the samples on the electron side: Dashed lines are fits to the curves using the midgap states theory described in the main text. Insets to this figure are the same plot focused at low densities. The vertical and horizontal axes have the same units as the main panel.
c) and (d) Logarithmic-scale plot of the conductivity of DG and TG samples versus carrier densities close to the Dirac point: The arrows show critical densities below which the conductivity of the samples saturate due to the formation of the electron-hole puddles. Insets to these graphs show the optical micro-graph of the corresponding samples.
d) Comparison of the gate dependence of the field effect mobility (μ_{FE}) and mean free path (mfp, inset figure) of the carriers in the DG and TG samples
All the measurements have been done at 80 K.

The main panel of Figure 3.10-a shows the gate dependence of the resistivity of the samples. The Dirac peaks for both samples are located very close to zero

which is an indication of clean graphene on a neutral h-BN substrates. Transferred graphene shows quite a sharp peak which is a signature of high mobility carriers. The curve is quite asymmetric in the electron and hole sides which could be due to the electrode charging effects [92]. The asymmetry for *DG* sample is more pronounced which may be due to the presence of the process residuals on the sample. While the residual resistance (resistance at the gate voltages very far from the Dirac point) is quite high for *TG* sample, it is even higher for the *DG* one; this observation together with the presence of the resistivity fluctuations at high gate voltages points out that both of the samples and especially the *DG* one suffer from the high population of the short range crystalline defects. In CVD graphene such defects can happen during the growth, transferring or fabrication process. Since both the samples have passed similar fabrication steps, this observation in the *DG* sample can be attributed to the formation of the defects during the growth.

The important models describing the transport in graphene including mid-gap states have been briefly presented in the Introduction chapter.

In Figure 3.10-b we compare the conductivity of both samples showing that the *TG* sample is more conductive than the *DG*. There are few models to describe the scattering near the Dirac point in graphene [32][39] however since the Raman analysis proves the existence of the crystalline vacancies in our sample and we see some signatures of them in Figure 3.10-a, we use a model which considers scattering by the *mid-gap states* [37]. In this model, strong disorder associated with the voids are modeled as a deep potential well [37][126]:

$$\sigma = \frac{2e^2}{h}\frac{k_F^2}{\pi n_d}(\ln k_F R_0)^2$$

Here, while k_F is the Fermi wave vector of graphene, n_d and R_0 refer to the density and characteristic size of the defects respectively. Black dashed lines in Figure 3.10-b are the fittings with this model showing that it is successful to describe our results to a large extent. Table 4 summarizes the results of this fitting. For the purpose of comparison, predictions for the pristine graphene [37] are also included in this table:

Table 4: Summary of the results obtained by fitting our data with the mid-gap states model and comparison with the reported data

	$n_d\ [cm^{-2}]$	R_0 [Å]
present work, TG	2.7×10^{12}	1.3
present work, DG	4×10^{12}	1.5
prediction [37]	$< 10^{11} cm^{-2}$	1.4

Clearly the size of the defects in our devices is in the atomic range and matches the predictions. However the defects in our samples are at least one order of magnitude higher than predicted by the theory, which tends to suppress the

mobility of the carriers in both our samples. Comparison of the data for *TG* and *DG* devices reveals that the non-direct access to the catalyst during the growth of the *DG* sample leads to increasing the population of defects, however the amount of defects added in proximity growth compared to the normal CVD process is much lower then the amount that a CVD grown graphene bears compared to the predictions.

Note that unlike the *TG*, the graphene of the *DG* sample was sandwiched and protected between a PMMA layer and h-BN flake during the transfer, thus extra vacancies have occurred during the growth. Assuming that these vacancies are homogeneously spread all over the graphene, the spacing between them is of the order of 8 nm. We will see later (Figure 3.10-e) that at high carer densities, the mean free path of the electrons in this sample falls below 10 nm which is comparable to the spacing between the defect *i.e.* the transport of the electrons are largely affected by the formation of such voids.

The inset of Figure 3.10-b, is the same graph which focuses on the vicinity of the Dirac point. Here we see that by reducing the density of electrons, the model fails to follow the experiment; around this area, the charged impurities close to the graphene sheet makes a random network of 2D electron and hole puddles which affects the conductivity of the samples. Interestingly, this transition happens at a higher carrier density for the *TG* sample. By plotting the low density regime in a logarithmic-scale plot (Figure 3.10-c and d), one can see by approaching the Dirac point, the conductivity of both of the samples reduces monotonically but saturates after a threshold density (n_{sat}, depicted by arrows there); The saturated conductivity for the samples ($\sigma_{sat\,DG} \approx 1.0 \times \frac{4e^2}{h}$ and $\sigma_{sat\,TG} \approx 1.1 \times \frac{4e^2}{h}$) are very close to the universal minimum conductivity predicted for the graphene [37] which happens below the threshold densities of $n_{sat\,TG} \approx 8 \times 10^{10} cm^{-2}$ and $n_{sat\,DG} \approx 4.5 \times 10^{10} cm^{-2}$ respectively. The ratio of the saturation density and the corresponding conductivity $n_{imp} \propto (\frac{n_{sat}}{\sigma_{sat}})$ can give us information about the population of the charged impurities [39]; this implies $n_{imp\,TG}/n_{imp\,DG} \approx 1.6$. This number shows the advantage of the utilized direct growth of the graphene in minimizing the charged impurities. The thicknesses of the *DG* flake is around 40 nm; knowing that the impurities located with a distance more than $\approx 10\,nm$ from the graphene have a tiny effect on its conductivity [127], the estimated impurities in *DG* sample are either located on top of the graphene or are some impurities in the utilized commercial h-BN flake which might have migrated close to the surface during the growth.

Now we use the equation $\mu_{FE} = \sigma/en$ to calculate the mobility of the samples. The results are plotted in Figure 3.10-d; At high carrier densities and while the conductivity of the *DG* sample is largely suppressed by vacancies, the mobility of the other sample is several times higher. For the whole density, the conductivity of the *TG* sample and this its mobility is higher. However the calculated mobilities are only valid until outside the conductivity saturation regions (only along the continuous lines), so while the maximum mobility of *TG* is some more than $14,000\,cm^2/Vs$ at $n_{sat\,DG}$, due to the less charged impurities and delayed saturation, the mobility of the *DG* continues to increase and approaches $20,000\,cm^2/Vs$ close to its saturation point. This mobility is the highest reported so far for graphene grown without direct access to the catalyst. With this curve,

the corresponding mean free path (mfp) of the electrons can be calculated using the equation: $l = (h/2e)\mu\sqrt{n/\pi}$, the results of which are shown in the inset of this figure. Like the mobility, early saturation of the conductivity for the *DG* accounts for reaching higher *meaningful* mean free paths for the *DG*.

3.7 Conclusion and Discussion

Using h-BN buffer layers in between graphene and the substrate is the best known technique for preserving the ultimate properties of graphene in transport applications of supported samples. However success of this technique is very much dependent on the cleanliness of the graphene/h-BN interface. Typical fabrication method of such structures is based on the transferring CVD or exfoliated graphene on h-BN flakes which have the risk of adding contamination. This is why directly growing graphene on h-BN is very appealing. Ease of fabrication and eliminating any risk for damaging graphene in the fabrication process are the other advantages direct growth techniques may have. Furthermore, *in situ* grown graphene is expected to follow the crystallographic orientation of the substrate to some extend, which minimizes the structural uncertainties.

The necessity of the presence of the catalyst materials is an important hindrance for developing direct growth methods; by replacing them with h-BN and even at the expense of very long growth durations, the grown graphene flakes are reported to be of low quality which diminishes all the advantages of h-BN layer.

In this chapter, we introduce a novel technique in which the catalyst is present besides the h-BN; precursor decomposes by reaction with the catalyst and the resultant carbon atoms migrate on top of the h-BN to form graphene layer; this is why we call it proximity-driven growth. In this mechanism, high mobility of carbon on h-BN which is a characteristic of van der Waals mechanism plays an important role.

Raman analysis on *as-grown* flakes right after the CVD process clearly confirm the growth of graphene. Also AFM investigations prove that the surface quality of the h-BN flake is conserved. Such analysis were also performed after transferring graphene/h-BN stacks on silicon wafers and compared to normally transferred graphene. Importantly, our analysis show that the weak van der Waals interaction is strong enough to align crystallographic orientation of graphene with h-BN. Also it is noticed that in this technique graphene can grow at the backside and/or in between the layers of h-BN. This is an important observation showing the possibility of *in-situ* fabricating more complex structures like h-BN/graphene/h-BN sandwiches.

This growth technique minimizes the risk of having unfavorable charge impurities close to graphene which reduces its quality at low carrier densities. By this, remarkably high mobilities are obtained which is the best reported for the CVD grown graphene without direct access to the catalyst. We also show that the maximum mobility of such devices may exceed that of normally transferred graphene/h-BN samples. At high density regime, the transport of the carriers are highly limited by the vacancies have occurred during the growth. A system-

atic study is needed to minimize the amount of these defects by fine tuning of the growth recipe.

Performance of CVD Graphene in Nano-Electro-Mechanical Systems

4.2 Introduction

Micro- and *nano-electro-mechanical systems* (*MEMS* and *NEMS*) are categories of devices in which moving objects at the micro- (nano-) scale are coupled to some electrical component, the latter being used either for excitation, for detection of motion, or both. This field of research has grown rapidly over the past few years thanks to fast progress in micro-/nano-fabrication, integration techniques (the advent of so-called *system-on-chip*), together with theoretical developments and computer-aided design and simulation softwares [128].

Traditionally different terms have been used to address such micro-scale devices depending on their application areas and country of development. While the term 'Micro-Machines' have been used in Japan, 'Micro-Systems Technology (MST)' is the name used to address them in Europe. The term 'Micro-Electro-Mechanical Systems (MEMS)' has been originally used in US and is now becoming the worldwide accepted name. Besides, 'Micro-Electro-Opto-Mechanical Systems (MOEMS)' is another family of such devices and used when they are combined with optical systems. Similar terms have been used for nano-scale devices.

MEMS and NEMS can be used either at low frequencies *i.e.* in quasi-static mode (using for example measuring the variation of capacitance of a membrane for position detection for pressure sensors, and accelerometers), or in the dynamic regime *e.g.* oscillators. Depending on their application, they might be composed of complex mechanisms for actuation and detection as well as miniaturized pumps, motors and so on. When they are used in the dynamic mode, the displacement can be in the form of mechanical vibrations and devices are set to work at resonance frequencies of one of their suspended sub-part. These systems are of great interest not only for the field of fundamental mechanics at small scales but also for their diverse applications, including force [129], position [130] [131] and mass [132] sensing.

Due to their extremely low mass (down to $\approx 10^{-21}$ Kg for carbon nano-tube [133]), high operating frequencies up to several gigahertz are expected in nano-scale devices. Also high surface to volume ratios and low fabrication costs are the important properties of the nano-/micro- scale electro-mechanical devices.

NEMS using graphene membrane as their moving parts is the topic of the research reported in this chapter. Such devices are used in the dynamic and vibrational modes; so throughout this chapter and by using the term NEMS, we will refer to nano-electromechanical resonators.

It is not clear what was the first NEMS device, however one can consider the invention of the atomic force microcopy (AFM) [134] as being one of the first revolutions in the NEMS world. This was done by Gerd Binnig and Heinrich Rohrer from IBM Research center in Zurich in the early 1980's; because of which they were awarded the 1986 Nobel Prize in Physics [135]. A later work in 2000 from IBM [136] is another important example of NEMS: a packed array of 32 by 32 (1024) cantilevers can heat/sense a deformable substrate in order to function as a memory device. Figure 4.1 shows SEM images of this array.

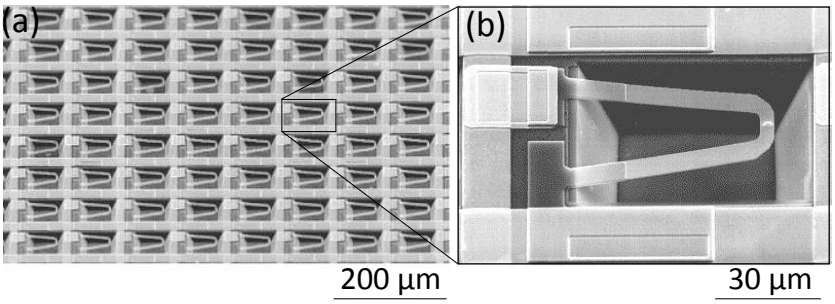

Figure 4.1: SEM images of one of the first NEMS devices
a) A compact array of the cantilevers made for thermal data storage
b) Focused image on one of the cantilevers

Writing about the fabrication techniques for NEMS devices, like in other micro-/nano-fabrication schemes, *top-down* and *bottom-up* approaches can be found: the top-down concerns the traditionally used micro-fabrication methods like optical and electron beam lithographies which involves device fabrication by reduction of the size of bulk materials. Devices made by these techniques are mainly limited by the resolution of the micro-fabrication techniques. In the bottom-up approach, the final material (device) is synthesized from corresponding atomic or molecular species through some chemical reactions which allow for the precursor particles to grow in size. This technique allows fabrication of much smaller structures compared to the top-down approach; also the final devices are typically cleaner in this technique since little fabrication residuals are normally left. Fabrication by a combination of these approaches is also conceivable.

Carbon-based devices possess unique mechanical and electrical properties (will be addressed in the next section) which make them ideal materials for NEMS in diverged applications. Furthermore, graphene and CNT integrated devices can be fabricated in clean bottom-up approaches and thus very high mechanical performance is expected.

In this chapter,focus will be on the fabrication along with room- and low-temperature performance of graphene based nano-electro-mechanical systems. Some works have been reported in this area using exfoliated graphene as the oscillating membrane [137][138][139], however only a couple of reports [140] [141] discuss about the performance of membranes based on chemically grown graphene which provide the outstanding advantage of integration and mass production of such devices.

This chapter starts by briefly describing the important advantages of graphene to be integrated in NEMS. In the next section, the basic physics of the mechanical resonators will be discussed. Topics like natural resonance frequency, quality factor and damping will be covered there. In order to excite a mechanical resonator and to detect its motion, certain schemes should be employed which are the topic of the next section. Following a review of the important reports in this area, we will describe the fabrication process for making a large array of devices. In this context, an improved recipe to preserve the quality of graphene during the fabrication also will be introduced. The data and results obtained at room and low temperatures will be described in the 'Measurements' section. Based

on the data acquired at low temperature, the coefficent of thermal expansion of graphene can be estimated.

4.3 Application of Graphene for NEMS

Carbon-based materials including graphene are among the most promising materials for NEMS applications. Their outstanding mechanical properties (including their very high Young's modulus [15]) are important issues not only for the stability of NEMS but also to improve their efficiency and operation frequency. In graphene and CNTs, this property comes together with ultra low mass (in the order of $\approx 10^{-21}$ Kg for CNT [133]). Due to this combination, very high natural resonance frequencies are expected. Furthermore, graphene can withstand strains up to $\approx 25\%$ which is ultrahigh compared to other materials. Considering the electrical properties, gate tunable carrier density in graphene is another important characteristics which makes graphene based NEMS capable to be functionalized as transistors [142]. It should be noted that some effective detection schemes [143] are developed for graphene based on this property and thus are not applicable for other materials that lack gate tunability. Besides, the extremely high surface-to-volume ratio of graphene [137] makes such devices capable to be used as sensors. Also because of this property, one can think about adding more functionalities in graphene-based NEMS by coupling them with other materials/molecules with diverse properties [144].

4.4 The Basics of Mechanical Vibrations

Simple harmonic oscillator is a model system to study the physics of mechanical resonators. In this section, the main principles and properties of this system will be reviewed.

4.4.1 Free and Forced Oscillations

Consider a model system composed of an object with mass m, connected to a spring with a constant k, as is illustrated on the left side of the Figure 4.2-a. The system is initially in the equilibrium condition meaning the weight of the object (gravity force) is in balanced with the initial stretching of the spring. Now the question is how does the object move if one displace it with a small distance δx from its equilibrium position (right side of the Figure 4.2-a) and release it?. The only unbalanced force acting on the object is the force from the spring, so Newton's second law for the motion reads: $F = m\ddot{x} \Rightarrow -kx = m\ddot{x}$ or equivalently:

$$m\ddot{x} + kx = 0. \tag{20}$$

This relation is referred to as the equation of the motion of the *freely* oscillating object; it is obtained considering the force generated by the spring that follows *Hooke's law* which is always opposite to the direction of the motion. Here $\ddot{x} =$

d^2x/dt^2 is the second derivative of the motion with respect to time. Solving this differential equation, one will end up with:

$$x(t) = \delta x \cos(\omega_n t), \ \omega_n = \sqrt{k/m}. \tag{21}$$

ω_n obtained here is the *natural frequency* of the system. This relation means that in such a system, after a small displacement of the object from its natural position, it will oscillate around the equilibrium position with the natural frequency of the system and constant amplitude in time. The system described here is the ideal system in which the effect of the *damping* which is the effect of losing the energy (amplitude of the oscillation) of the system is neglected. In normal applications, damping is modeled as proportional to the velocity of the system with a damping coefficient *c*. So a more realistic equation of the motion and its solution reads:

$$m\ddot{x} + c\dot{x} + kx = 0 \implies x(t) = \delta x\, e^{-\zeta\omega_n t}\cos(\omega_d t), \tag{22}$$

with $\zeta = \frac{c}{2\sqrt{mk}}$ and $\omega_d = \omega_n\sqrt{1-\zeta^2}$. So presence of the damping not only affects the amplitude of the oscillations, but also it reduces the frequency of the free oscillations. This equation is obtained assuming $\dot{x}(t=0) = 0$ and is interesting for our purpose when $0 \leqslant \zeta < 1$ which is referred to as the *underdamping* case. Figure 4.2-c shows the solution of Equation 21 and Equation 22 with no damping ($\zeta = 0$) and for the cases $\zeta = 0.01$ and $\zeta = 0.1$. The cases $\zeta = 1$ and $\zeta > 1$ are called *critical damping* and *over damping* respectively, in the later case the object returns to the equilibrium position without any oscillation.

So far we considered the *free oscillation* of the system in which a small displacement of the objects from the equilibrium position excites the vibrations of the system. In application, all the vibrating systems has a degree of damping, meaning that the amplitude of the vibration approaches to zero in relatively long periods. The other mode of exciting a vibrating system is called *force oscillation* in which an external periodic force is applied to the object and force it to vibrate. This method is illustrated in Figure 4.2-b.

The equation of the motion in the presence of the damping mechanism can be obtained in the similar way as above:

$$m\ddot{x} + c\dot{x} + kx = f_0\cos(\omega t), \tag{23}$$

where ω and f_0 are the frequency and amplitude of the periodic external force. The steady-state solution of this equation reads:

$$x = x_0\cos(\omega t - \phi), \tag{24}$$

with

$$x_0 = \frac{f_0/k}{\sqrt{\left(1-(\frac{\omega}{\omega_n})^2\right)^2 + \left(2\zeta\frac{\omega}{\omega_n}\right)^2}} \text{ and } \phi = \tan^{-1}\frac{2\zeta\frac{\omega}{\omega_n}}{1-(\frac{\omega}{\omega_n})^2}. \tag{25}$$

Interestingly, the maximum amplitude of oscillations (x_0) in this case depends on the ratio of $\frac{\omega}{\omega_n}$. Also the presence of the damping leads to the phase difference

ϕ between the external force and displacement. In Figure 4.2-d, x_0 is plotted as a function of the ω for few values of damping (ζ). In all the cases, x_0 is the highest when ω approaches the natural frequency of the system (ω_n). For the case $\zeta = 0$, $x_0 \to \infty$ as $\omega \to \omega_n$. For more realistic cases when ζ has finite values, increasing the damping attenuates the value of the x_0. We can see the interesting behavior of ϕ versus ω in part *e*. For the case $\zeta = 0$ and starting from $\omega = 0$, the object follows the oscillation of the force with no phase difference meaning that the motion of the object is in the same direction of the force; however once ω exceeds the natural frequency, the motion of the object becomes in the opposite direction of the force as is indicated by the π shift in ϕ. In the presence of damping, the general behavior is almost the same except the phase shift happens more smoothly.

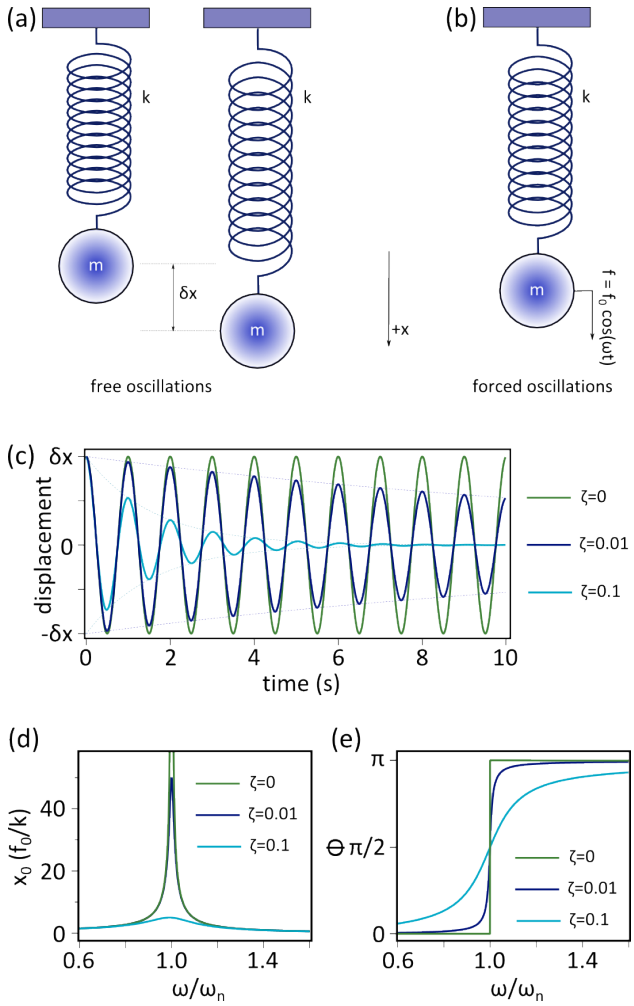

Figure 4.2: Free and forced oscillation in a spring-mass *system*
a) Free oscillation: The object with mass m *connected to a spring with constant* k *is initially in a equilibrium state (left side). By moving the object from its position by* δx *and releasing, it starts to oscillate about the equilibrium position in its natural resonance frequency* ω_n *and amplitude* δx*.*
b) Forced oscillation: By applying an external oscillating force following $f = f_0 \cos(\omega t)$ *one can push the object to oscillate in the frequency* ω *and with the amplitude and phase given by Equation 25.*
c) Plot of the motion of the object in the free oscillation mode (results of the Equation 22): Increasing the damping in the system (ζ*) attenuates the motion. The curves are plotted with the value* $\omega_n/2\pi = 1$*. The dotted lines show* $\pm\delta x\, e^{-\zeta\omega_n t}$*.*
d) and (e) Amplitude and phase behavior of the oscillator as a function of the deriving frequency (ω*) in the forced vibration case: The curves are plots of the Equation 25 for different levels of damping (*ζ*).*

4.4.2 Quality Factor

The concept of damping in an oscillating systems was introduced in the previous section. Viscous drag by the atmosphere enclosing the system is an example of such damping mechanisms. Here the parameter *quality factor* (or *Q-factor*) is used to describe the rate of the energy loss in comparison with the total energy of the

resonator: the higher the quality factor, the lower the rate of energy dissipation. It is defined as:

$$Q = 2\pi \times \frac{\text{total energy of the system}}{\text{dissipated energy per cycle}} \approx \frac{\omega_n}{\Delta\omega} = \frac{1}{2\zeta}. \tag{26}$$

The last part of this equation is valid for relatively high Q-factors [145]. Here $\Delta\omega$ is the bandwidth in which the power of the vibration is more than the power at the resonance condition; this is equal to the full width at half maximum of the peaks in Figure 4.2-d for the forced oscillation case. For freely oscillating objects Q can be calculated as the number of the cycles the resonator moves back and forth until its energy decreases by a factor of e [146].

4.4.3 NEMS, Free or Forced Oscillations?

Almost all the NEMS experiments reported so far have been performed in the forced oscillations mode where an actuation scheme is employed to apply oscillating external driving forces with the frequency ω. A set up is used to probe the amplitude of the vibration simultaneously. Starting the measurement, ω is swept in a window in which ω_n is expected to be as shown in Figure 4.2-d.

This common technique is very difficult to apply to systems with high quality factors in which the resonance peaks are very sharp *i.e.* very high sampling rates are necessary to capture the resonance state. In contrary, the system of a high quality factor can run for very long time in the free oscillation mode before attenuation and the resonance frequency can be readily extracted based on the modulation of the amplitude (Figure 4.2-c). All these confirm that for the devices with high quality factors, free oscillation mode can be a better choice than the forced oscillation to probe the nature of the system and more effort should be invested in this field in the future.

4.5 Techniques for NEMS Driving and Reading-Out

In this section, the most important schemes which are used to drive the nano-electro-mechanical systems and to probe the motion of their vibrating elements are introduced and discussed very briefly. The technique which is used in our experiments is also presented here in more detail.

4.5.1 Actuation Techniques

A series of methods can be used to excite nano- (micro-) mechanical resonators; In each case, based on the physical relations, an oscillating force is applied and makes the active part of the system vibrate. The most important actuation mechanisms used for the MEMS and NEMS are reviewed in in this section.

4.5.1.1 Photo-Thermal Methods

In this technique, an AC modulated laser beam is focused to heat up the oscillating system. As a consequence, an oscillating stress is produced in the materials forcing it to vibrate. An important advantage of this method is that there is no

need for electrical connections, which is ideal for testing small isolated structures such as graphene flakes. This not only facilitates the fabrication, but also makes it applicable for both conducting and non-conducting membranes. The thermal conductivity of the system plays an important role in the effectiveness of this scheme. By shrinking the size, this technique becomes less efficient. Also due to the production of heat, it is not usable at low temperature measurements. A schematic representation of this technique which is developed and patented by Ilic, Aubin and coworkers [147][148] is illustrated in Figure 4.3-a.

4.5.1.2 Magnetomotive Actuation

This actuation technique is based on the *Lorentz force* generated in a oscillating membrane: In the presence of a constant magnetic field B perpendicular to the plane of the vibration, an AC current I is biased through the doubly clamped beam. Consequently an oscillating Lorentz force $F = IBL$ is induced perpendicularly to the field and to the beam. This technique was first developed by Cleland *et al* [149] in 1996 who successfully measured with silicon-based mechanical resonators (Figure 4.3-b). It requires relatively high magnetic fields and significant driving current to operate which can be sometimes incompatible with the envisioned measurements *e.g.* in superconductive membranes.

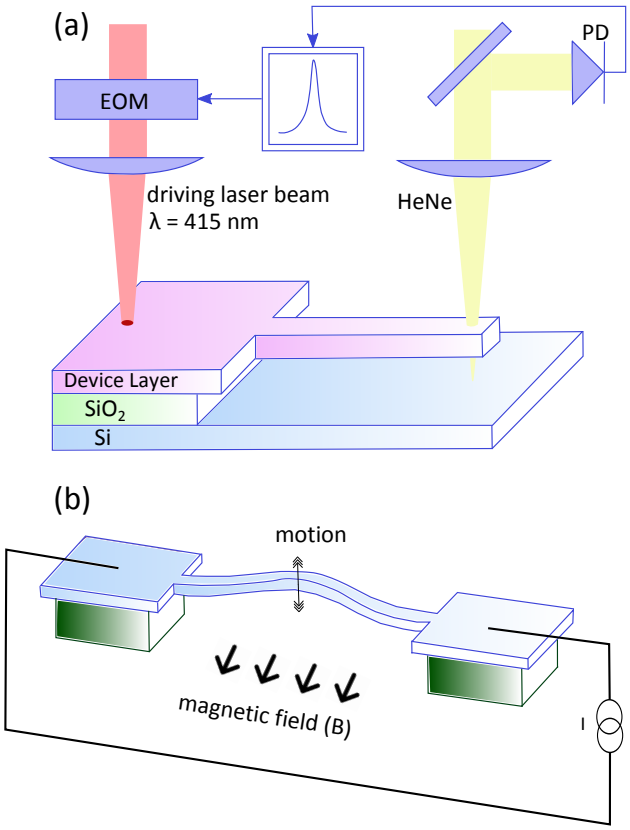

Figure 4.3: Schematic representations of the photo-thermal and magnetomotive actuation techniques
a) Laser heating derive for micro-mechanical systems: Modulating laser power pointed close to the cantilever makes it vibrate. The other laser beam (HeNe) pointed on the free end of the cantilever is used to monitor its motion. The signal collected at the single-cell photo-detector (PD) is passed to the spectrum analyzer which controls the driving electro-optic modulator (EOM). The figure is made by inspiration from [148].
b) Magnetomovite actuation set up: Lorentz force created in the beam due to the passing of ac current in the presence of the magnetic filed, drives the beam in a plane perpendicular to the direction of the field. Figure is made with inspiration from [150].

4.5.1.3 Electrostatic Actuation

This actuation mechanism is one of the most popular methods in NEMS. Here an AC voltage with tunable frequency is applied to the conducting membrane which is of capacitance C with respect to the substrate; the electrostatic oscillating force is generated in this way tending to actuate the oscillator at twice the voltage frequency. This technique is normally used together with the frequency and amplitude modulation detection methods which is described in detail in Section 4.5.3.

4.5.1.4 Piezoelectric actuation

Finally, there exists a way to excite motion in a micro-/nano-system using a piezoelectric effect. Piezoelectricity is a fundamental phenomenon which occurs

in a certain class of material in which stress can result from an applied electric field. A piezoelectric layer can be deposited either on the moving part of the MEMS/NEMS or in its vicinity. Alternatively the entire chip on which the oscillator is fabricated can be deposited on a macroscopic piezoactuator which excites the vibration by indirect mechanical coupling. These are very convenient for on-chip low frequency excitation but fail to operate above a few tens of MHz due to the self-resonance of the crystal.

4.5.2 Detection Techniques

Once a mechanical system is actuated, a set up is needed to monitor its vibration. A brief review of the already developed detection techniques are presented here.

4.5.2.1 Optical Methods

There are at least two approaches in using optical techniques in detection of the motion of resonators: The first approach is the same technique as what is used in atomic force microscopy to detect the motion of the oscillating cantilever. A laser beam is focused on the cantilever and reflects back to a *position-sensitive detector (PSD)*; its output signal reveals information about the angular displacement of the cantilever. Figure 4.4-a shows how this technique is applied in an AFM.

The other approach which is revealed in Figure 4.4-b works based on the *interferometry* principle: here the monochromatic laser beam can interfere with itself in the optical cavity made in between a semitransparent oscillator and a substrate. The produced fringes can be used to detect the motion of the cantilever.

The optical methods are best applicable in micro-scale devices. In the case of nanometer-scale oscillators, the size of membrane can be comparable with the size of the laser spot which reduces the sensitivity of the measurement; however it has already been utilized successfully in nano-resonators [151][152]. As an interesting effort, this technique was combined with the Raman spectroscopy to detect the motion and stress in graphite resonators simultaneously [153].

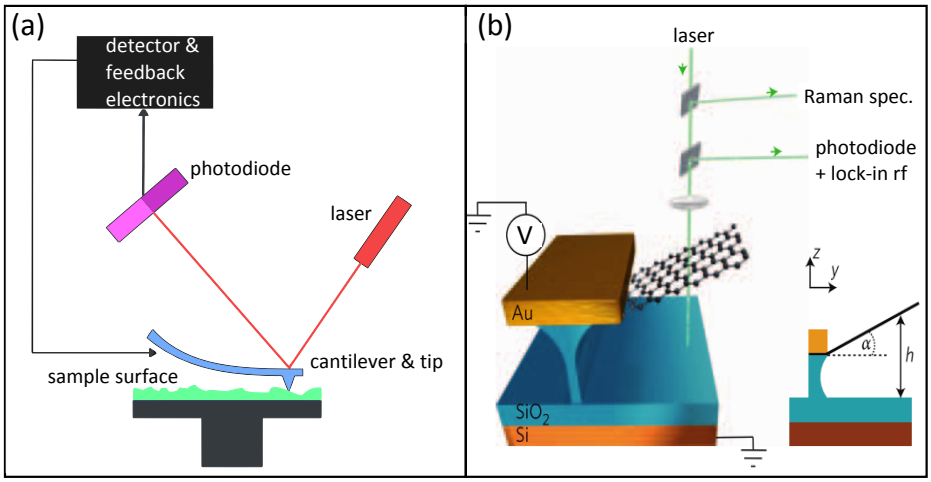

Figure 4.4: Optical detection methods
a) Basics of the laser detection scheme used in atomic force microscopy: Captured signal in the photodiod contains information about the angular deflection of the cantilever. The figure is adopted from [135].
b) Optical technique to probe the motion and stress simultaneously in the graphene resonators: figure is reprinted from [153].

4.5.2.2 Magnetomotive Detection

In the basic set up (Figure 4.5-a), a doubly clamped beam is assembled as a part of a conducting loop and exposed to magnetic field perpendicular to the plane of the vibration. By oscillation of the beam, the magnetic flux enclosed by the loop varies which accounts for the creation of the *electromotive force (EMF)* across the beam. The resultant signal contains information about the resonance state. This technique has been developed and employed for a long time in several systems [154][149].

The techniques classified in this category are considered as the most commonly used detection techniques for NEMS and are normally used together with magnetic actuation.

In an interesting effort, Etaki *et al* [155] embedded such a resonator into a *SQUID* loop; so vibration of the oscillating element changes the active area of the loop exposed to in-plane magnetic field which is detectable as a signal across the SQUID. A similar work has been done using carbon nanotubes which compose the weak links of a SQUID [156]. These schemes are shown in Figure 4.5-b and c.

For another approach in this category, one can refer to the work done by Usenko *et al* [157] (Figure 4.5-d). Unlike the previous examples, the resonator is in the cantilever shape rather than a doubly clamped beam. A magnetized particle is attached to the end of the resonator; the resultant alternating magnetic flux due to the oscillation of the cantilever is detected through the nearby detection coil coupled to a SQUID.

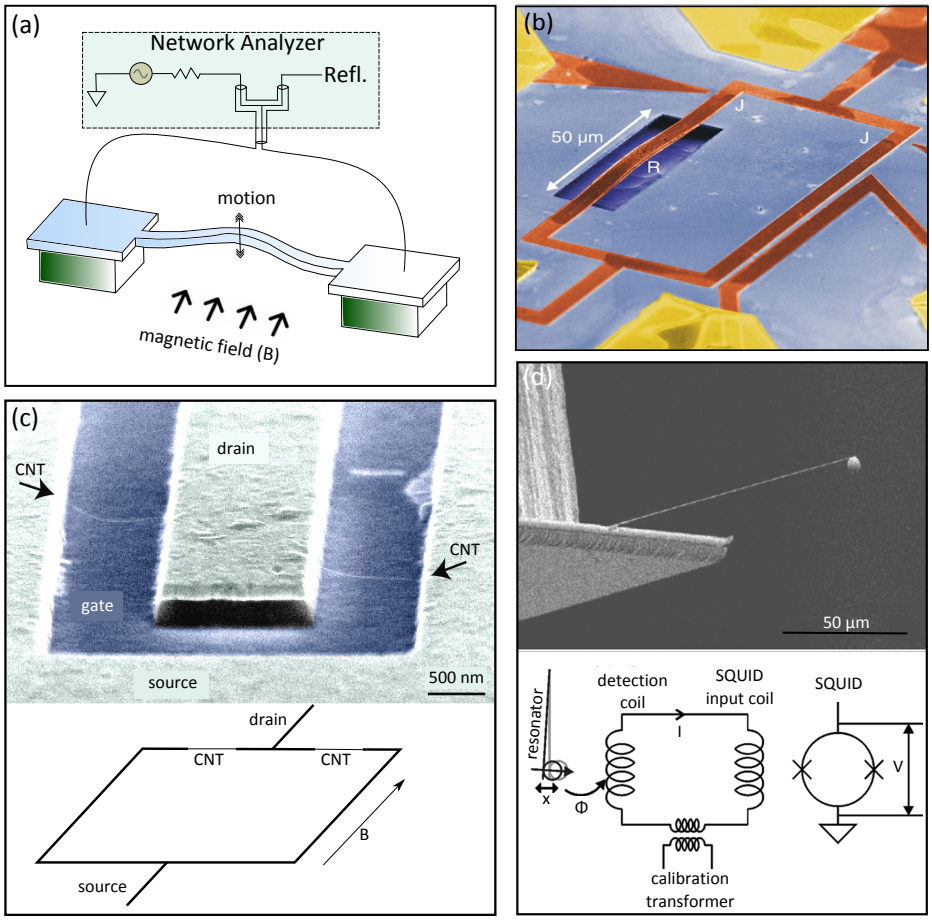

Figure 4.5: Magnetomotive detection techniques
a) Basics of the Magnetomotive detection: Electromotive force generated due to the crossing of the magnetic flux in the oscillating beam can be used to monitor the motion of the resonator. Figure is made with inspiration from [149].
b) A resonator assembled as a part of the SQUID loop: Upon the motion of the resonator, the effective area and hence the signal detected in the Nb-based dc-SQUID exposed to an in-plane magnetic field varies in time which is used to detect the motion of the resonator. Shown by R and J are the resonator and Josephson junctions. The figure is adopted from [155].
c) Similar technique as (b) to detect the motion of carbon nanotubes: The weak links are made up by a single CNT in this configuration. Schematic representation of the system is shown at the bottom part. Figure is adopted from [156].
d) Application of the magnetomotive detection in cantilever resonator: Motion of the silicon resonator with a magnetic sphere attached to its end is detected by using the electronics demonstrated in the circuit diagram. Figure is adopted from [157].

4.5.3 Capacitive Detection

In nano-electro-mechanical systems, charged metallic membranes are normally capacitively coupled to the substrate. Due to the oscillation of the membrane, this capacitance varies in time which can be used to detect the motion. We note that in order to be able to use this scheme, the signal should be large enough which is not always the case in nano-scale systems: Normally besides this ca-

pacitance which is sensitive to the motion of the membrane and scales with the area of the membrane, there are some sources of parasitic capacitance which are constant and not dependent on the motion; for example the constant capacitance between the macroscopic scale electrodes and substrate could be several orders of magnitude larger than the motion sensitive capacitance between the membrane and substrate which reduces the sensitivity of the measurement. Furthermore such parasitic capacitance defines an upper band for the frequency of the current biased to the membrane: solid-state devices like graphene often have a high impedance ($\gg 50\,\Omega$) which can be seen as a low-pass filter when it comes together with this unavoidable stray capacitance; the resultant cut-off frequency ($=1/RC$) is much lower than the mechanical resonance frequency of the system. These are two important challenges in the application of the electrical detection methods. Using local gates is a trick to improve the signal to noise ratio and to increase the cut-of frequency in micro-scale resonators [158][159] which makes it possible to measure the resonance signal directly by using a network analyzer; this improves drastically the measurement speed. However this technique is not easily applicable when the length of the device shrinks to nano-scale because of the difficulties in the fabrication process. Techniques based on mixing signals is another option to mitigate the effects associated to the parasitic capacitance. *Heterodyne mixing* and *frequency modulation* are two successful examples of signal mixing schemes which have been employed in MEMS and NEMS so-far. In both techniques the signal associated to the oscillations of the membrane (in the MHz range) is mixed with another signal, the frequency of which is selected in a manner that there is a component in the output with very low frequency which lays in the band-pass window.

4.5.3.1 Heterodyne Mixing

This technique was first developed by Sazonova *et al* [160] on carbon nanotube resonators in which a fully electrical and combined actuation and detection scheme is employed based on the signal mixing. Materials like carbon nanotubes and graphene which show a non-linear conductance property are the best candidates for this technique. Later it was used by Chan *et al* [138], Singh *et al* [58] and Van der Zande *et al* [140] for graphene based NEMS devices. Figure 4.6-a shows a circuit diagram of this technique. The heterodyne mixing method which is referred to as *amplitude modulation* technique, takes the advantages of the gate dependent conductance of graphene to detect its motion while it is driven electrostatically (Section 4.5.1.3) by applying an *RF* voltage to the backgate. A sum of the *AC* and *DC* voltage components needs to be applied as the gate voltage: $V_g = V_g^{DC} + V_g^{\omega}$.

The *AC* component tends to modulate the conductivity of the graphene membrane: $G = G(\omega)$ because of the small modulations of the carriers $\delta q_{el} = C_g V_g^{\omega}$ (purely electrical effect) and also because of the modulation of the capacitance while oscillating the membrane: $\delta C_g(\omega) = C_g' z(\omega)$ (electro-mechanical effect). The nonlinear conductance of graphene tends to amplify both effects.

Here C_g is the capacitance between the gate and the membrane, and C_g' shows the spatial derivative of the capacitance.

Besides the *RF* voltage to the gate, the sample also is biased with an *AC* voltage ($V_{sd}^{\omega+\delta\omega}$) with a frequency set slightly different from ω by $\delta\omega$. So the drain-source current equals to:

$$I_{ds} = G(\omega)V_{sd}^{\omega+\delta\omega}. \tag{27}$$

The product of the two terms in the right side of Equation 27 has two components in $(\omega+\delta\omega)+(\omega) = 2\omega+\delta\omega$ as well as in $(\omega+\delta\omega)-(\omega) = \delta\omega$ frequencies; both containing information about the resonance of the membrane. The signal in $\delta\omega$ frequency is very easy to detect using the lock-in which reveals the amplitude of the motion.

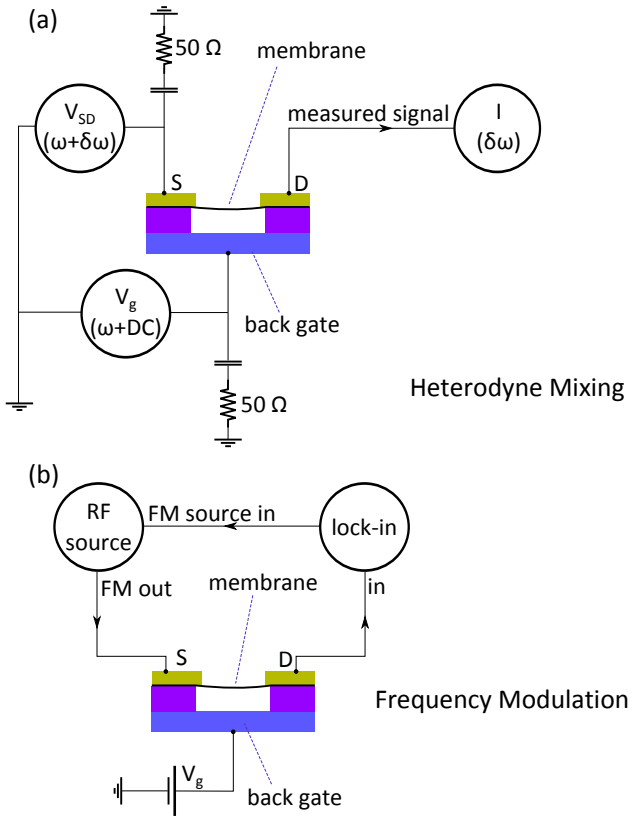

Figure 4.6: Schematic representation of the frequency mixing techniques
a) Heterodyne mixing: AC voltages with a small frequency difference of $\delta\omega$ are applied to the gate and source electrodes. As a result, a signal with a component in $\delta\omega$ which carries the information about the amplitude of the vibration of the membrane exits the drain electrode.
b) Frequency modulation: The low-frequency output of the lock-in is modulated with the high frequency signal in the RF source and is fed through the source electrode. Gate dependent conductance of the resonator leads to de-modulation of the signal with a component in frequency of the lock-in and with the information about the resonance of the membrane. Figure is made with inspiration from [143].

4.5.3.2 Frequency Modulation

This is another method which was first developed and employed on nanotubes by Gouttenoire *et al* [143]. A schematic representation of its circuit diagram is shown in Figure 4.6-b. Lock-in provides a low frequency signal ω_L on the order of kHz which is fed to the RF-signal generator as an external source. The device modulates this frequency with a carrier frequency (ω_c) in the MHz range; then the output is of the form:

$$V_{FM} = V_0 \sin\left[\omega_c t + f_\Delta \sin\left(\omega_L t\right)\right], \tag{28}$$

where V_0 is the drive amplitude of the resonator and f_Δ corresponds to the amplitude of the modulation which is in the order of tens of kHz. This signal is demodulated passing through the membrane with a component in the form of [161]:

$$I_{FM} = \frac{1}{2}\frac{dG}{dq} C_g' |V_g| \frac{dRe\left(z^*\left(\omega_c\right)\right)}{d\omega_c} f_\Delta \cos\left(\omega_L t\right), \tag{29}$$

here $z^*\left(\omega_c\right)$ shows the complex amplitude of the motion with a real part denoted by $Re\left(z^*\left(\omega_c\right)\right)$.

Unlike the output signal in the amplitude modulation technique, there is no background component due to pure electrical mixing in this equation. This remarkably improves sensitivity of the technique. The current which is detected by the lock-in is in the form [143]:

$$F\left(\omega_c\right) = \frac{2\omega_c \left(\omega_c^2 - \omega_n^2 - \frac{\omega_n^2}{Q}\right)\left(\omega_c^2 - \omega_n^2 + \frac{\omega_n^2}{Q}\right)}{\left[\left(\omega_c^2 - \omega_n^2\right)^2 + \left(\frac{\omega_n \omega_c}{Q}\right)^2\right]^2}. \tag{30}$$

Frequency modulation is the technique which we have used in the present work.

4.6 Review of the Important Reports in the Field

If we consider the invention of the atomic force microscope in 1986 [134] as one of the first milestones in this field, we can conclude that NEMS has a history of around 30 years or more. Throughout this relatively long period, different materials have been used as oscillators in these devices which include silicon [162][152][163], diamond [164][165], platinum [166], gallium nitride [167][168], rhodium [163], carbon nanotubes [160][169][170], etc. The isolation of mono- and few layer thick graphene in 2004 [28] is considered as an important event in the history of NEMS considering outstanding mechanical properties of graphene in such applications. In this section, we will review the important works in the field of graphene based nano-electro-mechanical systems. Table 5 also summarizes the techniques and achievements in these works.

The first graphene based nano-electro-mechanical device was fabricated and tested in the McEuen group at Cornell university in 2007 [137]. Their technique of fabrication includes mechanical exfoliation of graphene on pre-defined trenches

in silicon oxide wafer. Both optical and electrostatic schemes are employed to actuate the devices and the optical interferometry technique is used to read-out the oscillations. They probed several samples with different thicknesses ranging from monolayer graphene to 50 nm graphite; A quality factor of 1800 is the highest they reported at 50 K. Figure 4.7-a and b show examples of the devices they have made.

One year after, the Bachtold group in Barcelona reported the second work in graphene based NEMS [139]. They used a similar technique as the former work for the fabrication and the electrostatic method for actuation of the devices; however their detection method is very different: They directly map the shape of the resonance eigenmodes using a *scanning force microscope (SFM)*. The principle is schematically illustrated in Figure 4.7-c. This technique enabled them to image the mode of the vibration (Figure 4.7-d) which is not possible in the other detection techniques. In half of their samples they observe new unusual eigenmodes which is not predicted in the elastic beam theory. Modeling by finite element methods shows that such eigenmodes are generated because of the high amount of the non-uniform stress which is residual of the fabrication process.

The next important work was done in the Hone group at Columbia University [138](Figure 4.7-e and f). They successfully fabricated such devices by mechanical exfoliation of graphene layers on silicon wafer and then underetching. Heterodyne mixing was used for the electrical actuation and reading-out the devices. Their resonators show a quality factor as high as 10^4 at 5 K. Such high quality samples enable them to probe the response of graphene NEMS to variations in temperature and mass. The estimated mass sensitivity of their device is around 2 zepto grams (10^{-21} gr). A preliminary study about the non-linearity effects in the graphene membranes is included in this report. The coefficient of thermal expansion of graphene is another parameter studied there and they obtained the value of $\alpha = -7.4 \times 10^{-6} K^{-1}$ between 250 K and 295 K.

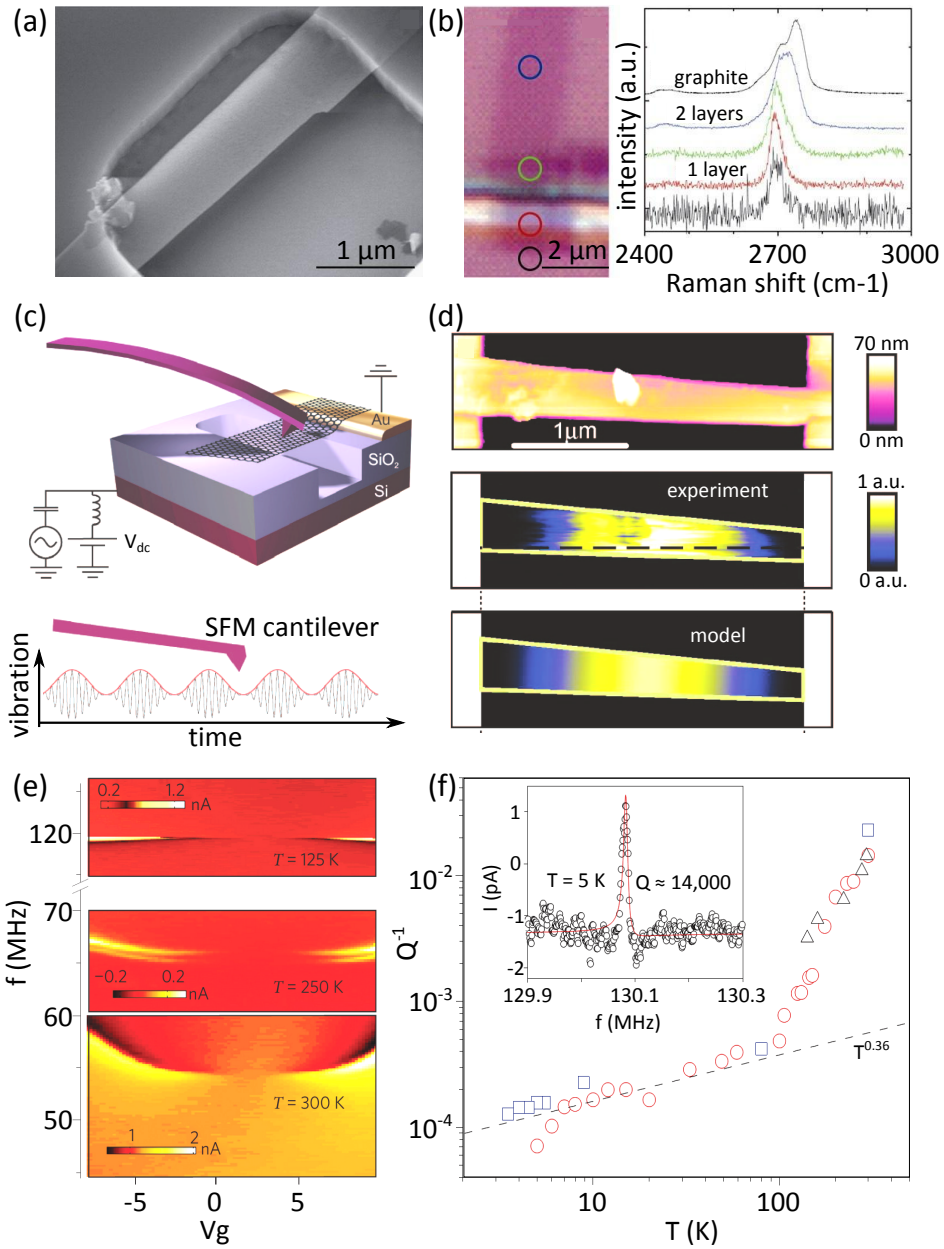

Figure 4.7: Early reports on graphene based nano-electro-mechanical systems
a) and (b): Data from the first report in this area [137]: SEM and optical micro-graphs of two of the devices are shown in (a) and (b-left). Raman data show the thickness of the graphene piece is not the same in the suspended and supported regions. Spectra correspond to the spots marked with the circles of the same color in the optical image.
c) and (d) Measurement technique results reported in [139]: c) A scanning force microscope cantilever is utilized to probe the resonance. The high-frequency voltage connected to the gate is matched to the resonance frequency of the graphene. Motion of the membrane probed by the tip is illustrated at the bottom part. d) Topography of the device and shape of the eigenmode as measured and simulated are presented in the panels from the top to the bottom.
e) and (f) examples of the data reported in [138]: e) Dispersion of the resonance frequency as a function of the gate voltage at different temperatures is one of the aspects addressed in this paper. f) Quality factor as a function of the temperature in graphene NEMS is plotted for the first time. Inset shows a resonance peak with high Q factor measured at 5 K.
All the figures are reprinted with adoptions.

The next important report in this field belongs to an Indian group led by M. Deshmukh [58] which was reported in 2010 and shown in Figure 4.8-a and b. They mainly focused on the effect of the temperature and gate voltage on the resonance properties of the samples. Precise models to estimate the resonance frequency and tension in the membrane as a function of the gate voltage and temperature are proposed. Such modeling and low temperature measurement enabled them to probe the coefficient of the thermal expansion of graphene down to very low temperatures. We will use the models developed by them as well as their results in our calculations (Section 4.8).

Later in 2010, the first report of NEMS obtained with CVD graphene came from Cornell [140] in 2010. Using CVD graphene, they fabricated and tested a large array of suspended, single-layer graphene resonators. They made devices in the doubly clamped form as well as square membranes clamped on all sides. Both underetching and transferring on the pre-patterned substrates techniques were employed to fabricate these devices. As a consequence of using CVD graphene, in each fabrication run, they produced hundreds to hundreds of thousands of graphene membranes. They not only show the possibility of using CVD graphene for making single layer graphene resonators; but also they claim that their devices were of the similar electronic and mechanical properties of exfoliated graphene devices. We note that their membranes clamped on all sides show higher resonance performance then the doubly-clamped ones. The fabricated samples and results are reported in Figure 4.8-c, d and e.

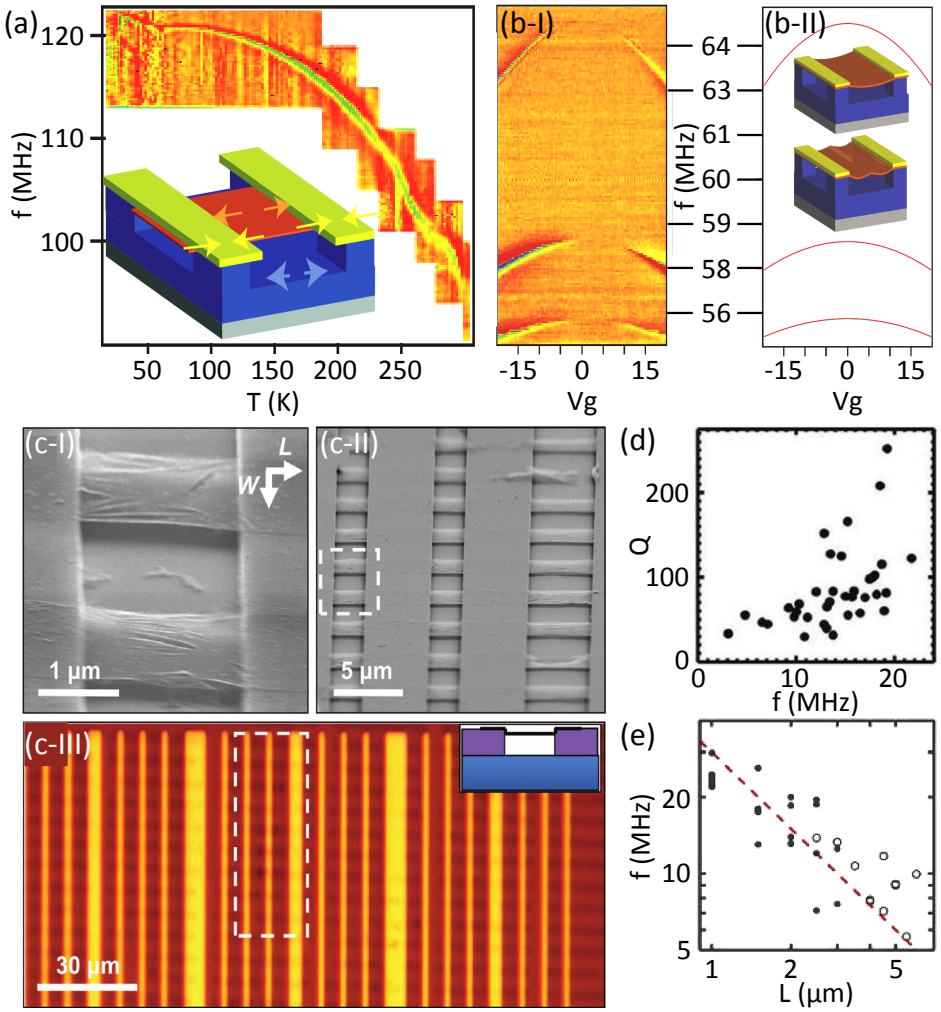

Figure 4.8: Selection from the data published in [58] (a-b) and [140] (c to e) which are among the pioneer works in the graphene based NEMS
a) Evolution of the resonance frequency as a function of the temperature of such devices is mapped and revealed for the first time in [58]. They have done modal analysis with the results of the sample showing 3 different vibration modes (b-I). The results of the fitting with the theories they have developed and schematic representation of two different modes are shown in (b-II).
C) SEM (c-I and -II) and optical microscope images appeared in [140] showing that they managed to fabricate large arrays of suspended CVD graphene samples. Dashed rectangles in each image indicate sizes of the areas in previous images. Quality factor as a function of the resonance frequency of their devices measured at room temperature is shown in (d). Plotting the resonance frequency as a function of the device length (e) shows that increasing the device length leads to reduction in the resonance frequency. All the figures are reprinted with adoptions.

The highest quality graphene based nano-electro-mechanical samples reported so far occurred in 2011 by the Bachtold group [133]. However the main objective of their work is to study the damping of mechanical resonators; they have performed this study on both graphene and carbon nanotubes. In both systems, they found that damping is largely affected by the amplitude of the motion:

damping$\propto x^2\dot{x}$ (x: position); this is opposite to the case of large samples in which damping is normally proportional to $\dot{x}$ with a constant coefficient (it is reviewed in Section 4.4.1). Underetching the exfoliated graphene and frequency modulation are the techniques they have chosen for the fabrication and measurement of their devices. Figure 4.9-a and b show selection of there results.

Before this project started in our group, there were some attempts to make graphene based NEMS devices by Adrien Allain [91]. The goal was to induce superconductivity into suspended graphene by decorating its surface with superconducting tin clusters. Even though this goal was not reached because of the complexity of the system, however interesting results were obtained with normal state devices at room and intermediate temperatures. Exfoliated graphene suspended by underetching is used in these experiments (Figure 4.9-c and d).

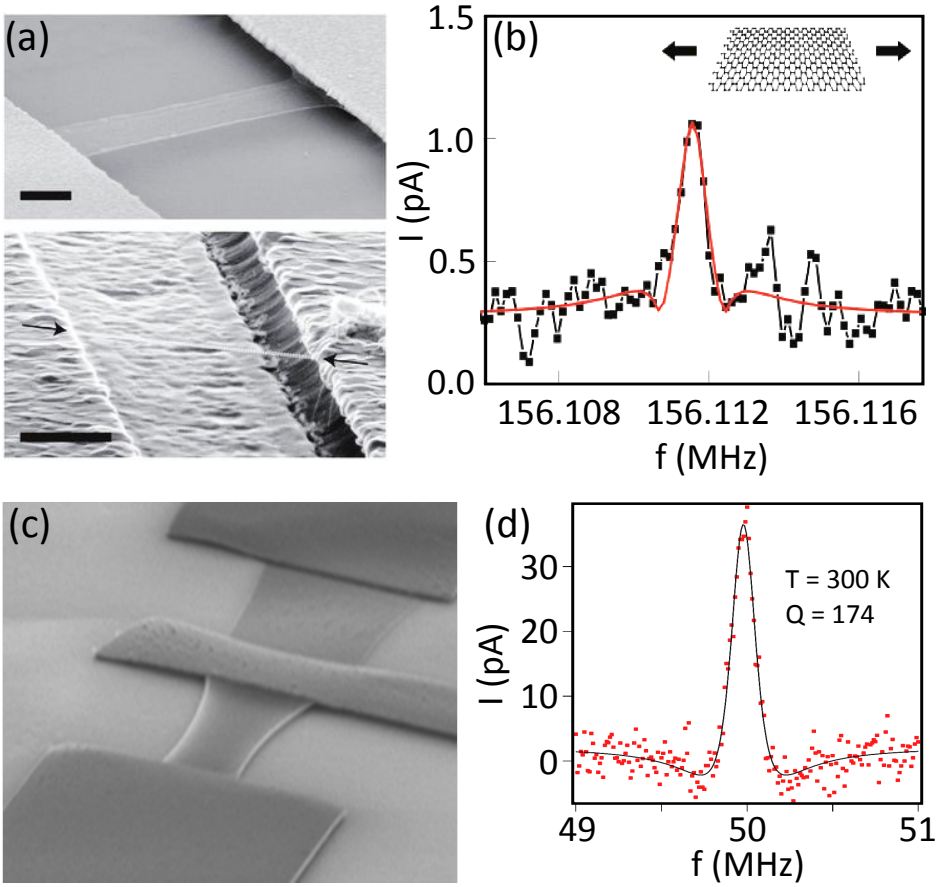

Figure 4.9: Selection from the data published in [133] (a and b) and an early work in our group [91] (c and d)
a) SEM images of examples of the graphene and carbon nanotube devices. Scale bars corresponds to 500 nm. The graphene sample under strain shows very high quality factor in (b).
c) SEM image of the devices made in our group before the present work: The borders curled up in the closer device indicate that the graphene is under stress. The other device is collapsed. The lengths of the membranes are in the order of 2 µm. d) Example of the resonance peak showing quality factor of 174.

Table 5: Summary of the techniques and results reported in the important graphene based NEMS papers so far

group	graphene	fabrication	measurement	highest Q
McEuen [137]	exfoliated mono- and few layer	exfoliation on pre-defined trenches	optical and electrostatic actuation, optical detection	1800 at 50 K
Bachtold [139]	exfoliated few layer	exfoliation on pre-defined trenches	electrostatic actuation, scanning force microscope detection	20-30 at 300 K
Hone [138]	exfoliated monolayer	exfoliation and under etching	heterodyne mixing	14,000 at 5 K
Deshmukh [58]	exfoliated monolayer	exfoliation and under etching	heterodyne mixing	≈3000 at <10 K
McEuen [140]	CVD mono-layer	transferring on pre-defined trenches and under etching	optical actuation/detection and hetero-dyne mixing	9000 at 9 K
Bachtold [133]	exfoliated monolayer	exfoliation and under etching	frequency modulation	10^5 at 90 mK
Bouchiat [91]	exfoliated monolayer	exfoliation and under etching	frequency modulation	174 at 300 K

4.7 Fabrication Technique

The important reports in the field of graphene based nano-electro-mechanical systems have been reviewed in the last section. There are two approaches in making such samples: either deposition of the graphene flakes on a flat substrate and then underetching to make them suspended or by depositing graphene on pre-defined trenches. We have chosen the first technique for making our samples with gold electrodes. The fabrication procedure for making this kind of samples is reviewed in this section.

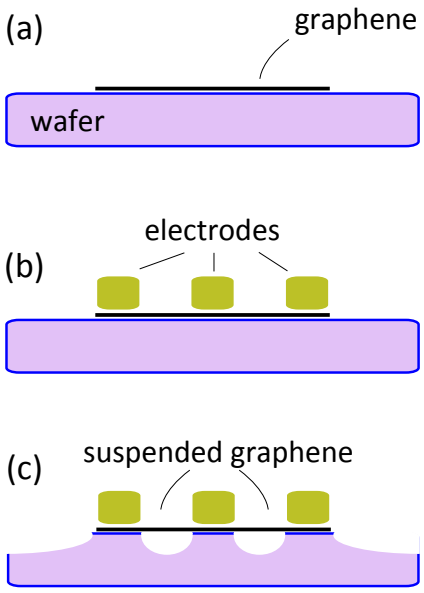

Figure 4.10: Standard fabrication process for making CVD graphene based NEMS
Fabrication starts by transferring graphene and etching it into ribbons (a). Electrodes are deposited after a lithography and development step (b). By underetching the ribbon and with the help of the critical point drier, the samples are ready for measurements (c).

In this way, after a brief review of the normal fabrication process, the improved fabrication recipe which we have developed to preserve the quality of the graphene will be introduced.

4.7.1 Standard Fabrication Recipe for Under-Etched Graphene Devices

The standard fabrication process of making such samples can be describe in 3 steps which are illustrated in Figure 4.10: At the first step, CVD graphene is transferred on to a typical silicon wafer in a well known *wet transferring* method [88]. Then the *PMMA* is removed and instead, a layer of UV sensitive resist like *UVIII* is spun on it. Subsequently, by using deep-UV lithography followed by an oxygen plasma step, graphene is patterned into the strips of few micrometer width and several hundreds of microns length.

This PMMA layer has been used for supporting graphene while etching the copper foil in the wet transferring method. For more information about this method one can refer to [171][88].

At the next step, electrode materials are deposited on the ribbon. To do so, first the old UVIII is stripped away and is replaced by a new one to cover the whole surface of the sample. Then by doing another step of deep-UV lithography the sample is ready for electrode deposition. Since the whole sample including the electrodes are going to be treated with HF acid at the following step, only some certain metals which are resistant to HF can be used as electrode materials. Like similar reports [58][91], we use chromium and gold for this purpose. The process of electrode deposition is done by lifting-off the excessive metal and removing the the resist using acetone.

Now series of graphene devices connected to electrodes and lying on the wafer are fabricated. At the next step, by etching and removing a thin layer at the surface of the wafer, one can make the samples suspended. For that, HF bath which is known to remove silicon without affecting graphene too much, is used. The etching rate is estimated to be around 2.25 nm/s and by dipping the sample into the bath for 60 s, we normally end up with 135 nm underetching. The process stops by rinsing the sample in DI water.

4.7.2 Improved Fabrication Recipe

The standard recipe for making underetched graphene membranes are reviewed in the previous section. During the fabrication process and before underetching the graphene, it is needed to spin PMMA and UVIII resists on the surface of the graphene and remove it at the next step for 3 times. This is an important drawback of this recipe since the process of spinning and stripping the resists may damage the graphene. Also contaminating the surface of graphene is likely to happen. Furthermore the microdeveloper which is very destructive and damaging for graphene, is used two times for developing the UVIII while it is in direct contact with graphene. Considering these limitations, we have developed a new recipe in which the PMMA that is initially used for transferring graphene is kept throughout the whole processes to the end. Thus not only the risk of damaging the graphene exposed to different chemicals is minimized, but also the PMMA layer covering the graphene prevents any contamination to be deposited on the graphene.

The process flow of this recipe is illustrated in Figure 4.11. We start by transferring graphene together with PMMA on a wafer (I). Deep-UV light and suitable masks are used to expose PMMA and pattern it into strips. The development and removing of the exposed PMMA is done with a MIBK solution. At the end of this step, the surface of the graphene is covered with graphene and patterned PMMA (II). Then exposing the sample into oxygen plasma etches away unprotected area of the graphene (III), patterning it into stripes. Now it is needed to pattern and deposit electrodes. To do that, without removing the PMMA, we spin LOR3A and UVIII resists on the sample (IV). An appropriate mask is used to expose the covering UVIII layer in DUV machine. By developing it using micro-developer or MF26A solutions both the UVIII and LOR3A layers are patterned into the shapes of electrodes (V). However one cannot deposit metal at this step because the surface of the graphene stripe is still covered with PMMA. So we expose the sample to DUV light with high enough dose. Already patterned UVIII and LOR3A layers can work as a mask to block the DUV light and only the unprotected areas of the PMMA are activated. UVIII by itself is not able to do this effectively and thus LOR3A is used too. By developing and removing exposed PMMA using MIBK, the sample is ready for metallization (VI). Chromium and gold electrodes with the total thickness of around 70 nm are deposited at step VII. For the lift-off, we use microdeveloper to remove the UVIII and LOR3A layers together with the excessive metallic parts; this is necessary since the underlying PMMA protects graphene of re-deposition of the metal. The process is finished by removing the PMMA and cleaning the graphene using acetone (VIII).

Even though PMMA is considered as an e-beam resist, but it is sensitive to the deep-UV light also; consequently with long enough exposure time, one can expose it like other deep-UV resists. Depending on the intensity of the deep-UV machine, the exposure may last between 30 minutes up to several hours.

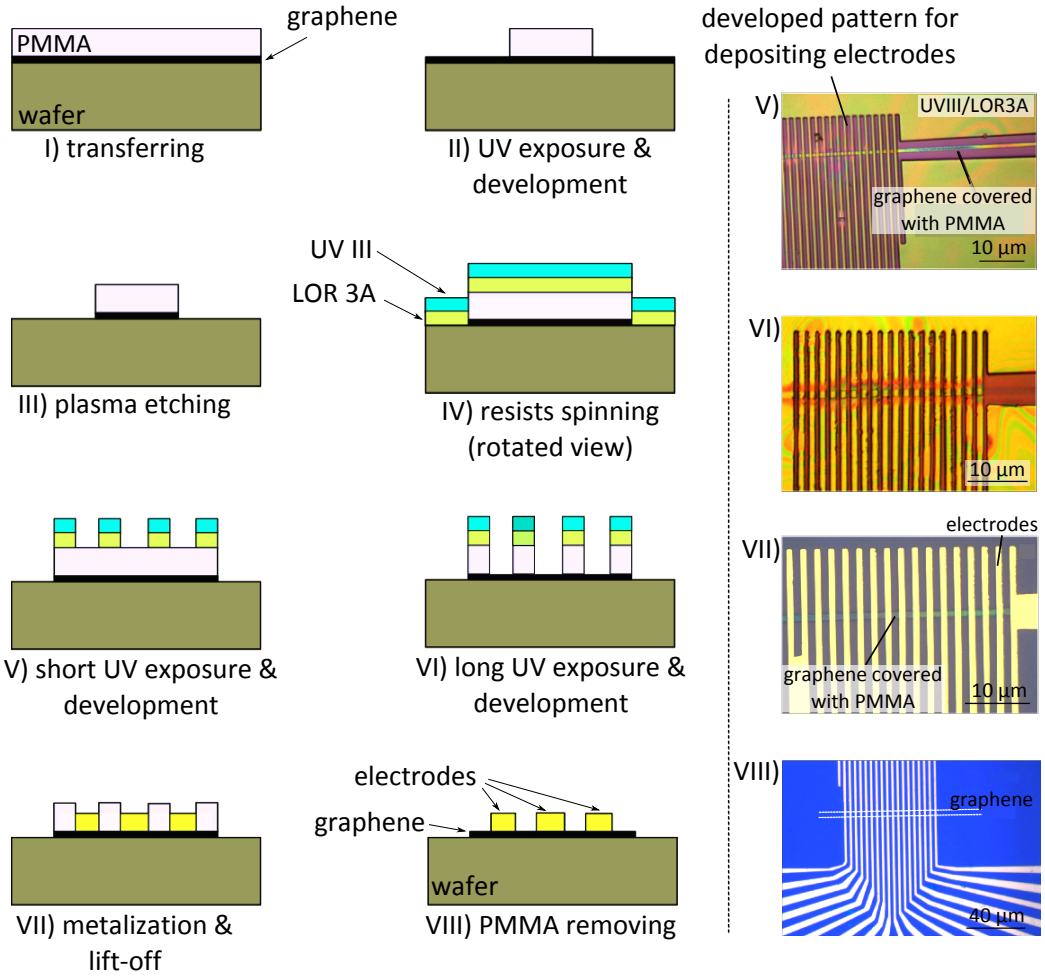

Figure 4.11: Process flow of the recipe developed for preserving the quality of the graphene
Different fabrication steps are demonstrated schematically in the left side and described in the text. Right: Optical micrographs taken at the steps V *through* VIII

Using this recipe and taking the advantages of deep UV lithography for mass production, we manage to fabricate a huge amount of the suspended devices in a single run. Figure Figure 4.12-a shows a cell of 18 suspended membranes. Each device can be electrically addressed separately using the gold electrodes at both sides. A focused SEM image on one of the devices is also shown in this figure. The borders of the membrane are curled up due to the residual fabrication stress. For the sake of comparison, we put the SEM images of similar samples reported in the earlier work with CVD graphene [140]. The graphene in their technique is patterned and transferred on the predefined trenches and thus there is no electrode. The average quality of the final membranes in this work is clear in the focused SEM image. Ripples, contamination and tears clearly exist in the devices which normally can happen during an unoptimized fabrication process. The lack of such defects in our sample is a measure of the success of the improved recipe.

We have reviewed the fabrication procedure as well as the achievements of this work before in Section 4.6 and Figure 4.8.

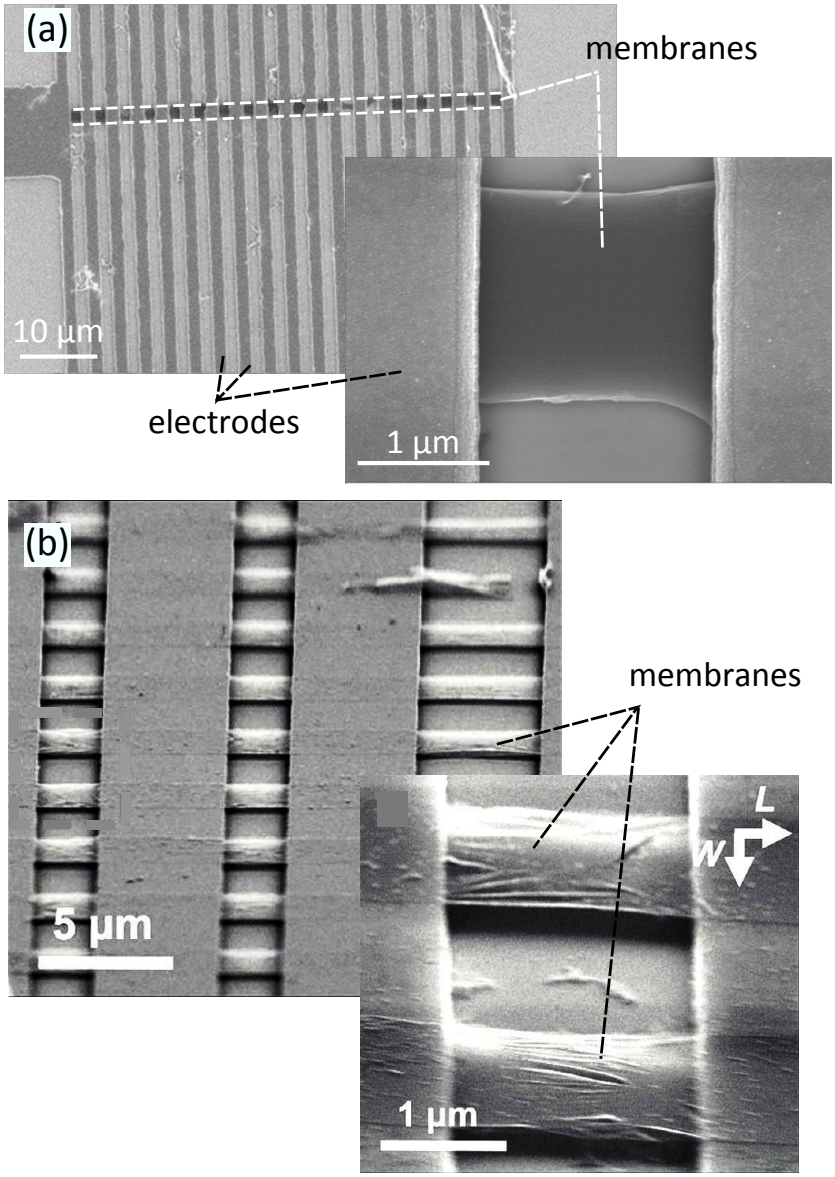

Figure 4.12: Final sample fabricated using the improved recipe a) SEM images of a series of the suspended graphene membrane at the final step of fabrication: Gold electrodes are used to support the suspended membranes. Inset figure focuses on one of the devices. b) Similar sample reported in the earlier work with CVD graphene [140]: As is clear in the focused image, the graphene membranes suffer from the ripples, contaminations and tears which probably have happened during the fabrication. These images are reprinted with adoptions.

4.7.3 Important Fabrication Considerations

For a successful fabrication and in order to realize high quality samples for measurements one has to consider following issues:

4.7.3.1 Supercritical Drying

Drying the sample after underetching and rinsing with DI water is an important challenge: by using a nitrogen gun or letting it dry in the atmosphere, surface tension of the water molecules exerts huge local force across suspended structure; such force could be large enough to break or cause the membranes to collapse. An example of such samples (partially collapsed) is shown in Figure 4.13-a.

To avoid this problem, an instrument called *supercritical dryer* is developed. Phase diagrams of materials are typically similar to what is shown in Figure 4.13-b. Normal drying of our samples corresponds to crossing the liquid-gas border of water which is marked by the green arrow in this figure; this is accompanied by the surface tension. However critical point dryer avoids crossing this border by passing through the supercritical region where the gas and liquid phases are not distinguishable. This path is marked by the red arrow and it does not cross any phase boundary. Carbon dioxide having an easily reachable critical point at 304.25 K and 7.39 MPa is one of the best fluids for supercritical drying.

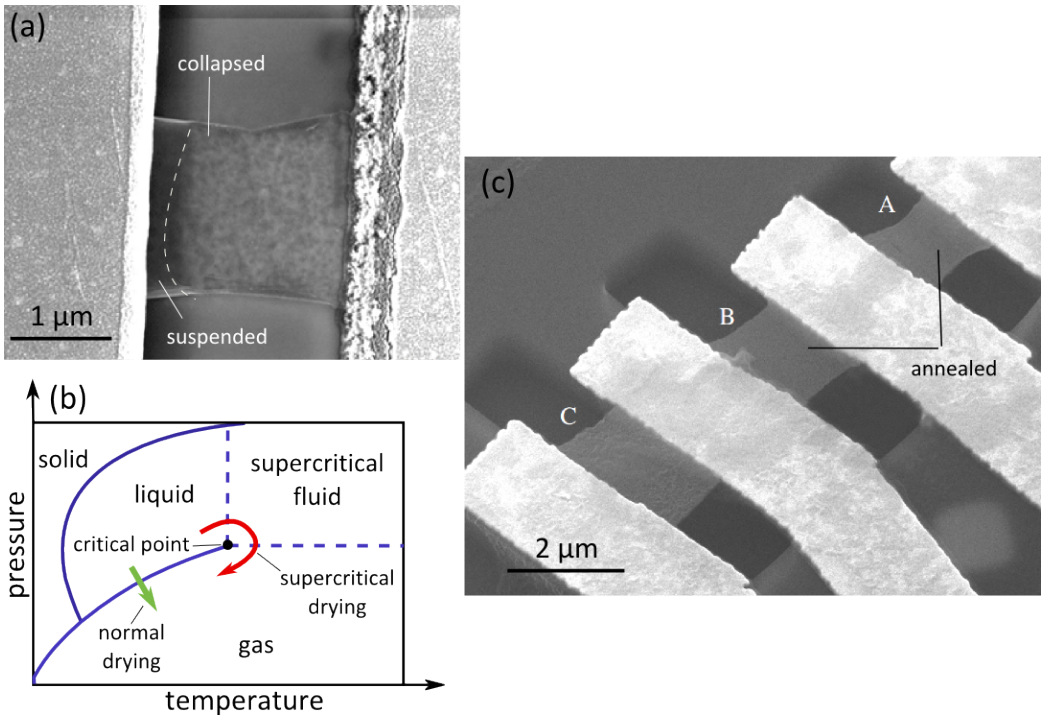

Figure 4.13: Important fabrication considerations
a) An example of the collapsed sample because of the failure in drying after underetching: Without using the supercritical dryer, surface tension of water causes the membrane to collapse.
b) Typical phase diagram of materials: shown by the red arrow, supercritical dryer leads the drying process in a way that avoids direct phase crossing (green arrow) and thus surface tension can be eliminated.
c) Effect of the current annealing on removing the process residuals: device A and B are current annealed, but C is left untreated for the purpose of comparison. The cleanliness of the two former devices is due to the removal of the process residuals in this technique. Image is adopted from [172].

4.7.3.2 Current Annealing

Right after underetching, the samples normally show very poor gate tunability with Dirac points very far from zero gate voltage (examples will be discussed in the next section). This is because a large amount of process residuals lay on graphene which tend to dope it; they can also work as scattering centers. *Oven annealing* at high temperature in the presence of active or inert atmospheres is one of the techniques to enhance the quality at this stage, which is typical for the supported graphene devices. A more efficient method known as *current annealing* [138] (also called *Joule heating*) has been used successfully for suspended devices [172]. In this technique, by passing a remarkably high *DC* current through the sample, one can heat up the graphene and thus remove the residuals. The obtained cleanliness depends on the density and duration of the current. This process should be done in very high vacuum, if not, oxidation of the graphene is likely to happen. Figure Figure 4.13-c shows the effectiveness of the current annealing in cleaning the samples.

The critical issue in this cleaning process is that one may destroy the device by applying too much current density. The maximum current that graphene can sustain before breakage not only depends on its geometries, but also on the presence of micro-scale defects like a tear due to fabrication. This is why the breakage moment of the devices is not easily predictable.

4.8 Measurements

In the previous section we reviewed the fabrication procedure of the devices. We see that by optimizing the fabrication recipe, it is possible to make high quality (as much as one can judge based on the SEM images) suspended graphene devices in large numbers. In this section the performance of these devices will be discussed. Field effect measurements is a technique to quantify the electronic properties of such devices. Then a frequency modulation scheme will be used to actuate and detect the resonance properties of the samples both at room and low temperature. Based on this data and employing the existing models, we extract the properties of graphene membranes.

4.8.1 Gate Dependence of the Resonance Parameters

Probing the conductivity of the devices as function of the gate voltage is the first measurement to be done after successfully fabricating the devices. Indeed the transistor characteristics provide information about the electronic properties of the membrane which are needed for the subsequent mechanical analysis, like the position of the neutral Dirac point and residual doping. In the series of the connected membranes (Figure 4.12-a, two electrodes electrically connected to both sides of a membrane can be used to address each membrane one by one. Such measurements can be done both before and after underetching for comparison. In this section, the results obtained from two typical samples will be discussed (which we will name *sample 1* and *2*).

Blue curve in the Figure 4.14-a shows an example of the two probe resistivity obtained after underetching and under vacuum, which corresponds to sample 1. We note that since graphene membranes are suspended, by applying the gate voltage, an electrostatic force is generated and attracts the membrane towards the gate. This may even collapse the membrane in a high gate voltage range. Thus unlike the supported samples, we have limited $|V_g| < 10\,V$ in all the measurements of suspended devices. The Dirac point is not present in the measured window which could be due to the doping during fabrication. We performed the current annealing cleaning technique on this device (Section 4.7.3.2) to remove such dopants: red curve in this figure corresponds to the measurements after such treatments. Now the Dirac point is very close to zero which is expected from a clean suspended sample. For later resonance measurements in frequency modulation technique, having a high derivative of the conductance versus gate voltage is of great importance to detect the signal (Equation 29); close to the Dirac point, the field effect curves exhibit the highest slope and thus it is important to have the Dirac point inside the measurement window. On the other hand, the absolute value of the resistance has increased a lot after current annealing; this could be partially because of the shifting of the Dirac point. However creation of some defects (oxidation) in the membrane during the annealing also can be the other reason. Note that since the signal measured in the FM technique is in the form of the current (not voltage) we do not care too much about the absolute value of the resistivity as it does not enter into the corresponding equation (Equation 29). This the reason that all the measurements shown here are done in two-probe configurations.

We compare the gate tunability of the resistance of sample 2 before and after underetching in Figure 4.15. Here and while the position of the Dirac point looks to be unchanged after the suspension, the absolute value of the resistance after suspension has increased a lot. It is believed that buffered HF does not affect chromium (which is in direct contact with graphene) and thus the contact resistance; so damaging graphene through the etching and/or super-critical drying (chemically or even mechanically) is the only explanation for this observation.

4.8.2 Gate Tunable Resonance Properties

At the next step and hooking the devices in the configuration shown in Figure 4.6-b, we start the resonance measurement of the devices. The important advantages of this combined actuation/detection scheme is reviewed in Section 4.5.3.2. The developed *LabVIEW VIs* sweeps the carrier frequency in a wide range of spectrum while the signal at the drain is measured by a SR830 lock-in (Stanford Research). A sharp increase in the amplitude can be a signature of the natural frequency of the membrane.

Electrostatic force generated by the applied gate voltage is an important parameter which can affect the stiffness and thus the resonance frequency of the system. In Figure 4.14-b and c one can find how the resonance frequency of sample 1 evolves with changing the backgate. Similar measurements have been performed on sample 2 with the results shown in Figure 4.14-b and c. Interestingly in sample 1 we can see two different resonance frequencies; even though

both of them disperse negatively in gate voltage, the gate tunability of the upper mode is stronger while the amplitude of the signal is lower; both these observations confirm that these frequencies correspond to two different vibrational modes. Similar behavior have been reported in exfoliated graphene before [58] which we have studied in Section 4.6. Two of the possible vibrational modes for such samples are schematically illustrated as insets in the Figure 4.8-bII which could be valid for our measured data.

Normally increasing the gate voltage leads to raising the tension in the membrane and thus the resonance frequency; this is referred to as *positive dispersion*. However the resonance frequencies of both of our samples show an opposite trend with gate which is referred to as *negative dispersion*. Similar trends have been reported in graphene membranes [58] and nanowires [173][174] before and is attributed to the mode softening as a result of the capacitive contribution to the energy of the resonator described below.

We have briefly reviewed the basics of the vibrating systems in Section 4.4. As we discussed there, the resonance frequency of a system depends on the square root of the effective spring constant (Equation 21). In our system, tension in the membrane (Γ) has an important effect on this constant which is related partially to the measurement temperature and gate voltage. Furthermore, depending on the fabrication process the membranes could be initially under stress corresponding to a constant residual tension (Γ_0). So the natural resonance frequency of the membrane can be described as [58]:

$$\omega_n(T, V_g) = \frac{1}{2L}\sqrt{\frac{\Gamma(T, V_g) + \Gamma_0}{\rho t w}}, \tag{31}$$

here L, w and t are the geometrical parameters and refer to the length, width and thickness of the membrane respectively. We note that ρ here is proportional to the total mass of the resonator *i.e.* mass of graphene plus mass of the process residuals on it; The later contributor normally is much larger than the mass of the clean graphene sheet and thus depending on the fabrication process, (ρ) could be tens to hundreds of times of the nominal density of graphene. Obtained in the basis of the elastic continuum theory [15][137][175], at zero gate voltage and room temperature, Equation 31 simplifies to:

$$\omega_n(V_g = 0) = \frac{1}{2L}\sqrt{\frac{\Gamma_0}{\rho t w}}, \tag{32}$$

here the Γ_0 and ρ are both unknown parameters and it is not possible to have an independent estimation of them. Equation 31 is built up considering that increasing the gate voltage always increases the tension in the membrane $\Gamma(V_g) > 0$ and thus is only valid for the positive dispersion case.

For a negative dispersion, the mode softening effect of the gate voltage can be modeled as the reduction of the effective spring constant. Then the resonance frequency can be described by [58]:

$$\omega_n^2(V) = \omega_n^2(V_g = 0) - \frac{1}{8\pi^2 m_{eff}}\left(V_g^{DC}\right)^2 \frac{d^2 C_g}{dz^2}, \tag{33}$$

here m_{eff} is the effective mass of the resonator. The term $\frac{d^2C_g}{dz^2}$ is the second derivative of the capacitance between the membrane and the backgate. We have fitted the resonance frequencies in the mapping of Figure 4.14-b with such a model considering the $\omega_n^2(V_g = 0)$, m_{eff} and $\frac{d^2C_g}{dz^2}$ as the fitting parameters. The results are shown as continuous lines. The parameters which we obtained by such fitting for the lower and higher resonances are listed in Table 6.

Table 6: Fitting results of the dispersion of the resonance modes of sample 1

	$\omega_n^2(V_g = 0)$ [MHz]	m_{eff} [gr]	$\frac{d^2C_g}{dz^2}$ [F/m^2]
higher mode	14.1	1.88×10^{-12}	0.019
lower mode	13.1	2.50×10^{-12}	0.016

By considering the graphene and wafer as a capacitor with parallel plates in which the whole graphene plate oscillates with small amplitude dz, we can have an estimation about the $\frac{d^2C_g}{dz^2}$ term:
$C = \frac{\epsilon_0 A}{z} \Longrightarrow \frac{d^2C}{dz^2} = \frac{2\epsilon_0 A}{z^3} = 0.03\,F/m^2$.

In this relation, $A = 4.18\,\mu m^2$ and $z = 135\,nm$ are the area of graphene and the vertical distance between the graphene and substrate respectively. $\epsilon_0 = 8.85 \times 10^{-12}\frac{F}{m}$ is the vacuum permittivity. This result is not very far from what we obtained from the fitting. The error could originate from our assumption that the graphene plate remains horizontal.

With such fitting we have obtained different $\frac{d^2C_g}{dz^2}$ values for the higher and lower modes which is consistent with assigning them to different vibration modes. The effective mass also is mode dependent; there could be different reasons for such observation including non-uniform loading of the mass on the membrane [58].

We note that the measured dispersion of the mode in sample 1 is not completely symmetrical in gate which is more visible in the single line sweeps in Figure 4.14-c. This is not consistent with the model (Equation 33) however the error is in an acceptable range. This is not the case for sample 2 (Figure 4.15-b) and because of the high degree of asymmetry, we failed to fit the dispersion.

By comparing the line sweeps of the samples depicted in parts *c* of the corresponding figures, one can find further discrepancies between the samples. The peaks corresponding to sample 1 (both higher and lower modes) are rather symmetrical which is not the case for sample 2 as we see a prominent shoulder in the left side of the peaks especially at high gate voltages. Such asymmetry can be attributed to the non-linear effects which will be discussed later. On the other hand, while the curves measured at positive gate voltages show a dip at resonance frequency, they show up as peaks at negative gate voltages. Just the other way around, measurements show peaks both for the negative and positive gate

voltages in sample 2. This discrepancy can be described considering the corresponding field effect curves and by recalling the statement for the current in the frequency modulation technique. Equation 29 shows that the measured current in FM technique scales with $\frac{dG}{dq} \propto \frac{dG}{dV_g}$ having the same sign. Unlike for sample 2, the Dirac point for sample 1 is located very close to zero and thus the change in the sign of the conductivity at the Dirac point leads to change in the sign of the current for sample 1. Increasing amplitude of the signal by gate voltage also can be described considering the $|V_g|$ term which appears in the Equation 29.

The concept of quality factor in resonating systems is introduced and discussed in Section 4.4.2. In the frequency modulation scheme, the quality factor can be easily calculated from the zeros of the $F(\omega_c)$ (Equation 30). We have done such kind of fitting for the curves in Figure 4.14-c and Figure 4.15-c, the results are summarized in parts *d*. For the sample 1, the quality factor is highest near zero gate and reduces as the $|V_g|$ is swept away from zero. This trend is very similar to the dispersion of the resonance frequency in this sample proposing the same origin. The mode softening caused by the gate voltages tends to increase the capacitance by reduction the distance between the plates; as a result the current passing through the sample increases and the resultant increased Joule heating accounts for increasing the dissipation and reduction of the Q factor. We have found a quadratic relation between the quality factor and V_g in this sample. The gate dependence of Q for the sample 2 is more complicated: Similar to sample 1, reduction of the gate voltage in a window at the center is accompanied by enhancements in the quality factor. This can be explained in similar terms as sample 1. However following minimas around $|V_g| \approx 6\,V$ we see it increases again by increasing the gate voltage. The origin of this observation is not totally clear.

Example of such fitting in the absence or presence of the nonlinearities are presented in Figure 4.16.

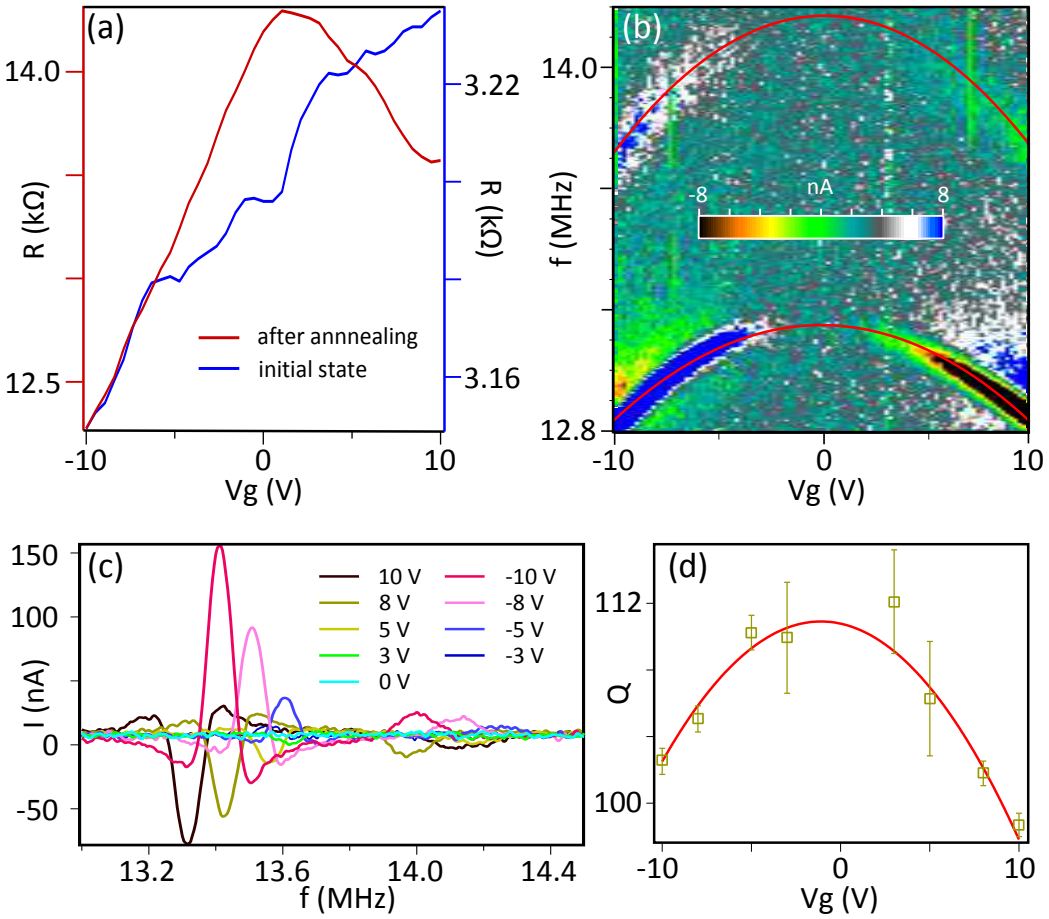

Figure 4.14: Room temperature electrical and mechanical measurements of sample 1
a) Two probe gate dependence of the resistance before and after current annealing: Initially shifted Dirac point returns back close to $Vg = 0\,V$ after current annealing.
b) Gate dependence of the mechanical resonance frequency: This sample shows two resonance frequencies corresponding to two different oscillation modes, both of them disperse negatively with the gate voltage. The solid lines are fits with the model of Equation 33.
c) Frequency sweeps at different gate voltages: The curves are not totally symmetric around $Vg = 0\,V$. The vertical shifts between the curves are removed.
d) Extracted quality factor of the resonances (lower mode) shown in (c) as a function of the gate voltage: The solid line is the fitting with a quadratic function.

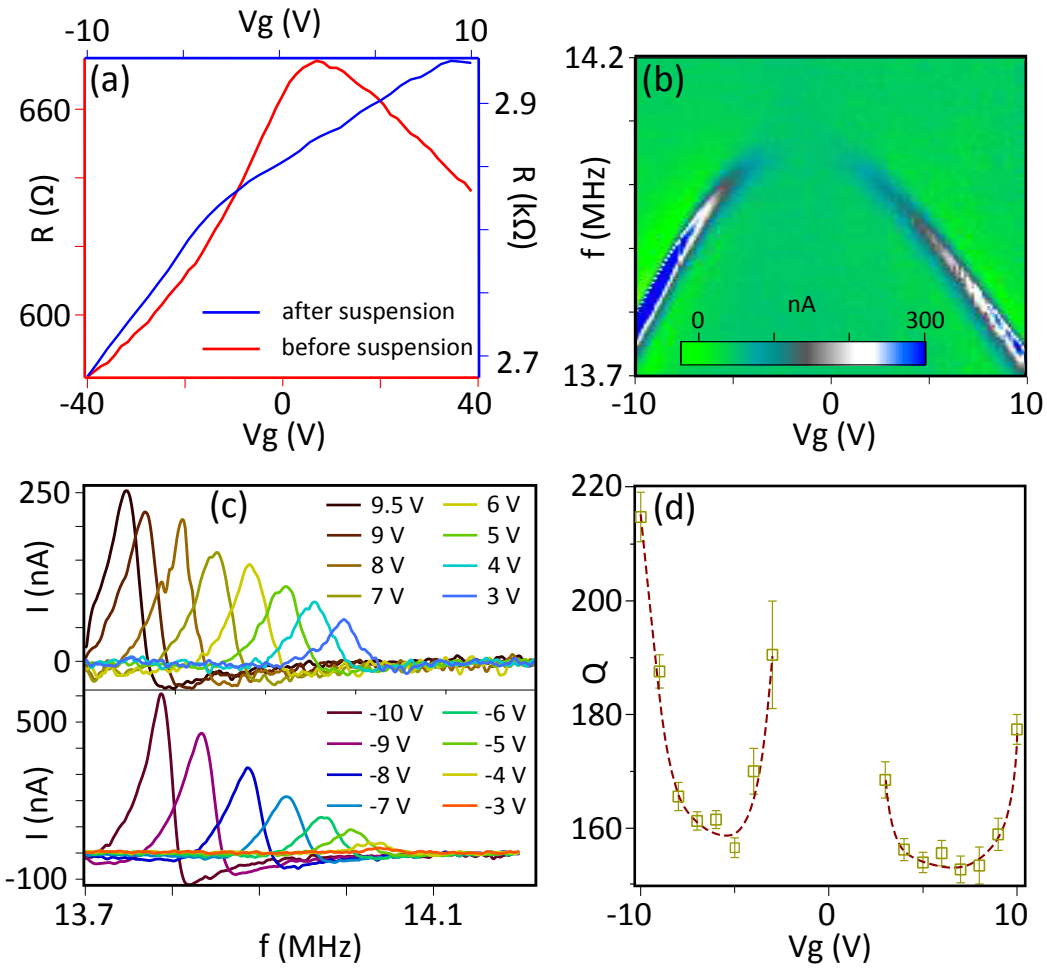

Figure 4.15: Room temperature electrical and mechanical measurements of sample 2
a) Two probe gate dependence of the resistance before and after under etching the sample
b) Gate dependence of the resonance frequency of the sample: The negative dispersion is remarkably asymmetric with respect the zero gate voltage and thus it is not possible to use the same fitting function of the sample 1 (Figure 4.14-b).
c) Line cuts at different gate voltages of figure (b): The vertical shifts between the curves are removed.
d) Extracted quality factor of the curves in (c) as a function of the gate voltage: The dashed lines are guides to the eyes.

4.8.3 Temperature Dependence of the Resonance Properties

Room temperature resonance properties of the samples were discussed in the previous section. We analyzed the effect of the gate voltage on the resonance frequency as well as the quality factor of the suspended samples. In this section, we use another knob -temperature- to measure the resonance properties of graphene based NEMS. The data presented here are obtained from sample 1.

We set the gate voltage to -10 V and measure the sample at different temperatures while cooling. Figure 4.16-a shows the results of this course. By cooling the sample, the resonance frequency shifts to the higher values. This is accompanied by increasing the resonance peak intensity and reduction of its width. The up-

shift in the resonance can be understood by considering the increased tension in the membrane: by lowering the temperature, the contraction of the electrodes leads to increasing the tension (stress) in the membrane which accounts for raising the resonance frequency. The relation between the tension and resonance frequency is given in Equation 32. Even though the term *sharpening* can be used to describe the combination of the enhancement of the signals and reduction of their width by cooling, but they have different origins: by cooling the sample, the mobility of the graphene increases mainly due to reduction in the phonon scattering. This improves the gate tunability of the carriers and thus $\frac{dG}{dq}$; as a result the signal improves (see Equation 29). The other observation (shrinking the width of the peaks) is identical to increase in the quality factor. There are some reports showing that high tension in the devices (due to cooling for example) is accompanied by higher quality factors [176]. The details of such dependency is not fully understood [177] but it seems it is the case for the devices presented here.

In Figure 4.16-b we see an example of the fitting of the resonance peaks which is obtained at 275 K. This peak (like others measured at high temperatures) is symmetrical an can be fitted easily by the corresponding model (Equation 29) to extract the quality factor. The increased tension in the membrane at lower temperatures is accompanied with an asymmetry in the signal; furthermore the signal captured at back and forth sweeps are completely different (Figure 4.16-b) which is the signature of the presence of non-linearity [133][178]. In this case it is not possible to have a quality fit for the whole signal range and thus only half of it is fitted. The effect of the frequency sweeping direction on the non-linearity affected resonance signals is schematically represented in Figure 4.16-d. Increasing the intensity of the non-linearity prevents the signal to develop by limiting the amplitude of the peak. This is the reason why the intensity of the signal at 30 K does not follow the trend we see for the other signals on the left.

In this experiment, we managed to cool down the sample down to 13 K. It died very rapidly after this point perhaps because of the high level of stress. The width and amplitude of the signal measured at this temperature do not follow the trend from the other signals and it seems the breakage of the device has already started at this temperature.

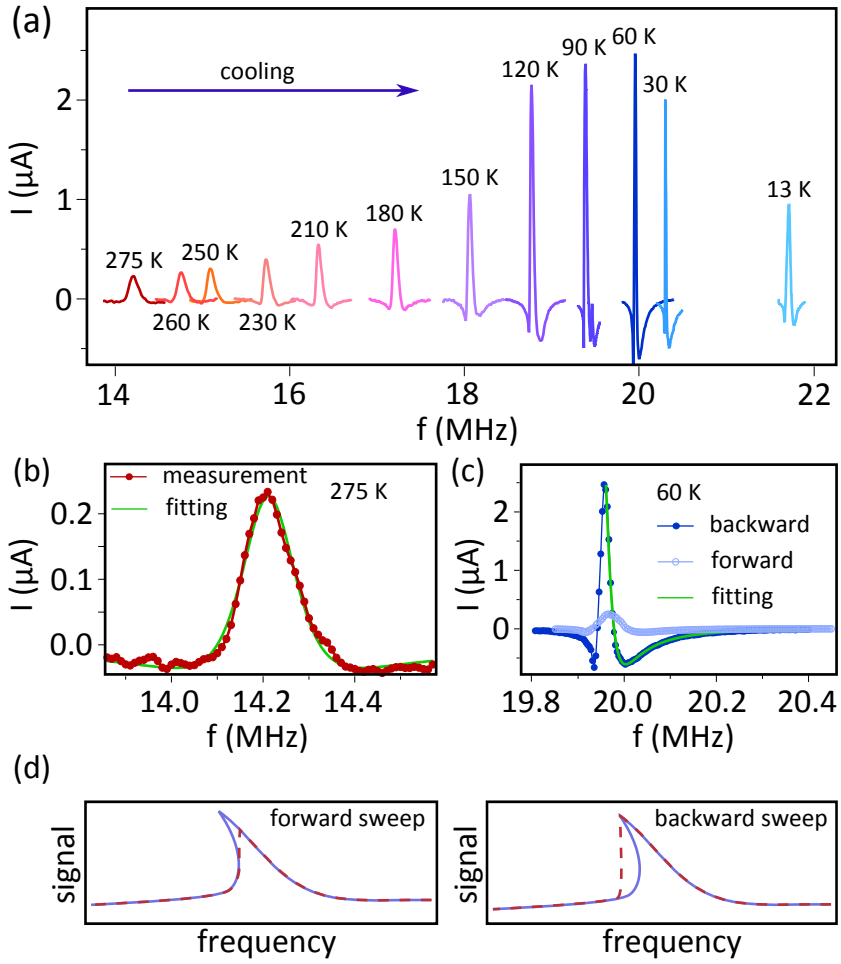

Figure 4.16: Temperature dependence of the resonance properties of sample 1
a) Resonance signals at different temperatures: This measurement is done at $V_g = -10\,V$.
b) Fitting the signal at 275 K with the model of Equation 30
c) Non-linearity in the signal measured 60 K: the measurements at backward and forward frequency sweeps are very different in terms of the amplitude which is the signature of non-linearity in the system. The signal follows the model only in backward sweep and half the way.
d) Schematic representation of the signal that can be measured in the backward and forward frequency sweeps in the presence of non-linearities

The data we obtain by fitting the signals while cooling are plotted in Figure 4.17. In part *a* we see the evolution of the resonance frequency with temperature. The slope is very fast at the beginning while it approaches a saturation regime close to zero. We have fitted the data with a polynomial function shown as a continuous red line which will be used for later analysis. The data at 13 K is not considered in this fitting.

The estimated quality factors at different temperatures are depicted in Figure 4.17. Cooling the sample is accompanied by increasing the quality factor as we see in the inset figure. The data at 13 K is skipped at this plot. Like the resonance frequency, the quality factor is strongly temperature dependent at higher temperature however the dependency becomes weaker when the sample is very

cold. This is why the reports normally split the *Q(T)* in high and low temperature regimes (see the plotting shown in Huttle's report [179] in Figure 4.7-f.).

A dependency of $T^{0.33}$ [140] to $T^{0.36}$ [179][138] is proposed for the inverse quality factor of the carbon nanotubes and graphene devices at low temperatures while much stronger dependency of $T^{2.3}$ is observed at high temperatures [140]. Together with our data, we plot the $T^{0.33}$ and $T^{2.3}$ lines which seem to describe the behavior of our data also.

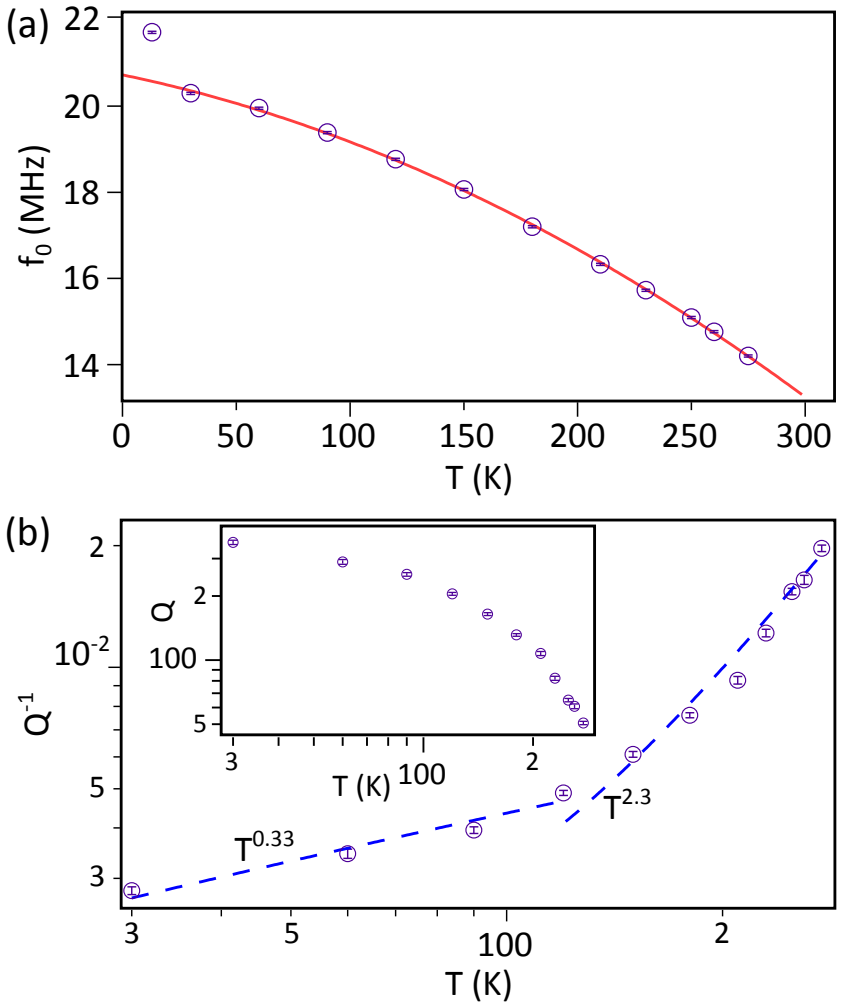

Figure 4.17: Extracted parameters from the temperature dependency of the resonance properties in Figure 4.16
a) Resonance frequency as a function of temperature: The solid line is the fitting with polynomial function.
b) Inverse quality factor (Q^{-1}) as a function of temperature: the dashed lines show $T^{0.33}$ and $T^{2.3}$ behaviors reported for nano-scale resonators at low and high temperatures respectively [179][138][140]. Inset shows the quality factor versus temperature.

4.8.4 Coefficient of the Thermal Expansion of Graphene

By cooling the sample, the thermal expansion/contraction of the electrodes, silicon wafer and graphene alter the tension in the membrane which results in changing the resonance frequency shown in Figure 4.17-a. The linear coefficient

of the thermal expansion (CTE, denoted by α) for gold and silicon have been studied extensively before [180][181][182] (Figure 4.18-a) meaning that by tracing the evolution of the resonance frequency at low temperature, one can calculate the remaining parameter: CTE of graphene. At least two theory papers have calculated the CTE for graphite and graphene [183][57] predicting negative CTE due to the out of plane vibrations of the atoms. Bao *et al* [184] first investigated the CTE of suspended graphene experimentally in the temperature range of 300 K to 400 K obtaining the value of $\alpha \approx -7 \times 10^{-6}\,K^{-1}$ at 300 K. Similar results obtained later by Chen *et al* [138] in a small temperature range (250 K to 295 K). However the most important work in this field is done by Singh *et al* [58] using exfoliated graphene. Here we use the model presented in this work to study the CTE of CVD graphene in our system.

As the device cools down from room temperature, the suspended gold electrodes start to contract which tends to increase the tension in the membrane; however the contraction of the silicon wafer and expansion of the graphene (due to its negative CTE) mitigate the tension. This can be described as:

$$\epsilon_{mem}(T) = \epsilon_{gr}(T) + \epsilon_w(T) - \frac{w_e}{L}\epsilon_e(T). \tag{34}$$

In this relation, ϵ_{mem}, ϵ_{gr}, ϵ_w and ϵ_e denote the temperature dependent strain in the membrane (clamped graphene), free graphene, wafer and electrodes respectively. Note that relation $\frac{d}{dT}\epsilon_{w,e,gr} = \alpha_{w,e\,gr}$ exist between the temperature induced strain and the corresponding CTE. w_e and L are geometrical parameters which represent the width of the electrodes and the distance between them. For the working temperature, we can find data about α_w and α_e in literatures which are replotted in the main panel of Figure 4.18-a. In order to calculate the $\epsilon_{gr}(T)$ information about $\epsilon_{mem}(T)$ is needed:

$$\epsilon_{mem}(T) = \frac{\Delta\Gamma(T)}{w_e t E_{gr}}. \tag{35}$$

In this equation which can be obtained from the strain-stress relation in the elastic limit $\Delta\Gamma(T) = \Gamma(T) - \Gamma(T = 300\,K)$ shows the temperature dependent alternation of the tension. This can be estimated considering the resonance frequency behavior in temperature and using the Equation 32. Note that $E_{gr} = 1\,TPa$ [15] is the Young's modulus and t=3.3Å corresponds to the thickness of monolayer graphene. Using these relations and assuming uniform expansions for all the materials, we can calculate α_{gr} using:

$$\alpha_{gr}(T) = -\frac{8L^2\rho}{E_{gr}}\omega_n\frac{d\omega_n}{dT} + \left(-\alpha_w(T) + \frac{w_e}{L}\alpha_e(T)\right). \tag{36}$$

The result of such calculation is plotted in Figure 4.18-b. For the sake of comparison, this calculation is done considering constant CTE for gold and silicon also which is plotted as a broken line. The results of the previously published theory work (Mounet [57]) as well as 2 measurement results for exfoliated graphene (Singh #1 and Singh #2 [58] are also replotted.

Our measurements show that CTE for CVD graphene is not very different from the exfoliated one, both are negative in the measured temperature range. However our data matches well with the prediction of Mounet *et al* both at high and very low temperatures; while Singh's results deviate from the red curve at high temperature, they are close while cooling. From their paper, it is not evident what values (constant or temperature dependent and from what source) have been used as the α_w and α_e, however comparison of our continuous and broken lines shows that considering temperature dependent values is very important.

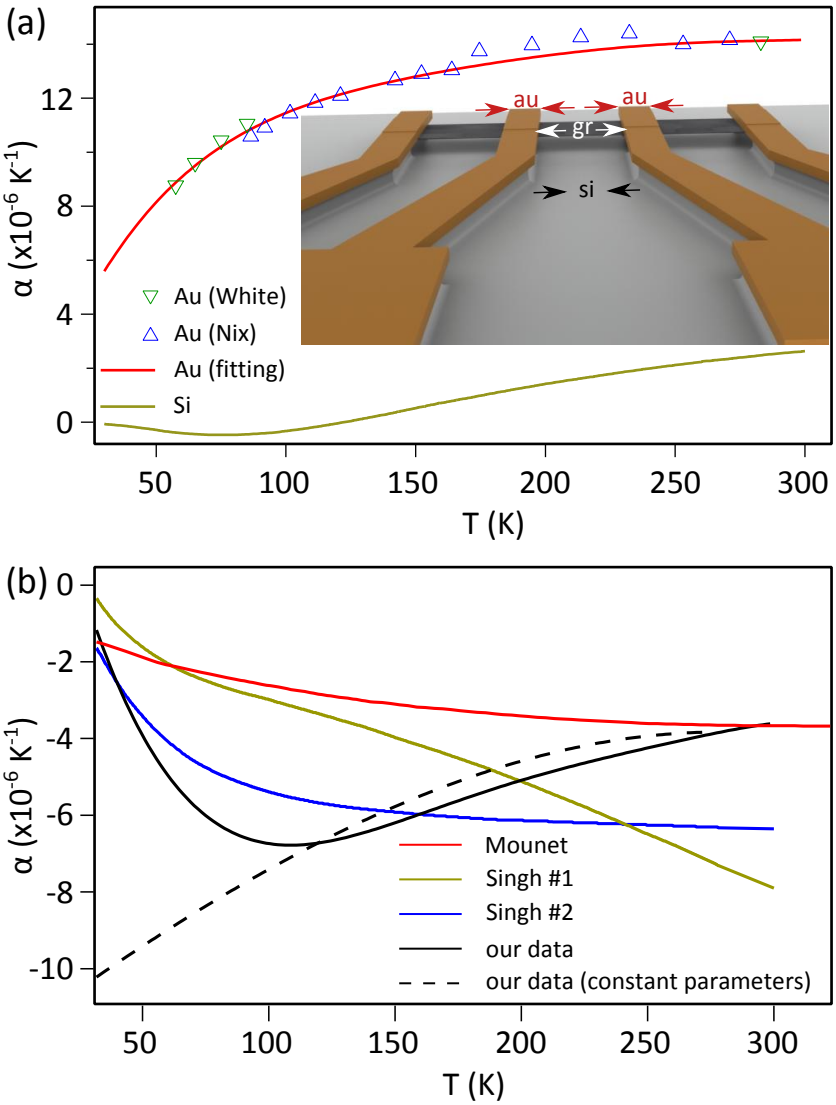

Figure 4.18: Temperature dependency of the coefficient of thermal expansion (CTE, α) of graphene
a) CTE of gold and silicon used in the calculation of the data in (b): While Au (White) and Au (Nix) refer to the data reported in [180] and [181] respectively, the CTE for silicon are reprinted from [182]. Red line is the polynomial fit for both sets of the gold data which we use to calculate the CTE of graphene.
b) Extracted CTE of graphene and comparison with the previous theoretical (Mounet2005) [57] and experimental (Singh2010 #1 and #2) [58] works. While the temperature dependency of the CTE of silicon and gold are not considered in the calculation for the dashed black line, the solid black curve is obtained by including these effects.

4.9 Conclusion

Outstanding mechanical properties of graphene makes it a promising material for nano-electro-mechanical applications. There have been some attempts to characterize graphene based NEMS before mainly with exfoliated graphene. Obtain-

ing very large graphene sheets is an important advantage of CVD graphene for mass production of nano-electro-mechanical devices. However our understanding about the performance of CVD graphene in such applications is limited because of the lack of studies. In this chapter we tried to analyze such systems.

Fabrication of NEMS with CVD graphene is challenging compared to the exfoliated one, since at least one more step is required to pattern very large graphene sheets into smaller segments. Such handling of graphene is normally accompanied by mechanical and electrical defects. In this chapter, we introduced an improved fabrication technique to make a large array of suspended grapene devices. This recipe is developed based on protecting the surface of graphene throughout the fabrication of the sample with a layer of resist; this covering layer not only supports graphene minimizing the risk of mechanically defecting, but also prevents deposition of the contamination during the fabrication. Comparison of the final device with already reported similar samples confirms the efficiency of the technique.

Electrical measurements show that to some extent, current annealing can remove the process residuals on the graphene membrane and improve its characteristics for NEMS detection. This process is largely used in similar applications however being dependent on crystalline defects, its efficiency is sample dependent.

At the next step and by employing the high efficiency frequency modulation technique, we managed to excite the membranes into resonance and detect it. The gate dependence of the oscillation properties have been under focus. We see that besides the main one, the resonators can show other resonance modes corresponding to different shapes. We have collected and employed the developed models to extract the important parameters affecting the dispersion of the resonance. Gate dependence of the quality factors is also probed.

Cooling the devices can also tune their performance. Here we see that the temperature dependent expansion/contraction of different components of the devices leads to increasing the stress in the membrane which accounts for upshifting the resonance frequencies as well as improving the quality factor. We noticed that cooling can increase the non-linear damping effects in the oscillation of the devices.

By tracing the resonance frequency of the sample and considering the low temperature mechanical properties of the other materials involved in the system, the coefficient of the thermal expansion of the CVD graphene is estimated for the first time. Comparing our results with theory and similar reports with exfoliated graphene, we see that at both high and very low temperatures our data matches well with predictions.

From these first investigations of CVD graphene-based NEMS, we can conclude that CVD graphene exhibits similar performance for NEMS as the exfoliated one, which makes it a good candidate for large scale integration of graphene NEMS.

General Conclusion and Perspectives

Graphene on h-BN and suspended graphene devices are the two systems which we have probed in this work. They look rather different topics nonetheless they share a common idea: Optimizing the environment of the graphene in order to promote its performance in application. However suspended graphene devices have other functionalities as nano-resonators. We started the topic of graphene/h-BN heterostructures by describing the fabrication process of such devices. The advantages of h-BN flake for supporting graphene are well described and probed by using AFM technique. The important feature of the fabricated devices is that the graphene on h-BN and graphene on silicon samples are located very close to each other. This gives the opportunity to directly compare the influence of the substrate on the measured data. Typical resistivity versus gate voltage measurements confirm the efficiency of such stacking. Longer mean free paths of the carriers obtained in graphene/h-BN devices is attributed to the reduced amount of the elastic scatterers which can be justified considering the crystalline quality of the h-BN surface. This was well studied and confirmed experimentally in the past. However the influence of the h-BN on the phase coherent transport in graphene which relies on the inelastic scattering events have never been probed before; It was done through weak localization measurements in different temperature and carrier density regimes. The data show that h-BN not only improves the mean free path of the electrons but also the coherence. This was the most important message of chapter 2 of this thesis. We also measured how intervalley and intravalley scattering mechanisms are dependent on the quality of the substrate.

A method for *in-situ* fabrication of graphene/h-BN samples is the achievement, introduced in this thesis. Considering the superior properties of h-BN flakes as a support for graphene, techniques to improve the efficiency of graphene/h-BN heterostructures is a great focus of current research. Here directly growing graphene (instead of transferring) on h-BN flakes is a potential technique to minimize the fabrication difficulties and improve the electrical performance of graphene. Such methods are in the initial stages now as the performance of *in-situ* grown graphene/h-BN samples are not comparable with those realized by transferring. Necessity for the presence of a catalyst is the greatest hindrance for the development of such techniques; efforts trying to skip it normally lead to the formation of small graphene flakes even after long growth processes. In our proposed method, for the first time, we resolve limitation by letting the precursors an indirect access to the catalyst. In a CVD method, methane molecules are decomposed on the normal copper foil and the resultant atoms migrate on top of the pre-exfoliated h-BN flakes to form graphene layers. Raman analyses show that the graphene follows the orientation of the substrate. We have exten-

sively probed the electrical performance of such samples and compared with typical transferred graphene/h-BN devices. The advantages of our technique in reduction of the charged impurities lead the electrical performance of the *in-situ* grown devices to outperform the transferred graphene, close to the Dirac point regime. We have measured a carrier mobility of $\approx 20,000 cm^2/V.s$ which is the highest reported among the other *in-situ* grown graphene/h-BN devices.

CVD graphene based nano-electro-mechanical systems is another topic which is covered in this thesis. We have worked on the fabrication of such devices and an enhanced fabrication recipe is developed. Comparison of the devices made in this technique with reported similar results in the literature qualifies the efficiency of this recipe. After analyzing the transport properties of such devices in the static mode, by externally exciting the membranes, we probed their mechanical performance. Room-temperature measurements show how the resonance frequency and quality factor of such devices are tunable by electrostatic forces. We assess the low temperature performance of such devices and the effect of the thermal stress in the membranes. Such measurements provide enough data for us to estimate the coefficient of the thermal expansion of the CVD graphene, for the first time in this work.

5.2 Perspectives

Our weak localization measurements clearly confirm that having an h-BN buffer layer in between graphene and silicon wafer leads to the improvements in the phase coherence length of the charge carriers. However the origin of this observation is not clear for us. What we gain by using h-BN buffer layers is the reduction of the elastic scattering events while the phase coherence of the carriers can be destroyed by inelastic scattering mechanisms. For the next step, systematic study and measurements should be performed to figure out the background physics. Some magnetic impurities lying at the surface of silicon which are covered with neutral h-BN flakes could be a reason for this. As another perspective, one can think about the proximity induced superconductivity in graphene/h-BN systems. The already proven advantages of h-BN in enhancing the mean free path and phase coherence of the carriers can account for probing the interesting physics of such systems *e.g.* multiple Andreev reflections.

In the line of our proposed *in-situ* graphene/h-BN growth technique some important *next steps* can be paved: The Raman and electrical measurements show that the grapene grown here suffers from a high population of crystalline defects which leads to the degradation of its electrical performance at high carrier concentrations. The growth parameters are needed to be fine tuned to increase the quality of the grown graphene at the next step. In this way, increasing the growth temperature as well as an annealing step right after finishing the growth which increases the mobility of the carbon atoms on top of the h-BN surface look to be efficient modifications. As another target, we propose to utilize this technique for *in-situ* fabrication of the sandwitched h-BN/graphene/h-BN structures. Our observations of grown graphene on the h-BN layers below the surface of the flake support this idea.

In the field of graphene based NEMS, several important experiments have been reported probing different aspects of such systems. As we discussed in the relevant chapter, very high mechanical resonance frequencies are expected for graphene nano-resonators considering its low mass and the possibility of withstanding very high internal mechanical stresses. However the bests samples reported in this field so-far show a resonance frequency as high as 250 MHz. Increasing the fabrication quality and removing the residual mass on the membrane as well as improving the device to induce an external mechanical stress in graphene are the techniques to raise the resonance frequency as well the quality factor of such devices. Like the case of graphene/h-BN, higher electrical performance of suspended graphene devices due to removing the substrate-related perturbations can lead to a good platform for probing the physics of the Josephson junctions in this system. Coupling the mechanical properties of the device to the phase coherence transport phenomena *e.g.* Josephson current or Fabry-Pérot oscillations are also on the horizon of such studies.

Annex 1: Superconductivity Proximity Effect in Suspended Graphene

6.2 Introduction

Unprotected two-dimensional electron gasses in graphene are very sensitive to the environmental conditions. The methods for immunizing the electrical transport performance of graphene in applications have been addressed in the previous chapters. However such easily accessible electrons can be utilized in making hybrid materials based on graphene *i.e.* by putting different materials with diverged properties in its vicinity, new properties can be induced in graphene. One of the most remarkable examples in this regard is the proximity induced superconductivity in graphene which was realized in 2007 [16]; They show that by depositing superconductive electrodes on, bipolar gate tunable supercurrent can follow in graphene. Josephson junction made in this manner if comes together with the ballistic transport expected in high quality graphene, could be an attractive platform to understand the two-dimensional Dirac-fermion physics and to explore quantum interference effects *e.g. Andreev bound states* in such systems.

Suspending graphene to get rid of the parasitic effects associated with the substrate is a potential way to reach high quality graphene. This technique looks even more interesting in making such hybrid systems since one can think about coupling mechanical vibrational properties of graphene with induced superconductivity. Furthermore by such coupling, we can get rid of some thermal losses in oscillating graphene which is accompanied by the normal current used in actuation/detection schemes; thus a vibrating system with higher quality factor is predictable.

Underetching graphene in the way described in Section 4.7.1 is only feasible with few noble metals like gold which do not show superconducting properties at low temperatures. This is because HF which is used for etching silicon effectively attacks and etches most metals. An interesting effort is done by my colleague, Adrien Allain [91] before my arrival to this lab (Figure 6.1). In his technique, small isolated tin islands are evaporated on graphene membrane suspended over gold electrode; Thus at low temperatures, these islands become superconductors and make the whole graphene a superconductor by the proximity effect. Deposition of the tin islands on graphene effectively dopes it and the Dirac point shifts outside the small gate voltage range we can sweep in the case of suspended graphene. Thus the gate tunability of such devices is rather low which makes detection of the vibration very difficult in application. This is the most important disadvantage of this technique. Also due to the deposition of

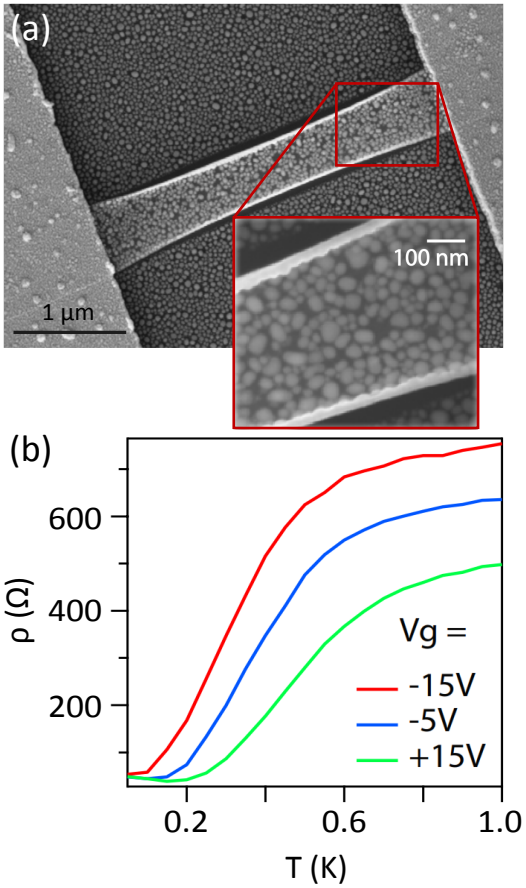

Figure 6.1: Suspended hybrid tin-graphene devices, fabricated and measured by A. Allain [91]
a) SEM image of the graphene membrane decorated with isolated superconductive islands
b) Sharp drops in the resistivity wile cooling confirm that the device falls into the superconducting state.

tin, the effective mass of the membrane is much higher than the bare graphene which eliminates most of the advantages of graphene in NEMS application.

During the last year of my PhD, I examined new fabrication recipes applicable with superconducting materials. The common idea in all these methods is realizing superconducting electrodes with a very short gap and then transferring a graphene membrane on top of them. Through the rest of this chapter, we I review the fabrication methods and some of the results obtained in this topic.

6.3 Oxygen Plasma for Etching Suspended Graphene Sheets

As the first recipe and after fabricating superconducting electrodes, a large graphene sheet is transferred on them. An step of e-beam lithography followed by oxygn plasma etching is necessary afterwards to pattern graphene into a ribbon of few micron width. Figure 6.2 shows the SEM illustration of the first sample I made in this way. It was successful in terms of realizing a suspended graphene, but as is clear that graphene suffers from contaminations (probably due to re-deposition of the process residuals) and a small amount of miss alignment. Also the surface of the electrode is not smooth enough to end up with a good interface and low contact resistance which is crucial for inducing superconductivity.

At the next step, we tried to optimize our fabrication technique. Figure 6.3 shows the next generation of such devices. An SEM image of the Al/Pd elec-

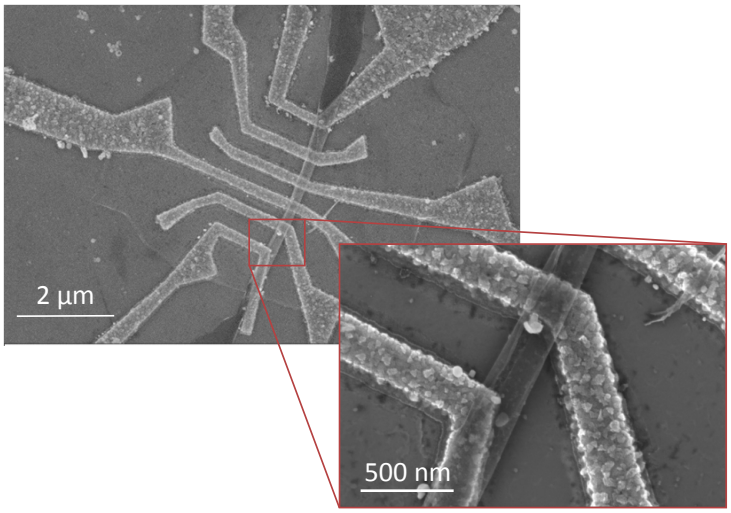

Figure 6.2: The first sample we made with transferring graphene on superconducting electrodes Fabrication of such samples are done by transferring large CVD graphene sheet on pre-defined Al superconducting electrodes. An step of e-beam lithography followed by oxygen plasma is required afterwards to pattern graphene into the ribbon.

trodes before transferring graphene on it is shown in *a*; One can confirm that the surface roughness of these electrodes are enhanced compared to the previous sample. Also we have reduced the gap between the electrodes, the minimum distance is now almost 100 nm. Panel *b* shows the graphene after transferring on the electrodes and patterning. Short graphene bridges suspended on the electrodes are realized. Dark areas correspond to the surfaces which are covered by PMMA. A focused image of the shortest junction after removing PMMA layer is visible in panel *c*. Graphene looks to be clean. However the field effect measurements (Figure 6.3-*d*) of such samples are not promising. Clear there, the filed tunability of the resistance is rather weak. This could be due to the screening effects of the electrodes which could be very remarkable for such short junctions or because of some scaling phenomena which is addressed in [92]. The third reason for this poor mobility could be the damaging effect of the oxygen plasma: the bottom surface of the suspended graphene was not protected during the fabrication, thus the oxygen ions in the plasma etching step can effectively damage the graphene and reduce its quality. On the other hand, the two probe resistance measured here is more than 20 kΩ which is rather high to obtain a good *bleeding* of the superconductivity into the graphene. Poor coupling of the graphene on pre-defined electrodes (*e.g.* due to the oxidation of Al) is a possible explanation.

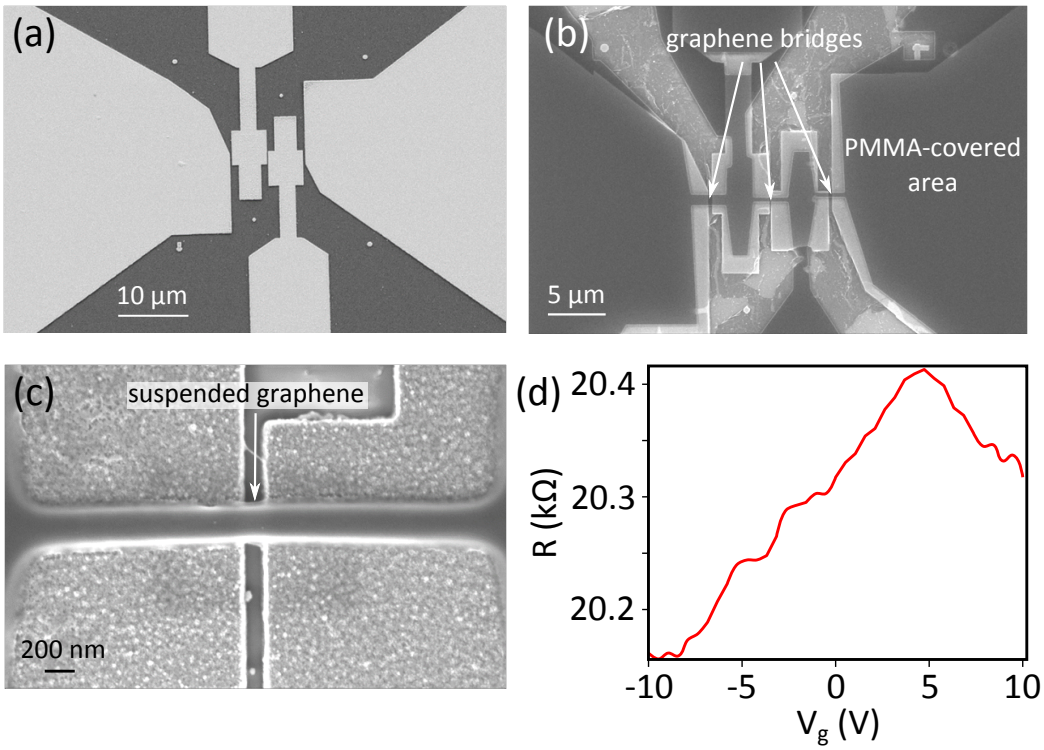

Figure 6.3: Second generation of our graphene on superconducting-lectrode devices
a) Superconducting Al/Pd electrodes are deposited at the first step.
b) CVD graphene covered with PMMA layer is transferred on the electrodes and is pattered.
c) By removing the PMMA layer, the sample is ready for the measurements.
d) Two-probe resistance versus gate voltage measurements of this sample shows the graphene ribbon is of low transport quality.

The simplest way to reduce the contact resistance is to increase the contact surface. It took a longtime for me to optimize the e-beam lithography step to fabricate very large electrodes with very small gaps in between (Figure 6.4). Now at each step of lithography, we can make a large number of devices (similar these figures) to increase the fabrication yield. Furthermore, by enhancing the evaporation technique, the surface roughness of the electrodes has been greatly enhanced.

Now by successfully fabricating such electrodes and in order to cope with the unfavorable side effects of the plasma etching, we took several approaches.

6.4 Focused Ion Beam for Patterning Graphene

As the first approach, we replaced the plasma etching step with *Focused Ion Beam (FIB)* etching. Compared to the oxygen plasma, high energy ions which are used in FIB technique are more directional; thus the possibility of damaging the backside of the graphene is greatly reduced. On the hand, the FIB technique is more time consuming than plasma etching and the gallium ion beam which is

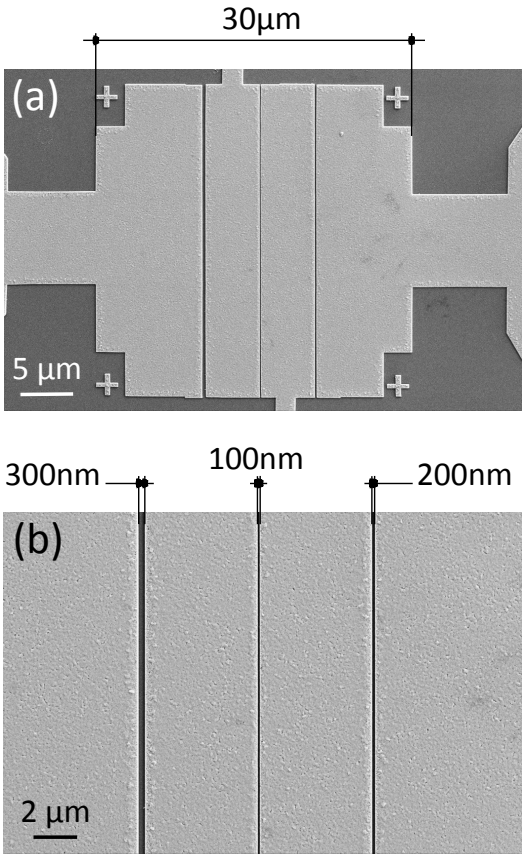

Figure 6.4: Optimized design and deposition of the electrodes
Increasing the area of the contact pads as well as reducing the roughness of the electrodes (by optimizing the deposition parameters) are the two important modifications in these samples in comparison to the previous samples (Figure 6.3) to minimize the contact resistance of the devices.
SEM image in panel b focuses on a small area in a.

used can easily contaminate the surface of the graphene. The latter problem can be solved by protecting the surface of graphene with a PMMA layer.

Figure 6.5-a shows how focused ion beam can be employed for cutting suspended graphene. Examples of the devices etched in this way with a PMMA protective layer are revealed in Figure 6.5-b. After removing the PMMA with acetone, we can have very short and suspended junctions like what we see in Figure 6.5-c. At the next step we started electrical measurements. Our data shows that such samples suffer from high gate-leakage pointing out that the ion beam has damaged the silicon wafer. More effort is needed to optimize the power and current of the beam to prevent this problem.

This sample is made with a lot of help from the Nanofab team of the Institut NÉEL and a FIB specialist, Jean-francois MOTTE.

6.5 Samples Made by Hexagonal Graphene

Considering the difficulties we had to pattern the graphene with oxygen plasma or FIB techniques, we took another approach for making suspended superconducting graphene devices: In this method, we transfer discrete hexagonal monocrystal graphene flakes on the electrodes rather than a continuous sheet. Skipping the step for patterning graphene is the main advantage of this recipe, however the geometry of the resultant membrane is not ideal for NEMS applications. Such kind of samples can only be used for probing Josephson junction properties in suspended graphene samples. Figure 6.6 shows some results we obtained.

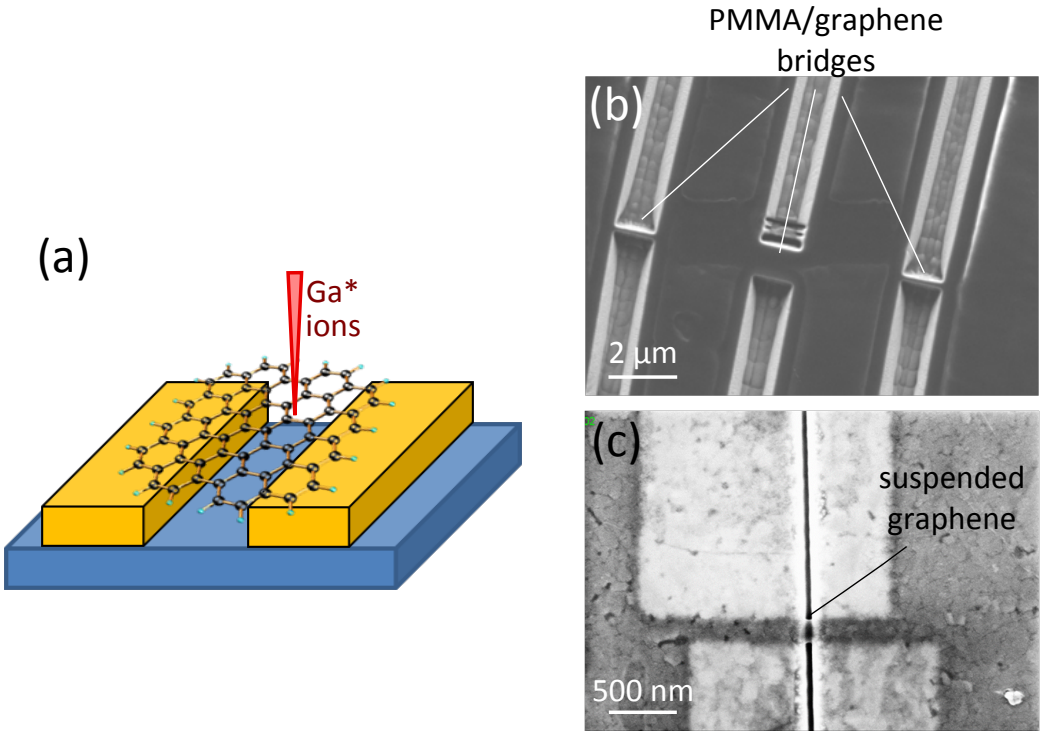

Figure 6.5: Focused ion beam for patterning suspended graphene samples
a) Basic principle of patterning graphene using FIB: Focused gallium ion beam is employed to cut graphene and pattern it.
b) Example of the sample after FIB patterning: The PMMA layer which is used for wet transferring graphene protects graphene from ion contamination.
c) Final device after removing the PMMA layer: Very fine and suspended structures can be made in this manner.

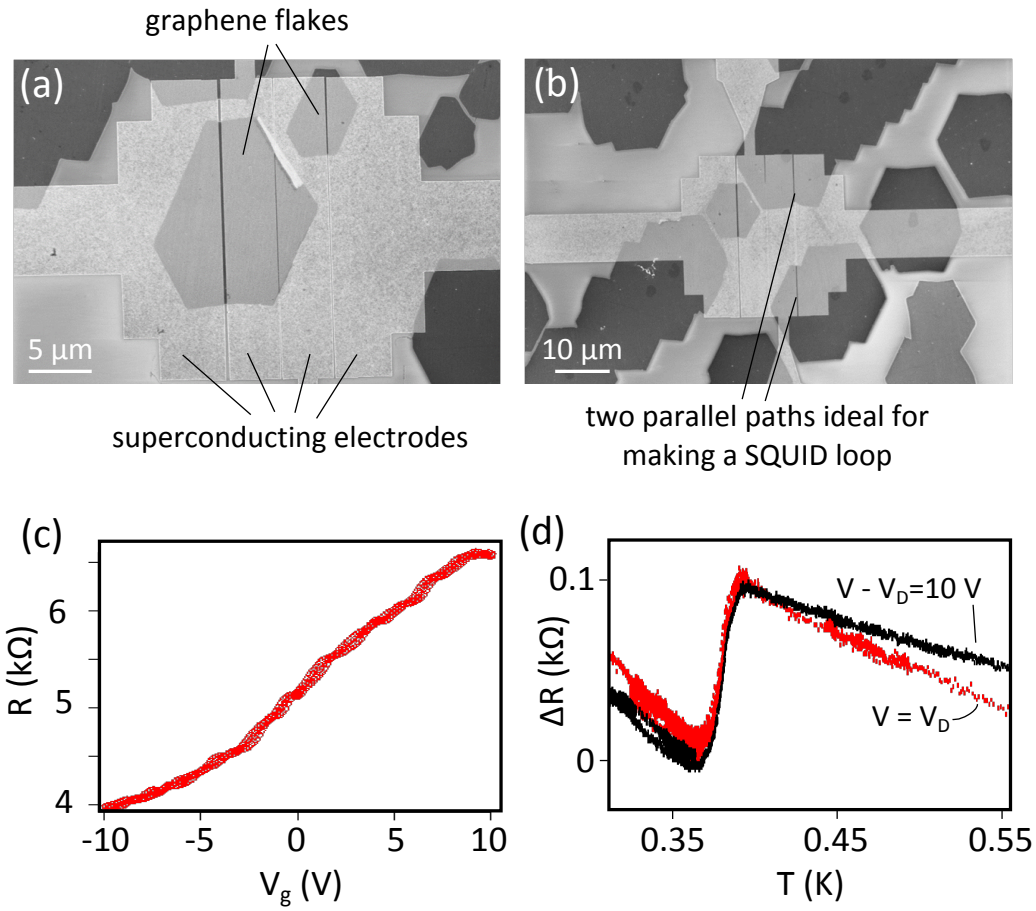

Figure 6.6: Hexagonal graphene for making suspended graphene-based Josephson junctions
a) SEM image of two hexagonal graphene grains transferred on superconducting Al electrodes with very short gap in between
b) Similar systems in which two parallel graphene grains resemble an SQUID loop
c) Two probe measurement of the resistance as a function of the gate voltage: This measurement has been performed on the small hexagonal graphene flake suspended over two left electrodes in b. d) Temperature dependency of the resistance of one of the the device in c: A sharp dip around 400 mK could be a signature of the proximity induction of superconductivity in graphene membrane. We have put the vertical axes in ΔR to simplify the comparison of the curves at two different gate voltages.

In this figure, the SEM images (panels *a* and *b*) show examples of the devices obtained in this technique. Very large contact area of graphene and the pads leads to low contact resistance. In panel *c*, one can see an example of the field effect curves, measured at 4 K. The Dirac point looks to be around 10 V and the gate tunability is good. During the cooling, a sharp drop of the resistance between 350 and 450 mK is seen, but the resistivity does not fall to zero and thus, full superconductivity is not achieved. This can be attributed to the high contact resistance.

6.6 Graphene Sandwitched Between Superconducting Layers

For the next generation of such samples, in order to reduce the contact resistance and after an step of e-beam lithography, a layer of tin is deposited on top of graphene; Thus graphene is sandwiched between two superconducting layers. Figure 6.7 shows the optical and SEM images of such samples. Unfortunately due to some problems with the fridge, we did not manage to cool this sample down and see how it behaves at low temperatures.

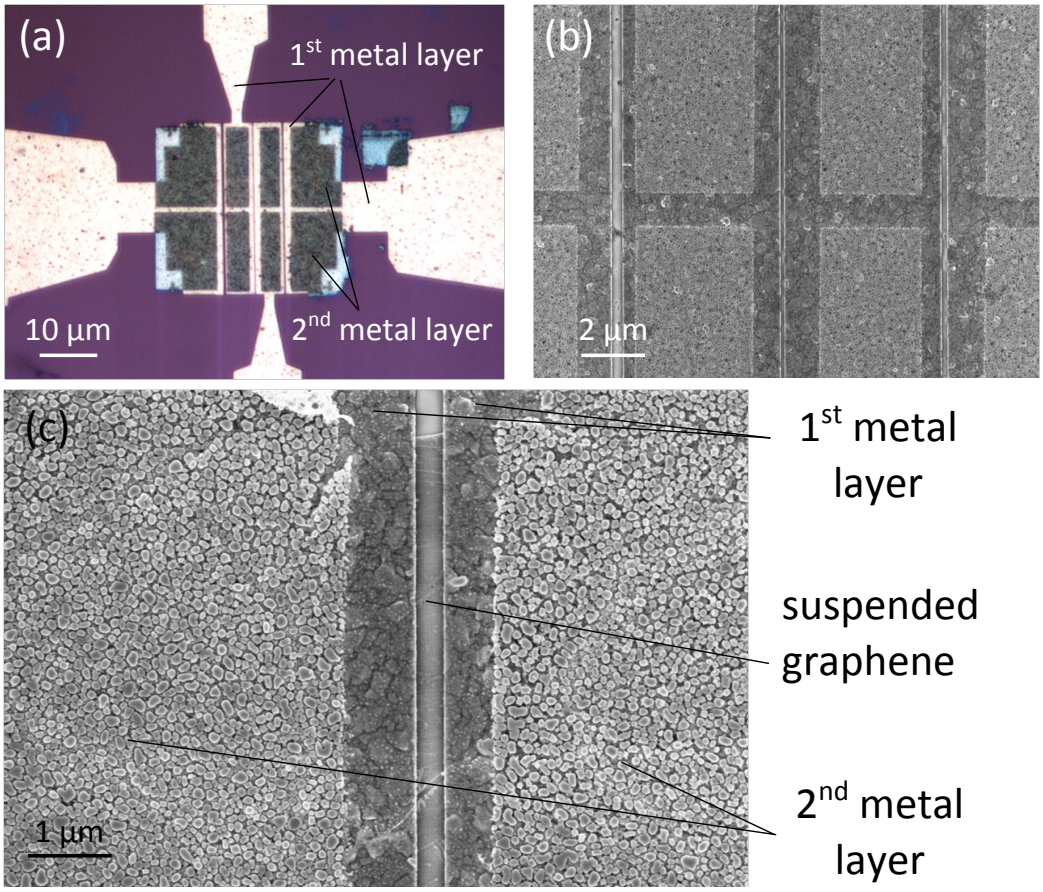

Figure 6.7: Suspended graphene sandwiched between superconducting electrodes Graphene as well as the bottom and top layers of tin electrodes are marked in the optical (a) and SEM images (b and c). Due to the small thickness of the material, tin at the top layer is deposited as isolated islands.

6.7 Exfoliated Graphene on Superconducting Electrodes

In this technique, after making a large array of superconducting electrodes, we mechanically exfoliate graphene on the sample hoping that by chance, we end up with a flake on top of the gap. Using high quality exfoliated graphene instead of CVD one as well as skipping the patterning step (in contrast to the case of large sheet of CVD graphene) are the main advantages of this technique over some

other previously utilized methods. However the yield is very low which makes the process very time consuming.

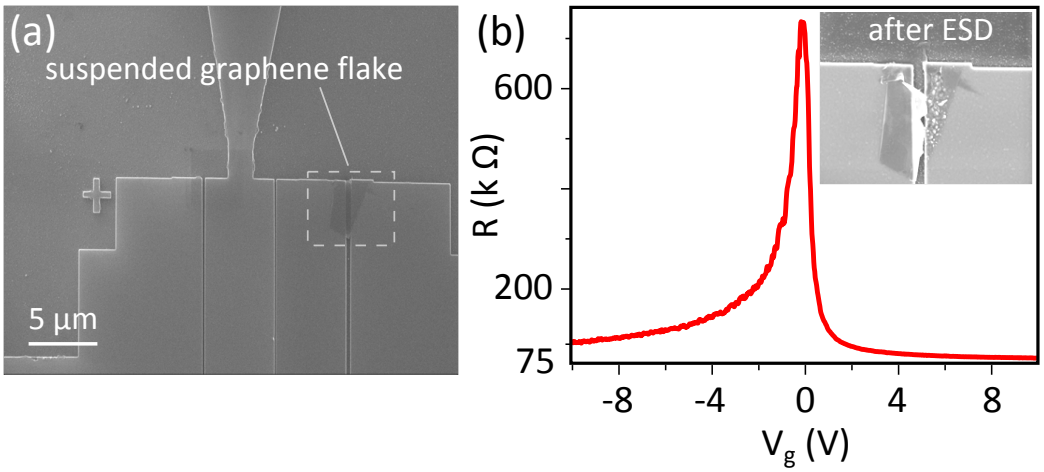

Figure 6.8: Exfoliated, suspended sample over superconducting electrodes
a) SEM image of a suspended graphene realized by directly exfoliating graphene on predefined array of superconducting electrodes
b) Corresponding field effect measurement at room temperature: Electrostatic discharge (ESD) killed the sample after mounting in the fridge for cooling. The inset shows the SEM image of the same sample after ESD.

The first device made (Figure 6.8) showed very nice transport properties: in a very small gate range, its resistance sweeps between 75 and 750 kΩ which is a signature of ultra high carrier mobilities. Very narrow Dirac peak and it position at exactly zero gate voltage points out that the population of the charged impurities is negligible which is due to the very clean fabrication procedure. Unfortunately this sample died very rapidly because of the electrostatic discharge and thus we did not managed to do more analyses on it. Afterwards, a lot of efforts to reproduce the same results were performed, but with no success.

Figure 6.9 shows another sample of this case. In the SEM image (*a*) we see a small graphene piece which is suspended over the trench. Our initial measurements (not included in this figure) did not show any remarkable field effect. The fact that this piece is very thick and is no more graphene, is the reason for this. I tried to mechanically exfoliate it using an AFM tip. In parts *b* and *c* one can see this flake before and after the manipulation. The thickness of this sample (*d*) measured along the dashed line in *c* shows that the thickness of the flake has indeed reduced a lot, but the field tunability (*e*) is still very weak. This sample died after further AFM manipulation.

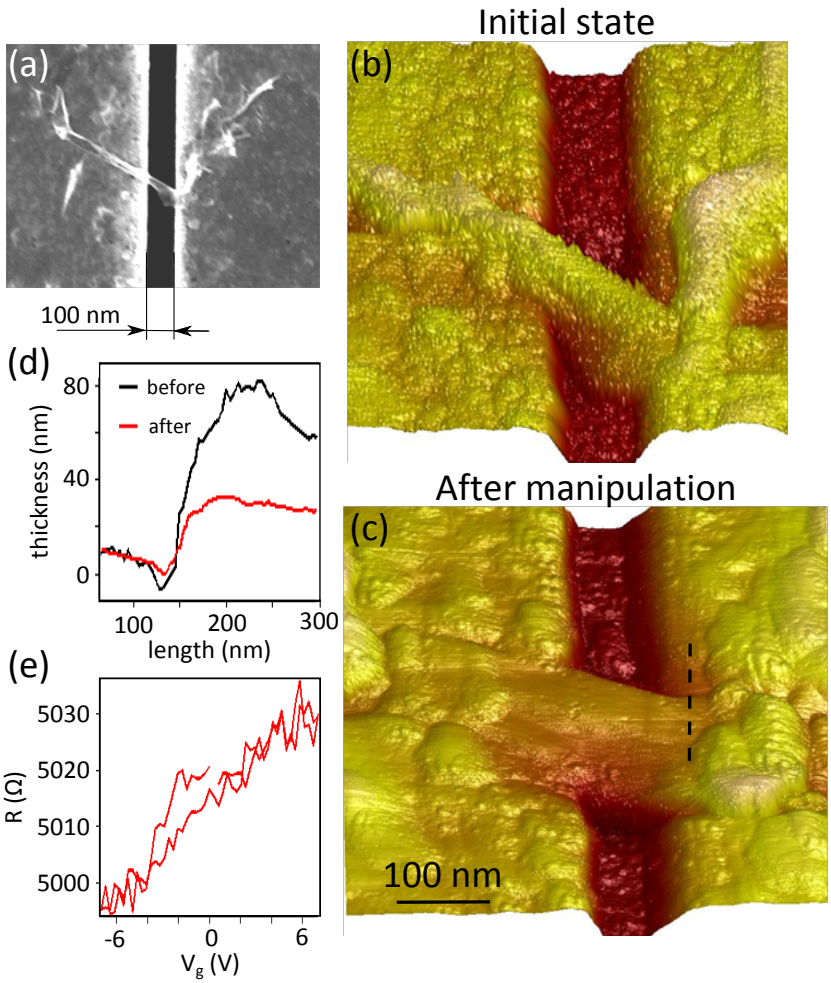

Figure 6.9: AFM manipulation to reduce the thickness of a suspended graphene flake
a) SEM image of a suspended graphene realized by directly exfoliating graphene on predefined array of superconducting electrodes
b) Corresponding AFM mapping of this sample at initial state
c) AFM mapping of the same sample after several steps of manipulation with AFM tip
d) Thickness profile of this flake before and after AFM manipulation measured along the dashed line marked in c
e) Corresponding field effect measurement after AFM manipulation

Acknowledgment

There are a lot of people who made this work possible. Foremost, I would like to express my sincere gratitude to my adviser Prof. Vincent Bouchiat for his strong support, for his patience, enthusiasm, and immense knowledge. His guidance has helped me throughout the duration of this research and the writing of this thesis. I feel incredibly privileged to have him as my supervisor.

My sincere thanks also goes to my former colleagues Adrien Allain and Zheng (Vitto) Han whom collaborated with me in different experiments addressed in this thesis. I was trained to use most of the fabrication and characterization techniques addressed in this thesis by them (e-beam lithography, SEM, graphene transferring and manipulation, etc). They also instructed me how to employ various experimental tools and instruments and taught me different measurement schemes. We have had plenty of nice discussions and they provided interesting ideas throughout my projects.

I would also like to give a heartfelt, special thanks to Laëtitia Marty for providing ideas for the improvement of this manuscript as well as the defense presentation. Her respectful demeanor led to a good working relationship and her gentle encouragements drove me towards favorable outcomes; I deeply believe that I would have had very difficult moments without her guidance.

Special thanks also go to the Nanoscience foundation and the nice people there not only for the financial support but also for the spiritual support during these years.

I am also thankful to Nedjma Bendiab for helping me with Raman measurements as well as the analysis, and also to John Landers whom kindly read this manuscript and polished my wrongful language. He has always been a polite and unforgettable friend.

Working inside the cleanroom, I have been aided in running the equipments by the Nanofab team of the Institut NÉEL; I would like to thank all the members of this team; especially Thierry Fournier and Thierry Crozes who helped me in developing fabrication recipes, Jean-Francois Motte who did FIB etching for me and Bruno Fernandez who kindly assisted me in the deposition of the materials.

Next, I would like to mention and thank Cécile Naud, Julien Renard and Johann Coraux for the insightful discussions regarding different topics covered in this thesis. Also, thanks goes to my other teammates in the Hybride group: Laurence Magaud, Amina Kimouche, Zoltan Osvath, Yani Chen, Dipankar Kalita, Cornelia Schwarz, Fabien Jean, Alexandre Artaud, Shashank Mathur, Mira Baraket and Sergio Vlaic for their collaborations in my projects and for the contributions they made which allowed me to live happily.

I am also very grateful to the other members of my dissertation committee: Martine Mayne, Anthony Ayari, Vincent Derycke, and Manuel Nunez-Regueiro. Their academic support and scientific input are greatly appreciated.

Of course no acknowledgments would be complete without giving thanks to my parents. They have taught me about hard working and self-respect, about persistence and how to be independent. Both have always expressed how proud they are of me and how much they love me. I am forever grateful.

Last, but certainly not least, I must acknowledge with deep thanks my wife, Zahra. Through her love, patience, support and unwavering belief in me, I have been able to complete this long dissertation journey. She has patiently endured many, many long hours alone while I worked on my projects. We have laughed together and she has also been kind when I needed to cry. Thank you with all my heart and soul.

Reference

[1] C. R. Dean, a. F. Young, I. Meric, C. Lee, L. Wang, S. Sorgenfrei, K. Watanabe, T. Taniguchi, P. Kim, K. L. Shepard, and J. Hone, "Boron nitride substrates for high-quality graphene electronics.," *Nature nanotechnology*, vol. 5, pp. 722–6, Oct. 2010.

[2] N. Petrone, C. R. Dean, I. Meric, A. M. van der Zande, P. Y. Huang, L. Wang, D. Muller, K. L. Shepard, and J. Hone, "Chemical vapor deposition-derived graphene with electrical performance of exfoliated graphene.," *Nano letters*, vol. 12, pp. 2751–6, June 2012.

[3] M. Yankowitz, J. Xue, D. Cormode, J. D. Sanchez-Yamagishi, K. Watanabe, T. Taniguchi, P. Jarillo-Herrero, P. Jacquod, and B. J. LeRoy, "Emergence of superlattice Dirac points in graphene on hexagonal boron nitride," *Nature Physics*, vol. 8, pp. 382–386, Mar. 2012.

[4] S. Tang, H. Wang, Y. Zhang, A. Li, H. Xie, X. Liu, L. Liu, T. Li, F. Huang, X. Xie, and M. Jiang, "Precisely aligned graphene grown on hexagonal boron nitride by catalyst free chemical vapor deposition.," *Scientific reports*, vol. 3, p. 2666, Jan. 2013.

[5] W. Yang, G. Chen, Z. Shi, C.-c. Liu, L. Zhang, G. Xie, M. Cheng, D. Wang, R. Yang, D. Shi, K. Watanabe, and T. Taniguchi, "Epitaxial growth of single-domain graphene on hexagonal boron nitride," *Nature materials*, no. July, pp. 792–797, 2013.

[6] a. K. Geim and K. S. Novoselov, "The rise of graphene.," *Nature materials*, vol. 6, pp. 183–91, Mar. 2007.

[7] C. Srinivasan, "Graphene -Mother of all graphitic materials," *Current Science*, vol. 92, no. 10, pp. 1338–1339, 2007.

[8] K. S. Novoselov, A. K. Geim, S. V. Morozov, D. Jiang, M. I. Katsnelson, I. V. Grigorieva, S. V. Dubonos, and A. A. Firsov, "Two-dimensional gas of massless dirac fermions in graphene," *Nature*, vol. 438, pp. 197–200, 2005.

[9] A. a. Balandin, S. Ghosh, W. Bao, I. Calizo, D. Teweldebrhan, F. Miao, and C. N. Lau, "Superior thermal conductivity of single-layer graphene.," *Nano letters*, vol. 8, pp. 902–7, Mar. 2008.

[10] S. Chen, Q. Wu, C. Mishra, J. Kang, H. Zhang, K. Cho, W. Cai, A. a. Balandin, and R. S. Ruoff, "Thermal conductivity of isotopically modified graphene.," *Nature materials*, vol. 11, pp. 203–7, Mar. 2012.

[11] A. Kuzmenko, E. van Heumen, F. Carbone, and D. van der Marel, "Universal Optical Conductance of Graphite," *Physical Review Letters*, vol. 100, p. 117401, Mar. 2008.

[12] Y. Zhang, Y.-W. Tan, H. L. Stormer, and P. Kim, "Experimental observation of the quantum Hall effect and Berry's phase in graphene.," *Nature*, vol. 438, pp. 201–4, Nov. 2005.

[13] X. Du, I. Skachko, F. Duerr, A. Luican, and E. Y. Andrei, "Fractional quantum Hall effect and insulating phase of Dirac electrons in graphene.," *Nature*, vol. 462, pp. 192–5, Nov. 2009.

[14] I. W. Frank, D. M. Tanenbaum, a. M. van der Zande, and P. L. McEuen, "Mechanical properties of suspended graphene sheets," *Journal of Vacuum Science & Technology B: Microelectronics and Nanometer Structures*, vol. 25, no. 6, p. 2558, 2007.

[15] C. Lee, X. Wei, J. W. Kysar, and J. Hone, "Measurement of the elastic properties and intrinsic strength of monolayer graphene.," *Science (New York, N.Y.)*, vol. 321, pp. 385–8, July 2008.

[16] H. B. Heersche, P. Jarillo-Herrero, J. B. Oostinga, L. M. K. Vandersypen, and A. F. Morpurgo, "Bipolar supercurrent in graphene.," *Nature*, vol. 446, pp. 56–9, Mar. 2007.

[17] X. Du, I. Skachko, and E. Andrei, "Josephson current and multiple Andreev reflections in graphene SNS junctions," *Physical Review B*, vol. 77, p. 184507, May 2008.

[18] H.-p. Boehm, R. Setton, and E. Stumpp, "Nomenclature and terminology of graphite," *Internaional Union of Pure and Solid State Chemistry*, vol. 66, no. 9, pp. 1893–1901, 1994.

[19] V. H. P. Boehm, A. Clauss, and G. O. F. U. Hofmann, "Dünnste Kohlenstoff-Folien," *Z. Naturforschg*, vol. 17 b, pp. 150–153, 1962.

[20] G. Ruess and F. Vogt, "Hochstlamellarer kohlenstoff aus graphitoxyhydroxyd," *Monatshefte fÃŒr Chemie und verwandte Teile anderer Wissenschaften*, vol. 78, pp. 222–242, 1948.

[21] C. Schafhaeutl, "On the combinations of carbon with silicon and iron, and other metals, forming the different species of cast iron, steel, and malleable iron," *Philosophical Magazine Series 3*, vol. 16, p. 570â90, 1840.

[22] E. Fradkin, "Critical behavior of disordered degenerate semiconductors," *Phys Rev B*, vol. 33, pp. 3263–3268, 1986.

[23] B. Z. Jang and W. C. Huang, "Nano-scaled graphene plates," 2002.

[24] J.-L. Li, K. Kudin, M. McAllister, R. Prudâhomme, I. Aksay, and R. Car, "Oxygen-driven unzipping of graphitic materials," *Physical Review Letters*, vol. 96, p. 176101, May 2006.

[25] Q. Liu, T. Fujigaya, and N. Nakashima, "Graphene unrolled from cup-stacked carbon nanotubes," *Carbon*, vol. 50, pp. 5421–5428, Dec. 2012.

[26] S. Horiuchi, T. Gotou, M. Fujiwara, R. Sotoaka, M. Hirata, K. Kimoto, T. Asaka, T. Yokosawa, Y. Matsui, K. Watanabe, and M. Sekita, "Carbon Nanofilm with a New Structure and Property," *Japanese Journal of Applied Physics*, vol. 42, pp. L1073–L1076, Sept. 2003.

[27] S. Horiuchi, T. Gotou, M. Fujiwara, T. Asaka, T. Yokosawa, and Y. Matsui, "Single graphene sheet detected in a carbon nanofilm," *Applied Physics Letters*, vol. 84, no. 13, p. 2403, 2004.

[28] K. S. Novoselov, a. K. Geim, S. V. Morozov, D. Jiang, Y. Zhang, S. V. Dubonos, I. V. Grigorieva, and a. a. Firsov, "Electric field effect in atomically thin carbon films.," *Science (New York, N.Y.)*, vol. 306, pp. 666–9, Oct. 2004.

[29] P. R. Wallace, "The band theory of graphite," *Physical Review*, vol. 71, pp. 622–634, 1947.

[30] S. Das Sarma, S. Adam, E. H. Hwang, and E. Rossi, "Electronic transport in two-dimensional graphene," *Reviews of Modern Physics*, vol. 83, pp. 407–470, May 2011.

[31] P. Drude, "Zur elektronentheorie der metalle," *Annalen der Physik*, vol. 306, 1900.

[32] E. Hwang, S. Adam, and S. Sarma, "Carrier Transport in Two-Dimensional Graphene Layers," *Physical Review Letters*, vol. 98, pp. 2–5, May 2007.

[33] A. S. Mayorov, R. V. Gorbachev, S. V. Morozov, L. Britnell, R. Jalil, L. a. Ponomarenko, P. Blake, K. S. Novoselov, K. Watanabe, T. Taniguchi, and a. K. Geim, "Micrometer-scale ballistic transport in encapsulated graphene at room temperature.," *Nano letters*, vol. 11, pp. 2396–9, June 2011.

[34] A. S. Mayorov, D. C. Elias, I. S. Mukhin, S. V. Morozov, L. a. Ponomarenko, K. S. Novoselov, a. K. Geim, and R. V. Gorbachev, "How close can one approach the Dirac point in graphene experimentally?," *Nano letters*, vol. 12, pp. 4629–34, Sept. 2012.

[35] L. Wang, I. Meric, P. Y. Huang, Q. Gao, Y. Gao, H. Tran, T. Taniguchi, K. Watanabe, L. M. Campos, D. a. Muller, J. Guo, P. Kim, J. Hone, K. L. Shepard, and C. R. Dean, "One-dimensional electrical contact to a two-dimensional material," *Science (New York, N.Y.)*, vol. 342, pp. 614–7, Nov. 2013.

[36] N. M. R. Peres, "The transport properties of graphene," *Journal of physics. Condensed matter : an Institute of Physics journal*, vol. 21, p. 323201, Aug. 2009.

[37] T. Stauber, N. Peres, and F. Guinea, "Electronic transport in graphene: A semiclassical approach including midgap states," *Physical Review B*, vol. 76, p. 205423, Nov. 2007.

[38] E. Hwang and S. Das Sarma, "Acoustic phonon scattering limited carrier mobility in two-dimensional extrinsic graphene," *Physical Review B*, vol. 77, p. 115449, Mar. 2008.

[39] S. Adam, E. H. Hwang, V. M. Galitski, and S. Das Sarma, "A self-consistent theory for graphene transport," *Proceeding of the National Academy of Sciences PNAS*, vol. 104, no. 47, pp. 18392–18397, 2007.

[40] Y. W. Tan, Y. Zhang, K. Bolotin, Y. Zhao, S. Adam, E. H. Hwang, S. Das Sarma, H. L. Stormer, and P. Kim, "Measurement of Scattering Rate and Minimum Conductivity in Graphene," *Physical Review Letters*, vol. 99, p. 246803, Dec. 2007.

[41] Y. Zhang, V. W. Brar, C. Girit, A. Zettl, and M. F. Crommi, "Origin of spatial charge inhomogeneity in graphene," *Nature Physics*, vol. 5, pp. 722–726, 2009.

[42] J. Martin, N. Akerman, G. Ulbricht, T. Lohmann, J. H. Smet, K. Von Klitzing, and A. Yacoby, "Observation of electronâhole puddles in graphene using a scanning single-electron transistor," *Nature Physics*, vol. 4, no. 2, pp. 144–148, 2007.

[43] J. M. Ziman, *Principles of the Theory of Solids*. Cambridge University Press, 1972.

[44] X. Du, I. Skachko, A. Barker, and E. Y. Andrei, "Approaching ballistic transport in suspended graphene.," *Nature nanotechnology*, vol. 3, pp. 491–5, Aug. 2008.

[45] D. R. Cooper, B. D. Anjou, N. Ghattamaneni, B. Harack, M. Hilke, N. Majlis, M. Massicotte, L. Vandsburger, E. Whiteway, V. Yu, B. D Anjou, A. Horth, and B. DâAnjou, "Experimental Review of Graphene," *ISRN Condensed Matter Physics*, vol. 2012, pp. 1–56, 2012.

[46] B. L. Altshuler, D. Khmel'Nitzkii, A. I. Larkin, and P. A. Lee, "Magnetoresistance and Hall effect in a disordered two-dimensional electron gas," , vol. 22, pp. 5142–5153, Dec. 1980.

[47] G. Bergmann, "Weak localization in thin films: a time-of-flight experiment with conduction electrons," *Physics*, vol. 107, p. 1â58, 1984.

[48] H. Suzuura and T. Ando, "Crossover from symplectic to orthogonal class in a two-dimensional honeycomb lattice," *Phys. Rev. Lett.*, vol. 89, p. 266603, Dec 2002.

[49] S. V. Morozov, K. S. Novoselov, M. I. Katsnelson, F. Schedin, L. A. Ponomarenko, D. Jiang, and A. K. Geim, "Strong Suppression of Weak Localization in Graphene," *Physical Review Letters*, vol. 97, p. 016801, 2006.

[50] F. V. Tikhonenko, D. W. Horsell, R. V. Gorbachev, A. K. Savchenko, and S. Road, "Weak localization in graphene flakes," *Physical Review Letters*, vol. 100, no. 5, p. 056802, 2008.

[51] X. Wu, X. Li, Z. Song, C. Berger, and W. a. de Heer, "Weak Antilocalization in Epitaxial Graphene: Evidence for Chiral Electrons," *Physical Review Letters*, vol. 98, p. 136801, Mar. 2007.

[52] F. V. Tikhonenko, a. a. Kozikov, a. K. Savchenko, and R. V. Gorbachev, "Transition between Electron Localization and Antilocalization in Graphene," *Physical Review Letters*, vol. 103, p. 226801, Nov. 2009.

[53] E. McCann, "Staying or going, chirality decides," *Physics*, vol. 2, 2009.

[54] J. Jain, *Composite Fermions*. Cambridge University Press, 2007.

[55] *http://www.physics.rutgers.edu/ aluican/research.html*.

[56] F. Beer, E. R. Johnston, J. DeWolf, and D. Mazurek, *Mechanics of Materials*. McGraw-Hill Science, 2011.

[57] N. Mounet and N. Marzari, "First-principles determination of the structural, vibrational and thermodynamic properties of diamond, graphite, and derivatives," *Physical Review B*, vol. 71, pp. 1–14, May 2005.

[58] V. Singh, S. Sengupta, H. S. Solanki, R. Dhall, A. Allain, S. Dhara, P. Pant, and M. M. Deshmukh, "Probing thermal expansion of graphene and modal dispersion at low-temperature using graphene nanoelectromechanical systems resonators.," *Nanotechnology*, vol. 21, p. 165204, Apr. 2010.

[59] M. S. Fuhrer and J. Hone, "Measurement of mobility in dual-gated MoS2 transistors.," *Nature nanotechnology*, vol. 8, pp. 146–7, Mar. 2013.

[60] B. Radisavljevic, a. Radenovic, J. Brivio, V. Giacometti, and a. Kis, "Single-layer MoS2 transistors.," *Nature nanotechnology*, vol. 6, pp. 147–50, Mar. 2011.

[61] L. a. Ponomarenko, a. K. Geim, a. a. Zhukov, R. Jalil, S. V. Morozov, K. S. Novoselov, I. V. Grigorieva, E. H. Hill, V. V. Cheianov, V. I. Falko, K. Watanabe, T. Taniguchi, R. V. Gorbachev, and V. I. Falâko, "Tunable metalâinsulator transition in double-layer graphene heterostructures," *Nature Physics*, vol. 7, pp. 958–961, Oct. 2011.

[62] a. K. Geim and I. V. Grigorieva, "Van der Waals heterostructures.," *Nature*, vol. 499, pp. 419–25, July 2013.

[63] L. Britnell, R. V. Gorbachev, R. Jalil, B. D. Belle, F. Schedin, A. Mishchenko, T. Georgiou, M. I. Katsnelson, L. Eaves, S. V. Morozov, N. M. R. Peres, J. Leist, a. K. Geim, K. S. Novoselov, and L. A. Ponomarenko, "Field-effect tunneling transistor based on vertical graphene heterostructures.," *Science (New York, N.Y.)*, vol. 335, pp. 947–50, Feb. 2012.

[64] D. Jena and A. Konar, "Enhancement of Carrier Mobility in Semiconductor Nanostructures by Dielectric Engineering," *Physical Review Letters*, vol. 98, p. 136805, Mar. 2007.

[65] C. Jang, S. Adam, J. H. Chen, E. D. Williams, S. Das Sarma, and M. S. Fuhrer, "Tuning the Effective Fine Structure Constant in Graphene: Opposing Effects of Dielectric Screening on Short- and Long-Range Potential Scattering," *Physical Review Letters*, vol. 101, p. 146805, Oct. 2008.

[66] a. Fasolino, J. H. Los, and M. I. Katsnelson, "Intrinsic ripples in graphene.," *Nature materials*, vol. 6, pp. 858–61, Nov. 2007.

[67] M. I. Katsnelson and a. K. Geim, "Electron scattering on microscopic corrugations in graphene.," *Philosophical transactions. Series A, Mathematical, physical, and engineering sciences*, vol. 366, pp. 195–204, Jan. 2008.

[68] M. Ishigami, J. H. Chen, W. G. Cullen, M. S. Fuhrer, and E. D. Williams, "Atomic structure of graphene on SiO2.," *Nano letters*, vol. 7, pp. 1643–8, June 2007.

[69] S. Morozov, K. Novoselov, M. Katsnelson, F. Schedin, D. Elias, J. Jaszczak, and a. Geim, "Giant Intrinsic Carrier Mobilities in Graphene and Its Bilayer," *Physical Review Letters*, vol. 100, p. 016602, Jan. 2008.

[70] C. H. Lui, L. Liu, K. F. Mak, G. W. Flynn, and T. F. Heinz, "Ultraflat graphene.," *Nature*, vol. 462, pp. 339–41, Nov. 2009.

[71] S. Babaee Touski and M. Pourfath, "Substrate surface corrugation effects on the electronic transport in graphene nanoribbons," *Applied Physics Letters*, vol. 103, no. 14, p. 143506, 2013.

[72] a. Deshpande, W. Bao, F. Miao, C. Lau, and B. LeRoy, "Spatially resolved spectroscopy of monolayer graphene on SiO2," *Physical Review B*, vol. 79, p. 205411, May 2009.

[73] L. Liu, S. Ryu, M. R. Tomasik, E. Stolyarova, N. Jung, M. S. Hybertsen, M. L. Steigerwald, L. E. Brus, and G. W. Flynn, "Graphene oxidation: thickness-dependent etching and strong chemical doping.," *Nano letters*, vol. 8, pp. 1965–70, July 2008.

[74] G. Giovannetti, P. Khomyakov, G. Brocks, P. Kelly, and J. van den Brink, "Substrate-induced band gap in graphene on hexagonal boron nitride: Ab initio density functional calculations," *Physical Review B*, vol. 76, p. 073103, Aug. 2007.

[75] K. S. Novoselov, a. K. Geim, S. V. Morozov, D. Jiang, Y. Zhang, S. V. Dubonos, I. V. Grigorieva, and a. a. Firsov, "Electric Field Effect in Atomically Thin Carbon Films SOM," *Science (New York, N.Y.)*, vol. 306, pp. 1–12, Oct. 2004.

[76] "The boron group: B, al, ga, in, tl," *http://131.104.156.23/lectures/231/231boron − group.htm*.

[77] "Boron nitride powder," *http://131.104.156.23/lectures/231/231boron − group.htm*.

[78] R. T. Weitz and A. Yacoby, "Nanomaterials: Graphene rests easy.," *Nature nanotechnology*, vol. 5, pp. 699–700, Oct. 2010.

[79] E. K. Sichel, R. E. Miller, M. S. Abrahams, and C. J. Buiocchi, "Heat capacity and thermal conductivity of hexagonal pyrolytic boron nitride," *Physical Review B*, vol. 13, no. 10, pp. 4607–4611, 1976.

[80] *Material Safety Data Sheet, polar therm boron nitride powder*.

[81] "Properties and characteristics of graphite for the semiconductor industry," *Entegris, Inc.*, vol. 29, May 2013.

[82] K. Watanabe, T. Taniguchi, and H. Kanda, "Direct-bandgap properties and evidence for ultraviolet lasing of hexagonal boron nitride single crystal.," *Nature materials*, vol. 3, pp. 404–9, June 2004.

[83] "Boron nitride," *http://en.wikipedia.org/wiki/Boron*$_{n}$*itride*.

[84] B. Stagg and T. Charalampopoulos, "Refractive indices of pyrolytic graphite, amorphous carbon, and flame soot in the temperature range 25Â° to 600Â°C," *Combustion and Flame*, vol. 94, pp. 381–396, Sept. 1993.

[85] "Graphite 2h properties," *http://www.phy.mtu.edu/ jaszczak/graphprop.html*.

[86] R. L. Powell and G. E. Childs, *American Institute of Physics Handbook*. Cambridge University Press, 1972.

[87] Y. Wang, V. W. Brar, W. Regan, H.-z. Tsai, Q. Wu, W. Gannett, A. Zettl, and M. F. Crommie, "Scanning Tunneling Microscopy," *Nano letters*, vol. 11, pp. 2291–2295, 2011.

[88] Z. V. Han, *Macroscopic CVD graphene for nanoelectronics: from growth to proximity-induced 2D superconductivity*. PhD thesis, university of Grenoble, 2013.

[89] J. W. Turrentine, "Action of ammonium persulphate on metals," *Journal of Physical Chemistry, Volume = 11, Issue = 8, Pages = 623â-631, Year = 1907*.

[90] C. R. Dean, A. F. Young, I. Meric, C. Lee, L. Wang, S. Sorgenfrei, K. Watanabe, T. Taniguchi, P. Kim, K. L. Shepard, and J. Hone, "Boron nitride substrates for high quality graphene electronics: Supplementary information," *Nature nanotechnology*, vol. 5, pp. 1–5, 2010.

[91] A. Allain, *Superconductivity induction in graphene doped by metalic nanoparticles*. PhD thesis, Grenoble, 2012.

[92] Y. Wu, V. Perebeinos, Y.-m. Lin, T. Low, F. Xia, and P. Avouris, "Quantum behavior of graphene transistors near the scaling limit.," *Nano letters*, vol. 12, pp. 1417–23, Mar. 2012.

[93] K. I. Bolotin, F. Ghahari, M. D. Shulman, H. L. Stormer, and P. Kim, "Observation of the fractional quantum Hall effect in graphene.," *Nature*, vol. 462, pp. 196–9, Nov. 2009.

[94] E. Mccann, K. Kechedzhi, H. Suzuura, T. Ando, and B. L. Altshuler, "Weak localisation magnetoresistance and valley symmetry in graphene," *Physical Review Letters*, vol. 97, no. 14, pp. 1–4, 2006.

[95] a. Morpurgo and F. Guinea, "Intervalley Scattering, Long-Range Disorder, and Effective Time-Reversal Symmetry Breaking in Graphene," *Physical Review Letters*, vol. 97, p. 196804, Nov. 2006.

[96] F. Pierre, a. Gougam, a. Anthore, H. Pothier, D. Esteve, and N. Birge, "Dephasing of electrons in mesoscopic metal wires," *Physical Review B*, vol. 68, p. 085413, Aug. 2003.

[97] L. Saminadayar, P. Mohanty, R. a. Webb, P. Degiovanni, and C. Bäuerle, "Electron coherence at low temperatures: The role of magnetic impurities," *Physica E*, vol. 40, pp. 12–24, Oct. 2007.

[98] H. B. Heersche, P. Jarillo-Herrero, J. B. Oostinga, L. M. K. Vandersypen, and a. F. Morpurgo, "Manifestations of phase-coherent transport in graphene," *The European Physical Journal Special Topics*, vol. 148, pp. 27–37, Sept. 2007.

[99] C. W. J. Beenakker and v. H. H, "Quantum transport in semiconductor nanostructures," *Solid State Physics*, vol. 44, p. 1â228, 1991.

[100] S. Das Sarma and E. H. Hwang, "Conductivity of graphene on boron nitride substrates," *Phys. Rev. B*, vol. 83, p. 121405(R), 2011.

[101] X. Ding, G. Ding, X. Xie, F. Huang, and M. Jiang, "Direct growth of few layer graphene on hexagonal boron nitride by chemical vapor deposition," *Carbon*, vol. 49, pp. 2522–2525, June 2011.

[102] M. Son, H. Lim, M. Honga, and H. C. Choi, "Direct growth of graphene pad on exfoliated hexagonal boron nitride surface," *Nanoscale*, vol. 3, pp. 3089–3093, 2011.

[103] S. Tang, G. Ding, X. Xie, J. Chen, C. Wang, X. Ding, F. Huang, W. Lu, and M. Jiang, "Nucleation and growth of single crystal graphene on hexagonal boron nitride," *Carbon*, vol. 50, pp. 329–331, Jan. 2012.

[104] J. Chen, Y. Guo, L. Jiang, Z. Xu, L. Huang, Y. Xue, D. Geng, B. Wu, W. Hu, G. Yu, and Y. Liu, "Near-equilibrium chemical vapor deposition of high-quality single-crystal graphene directly on various dielectric substrates," *Advanced materials (Deerfield Beach, Fla.)*, pp. 1348–1353, Dec. 2013.

[105] M. Wang, S. K. Jang, W.-J. Jang, M. Kim, S.-Y. Park, S.-W. Kim, S.-J. Kahng, J.-Y. Choi, R. S. Ruoff, Y. J. Song, and S. Lee, "A Platform for Large-Scale Graphene Electronics - CVD Growth of Single-Layer Graphene on CVD-Grown Hexagonal Boron Nitride.," *Advanced materials (Deerfield Beach, Fla.)*, vol. 25, pp. 2746–52, May 2013.

[106] S. Roth, F. Matsui, T. Greber, and J. Osterwalder, "Chemical vapor deposition and characterization of aligned and incommensurate graphene/hexagonal boron nitride heterostack on Cu(111).," *Nano letters*, vol. 13, pp. 2668–75, June 2013.

[107] Z. Liu, L. Song, S. Zhao, J. Huang, L. Ma, J. Zhang, J. Lou, and P. M. Ajayan, "Direct growth of graphene/hexagonal boron nitride stacked layers.," *Nano letters*, vol. 11, pp. 2032–7, May 2011.

[108] S. M. Kim, A. Hsu, P. T. Araujo, Y.-H. Lee, T. Palacios, M. Dresselhaus, J.-C. Idrobo, K. K. Kim, and J. Kong, "Synthesis of patched or stacked graphene and hBN flakes: a route to hybrid structure discovery.," *Nano letters*, vol. 13, pp. 933–41, Mar. 2013.

[109] M. I. Katsnelson, K. S. Novoselov, and A. K. Geim, "Chiral tunnelling and the Klein paradox in graphene," *Nature Physics*, vol. 2, no. September, 2006.

[110] "Moiré pattern," *http://en.wikipedia.org/wiki/Moire*$_{\mathrm{p}}$attern.

[111] J. Xue, J. Sanchez-Yamagishi, D. Bulmash, P. Jacquod, A. Deshpande, K. Watanabe, T. Taniguchi, P. Jarillo-Herrero, and B. J. LeRoy, "Scanning tunnelling microscopy and spectroscopy of ultra-flat graphene on hexagonal boron nitride.," *Nature materials*, vol. 10, pp. 282–5, Apr. 2011.

[112] R. Decker, Y. Wang, V. W. Brar, W. Regan, H.-z. Tsai, Q. Wu, W. Gannett, A. Zettl, and M. F. Crommie, "Local electronic properties of graphene on a BN substrate via scanning tunneling microscopy.," *Nano letters*, vol. 11, pp. 2291–2295, 2011.

[113] A. Eckmann, J. Park, H. Yang, D. Elias, A. S. Mayorov, G. Yu, R. Jalil, K. S. Novoselov, R. V. Gorbachev, M. Lazzeri, A. K. Geim, and C. Casiraghi, "Raman Fingerprint of Aligned Graphene/h-BN Superlattices.," *Nano letters*, vol. 13, pp. 5242–6, Nov. 2013.

[114] J. M. Garcia, U. Wurstbauer, A. Levy, L. N. Pfeiffer, A. Pinczuk, A. S. Plaut, L. Wang, C. R. Dean, R. Buizza, A. M. Van Der Zande, J. Hone, K. Watanabe, and T. Taniguchi, "Graphene growth on h-BN by molecular beam epitaxy," *Solid State Communications*, vol. 152, pp. 975–978, June 2012.

[115] J. M. Garcia, U. Wurstbauer, S. Wang, L. Fernandes, L. Wang, A. Levy, K. Watanabe, T. Taniguchi, C. R. Dean, L. N. Pfeiffer, J. Hone, and A. Pinczuk, "Graphene growth on h - BN by Van der Waals MBE," in *March Meeting 2013*, vol. 2, American Physical Society, APS, 2013.

[116] H. Search, C. Journals, A. Contact, M. Iopscience, and I. P. Address, "Epitaxial Growth of Organic Thin Films by Organic Molecular Beam Epitaxy," *Japanese Journal of Applied Physics*, vol. 28, no. 2, p. L306, 1989.

[117] K. Ueno, K. Sasaki, N. Takeda, K. Saiki, and A. Koma, "Nanostructure fabrication by selective growth of molecular crystals on layered material substrates," *Applied Physics Letters*, vol. 70, no. 9, p. 1104, 1997.

[118] K. Sasaki, K. Ueno, and A. Koma, "Nanostructure Fabrication Using Selective Growth on Nanosize Patterns Scanning Probe Microscope Drawn by a," *Japanese Journal of Applied Physics*, vol. 36, no. 6B, pp. 4061–4064, 1997.

[119] A. Koma, "Van der Waals epitaxyâa new epitaxial growth method for a highly lattice-mismatched system," *Thin Solid Films*, vol. 216, pp. 72–76, Aug. 1992.

[120] P.-Y. Teng, C.-C. Lu, K. Akiyama-Hasegawa, Y.-C. Lin, C.-H. Yeh, K. Suenaga, and P.-W. Chiu, "Remote catalyzation for direct formation of graphene layers on oxides.," *Nano letters*, vol. 12, pp. 1379–84, Mar. 2012.

[121] H. Kim, I. Song, C. Park, M. Son, M. Hong, Y. Kim, J. S. Kim, H.-J. Shin, J. Baik, and H. C. Choi, "Copper-Vapor-Assisted Chemical Vapor Deposition for High-Quality," *ACS nano*, vol. 7, no. 8, pp. 6575–6582, 2013.

[122] A. Zunger, A. Katzir, and A. Halperin, "Optical properties of hexagonal boron nitride," *Phys Rev B*, vol. 13, pp. 5560–5573, 1976.

[123] L. Wang, Z. Chen, C. R. Dean, T. Taniguchi, K. Watanabe, L. E. Brus, and J. Hone, "Negligible Environmental Sensitivity of Graphene in a Hexagonal Boron Nitride/Graphene/h-BN Sandwich Structure," *ACS nano*, vol. 6, no. 10, pp. 9314–9319, 2012.

[124] a. C. Ferrari, J. C. Meyer, V. Scardaci, C. Casiraghi, M. Lazzeri, F. Mauri, S. Piscanec, D. Jiang, K. S. Novoselov, S. Roth, and a. K. Geim, "Raman Spectrum of Graphene and Graphene Layers," *Physical Review Letters*, vol. 97, p. 187401, Oct. 2006.

[125] A. Eckmann, A. Felten, A. Mishchenko, L. Britnell, R. Krupke, K. S. Novoselov, and C. Casiraghi, "Probing the nature of defects in graphene by Raman spectroscopy.," *Nano letters*, vol. 12, pp. 3925–30, Aug. 2012.

[126] M. Hentschel and F. Guinea, "Orthogonality catastrophe and Kondo effect in graphene," *Physical Review B*, vol. 76, p. 115407, Sept. 2007.

[127] J.-H. Chen, W. Cullen, C. Jang, M. Fuhrer, and E. Williams, "Defect Scattering in Graphene," *Physical Review Letters*, vol. 102, p. 236805, June 2009.

[128] S. E. Lyshevski, *MEMS and NEMS Systems, Devices, and Structures*. CRC press, 2001.

[129] H. J. Mamin and D. Rugar, "Sub-attonewton force detection at millikelvin temperatures," *Applied Physics Letters*, vol. 79, no. 20, p. 3358, 2001.

[130] R. G. Knobel and A. N. Cleland, "Nanometre-scale displacement sensing using a single electron transistor.," *Nature*, vol. 424, pp. 291–3, July 2003.

[131] M. D. LaHaye, O. Buu, B. Camarota, and K. C. Schwab, "Approaching the quantum limit of a nanomechanical resonator.," *Science (New York, N.Y.)*, vol. 304, pp. 74–7, Apr. 2004.

[132] Y. T. Yang, C. Callegari, X. L. Feng, K. L. Ekinci, and M. L. Roukes, "Zeptogram-scale nanomechanical mass sensing.," *Nano letters*, vol. 6, pp. 583–6, Apr. 2006.

[133] A. Eichler, J. Moser, J. Chaste, M. Zdrojek, I. Wilson-Rae, A. Bachtold, and I. W. Rae, "Nonlinear damping in mechanical resonators made from carbon nanotubes and graphene.," *Nature nanotechnology*, vol. 6, pp. 339–42, June 2011.

[134] G. Binnig and C. F. Quate, "Atomic Force Microscope," *physical review letters*, vol. 56, no. 9, pp. 930–934, 1986.

[135] "Atomic force microscopy," *http://en.wikipedia.org/wiki/Atomic_force_microscopy*.

[136] M. Despont, J. Brugger, U. Drechsler, U. Durig, M. Lutwyche, H. Rothuizen, and W. Haberle, "VLSI-NEMS chip for parallel AFM data storage," *Sensors and Actuators A: Physical*, vol. 80, no. 2, pp. 100–107, 2000.

[137] J. S. Bunch, A. M. van der Zande, S. S. Verbridge, I. W. Frank, D. M. Tanenbaum, J. M. Parpia, H. G. Craighead, and P. L. McEuen, "Electromechanical resonators from graphene sheets.," *Science (New York, N.Y.)*, vol. 315, pp. 490–3, Jan. 2007.

[138] C. Chen, S. Rosenblatt, K. I. Bolotin, W. Kalb, P. Kim, I. Kymissis, H. L. Stormer, T. F. Heinz, and J. Hone, "Performance of monolayer graphene nanomechanical resonators with electrical readout-SOI," *Nature nanotechnology*, vol. 4, pp. 861–7, Dec. 2009.

[139] D. Garcia-Sanchez, A. M. van der Zande, A. S. Paulo, B. Lassagne, P. L. McEuen, and A. Bachtold, "Imaging mechanical vibrations in suspended graphene sheets.," *Nano letters*, vol. 8, pp. 1399–403, May 2008.

[140] A. M. Van Der Zande, R. a. Barton, J. S. Alden, C. S. Ruiz-Vargas, W. S. Whitney, P. H. Q. Pham, J. Park, J. M. Parpia, H. G. Craighead, and P. L. McEuen, "Large-Scale Arrays of Single-Layer Graphene Resonators.," *Nano letters*, pp. 4869–4873, Nov. 2010.

[141] R. a. Barton, B. Ilic, A. M. van der Zande, W. S. Whitney, P. L. McEuen, J. M. Parpia, and H. G. Craighead, "High, size-dependent quality factor in an array of graphene mechanical resonators.," *Nano letters*, vol. 11, pp. 1232–6, Mar. 2011.

[142] R. M. Westervelt, "Applied physics. Graphene nanoelectronics.," *Science (New York, N.Y.)*, vol. 320, pp. 324–5, Apr. 2008.

[143] V. Gouttenoire, T. Barois, S. Perisanu, J.-L. Leclercq, S. T. Purcell, P. Vincent, and A. Ayari, "Digital and FM demodulation of a doubly clamped single-walled carbon-nanotube oscillator: towards a nanotube cell phone.," *Small (Weinheim an der Bergstrasse, Germany)*, vol. 6, pp. 1060–5, May 2010.

[144] T. Kuila, S. Bose, A. K. Mishra, P. Khanra, N. H. Kim, and J. H. Lee, "Chemical functionalization of graphene and its applications," *Progress in Materials Science*, vol. 57, pp. 1061–1105, Sept. 2012.

[145] "Q factor," *http://en.wikipedia.org/wiki/Q_factor*.

[146] M. Poot and H. S. van der Zant, "Mechanical systems in the quantum regime," *Physics Reports*, vol. 511, pp. 273–335, Feb. 2012.

[147] B. Ilic, S. Krylov, K. Aubin, R. Reichenbach, and H. G. Craighead, "Optical excitation of nanoelectromechanical oscillators," *Applied Physics Letters*, vol. 86, no. 19, p. 193114, 2005.

[148] K. Aubin, B. Ilic, M. Zalalutdinov, R. B. Reichenbach, J. M. Parpia, and H. G. Craighead, "United States Patent," 2008.

[149] A. N. Cleland and M. L. Roukes, "Fabrication of high frequency nanometer scale mechanical resonators from bulk Si crystals," *Applied Physics Express*, vol. 69, no. June, pp. 2653–2655, 1996.

[150] K. L. Ekinci and M. L. Roukes, "Nanoelectromechanical systems," *Review of Scientific Instruments*, vol. 76, no. 6, p. 061101, 2005.

[151] D. W. Carr, S. Evoy, L. Sekaric, H. G. Craighead, and J. M. Parpia, "Measurement of mechanical resonance and losses in nanometer scale silicon wires," *Applied Physics Letters*, vol. 75, no. 7, pp. 920–922, 1999.

[152] M. Belov, N. J. Quitoriano, S. Sharma, W. K. Hiebert, T. I. Kamins, and S. Evoy, "Mechanical resonance of clamped silicon nanowires measured by optical interferometry," *Journal of Applied Physics*, vol. 103, no. 7, p. 074304, 2008.

[153] A. Reserbat-Plantey, L. Marty, O. Arcizet, N. Bendiab, and V. Bouchiat, "A local optical probe for measuring motion and stress in a nanoelectromechanical system," *Nature nanotechnology*, vol. 7, pp. 151–155, 2012.

[154] D. S. Greywall, B. Yurke, P. A. Busch, A. N. Pargellis, and R. L. Willett, "Evading Amplilier Noise in Nonlinear Oscillators," *Physical Review Letters*, vol. 72, pp. 2992–2995, Mar. 1994.

[155] S. Etaki, M. Poot, I. Mahboob, K. Onomitsu, H. Yamaguchi, and H. S. J. van der Zant, "Motion detection of a micromechanical resonator embedded in a d.c. SQUID," *Nature Physics*, vol. 4, pp. 785–788, Aug. 2008.

[156] B. H. Schneider, S. Etaki, H. S. J. van der Zant, and G. a. Steele, "Coupling carbon nanotube mechanics to a superconducting circuit," *Scientific reports*, vol. 2, p. 599, Jan. 2012.

[157] O. Usenko, a. Vinante, G. H. C. J. Wijts, and T. H. Oosterkamp, "A superconducting quantum interference device based read-out of a subattonewton force sensor operating at millikelvin temperatures," *Applied Physics Letters*, vol. 98, no. 13, p. 133105, 2011.

[158] Y. Xu, C. Chen, V. V. Deshpande, F. a. DiRenno, A. Gondarenko, D. B. Heinz, S. Liu, P. Kim, and J. Hone, "Radio frequency electrical transduction of graphene mechanical resonators," *Applied Physics Letters*, vol. 97, no. 24, p. 243111, 2010.

[159] T. S. Abhilash, J. P. Mathew, S. Sengupta, M. R. Gokhale, A. Bhattacharya, and M. M. Deshmukh, "Wide bandwidth nanowire electromechanics on insulating substrates at room temperature.," *Nano letters*, vol. 12, pp. 6432–5, Dec. 2012.

[160] V. Sazonova, Y. Yaish, H. Ustünel, D. Roundy, T. a. Arias, and P. L. McEuen, "A tunable carbon nanotube electromechanical oscillator.," *Nature*, vol. 431, pp. 284–7, Sept. 2004.

[161] A. van der Zande, *Atomically-thin graphene membranes*. PhD thesis, 2011.

[162] X. L. Feng, R. He, P. Yang, and M. L. Roukes, "Very High Frequency Silicon Nanowire Electromechanical Resonators," *Nano letters*, vol. 7, no. 7, pp. 1953–1959, 2007.

[163] M. Li, R. B. Bhiladvala, T. J. Morrow, J. a. Sioss, K.-K. Lew, J. M. Redwing, C. D. Keating, and T. S. Mayer, "Bottom-up assembly of large-area nanowire resonator arrays," *Nature nanotechnology*, vol. 3, pp. 88–92, Feb. 2008.

[164] Y. Tao, J. M. Boss, B. A. Moores, and C. L. Degen, "Single-Crystal Diamond Nanomechanical Resonators with Quality Factors > 1 Million," *arXiv:1212.1347 [cond-mat.mes-hall]*, 2012.

[165] Y. Tao and C. Degen, "Facile fabrication of single-crystal-diamond nanostructures with ultrahigh aspect ratio.," *Advanced materials (Deerfield Beach, Fla.)*, vol. 25, pp. 3962–7, Aug. 2013.

[166] A. Husain, J. Hone, H. W. C. Postma, X. M. H. Huang, T. Drake, M. Barbic, A. Scherer, and M. L. Roukes, "Nanowire-based very-high-frequency electromechanical resonator," *Applied Physics Letters*, vol. 83, no. 6, p. 1240, 2003.

[167] C.-Y. Nam, P. Jaroenapibal, D. Tham, D. E. Luzzi, S. Evoy, and J. E. Fischer, "Diameter-dependent electromechanical properties of GaN nanowires.," *Nano letters*, vol. 6, pp. 153–8, Feb. 2006.

[168] T. Henry, K. Kim, Z. Ren, C. Yerino, J. Han, and H. X. Tang, "Directed growth of horizontally aligned gallium nitride nanowires for nanoelectromechanical resonator arrays.," *Nano letters*, vol. 7, pp. 3315–9, Nov. 2007.

[169] B. Witkamp, M. Poot, and H. S. J. van der Zant, "Bending-mode vibration of a suspended nanotube resonator.," *Nano letters*, vol. 6, pp. 2904–8, Dec. 2006.

[170] D. Garcia-Sanchez, A. San Paulo, M. Esplandiu, F. Perez-Murano, L. Forró, A. Aguasca, and A. Bachtold, "Mechanical Detection of Carbon Nanotube Resonator Vibrations," *Physical Review Letters*, vol. 99, p. 085501, Aug. 2007.

[171] X. Li, W. Cai, J. An, S. Kim, J. Nah, D. Yang, R. Piner, A. Velamakanni, I. Jung, E. Tutuc, S. K. Banerjee, L. Colombo, and R. S. Ruoff, "Large-area synthesis of high-quality and uniform graphene films on copper foils," *Science (New York, N.Y.)*, vol. 324, pp. 1312–4, June 2009.

[172] N. Tombros, A. Veligura, J. Junesch, M. H. D. Guimarães, I. J. Vera-Marun, H. T. Jonkman, and B. J. van Wees, "Quantized conductance of a suspended graphene nanoconstriction," *Nature Physics*, vol. 7, pp. 697–700, June 2011.

[173] I. Kozinsky, H. W. C. Postma, I. Bargatin, and M. L. Roukes, "Tuning nonlinearity, dynamic range, and frequency of nanomechanical resonators," *Applied Physics Letters*, vol. 88, no. 25, p. 253101, 2006.

[174] H. S. Solanki, S. Sengupta, S. Dhara, V. Singh, S. Patil, R. Dhall, J. Parpia, A. Bhattacharya, and M. M. Deshmukh, "Tuning mechanical modes and influence of charge screening in nanowire resonators," *Physical Review B*, vol. 81, p. 115459, Mar. 2010.

[175] J. Atalaya, A. Isacsson, and J. M. Kinaret, "Continuum elastic modeling of graphene resonators.," *Nano letters*, vol. 8, pp. 4196–200, Dec. 2008.

[176] J. T. Robinson, M. Zalalutdinov, J. W. Baldwin, E. S. Snow, Z. Wei, P. Sheehan, and B. H. Houston, "Wafer-scale reduced graphene oxide films for nanomechanical devices.," *Nano letters*, vol. 8, pp. 3441–5, Oct. 2008.

[177] C. Chen, *Graphene NanoElectroMechanical Resonators and Oscillators*. PhD thesis, Columbia University, 2013.

[178] X. Song, M. Oksanen, M. a. Sillanpää, H. G. Craighead, J. M. Parpia, and P. J. Hakonen, "Stamp transferred suspended graphene mechanical resonators for radio frequency electrical readout.," *Nano letters*, vol. 12, pp. 198–202, Jan. 2012.

[179] A. K. Huttle, G. A. Steele, B. Witkamp, M. Poot, L. P. Kouwenhoven, and H. S. J. Van Der Zant, "Carbon nanotubes as ultrahigh quality factor mechanical resonator," *Nano letters*, vol. 9, no. 7, pp. 2547–2552, 2009.

[180] G. K. White and J. G. Collins, "Thermal expansion of copper, silver, and gold at low temperatures," *Journal of Low Temperature Physics*, vol. 7, pp. 43–75, Apr. 1972.

[181] F. C. Nix and D. MacNair, "Thermal expansion of pure metals, copper, gold, Aluminium, nickel and iron.pdf," *Physical Review Rev*, vol. 60, pp. 597–605, 1941.

[182] K. G. Lyon, G. L. Salinger, C. a. Swenson, and G. K. White, "Linear thermal expansion measurements on silicon from 6 to 340 K," *Journal of Applied Physics*, vol. 48, no. 3, p. 865, 1977.

[183] R. A. Suleimanov and N. A. Abdullaev, "The nature of negative linear expansion of graphite crystals," *Carbon*, vol. 31, no. 7, pp. 1011–1013, 1993.

[184] W. Bao, F. Miao, Z. Chen, H. Zhang, W. Jang, C. Dames, and C. N. Lau, "Controlled ripple texturing of suspended graphene and ultrathin graphite membranes.," *Nature nanotechnology*, vol. 4, pp. 562–6, Sept. 2009.

Index